# Letter from the Editors

Dear readers of *Acta Naturae*,

We are delighted to bring you the 20th issue of the journal. The Forum Section in this issue is unusual in the sense that it features a purely scientific communication by A.A. Kruglov and S.A. Nedospasov. Despite its seemingly frivolous title, it is a perfectly serious publication devoted to the approaches to the problem of solving an intriguing puzzle extremely important both for the understanding of the fundamental problems of biochemistry and human physiology and for practical issues in medicine. The authors attempted to pull back the veil on how the immune system provides a balance in the gut without, normally, allowing for the development of an inflammatory response by using as models transgenic mice that differ from common mice by defects in their cytokine expression in different cell types of both innate and adaptive immunity. It makes little sense to paraphrase the content of this communication here: we would only note that, based on the data collected through this work, the authors have just published a paper in *Science*, which, we have to admit, is a rare achievement for Russian scientists in our times. We congratulate A.A. Kruglov and S.A. Nedospasov and their co-authors on this outstanding feat and hope that this communication will reach a wide audience.

Furthermore, three reviews are brought to the reader's attention. The first (by E.A. Nikitina, et al.) is devoted to one of the most attractive models allowing one to directly connect the genes, brain, behavior, and cognitive functions to the so-called Williams syndrome. The second (by I.O. Petruseva et al.) is dedicated to nucleotide excision repair, and the third (by V.V. Makarov et al.) delves into the biotechnological approaches in the production of metal nanoparticles. It is, therefore, obvious that the topics of the reviews are very diverse, in conformity with the ideology of the journal.

The research articles also cover a broad range of topics. We believe (although our position is sometimes criticized) that such a wide scope of problems of modern biology in a century of increased specialization (up to a misunderstanding of the terminology of different biological specialties by many researchers) makes the journal invaluable in many ways. By the way, on this occasion, we would like to inform you that the portfolio of the editorial board is now full, which leaves us no choice but to be more stringent to submitted communications in the future. We express the hope that this attitude will be met with understanding among our readers and will further enhance the level of your (and our) publications.

Until next time! ●

*Editorial Board*

15-17 october 2014

SAINT-PETERSBURG

EXPOFORUM

St.Petersburg International HEALTH FORUM SPIHF

# ST. PETERSBURG INTERNATIONAL HEALTH FORUM

**MEDIZ SAINT-PETERSBURG**
Medicine and Health
www.mediz-spb.ru

**PHARMACY**
www.pharma.primexpo.ru

**BIOINDUSTRY**
www.bio.expoforum.ru

**HEALTHCARE TOURISM**
www.healthtourism.primexpo.ru

**VISUS-EXPO**
www.kmc-med.com

**AESTHETIC MEDICINE**
www.primexpo.ru

www.pmfz.expoforum.ru

+7 812 240 40 40

EXPOFORUM

0+

Messe Düsseldorf Moscow

primexpo

Конгресс • медиа центр МЕДИЦИНА XXI век

# Patient-Specific Induced Pluripotent Stem Cells for SOD1-Associated Amyotrophic Lateral Sclerosis Pathogenesis Studies

I. V. Chestkov, E. A. Vasilieva, S. N. Illarioshkin, M. A. Lagarkova, S. L. Kiselev

Amyotrophic lateral sclerosis (ALS) is an incurable neurodegenerative disorder that leads to the loss of upper and lower motor neurons. About 10% of cases are genetically inherited, and the most common familial form of ALS is associated with mutations in the *SOD1* gene. Patient-specific induced pluripotent stem (iPS) cells have been obtained These iPS cells have the properties of pluripotent cells and are capable of direct differentiation into motor neurons.

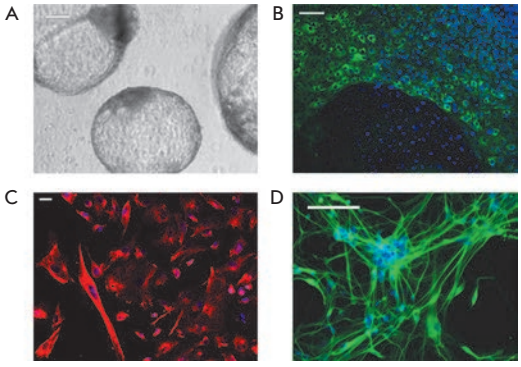


Spontaneous differentiation of iPS cells into three germ layers

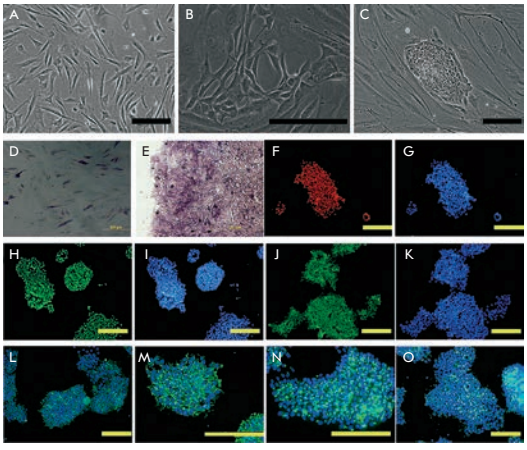


Generation of human iDP cells

# Reprogramming of Human Dermal Papilla Cells to Pluripotent State

I. A. Muchkaeva, E. B. Dashinimaev, A. S. Artyuhov, E. P. Myagkova, E. A. Vorotelyak, Y. Y. Yegorov, K. S. Vishnyakova, I. E. Kravchenko, P. M. Chumakov, V. V. Terskikh, A.V. Vasiliev

Dermal papilla (DP) cells are unique regional stem cells of the skin that induce the formation of hair follicle and its regeneration cycle. We generated induced pluripotent stem cells from human DP cells using lentiviral transfection with Oct4, Sox2, Klf4, and c-Myc, and addition of valproic acid at the physiological level of oxygen. The suitability of DP cells as an alternative source of iPS cells was demonstrated

# Fusion to the Lysosome Targeting Signal of the Invariant Chain Alters the Processing and Enhances the Immunogenicity of HIV-1 Reverse Transcriptase

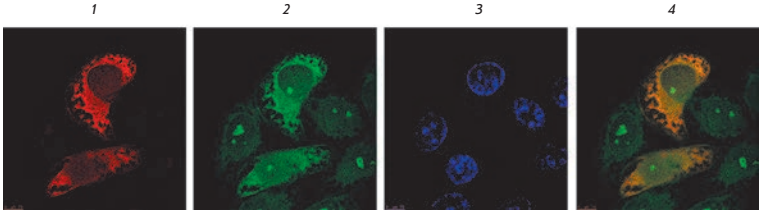


Intracellular localization of the chimeric RT-Ii

E. S. Starodubova, M. G. Isaguliants, Y. V. Kuzmenko, A. A. Latanova, O. A. Krotova, V. L. Karpov

Intracellular processing of the antigen encoded by a DNA vaccine is one of the key steps in generating an immune response. Immunization with DNA constructs targeted to the endosomal-lysosomal compartments and to the MHC class II pathway can elicit a strong immune response. The chimeric gene of HIV-1 reverse transcriptase was constructed. This gene encodes the recombinant protein with the N-terminal minimal lysosomal targeting motif of the human MHC class II invariant chain. DNA immunization of BALB/c mice with the plasmid encoding the chimeric protein enhances the immune response.

ActaNaturae
JANUARY–MARCH 2014 VOL. 6 №1 (20)

**Founders**
Ministry of Education and
Science of the Russian Federation,
Lomonosov Moscow State University,
Park Media Ltd



Address: 119234 Moscow, Russia, Leninskiye Gory, Nauchny
Park MGU, vlad.1, stroeniye 75G.
Phone/Fax: +7 (495) 930 88 50
E-mail: vera.knorre@gmail.com, mmorozova@strf.ru,
actanaturae@gmail.com



Номер подписан в печать 17 марта 2014 г.
Тираж 200 экз. Цена свободная.
Отпечатано в типографии «МЕДИА-ГРАНД»

**Indexed in Pubmed, Web of Science, Scopus, and RISC**

# CONTENTS

## SHORT REPORTS



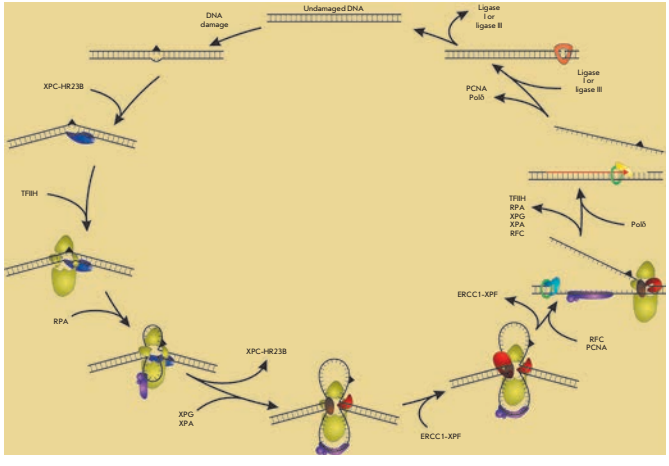


**IMAGE ON THE COVER PAGE**
Scheme of global genome excision repair for nucleotides (article by Petruseva et al.)

# Microbiota, Intestinal Immunity, and Mouse Bustle

A. A. Kruglov[1,3], S. A. Nedospasov[1,2,3*]
[1] Belozersky Research Institute of Physico-Chemical Biology and Department of Immunology, Biological Faculty, Lomonosov Moscow State University, Leninskie Gory, 1, 119991, Moscow, Russia
[2] Engelhardt Institute of Molecular Biology, Russian Academy of Sciences, Vavilova Str., 32, 119991, Moscow, Russia
[3] German Rheumatism Research Center, Chariteplatz 1, 10117, Berlin, Germany
* E-mail: sergei@nedos.net

The composition of the intestinal microbiota is regulated by the immune system. This paper discusses the role of cytokines and innate immunity lymphoid cells in the intestinal immune regulation by means of IgA.

Our gut is filled with quadrillions of symbionts, commensal bacteria that fulfill, as demonstrated by Honda and Littman [1], additional functions useful to the host. The discovery of the mechanisms that regulate innate immunity has brought forth a surprising riddle: how does the immune system establish a balance in the intestines that does not allow an inflammatory response to develop. Indeed, pattern recognition receptors on the cells of innate immunity, such as macrophages and dendritic cells, recognize commensal bacteria in the same way as they recognize opportunistic pathogenic and pathogenic bacteria. As a result of such recognition, defense reactions are triggered that may be dangerous to the host.

Another aspect of the problem relates to the use of antibiotics, because "good" bacteria respond to antibiotics in about the same way as pathogenic ones do. Recently, Ubeda *et al* [2] demonstrated convincingly that, upon systemic antibiotic therapy, undesirable pathophysiological reactions may develop in model organisms, up to the formation of neoplasia. A new concept has emerged, holding that commensal bacteria are "tuning" the immune system in the gut, providing it with a "tonic" signal.

Analysis of the diversity of commensal organisms in the human gut and in experimental animals (microbiota) conducted using new technologies over recent years has led to the understanding that not only a predisposition to various diseases, but also the response to the therapy depend on microbiota composition.

Intestinal immunity is provided by the same tools that the immune system generally has. These include lymphoid organs (Peyer's patches and lymph nodes draining the intestine), the arsenal of innate immune cells (part of which perform regulatory functions), and lymphocytes that, in particular, produce protective antibodies (*Fig. 1*).

Antibodies, primarily IgA, participate in both the protection of the gut and in the regulation of the intestinal microbiota composition. For their production, B-lymphocytes, which initially express membrane-bound antibodies of the IgM type, need to first reach the gut compartments associated with immune responses and, then, "switch," under the influence of the microenvironment and soluble factors, to the production of IgA and to become plasma cells (*Fig. 1*). Several mechanisms responsible for the recruitment of B-lymphocytes into the intestinal lamina propria and for their switching to IgA production are known.

Unique mice were previously generated in our laboratory and used to study the mechanisms controlling the production of IgA antibodies in the intestine [3]. These models employed the methods of "reverse genetics," in particular, the so-called "conditional knockout" in mice. Such technology is based on manipulations with embryonic stem cells and, for mammals, was developed only for rodents, such as mice and (very recently) rats. This explains why most of the information about immunity mechanisms has been obtained primarily in mice.

By using the conditional knockout technology, we generated unique mice that differed from wild type mict by defects in cytokine expression in different types of cells of both innate and adaptive immunity. If the phenotypic difference, such as functional defects

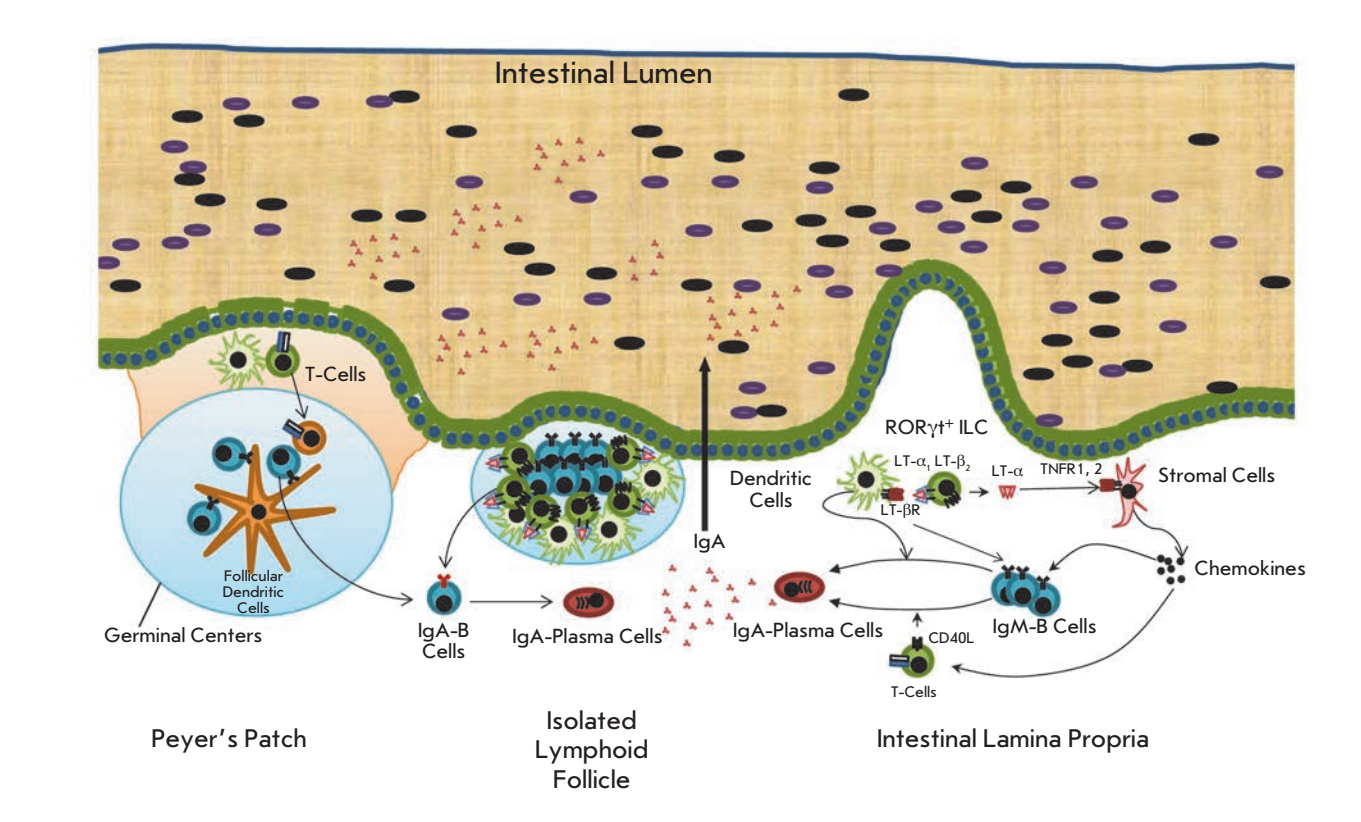


Fig. 1. The lymphoid system in the small intestine and a scheme of the IgA production. The switch to IgA can be induced in the Peyer's patches, isolated lymphoid follicles, and in lamina propria. In the lamina propria, IgA induction is controlled by LT-α and LT-β, which are produced by type III innate lymphoid cells

in the intestinal immune system are observed in these mice, then the function of a certain cytokine produced by a specific cell type can be deduced.

One of the areas of our research interests is the cytokines of the tumor necrosis factor (TNF) family; in particular, the lymphotoxins (LT) α and β. These two molecules form a single membrane complex. It was, therefore, believed that most of the physiological functions of LTα and LTβ coincide, because the signal is transmitted through a single receptor, the LT-β receptor (TNFRSF3). At the same time, lymphotoxin-α can occur in soluble trimeric form. In this case, it is very similar to the classic TNF and uses its receptors (p55 and p75). To date, separate, unique (non-redundant) functions of soluble LT-α *in vivo* have not been demonstrated: so the TNF-like properties of this cytokine *in vitro* have been perceived as a curiosity.

However, when we "turned off" the LT-α and LT-β genes in type III innate lymphoid cells (ILC3), which are characterized by the expression of the RORyt transcription factor, we detected differences that allowed us to suggest a new mechanism for immunity regulation in the gut.

It turns out that, on one hand, the LT-α/LT-β membrane complex, when transmitting a signal from ILC to stromal and dendritic cells, regulates the recruitment of B-lymphocytes of the B1 and B2 types to lamina propria and triggers the controls antibody isotype switch through a special mechanism in which reactive nitrogen species play an important role (*Fig. 1*). On the other hand, soluble trimeric LT-α, acting through the TNF receptors, recruits not only B-, but also T-lymphocytes, and these are T-lymphocytes that regulate the switch from IgM to IgA and that express a ligand for the CD40 receptor of B-lymphocytes (*Fig. 1, 2*).

Thus, we stumbled on the function of LT-α (different from LT-β) *in vivo*, and this paradoxical TNF-like function of soluble trimeric LT-α is associated with the regulation of IgA production in the intestines and with microbiota composition control (*Fig. 2*).

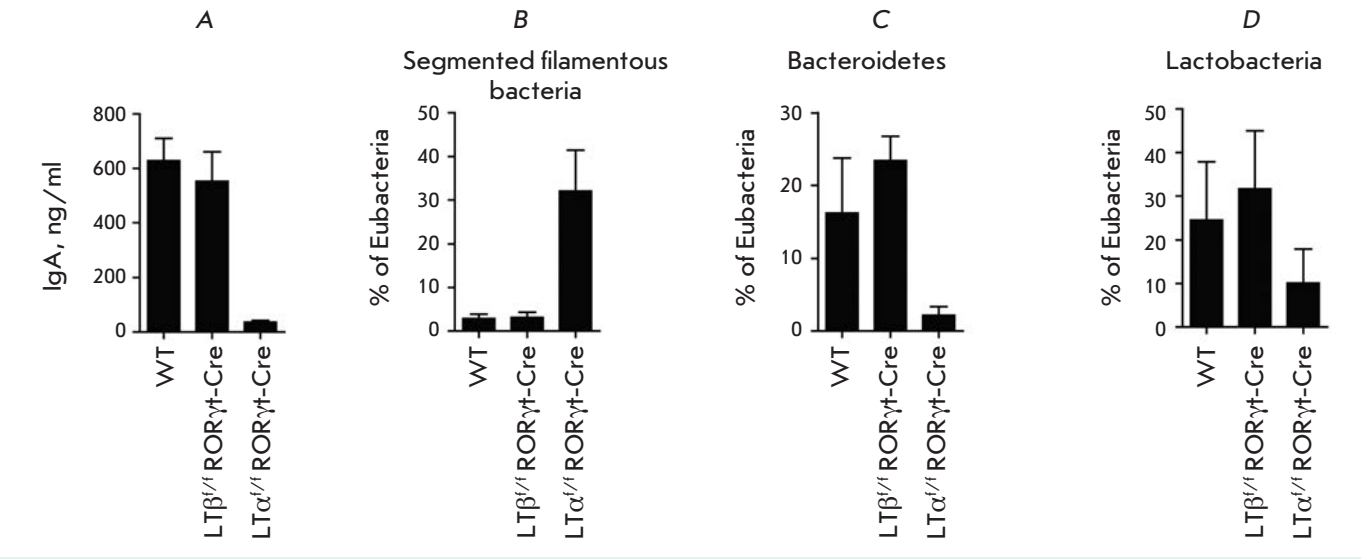


Fig. 2. The role of LT-α and LT-β, produced by type III innate lymphoid cells, in the control of IgA and in regulation of microbiota composition. *A* - the IgA content in the feces of wild type (WT) mice and mice with deletion of the gene LT-α ($LT\alpha^{f/f}$RORγt-Cre) and LT-β ($LT\beta^{f/f}$RORγt-Cre) in type III innate lymphoid cells. *B* - fraction of segmented filamentous bacteria, *C* – Bacteroidetes, and *D* - Lactobacteria in the contents of the terminal ileum of WT mice, $LT\alpha^{f/f}$RORγt-Cre, and $LT\beta^{f/f}$RORγt-Cre

An important clinical aspect of our study that needs further investigation is the fact that one of the most popular therapeutic TNF inhibitors, etanercept (Enbrel), which is already being used in millions of patients with rheumatoid arthritis, blocks soluble LT-α. Before our study, it had been believed that this cytokine has no individual functions, and so its inhibition had not been considered as a potential source of side effects.

Interestingly, the only known type of autoimmune diseases, when all TNF inhibitors, except for etanercept, are effective, is actually intestinal inflammatory pathologies [4]. An explanation of this paradox has yet to be provided... ●

REFERENCES
1. Honda K., Littman D.R. // Annu. Rev. Immunol. 2012. V. 30. P. 759–795.
2. Ubeda C., Taur Y., Jenq R.R., Equinda M.J., Son T., Samstein M., Viale A., Socci N.D., van den Brink M.R., Kamboj M., Pamer E.G. // J. Clin. Invest. 2010. V. 120. P. 4332–4341.
3. Kruglov A.A., Grivennikov S.I., Kuprash D.V., Winsauer C., Prepens S., Seleznik G.M., Eberl G., Littman D., Tumanov A.V., Nedospasov S.A. // Science. 2013. V. 342. № 6163. P. 1243–1246.
4. Sandborn W.J., Hanauer S.B., Katz S., Safdi M., Wolf D.G., Baerg R.D., Tremaine W.J., Johnson T., Diehl N.N., Zinsmeister A.R. // Gastroenterology. 2001. V. 121. P. 1088–1094.

# Williams Syndrome As a Model for Elucidation of the Pathway Genes – the Brain – Cognitive Functions: Genetics and Epigenetics

E. A. Nikitina[1,2*], A. V. Medvedeva[1,3], G. A. Zakharov[1,3], E. V. Savvateeva-Popova[1,3]
[1]Pavlov Institute of Physiology, Russian Academy of Sciences, nab. Makarova, 6, 199034, St. Petersburg, Russia
[2]Herzen State Pedagogical University, nab. r. Moyki, 48, 191186, St. Petersburg, Russia
[3]Saint Petersburg State University, Universitetskaya nab., 8-9, 199034, St. Petersburg, Russia
*E-mail: 21074@mail.ru
Received 16.07.2013


**ABSTRACT** **Genomic diseases or syndromes with multiple manifestations arise spontaneously and unpredictably as a result of contiguous deletions and duplications generated by unequal recombination in chromosomal regions with a specific architecture. The Williams syndrome is believed to be one of the most attractive models for linking genes, the brain, behavior and cognitive functions. It is a neurogenetic disorder resulting from a 1.5 Mb deletion at 7q11.23 which covers more than 20 genes; the hemizigosity of these genes leads to multiple manifestations, with the behavioral ones comprising three distinct domains: 1) visuo-spatial orientation; 2) verbal and linguistic defect; and 3) hypersocialisation. The shortest observed deletion leads to hemizigosity in only two genes: *eln* and *limk1*. Therefore, the first gene is supposed to be responsible for cardiovascular pathology; and the second one, for cognitive pathology. Since cognitive pathology diminishes with a patient's age, the original idea of the crucial role of genes straightforwardly determining the brain's morphology and behavior was substituted by ideas of the brain's plasticity and the necessity of finding epigenetic factors that affect brain development and the functions manifested as behavioral changes. Recently, non-coding microRNAs (miRs) began to be considered as the main players in these epigenetic events. This review tackles the following problems: is it possible to develop relatively simple model systems to analyze the contribution of both a single gene and the consequences of its epigenetic regulation in the formation of the Williams syndrome's cognitive phenotype? Is it possible to use *Drosophila* as a simple model system?**
**KEYWORDS** **Williams syndrome; LIMK1; non-coding RNAs; *Drosophila*.**
**ABBREVIATIONS** **WBS – Williams-Beuren syndrome; LCR – low copy repeat; NAHR – non-allelic homologous recombination; miRs – microRNAs.**

## WILLIAMS SYNDROME AND DISCOVERY OF GENOTYPE-PHENOTYPE CORRELATIONS

In 1961, J.C.P Williams, summarizing his observations in four patients, suggested that "the simultaneous occurrence of supravalvular stenosis and typical physical and mental characteristics correspond to a new syndrome that was not previously reported" [1]. Soon after, in 1962, A.J. Beuren described another 11 similar patients. All of them displayed specific facial features and mental retardation, along with supravalvular aortic stenosis [2]. Since then, the eponym "Williams–Beuren syndrome (WBS)" has become a common name for this set of symptoms, which is also often known as the Williams syndrome. This syndrome occurs due to a deletion spanning 1,500 kb at the q11.23 region of human chromosome 7. The specific architecture of this region predisposes it to unequal recombination. The deletion covers about 20 genes; the hemizygosity of these genes has multiple effects: a specific, "elfin" facial appearance (*Fig. 1*), developmental disorders, a variety of cardiovascular diseases, neurological abnormalities and cognitive features, hypersocialisation, and musical talent [3]. This combination of unusual properties has been intriguing and has attracted neuroscientists as an opportunity to understand the modular principle of mental abilities and social behavior structure, reflecting the features of brain development. Over the past 20 years, the Williams syndrome has been considered to be one


Fig. 1. Distinctive facial appearance of persons with WBS (A) [5]. Young child with WBS at the age of 15 months (B) and 3 years (C). Note subtle characteristic facial features, including wide mouth, chubby cheeks, long philtrum, small nose, and delicate chin. The same patient is shown in *Figs. 1B, 1C, and 1D (left; 21 years)*; another individual with WBS aged 28 years is shown in *Fig. 1D (right)* [3]

of the most attractive models that directly link genes, the brain, behavior, and cognitive functions [4, 5].

Neurological abnormalities include hyperactivity, as well as deficiency of motor coordination and gait [6, 7]. Cognitive manifestations are very specific; for this reason, they are used to diagnose WBS in young children, along with neurological symptoms. The first manifestation is a pronounced deficiency in visuo-spatial orientation; patients cannot reproduce the shape of an object in standard tests, but they can reflect all its parts (*Fig. 2*) [8].

Visuo-spatial construction is the ability to perceive an object or a picture as a set of parts and then use these parts to build a replica (i.e., an exact copy or reproduction of what a person saw). People use visuo-spatial construction when they draw, button up a shirt, make their bed, create models of sailing ships and aircrafts, piece together LEGO building blocks, or furniture purchased unassembled at an IKEA store. Visuo-spatial construction is very important in daily life; for this reason, it is considered to be the central cognitive ability. Therefore, measuring this ability is an integral part of any complete testing of the mental abilities of an individual.

Japanese children with visuo-spatial construction deficiency have difficulty when learning hieroglyphic writing [9]. When requested to draw a bicycle, children

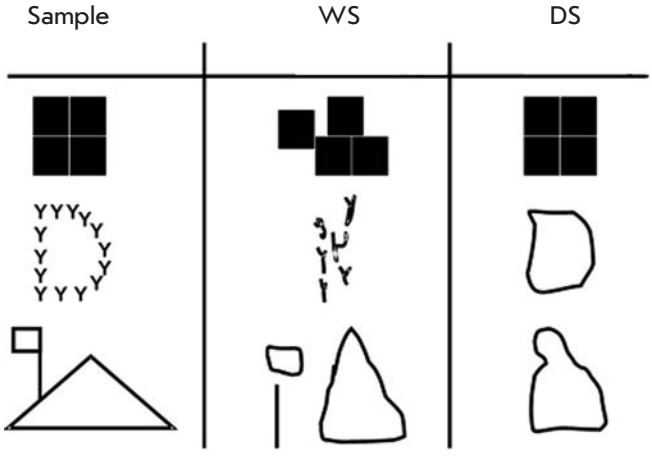


Fig. 2. Visuo-spatial deficiency in WBS patients [8]. Left: images the patients were asked to draw. Middle: WS – WBS patients reproduce only disconnected elements, ignoring the global form. Right: DS – Down syndrome patients (age- and IQ-matched) reproduce only the global forms. This figure demonstrates a featural perception in WBS patients compared with a holistic perception in DS patients

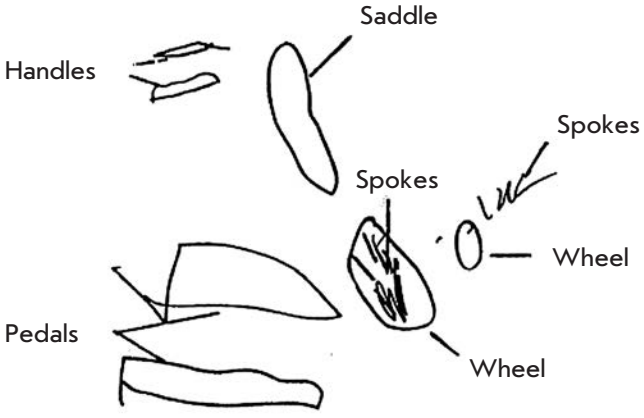


Fig. 3. Drawings of a bicycle by a girl aged 9 years 7 months with the Williams syndrome [10]

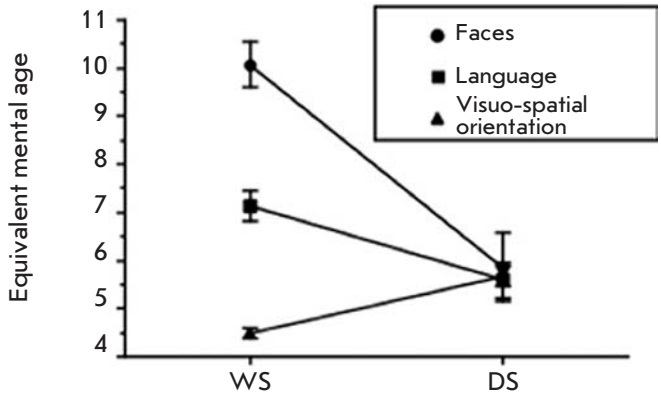


Fig. 4. Three distinct domains of cognition in Williams syndrome (WS) patients and Down syndrome (DS) patients (age- and IQ-matched) [5]. Labels: Faces – fixation on faces; Language – linguistic abilities; Visuo-spatial – visuo-spatial orientation. Patients with DS demonstrate equally low levels of all the parameters of cognitive ability as expected in mental deficiency. Patients with WBS show pronounced defects of visuo-spatial orientation, have reduced linguistic abilities, and show extreme hypersocialization (fixing on the faces of onlookers)

draw an image including separate, clearly reproduced and signed items: handles, a saddle, pedals, wheels, and spokes (*Fig. 3*) [10]. Furthermore, many patients have neither binocular vision nor normal perception of space and its depth. For this reason, they face daily challenges when walking or playing games on uneven surfaces. The second manifestation is the immensely high level of evaluative vocabulary in prejudice of grammar, when plenty of emotional interjections, sighs and accents serve as a "hook" to attract and hold the attention of onlookers. This is related to the third manifestation, hypersocialisation: i.e., the need to establish contact with any persons, including strangers, unusually high sympathy for them, and the desire to make everyone happy. This manifestation is currently considered to be one of the leading cognitive features; regardless of the proposed test, patients always closely examine the faces of the experimenters, ignoring the matter of the test [11]. Thus, cognitive impairment in the Williams syndrome patients includes a triad of manifestations: 1) a pronounced deficiency of visuo-spatial orientation; 2) intermediate verbal-linguistic defect, varying depending on the complexity of the language culture; and 3) unusually intense gaze with fixation on faces (*Fig. 4*).

The life inconveniences caused by manifestations of this triad are compensated for by the high musical talent. Every patient perfectly plays a musical instrument or sings. Unusually, high thirst for music allows them to perceive and reproduce the phenomena of the world in musical, rather than visual, images. Thus, magnetic resonance imaging of the brain shows activation of the visual cortex upon presentation of music or any sound stimuli in patients with WBS, unlike their healthy peers [12]. On the one hand, the phenomenon of WBS redefines the old stereotypes. Is it true that everything should be perfect in a person? Is it important for us whether Paganini, Beethoven, and Bach could draw well? On the other hand, clear and discrete cognitive manifestations constantly inspire to associate them with a certain gene, falling within deletion critical for WBS. Let us recall the mechanism of genomic disease occurrence: i.e., deletion-duplication syndromes.

## NON-ALLELIC RECOMBINATION PRODUCING THE WILLIAMS SYNDROME

Genomic diseases or syndromes with multiple manifestations occur spontaneously and unpredictably (sporadically) as a result of extensive deletions and duplications generated due to unequal recombination in chromosomal regions with a specific architecture. These are the Williams syndrome in 7q11.23 [3], Smith-Magenis syndrome in 17p11.2 [13], DiGeorge syndrome in 22q11.2 [14], Prader-Willi and Angelman syndrome in 15q11-q13 [15], duplication syndrome (17) (p11.2p11.2), and syndromes with Y-chromosome deletions [16]. A high frequency of such structural rearrangements of the genome, significantly exceeding the frequency of occurrence of a disease due to mutations of a single gene, drew the attention of clinicians and led to the appearance of the concept of "genomic diseases."

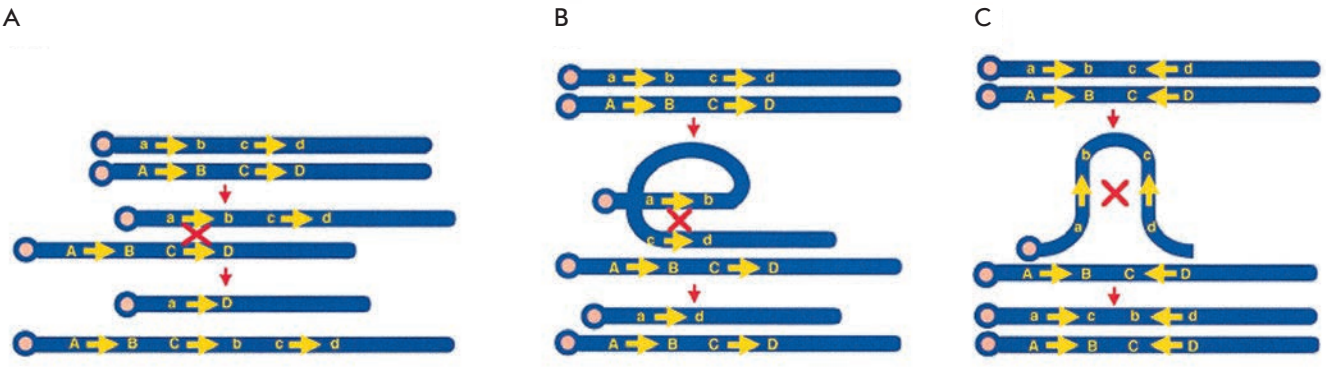


Fig. 5. Genomic rearrangements resulting from recombination between duplicons [17]. (A) – interchromosomal recombination between direct repeats results in deletion and/or duplication; (B) – intrachromosomal recombination between direct repeats (in one homolog) results in deletion; (C) – intrachromosomal recombination between inverted repeats results in an inversion. Repeated sequences are depicted by yellow arrows with the orientation indicated by the direction of the arrows. Recombination is shown by red X. Upper- and lowercase letters (e.g., A and a) refer to a unique flanking sequence in different allelic states

In most deletion-duplication syndromes, the reconstructed chromosomal segment is flanked by large (usually 10–500 kb), highly homologous low copy repeat sequences (LCR), for which the recombination occurs. Due to the fact that in this case recombination involves homologous, but not allelic sequences, the term "non-allelic homologous recombination" (NAHR) appeared. As a result of NAHR between direct repeats in the same chromosome duplications and deletions occur, and reverse orientation results in inversion (*Fig. 5*). NAHR between different chromosomes leads to the formation of translocations [17].

The most detailed study of the role of LCR in genomic diseases was conducted using WBS as an example [18]. WBS deletion is flanked by three LCRs (centromeric, telomeric, and medial); each of them consists of blocks A, B and C [19]. Blocks of centromeric and medial repeats are arranged in the same orientation, but in different order, while the telomeric segment is in the same order, but in opposite orientation (*Fig. 6*). Block B consists of three genes in the medial location (Bm) (GTF21, NCF1, GTF21RD2), alleged pseudogenes in the centromeric region (Bc) (GTF21P1, NCF1P1, GTF21RD2P1), and telomeric region (Bt) (GTF21P2, NCF1P2, GTF21RD2P2). In most patients (95%), the deletion of 1,550 kb occurred as a result of nonhomologous crossover between the centromeric (Bc, or telomeric Bt in the case of inversion in parents) and medial blocks of repeats. A more extended deletion (1,840 kb) is caused by the exchange between the Ac and Am blocks, registered in 5 % of cases. The preferred localization of exchanges in block B is obvious. Breaks can occur anywhere in the repeat; nevertheless, there is a tendency toward the formation of clusters of breaks in the proximal region of Bc/Bm blocks, where, apparently, a hot spot sized 12 kb is localized, which is 11.4 % of the whole sequence of the block. This area accounts for 67% of the recombinations.

Polymorphism in the organization of the LCR flanking the deletion allows one to suggest the possibility of other genomic rearrangements. Indeed, 30% of parents of children with WBS have an inversion spanning the entire WBS interval [20]. It is believed that WBS deletion occurs due to non-allelic intrachromosomal or interchromosomal recombination; in this case, the identity of the repeats plays a crucial role [21]. However, in the case of inversion in the parents [18], nonhomologous crossover occurs during the first meiotic division and affects the last 38 kb of the Bt block, which are absent in the Bc block. The positional preference of NAHR exchanges may be due to the additional architectural features of these areas. It is important to note for further consideration that in some cases palindromes capable of forming a hairpin are located close to the hot spot [22].

## Genes localized within the deletion

The following genes are located within the deletion (*Fig. 6*). Most of them (two-thirds) encode proteins that to some extent organize the space in the nucleus or cytoplasm. Thus, some of them encode transcription factors (WBSCR9/WSTF, WS-bHLH, WBSCR11/GTF2IRD1) which form the core protein compartments, and others are involved in the reorganization of cytoskeletal and membrane-bound structures (LIMK1, STX1A, CYLN2, TBL2, CLDN4 / CPTER1, CLDN3/CPTER2). A brief description of some genes is presented below.

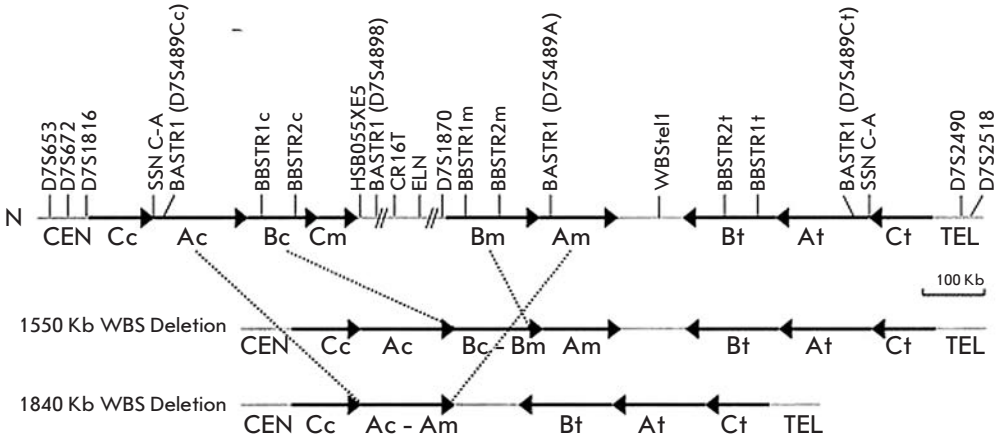


Fig. 6. Schematic representation of the 7q11.23 genomic region in normal chromosomes (N) and chromosomes with WBS deletions [18]. A, B, and C blocks of centromeric (c), medial (m), and telomeric (t) LCRs are represented by black arrows that indicate their relative orientation. The single-copy regions between and outside the LCRs are shown as gray lines. The limits of typical deletion (1.55 Mb) and rarer deletion (1.84 Mb) found in our WBS patients are indicated by dotted lines

*frizzled-9 (fzd9)* encodes the Frizzled-9 protein, similar to the *Drosophila* wnt receptor. This gene is involved in the development of the hippocampus in mice. Hemizygous state of only this gene leads to severe cognitive impairment, including defects in the neuroanatomy of the hippocampus and, as a consequence, impairment of memory and spatial orientation [23], which is very similar to the manifestations of the complex effect of deletion in the Williams syndrome.

*stx1a* encodes STX1A, syntaxin 1A, a syntaxin family member, specific for the brain protein with a molecular weight of 35 kDa. It is required for the release of a neurotransmitter from the synaptic vesicle. Syntaxin 1A interacts with synaptotagmin and other proteins of synaptosomes [24]; therefore, an assumption was made about the role of syntaxin gene hemizygosity in the neurological symptoms of WBS [25].

*eln* encodes tropoelastin, a component of elastic fibers. This gene is located in the middle of the deletion region; thus, it is a deletion marker. Hemizygosity of the tropoelastin gene leads to the formation of stenosis, thinning of the arterial walls, and underdevelopment of muscles. Apparently, it is responsible for the specific elfic appearance of WBS patients [26].

*cyln2* encodes the cytoplasmic linker protein CLIP-115, which connects the endosomes to the growing microtubules through specific binding to their ends. Thus, CLIP-115 is involved in the reorganization of microtubules and effects their interaction with various cellular structures. CLIP-115 is expressed predominantly in the brain and localizes in the lamellar body of dendrites.

*wbscr11/gtf21rd1* encodes the transcription factor GTF2I containing a characteristic helix-loop-helix motif and TFII-I calcium channel regulator with a high and ubiquitous expression.

*limk1* encodes non-receptor serine-threonine protein kinase, the key enzyme in actin remodeling [22, 27].


Fig. 7. Domain structure of LIMK1. Top – C isoform; bottom –D isoform, both the LIM domains and PDZ domain are absent

The LIMK1 molecule consists of four domains: the kinase domain, as well as two LIM and one PDZ domains (*Fig.* 7). Deletion of the LIM and PDZ that are responsible for interaction with other proteins increases the kinase activity of the molecule, which is indicative of the regulatory function of these domains [28]. LIMK1 interacts through the LIM-domain with a variety of proteins, including protein kinase C, the cytoplasmic domain of the transmembrane neuregulin ligand [29]. *Fig. 8* illustrates the signaling pathway of actin remodeling.

LIMK1 activity is regulated by members of the Rho GTPase family; namely, Rho, Rac, and Cdc42, through protein kinase ROCK, p21-activated kinase (PAK), i.e. PAK1 and PAK4, respectively. These kinases phosphorylate Thr508 in a loop of the kinase domain of LIMK1, leading to its activation [30]. Cofilin acts as a target for the LIMK1 involved in actin depolymerization when attached to the sharp end of the actin filament. When cofilin is phosphorylated by LIMK1, it is inhibited and disconnected from the actin filaments. Thus, LIMK1 controls actin dynamics by cofilin switching from the active to the inactive state [31]. Reorganization of the actin cytoskeleton is involved in neuron movement and neurite growth. Actin remodeling is required for the emergence and modification of dendritic spines, which

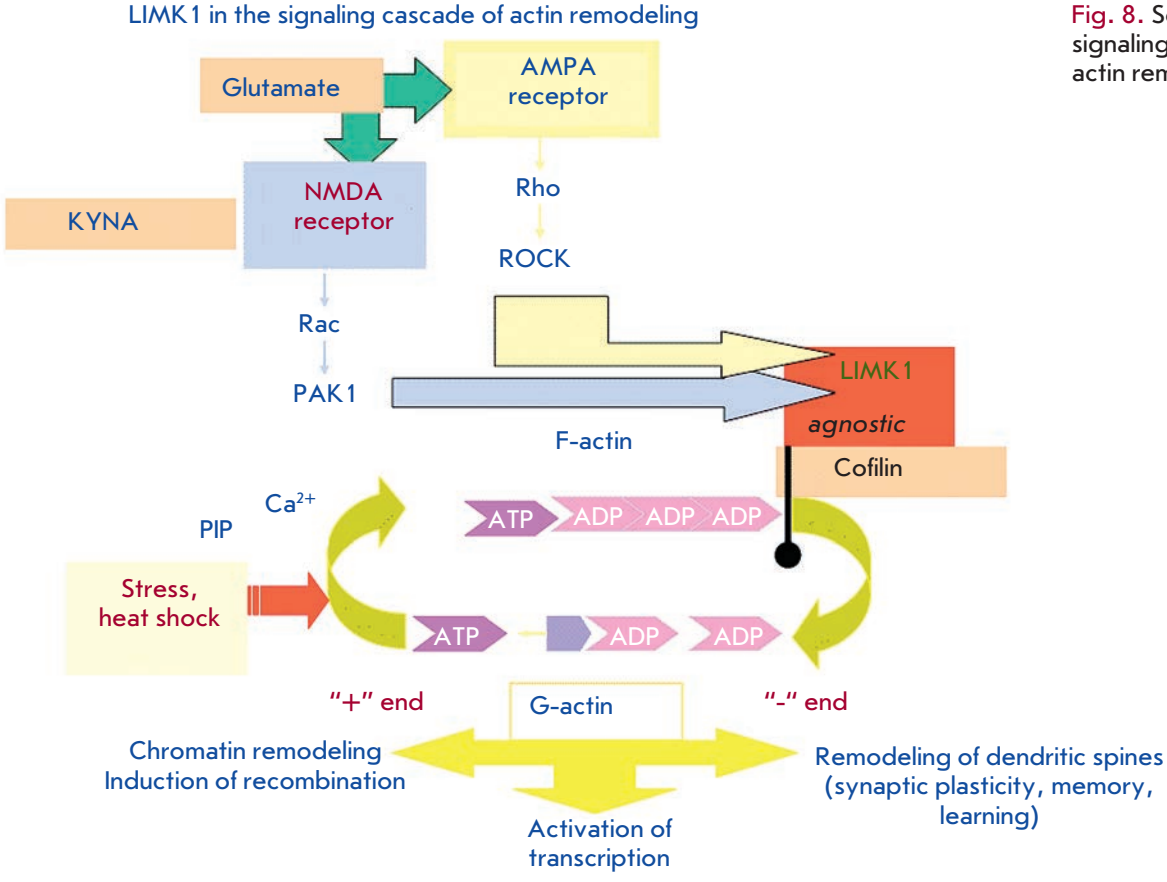


Fig. 8. Scheme of the signaling cascade of actin remodeling

form most synaptic connections in the hippocampus and other brain areas, and thus mediate learning and retention of the memory trace. In addition, the transcription factors CREB and Nurr1 act as a physiological substrate for LIMK1. LIMK1 also phosphorylates myelin basic proteins and histones *in vitro* [29].

The partner genes that produce the proteins that interact with LIMK1 have been identified (*Fig. 9*).

It is assumed that hemizygosity of this gene is one of the factors that determine the appearance of defects of visuo-spatial behavior in WBS patients. The list of genes affected by the deletion continues to grow and currently includes 28 genes. This list is adequately represented in the survey [8], which purports to establish genotype-phenotype correlations.

A deletion of minimum length leads to hemizygosity for only two genes, *eln* and *limk1* (*Fig. 6*). As a result of studying their manifestations, the former gene was considered to be the crucial one in the genesis of cardiovascular pathology; the latter gene, of cognitive pathology. This viewpoint was based on comparative characteristics of the expression of both genes in the brain: expression of *eln* was very low, whereas the expression level of *limk1* was very high and reached a maximum in the cerebral cortex [32]. However, although this study has conclusively proven the role of hemizygosity of the *limk1* gene in the formation of visuo-spatial orientation defects, the other one could not confirm this role [33].

It should be recalled that, although the deletion resulting in the Williams syndrome occurs with a frequency exceeding the frequency of mutations in a single gene due to a higher frequency of unequal recombination, each study includes not that many patients (so far there have been five of them in St. Petersburg). As a rule, the deletion boundaries (breakpoints in the chromosome) are not identified when confirming the deletions; the spontaneity and unpredictability of deletions prevents an intrafamilial analysis. However, this is possible in rare cases, because there are families with identical deletions [34].

Thus, in five families with supravalvular arterial stenosis a small deletion was revealed; it led to the Williams syndrome in all of them and affected the *limk1* gene, but not *fkbp6* or *gtf2i*. All carriers of this deletion demonstrated defects of visuo-spatial orientation, but not mental retardation; therefore, the role in the genesis of the former was left to LIMK1, whereas the GTF2I transcription factor was suspected to be involved in the genesis of mental retardation [ 35].

However, the known limitations of studies on human objects necessitated a recourse to animal models. Obviously, the first attempts to establish the role of a specific gene in the Williams syndrome manifestations were made on mice. This object provides an easy way to obtain carriers of null mutations, as well as hypomorphic and point mutations and deletions involving many genes in the region of interest [36]. Moreover, unlike humans, who can have only one affected child with a random chromosome deletion obtained from mother or father, it is possible to obtain numerous offspring of mice with the same genetic disorders.

It should be noted that the order of the genes within the deletion is evolutionarily conserved and is the same in mice as in humans (*Fig. 10*). However, the region with breakpoints in identical flanking sequences is inverted with respect to the genomic map of the similar region in humans and contains no low copy repeats [18].

Data accumulated over the past 10 years indicate that hemizygosity in similar genes in humans and mice do not always lead to similar manifestations. Nevertheless, it was conclusively proven that the formation of cognitive and behavioral manifestations involves two genes that control the cytoskeleton function by regulating actin dynamics (*limk1*) [37] and the microtubule network (*clip2*) [38], similarly to those in humans. Hemizygosity at the *cyln2* gene (*clip2*) in mice leads to damage typical of WBS, moderate developmental disorders, abnormalities in motor coordination, brain morphology, and hippocampal dysfunction.

However, very little attention has been paid to the analysis of the participation of this (as well as all other investigated genes of mice) in the control of visuo-spatial orientation [36]. This process is also known as spatial memory, which is responsible for the hippocampus. It can be tested in mice in a Morris water maze. Mice placed in the maze learn to escape quickly and correctly to the invisible underwater platform, localizing it by means of "signals" of the environment; i.e., signs specially painted on the walls of the room around the maze or randomly located objects (switches, etc.). Knockdown of only one *limk1* gene leads to strong visuo-spatial dysfunction due to physiological and morphological hippocampal dysfunction [37]. The former manifests itself as impairment of synaptic plasticity (long-lasting potentiation), induced by NMDA receptors defectiveness; the latter manifests itself as a change in the morphology of the dendritic spines of hippocampal pyramidal cells, which is indicative of the direct function of LIMK1, the key enzyme in actin remodeling that determines the morphology of spines.

Apparently, cognitive disorders can be induced both by hemizygosity of LIMK1 itself and violation of the interaction with partner proteins of LIMK1 due to hemizygosity (*Fig. 9*), such as the product of the *park2* autosomal recessive gene (*parkin*). Let us recall that this gene is responsible for the early onset of Parkinson's disease; it produces E3 ubiquitin ligase. A recent analysis of the WBS deletion in mice has led to the discovery of a previously unknown fact that the *trim50* gene encodes E3 ubiquitin ligase [39].

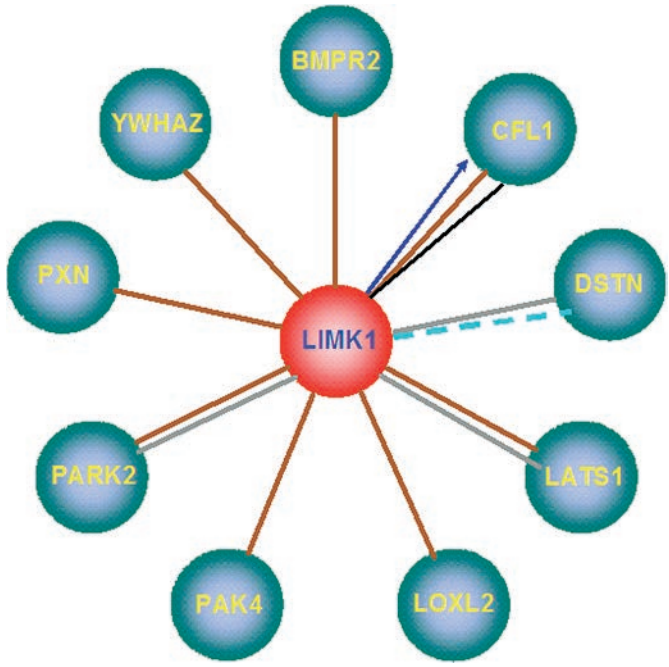


Fig. 9. Interaction of LIMK1 with other proteins. BMPR2 – Bone morphogenetic protein receptor, type II (serine/threonine kinase); CFL1 – Cofilin 1 (non-muscle); DSTN – Destrin (actin depolymerizing factor); LATS1 – LATS, large tumor suppressor, homolog 1 (*Drosophila*); LOXL2 – Lysyl oxidase-like 2 (*Drosophila*); PAK4 – P21 protein (Cdc42/Rac)-activated kinase 4; PARK2 – parkin 2 (*Drosophila*); PXN – Paxillin; YWHAZ – Tyrosine 3-monooxygenase/tryptophan 5-monooxygenase activation protein, zeta polypeptide Drosophila gene *leonardo* (affects olfactory learning)

## FROM GENETICS TO EPIGENETICS

It would seem that the functional role of the LIMK1 enzyme and the gene encoding it in the formation of the Williams syndrome's pathology has been proved. However, there is now data on a long-term analysis of cognitive manifestations in the same patients who have grown from small children to teenagers and young adults. It has been established [9, 40] that both visual and linguistic defects smoothen with age. Perception and display of the whole shape, rather than separate details, become pos-

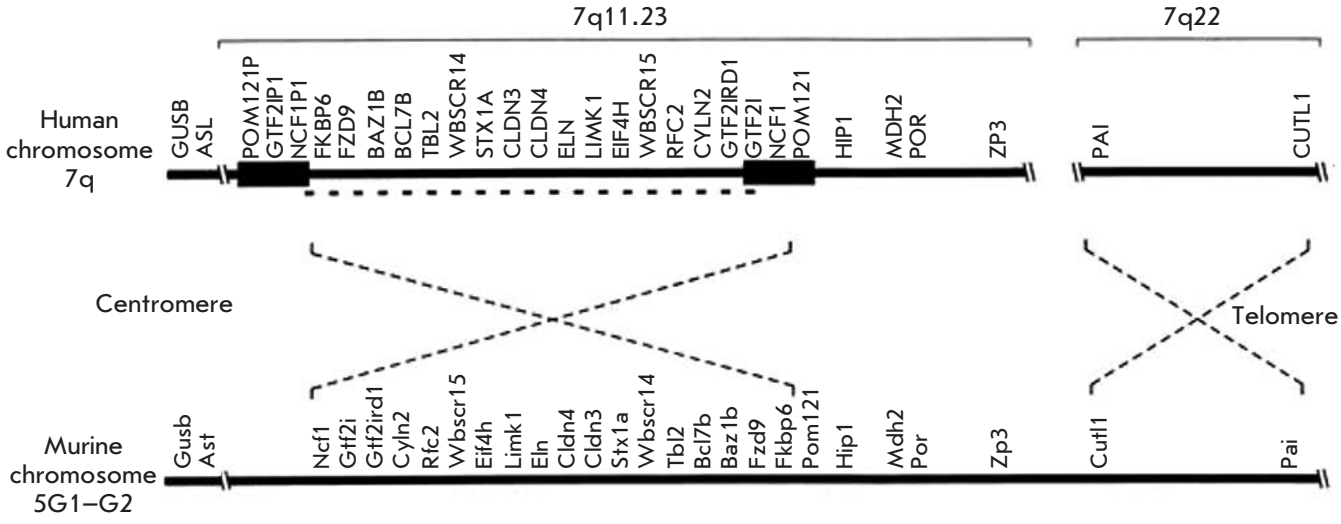


Fig. 10. Order of genes within the WBS region in a human and a mouse. The dotted line shows an inversion of each type with respect to telomere and centromere [19]

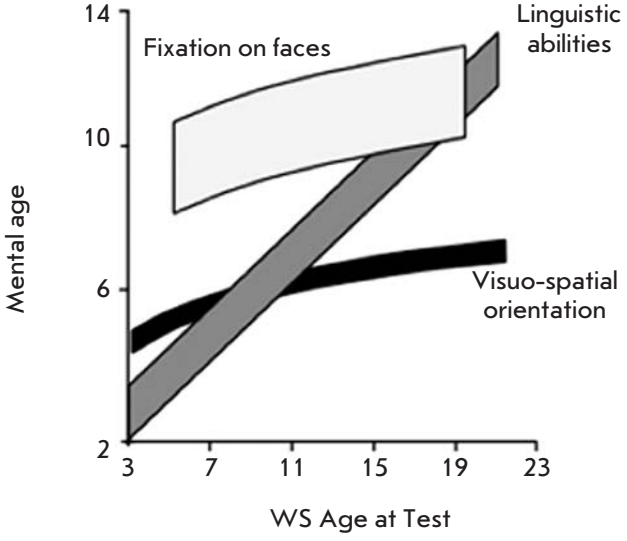


Fig. 11. Changes in three main cognitive features vs. age of WBS patients [5]

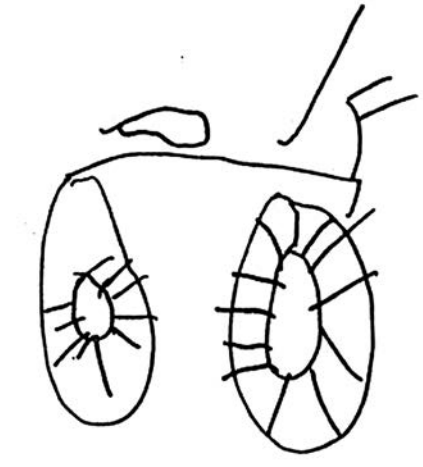

Age: 12 years and 11 months

Fig. 12. Drawings of a bicycle by a girl aged 12 years and 11 months with the Williams syndrome [10]

sible; verbal intelligence increases, while evaluative and emotional coloring are retained (*Fig. 11*). For example, at the age of 9 years, a child who was asked to draw a picture of a bicycle drew signed details; i.e., he perceived only parts of the whole (*Fig. 3*); however, at the age of 12, the same child was already able to synthesize the whole object and its parts (*Fig. 12*).

Therefore, the original understanding of the exclusive role of genes directly determining the path to brain morphology and behavior has evolved to a suggestion of the relevance of searching for the epigenetic factors of brain plasticity that affect its development and functions (reflected in changing behavior) [40].

This has led to a different interpretation of the seemingly contradictory data. Let us recall that in most cases a limited number of patients of all ages (from toddlers to 14- and 19-year-olds) are being studied. Thus, a clear picture of the genetic determination at the beginning of life (one gene – one enzyme – behavioral manifestation) is superimposed on the different epigenetic changes in

the gene's action, depending on the experienced social (family and school) stress and individual experience (learning, conditioned reflex). Therefore, research into the Williams syndrome, supported by nuclear magnetic resonance data and modern brain-imaging to identify some particular areas of the brain that are activated upon testing for the behavioral triad, has veered toward looking at the individual development of children upon interaction with the environment [5].

It is the individual development of an organism, including humans [41, 42], that is considered in the tideway of the transactional analysis; i.e., transactions (interactions) between the genotype and the environment. It is assumed that biobehavioral systems are capable of adaptive self-organization and self-stabilization through conditioned reflexes to environmental signals [43].

According to modern concepts, such transactions lead to epigenetic changes. They occur not only due to the already known phenomena, such as methylation of gene promoters and acetylation of histones, but also due to a new phenomenon: the regulation of gene activity by small non-coding (nc) RNAs.

As regards the first aspect, the epigenetics of changes in gene activity with age becomes an independent field of research [44]. It is believed that the genes are "turned on" when DNA is unmethylated and histones are acetylated, and, conversely, genes are "turned off" when the DNA is methylated and histones are non-acetylated. This is a dynamic process that depends on age, diet, and stress [45].

The second aspect is new and unusual. Thus, we are witnessing growth in research into a direction contradicting the established molecular genetics paradigm. It has been established that only 1.2% of mammalian genes encode protein products, while the rest of the genome generates various classes of ncRNAs. For this reason, a new paradigm has appeared [46]. According to this paradigm, the known classes of ncRNAs and those that are yet to be discovered allow for the regulation of the expression of the genes encoding proteins in normal and pathological conditions.

This interaction between the two "worlds," i.e. RNA and proteins, is the basis for a flexible relationship between the genes and the environment, which is essential for the functioning of the nervous system. Moreover, ncRNA is a device for communication between the digital information in the nucleic acids of cell nucleus and the analogous information in cellular proteins [47, 48].

Functioning of ncRNAs, which are predominantly present in the nervous system, provides synaptic plasticity, the molecular foundation of memory formation. While short-term memory (up to 3 h), i.e. memory about

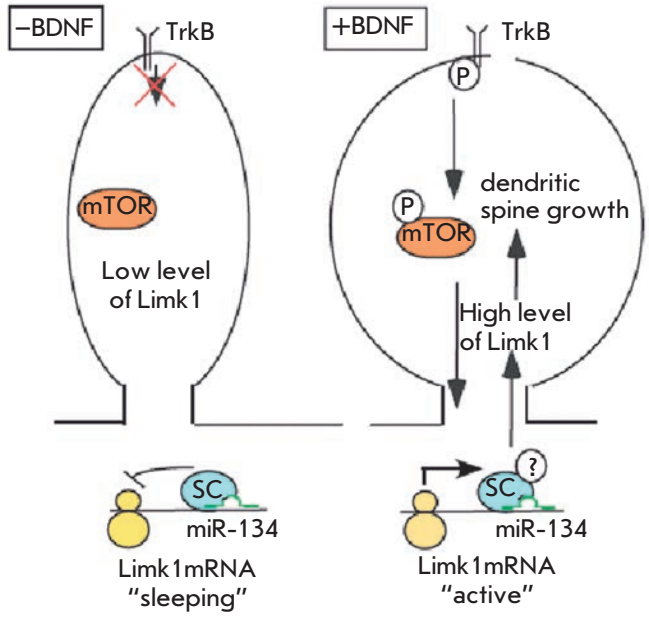


Fig. 13. miR-134 in the regulation of local translation of LIMK1 [49]. In the absence of BDNF, translation of LIMK1 is blocked by miR-134 through a silencing complex (SC) leading to a reduction in dendritic spines. In the presence of BDNF, translation of LIMK1 and dendritic spine growth are activated

events that have just occurred, is based on a modification (generally phosphorylation) of pre-existing proteins, the medium-term memory (2-8 h) depends on the synthesis of new proteins based on pre-existing messenger RNA (mRNA), i.e. local translation in dendrites and synapses distant from the nucleus of the nerve cell, regulated by miRNAs. They participate in the formation of "silent" miRNA-mRNA complexes convenient for transportation from the nucleus to the dendrite, which requires some transport machinery (the actin-tubulin microtubules of dendrites). Dendritic transport of many mRNAs may be regulated via the interaction of the PDZ-domains of LIMK1 with the tubulin of microtubules [29]. It is worth recalling that development of the cognitive and behavioral manifestations in the Williams syndrome involves two genes that control cytoskeleton functions by regulating actin dynamics (*limk1*) [37] and the microtubule network (*clip2*) [38]. This group of mRNAs includes templates for a rapid local synthesis of glutamate receptor subunits, in particular NMDA and GluR, postsynaptic density (PSD) proteins, transcription factors, and components of a signal cascade of actin remodeling (LIMK1, cofilin). The widely cited example [49] reports interaction between miR-134 miRNAs and the mRNA of the LIMK1 protein, the key enzyme in actin remodeling, to cre-

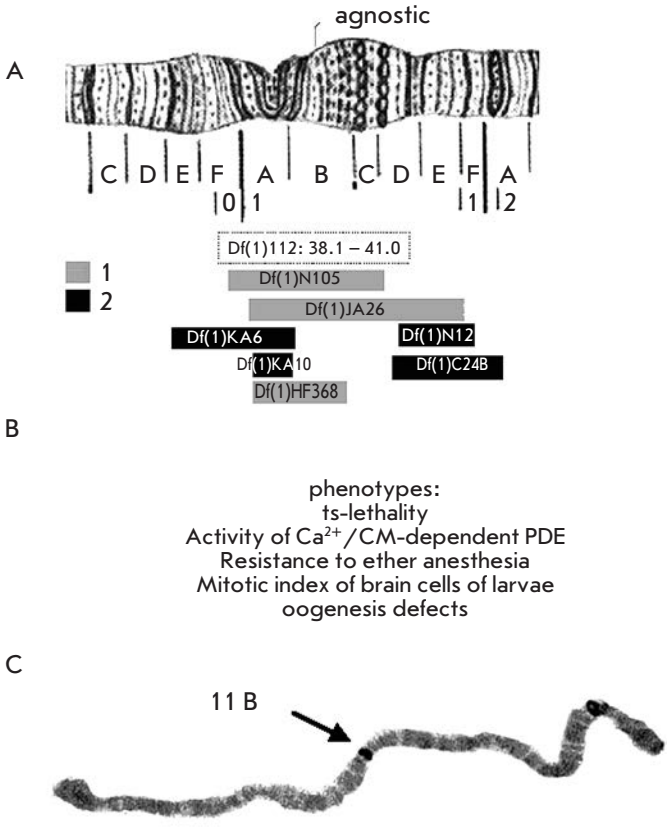


Fig. 14. Localization of the *agnostic* locus within the X chromosome [54]. (a) Deletion mapping. The length of rectangles (except for *Df(1)112* microdeletion, for which the limits of recombinational mapping are shown) represents the length of the deletions in the X chromosome, resulting (1) and not resulting (2) in phenotypic manifestations of mutations (b) at the *agnostic* locus; (c) *in situ* hybridization of P-element DNA with the polytene chromosomes of the P-insertional mutant *P40*

ate a "silent" complex and local translation of mRNA encoding the LIMK1 protein in dendrites in response to neuronal activity (*Fig. 13*). miR-134 is partially complementary to the 3'-untranslated region of the mRNA of LIMK1 (3'UTR).

microRNA is the most intensively studied class of ncRNAs sized 20-30 nucleotides in length and operating according to the principle of RNA interference. Heterochromatin is a source of small RNAs. It is the key factor in epigenetic regulation of gene expression, chromosome behavior, nervous system functions in health and disease, as well as evolutionary transformations [50]. Chromatin modifications are coordinated with the activation of transcription cascades in synaptic plasticity and directly related to the CREB-dependent signaling pathways.

New models are required to explore this new phenomenon. This raises a number of questions.

Is it possible to find and design fairly simple systems to analyze the contribution of both a single gene and the consequences of its epigenetic regulation in the formation of a cognitive profile in Williams syndrome's patients, abstracting from the complex epigenetic factors of individual brain development from infancy to adolescence (in humans) or postnatal development (in mice)? Is it possible to use drosophila for this purpose?

## *Drosophila melanogaster* AS A PLAUSIBLE MODEL TO EXPLORE THE PATHWAYS GENES — BRAIN — MIND: GENETICS AND EPIGENETICS

On the one hand, the functions of the so-called pathological human genes are often identified by the nature of the manifestations of mutations in the same gene of *Drosophila*, if this gene has the same sequence as that of the human gene. On the other hand, all the genes concentrated in one critical region in the mammalian genome (let us recall that the *frizzled-9* gene within the Williams syndrome deletion was the first to be described in Drosophila) are scattered on different chromosomes in *Drosophila*. Despite the other path of evolutionary organization, i.e. different localization of genes that are linked in mammals, this approach to the analysis of the function of a specific gene in the genesis of the Williams syndrome is possible under the following conditions:

1) the mutations in a given gene must be known, and the hemizygosity of this gene lead to the manifestation of a mutant phenotype in Drosophila;

2) the architecture of the chromosomal region where the Drosophila gene is localized may be a predisposition to the occurrence of chromosomal rearrangements by unequal recombination;

3) increased frequency of recombinations is registered in the region of gene localization, which might lead to spontaneous generation of deletions or other rearrangements; and

4) wild-type lines are characterized by a polymorphism specific to this region.

We have found and described *agnostic D. melanogaster* locus carrying the gene encoding the LIMK1 protein, which meets all these criteria.

### The *agnostic* locus

The *agnostic* locus was found in the 11B region of the X chromosome of *D. melanogaster* during the targeted screening of temperature-sensitive (*ts*) mutations induced by ethylmethane sulfonate (EMS) in the *Canton-S (CS)* line, which can affect the activity of the enzymes of cAMP synthesis and degradation [51].

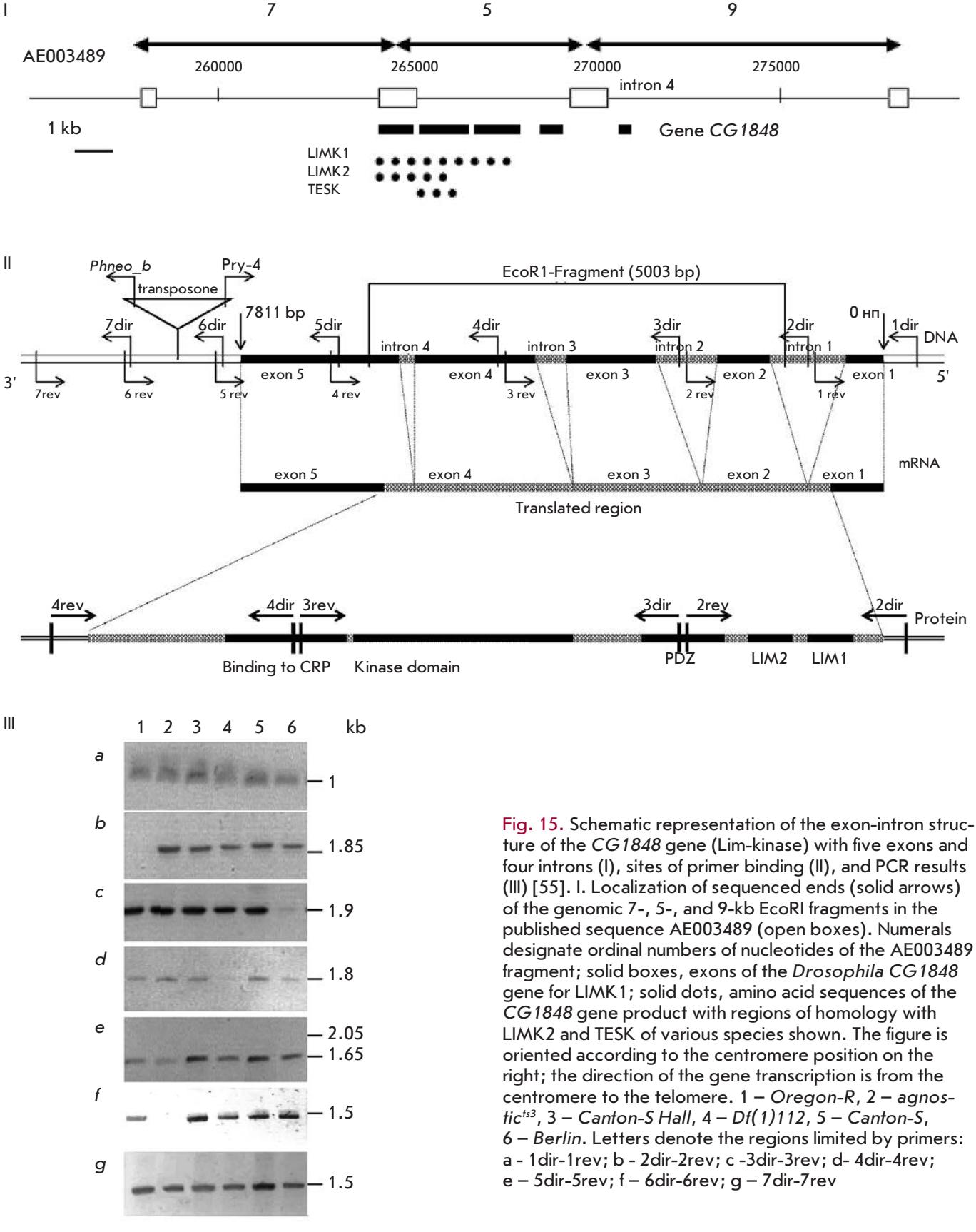


Fig. 15. Schematic representation of the exon-intron structure of the *CG1848* gene (Lim-kinase) with five exons and four introns (I), sites of primer binding (II), and PCR results (III) [55]. I. Localization of sequenced ends (solid arrows) of the genomic 7-, 5-, and 9-kb EcoRI fragments in the published sequence AE003489 (open boxes). Numerals designate ordinal numbers of nucleotides of the AE003489 fragment; solid boxes, exons of the *Drosophila CG1848* gene for LIMK1; solid dots, amino acid sequences of the *CG1848* gene product with regions of homology with LIMK2 and TESK of various species shown. The figure is oriented according to the centromere position on the right; the direction of the gene transcription is from the centromere to the telomere. 1 – *Oregon-R*, 2 – *agnostic*$^{ts3}$, 3 – *Canton-S Hall*, 4 – *Df(1)112*, 5 – *Canton-S*, 6 – *Berlin*. Letters denote the regions limited by primers: a - 1dir-1rev; b - 2dir-2rev; c -3dir-3rev; d- 4dir-4rev; e – 5dir-5rev; f – 6dir-6rev; g – 7dir-7rev

The *agn*$^{ts3}$ mutant at this locus displays an unusually high activity of $Ca^{2+}$/calmodulin-dependent phosphodiesterase Pde1 [52].

A molecular genetic study of the locus revealed a 21 kb DNA fragment within the region of deletions. EcoRI fragments of 7, 5. and 9 kb within this region were subcloned, and their terminal nucleotide sequences were identified.

We used Southern blot hybridization to demonstrate that the wild-type lines *Canton-S (CS), Berlin* and *Oregon-R (Or-R)* are characterized by a pronounced polymorphism precisely in this region. The results of a bioinformatic analysis allowed us to arrange these fragments within the AE003489 segment of the 11B region of the X chromosome of Drosophila (*Fig. 14*).

It turned out that this area, which falls within both the known deletion *Df(1)368* and the narrow deletion *Df(1)112* we have obtained, contains the gene encoding the LIMK1 protein, which is homologous for a huge number of species, including humans.

The results of our bioinformatic analysis revealed the homology of *agnostic* locus, mainly the 5 kb EcoRI-fragment, with three known forms of LIM kinases from different vertebrate species [53, 54].

The occurrence of *agn*$^{ts3}$ mutant phenotypes was observed under conditions of *(Df ( 1 ) 112/CS)* hemizygosity (e.g. high levels of activity of $Ca^{2+}$/calmodulin-dependent kinase Pde1 and nonhomologous chromosome pairing). It was shown [53, 54] that the region of the *agnostic* gene contains repetitive sequences both within (repeat of two LIM domains), and around, the gene. The gene is flanked by extensive AT-rich repeats (The National Center for Biotechnology Information, NCBI). Therefore, the high polymorphism of the spontaneous and mutant alleles of this gene *(Fig. 15)*, shown by D.A. Molotkov using PCR [55], is probably due to non-homologous crossover.

Thus, the *agnostic* gene can play the role of a genetic reserve of polymorphism and be a convenient model of genomic disorders, such as the Williams syndrome, because of its structure and environment. In the region of the *agnostic* gene localization, crossover frequency is threefold higher compared with that in the control. The highest numbers of double exchanges, negative interference, and nonreciprocal complementary crossover classes are observed under thermal action (29°C) at the end of the embryonic or at the beginning of the larval stage of development, rather than at the stage of premeiotic DNA synthesis (late larva III- chrysalis).

This proves that the mutation does not affect the crossover itself, but rather its background, changing the pairing features of chromosomes.

A southern blot analysis of the genomic DNA reveals an additional SalI fragment of 11 kb in *agn*$^{ts3}$ mutants. Therefore, it has been suggested that the frequency of exchanges increases due to unequal crossover, resulting in the occurrence of a SalI fragment in the *agn*$^{ts3}$ mutant, presumably due to insertions or duplication.

Indeed, PCR mapping of the *agn*$^{ts3}$ mutant in the regulatory region of the *limk1* gene revealed an insertion of 1.7 kb, located approximately 1 kb below the 3'UTR.

The insertion site is consistent with the AT-rich region, which is capable of forming a hairpin in the single-stranded conformation and structure of club cross in a double-stranded conformation identified in the database. We assume that this anomalous structure can serve as a preferred spot of insertion of natural transposon and is also capable of producing miRNA with a complex secondary structure and properties similar to those of miR-134 during its transcription. The possibility of the participation of these miRNAs allows one to explain many aspects of the regulation of the gene's action [55].

The *agnostic* gene displays the following characteristic features:

1. Immunofluorescence studies of the distribution of LIMK1, the key enzyme of actin remodeling the signal cascade, in the brain areas of Drosophila revealed that it preferentially localizes in the central complex of the brain and in the visual system. Mutational damage in the *limk1* gene (at *agn*$^{ts3}$) leads to a sharp increase in LIMK1 activity in all brain areas. The same effect in wild-type *Canton-S* flies is caused by thermal exposure.

2. The hemizygous state of the *limk1* gene in Drosophila leads to a change in LIMK1 distribution in the brain areas, similarly to that in the Williams syndrome in humans. The enzyme is localized exclusively in the visual system and loses its dependence on the thermal effect.

3. The immunofluorescence study of the distribution of LIMK1 and cofilin phosphorylated by the enzyme (p-cofilin) in the cells of the salivary glands of Drosophila larvae revealed their predominantly cytoplasmic localization in wild-type flies. A heat shock causes the transfer of components of the signaling cascade of actin remodeling into the nucleus and leads to a sharp increase in the activity of LIMK1 and p-cofilin. Mutational damage in the LIMK1 gene (*agn*$^{ts3}$ mutation) increases the content and activity of LIMK1: this effect is disappears under the influence of a heat shock.

4. Mutational damage to the *limk1* gene (EMS- and P-insertional mutations at *agnostic* locus) affects the pairing properties of chromosomes in Drosophila. Thus, the frequency of formation of ectopic contacts in the regions of intercalary heterochromatin in salivary gland polytene chromosomes dramatically increases the hemizygosity of the gene, identically to that in hu-

mans with the Williams syndrome, and results in the expression of the mutant phenotype.

5. The *agnostic* gene is involved in the mechanisms of homologous synapsis of chromosomes, resulting in a sharp decrease in the asynapsis frequency in the $agn^{ts3}$ line and abnormalities in the distribution of long and short asynapses along the chromosome. This is indicative of differences in the localization of chromosomal arms in the nucleus with respect to each other in the wild-type and $agn^{ts3}$, i.e. different ways of three-dimensional spatial organization of the nucleus.

6. Mutational damage to the signaling cascade of actin remodeling leads to the formation of amyloid aggregates in the brain of imago and in the larval tissues of all $agn^{ts3}$ samples. The incidence of aggregates is reduced to the standard level after a heat shock. This correlates with learning ability and memory formation. Overexpression of LIMK1 in mutants is accompanied by a significant reduction in the learning ability and medium-term memory revealed in the conditioned-reflex suppression of courtship in males. The method is based on stimuli that are natural to the sexual behavior of Drosophila [56].

## CONCLUSION

A high frequency of deletion-duplication syndromes, including the Williams syndrome, leads to the emergence of the concept of "genomic diseases," which allows one to link genes, the brain, behavior, and the cognitive function. Clarity and discretization of cognitive manifestations made it possible to identify the key gene responsible for the cognitive component of the syndrome, i.e. the *limk1* gene. A study of the occurrence of intragenomic reserves of the syndrome (i.e. clusters of repetitive sequences), the distribution of these regions over zones with different conformations in the chromosome, and creation of a specific organization of the nucleus, in which the spatial convergence of functionally and structurally related regions of chromosomes is achieved, was required. This was the motivation behind designing animal models. In particular, the study of *agnostic* locus for LIMK1 of Drosophila revealed the presence of repetitive sequences in the region of the gene. Mutant expression of this gene is associated with changes in the pairing properties of the chromosome and three-dimensional organization of the nucleus, which is an epigenetic derivative of mutational damage.

In the language of genetics, the following chain of events emerges when analyzing the mutant and spontaneous variants of *agnostic* locus: external signal – activation of LIMK1 – cofilin phosphorylation – state of actin – normal cognitive abilities or abnormal memory loss, accompanied by the formation of congophilic (amyloid) deposits.

Thus, we can assume that the $agn^{ts3}$ mutant line is a model of the Williams syndrome in Drosophila. The revealed relation between mutational damage to the *limk1* gene, change in the expression and activity of LIMK1, presence of amyloid-like inclusions and cognitive impairments allow one to be able to apply this model in the study of both neurodegenerative and genomic diseases. The availability of natural polymorphic variants in the *limk1* gene allows one to use them as a tool when studying neurodegenerative diseases, which in most cases occur spontaneously under the influence of adverse environmental factors. The possibility of using the described tools is the subject matter of special experimental studies being conducted in our laboratory [57]. ●

*This work was supported by the Russian Foundation for Basic Research (grant № 12-04-01737-a) and the programs of the Presidium of the Russian Academy of Sciences (№ 7 and 30).*

REFERENCES

1. Williams J.C., Barratt-Boyes B.G., Lowe J.B. // Circulation. 1961. V. 24. P. 1311–1318.
2. Beuren A.J., Apitz J., Harmjanz D. // Circulation. 1962. V. 26. P. 1235–1240.
3. Pober B.R., Johnson M., Urban Z. // J. Clin. Invest. 2008. V. 118. № 5. P. 1606–1615.
4. Bellugi U., Adolphs R., Cassady C., Chiles M. // Neuroreport. 1999. V. 10. № 8. P. 1653–1657.
5. Järvinen-Pasley A., Bellugi U., Reilly J., Mills D.L., Galaburda A., Reiss A.L., Korenberg J.R. // Dev. Psychopathol. 2008. V. 20. № 1. P. 1–35.
6. Carrasco X., Castillo S., Aravena T., Rothhammer P., Aboitiz F. // Pediatr. Neurol. 2005. V. 32. № 3. P. 166–172.
7. Gagliardi C., Martelli S., Burt M.D., Borgatti R. // Pediatr. Neurol. 2007. V. 36. № 5. P. 301–306.
8. Tassabehji M. // Human Mol. Gen. 2003. V.12. P. 229–237.
9. Nakamura M., Mizuno S., Douyuu S., Matsumoto A., Kumagai T., Watanabe S., Kakigi R. // Pediatr. Neurol. 2009. V. 41. № 2. P. 95–100.
10. Mervis C.B., Robinson B.F., Pani J.R. // Am. J. Hum. Genet. 1999. V. 65. № 5. P. 1222–1229.
11. Doherty-Sneddon G., Riby D.M., Calderwood L., Ainsworth L. // Cogn. Neuropsychiatry. 2009. V. 14. № 6. P. 510–523.
12. Thorton-Wells T.A., Cannistraci C.J., Anderson A.W., Kim C.Y., Eapen M., Gore J.C., Blake R., Dykens E.M. // Am. J. Intellect. Dev. Disabil. 2010. V. 115. № 2. P. 172–189.
13. Chen K.S., Mnian P., Koeuth T., Potocki L., Zhao Q., Chinault A.C., Lee C.C., Lupski Jr. // Nat. Genet. 1997. V. 17. P. 154–163.
14. Shaikh T.H., Kurahashi H., Saitta S.C., O'Hare A.M., Hu P., Roe B.A., Driscoll D.A., McDonald-McGinn D.M., Zackai E.H., Budarf M.L., et al. // Hum. Mol. Genet. 2000. V. 9. P. 489–501.

15. Amos-Landgraf J.M., Ji Y., Gottlieb W., Depinet T., Wandstrat A.E., Cassidy S.B., Driscoll D.J., Rogan P.K., Schwartz S., Nichllos R.D. // Am. J. Hum. Genet. 1999. V. 65. P. 370–386.
16. Shaw C.J., Lupski J.R. // Human Mol. Gen. 2004. V. 13. P. 57–64.
17. Lupski J.R. // Trends Genet. 1998. V. 14. P. 417–422.
18. Bayes M., Magano L.F., Rivera N., Flores R., Perez-Jurado L.A. // Am. J. Hum. Genet. 2003. V. 73. P. 131–151.
19. Valero M.C., De Lues O., Cruses L., Perez-Jurado L.A. // Genomics. 2000. V. 69. P. 1–13.
20. Osborne L.R., Li M., Pober B., Chitayat D., Bodurtha J., Mandel A., Costa T., Crebe T., Cox S., Tsui L.C., Scerer S.W. // Nat. Genet. 2001. V. 29. P. 321–325.
21. Urban Z., Helms C., Fekete G., Csiszar K., Bonnet D., Munnich A., Donis-Keller H., Boyd C.D. // Am. J. Hum. Genet. 1996. V. 59. P. 958–962.
22. Weber E.J., Levenson J.M., Sweat J.D. // Molecular Interventions. 2002. V. 2. P. 376–391.
23. Zhao C., Aviles C., Abel R.A., Almli C.R., McQuillen P., Pleasure S.J. // Development. 2005. V. 132. P. 2917–2927.
24. Zhang R., Maksymowych A.B., Simpson L.L. // Gene. 1995. V. 159. P. 293–294.
25. Nakayama T., Matsuoka R., Kimura M., Hirota H., Mikoshiba K., Shimizu Y., Shimizu N., Akagawa K. // Cytogenet. Cell Genet. 1998. V. 82. P. 49–51.
26. Francke U. // Hum. Mol. Genet. 1999. V. 8. P. 1947–1954.
27. Tassabehji M., Metcalfe K., Fergusson W.D., Carette M.J.A., Dore J.K., Donnai D., Read A.P., Proschel C., Gutowski N.J., Mao X., Sheer D. // Nat. Genet. 1996. V. 13. P. 272–273.
28. Arber S., Barbayannis F.A., Hansen H., Schneider C., Stanyon C.A., Bernard O., Caroni P. // Nature. 1998. V. 393. P. 805–809.
29. Scott R.W., Olson M.F. // J. Mol. Med. 2007. V. 85. P. 555–568.
30. Gorovoy M., Niu J., Bernard O., Profirovic J., Minshall R., Neamu R., Voyno-Yasenetskaya T. // J. Biol. Chem. 2005. V. 280. № 28. P. 26533–26542.
31. Yang H., Higuchi O., Ohashi K., Nagata K., Wada A., Kangawa K., Nishida E., Mizuno K. // Nature. 1998. V. 393. P. 809–812.
32. Frangiskakis J.M., Ewart A.K., Morris C.A., Mervis C.B., Bertrand J., Robinson B.F., Klein B.P., Ensing G.J., Everett L.A., Green E.D., et al. // Cell. 1996. V. 86. № 1. P. 59–69.
33. Tassabehji M., Metcalfe K., Karmiloff-Smith A., Carette M.J., Grant J., Dennis N., Reardon W., Splitt M., Read A.P., Donnai D. // Am. J. Hum. Genet. 1999. V. 64. № 1. P. 118–125.
34. Morris C.A., Mervis C.B., Hobart H.H., Gregg R.G., Bertrand J., Ensing G.J., Sommer A., Moore C.A., Hopkin R.J., Spallone P.A., et al. // Am. J. Med. Genet. A. 2003. V. 123A. № 1. P. 45–59.
35. Sakurai T., Dorr N.P., Takahashi N., McInnes L.A., Elder G.A., Buxbaum J.D. // Autism Res. 2011. V. 4. № 1. P. 28–39.
36. Osborne L.R. // Am. J. Med. Genet. C. Semin. Med. Genet. 2010. V. 154C. № 2. P. 209–219.
37. Meng Y., Zhang Y., Tregoubov V., Janus C., Cruz L., Jackson M., Lu W.-Y., MacDonald J.F., Wang J.Y., Falls D.L., et al. // Neuron. 2002. V. 35. P. 121–133.
38. Hoogenraad C.C., Koekkoek B., Akhmanova A., Krugers H., Dortland B., Miedema M., van Alphen A., Kistler W.M., Jaegle M., Koutsourakis M., et al. // Nat. Genet. 2002. V. 32. P. 16–27.
39. Micale L., Fusco C., Augello B., Napolitano L.M.R., Dermitzakis E.T., Meroni G., Merla G., Reymond A. // Eur. J. Hum. Genet. 2008. V. 16. № 9. P. 1038–1049.
40. Karmiloff-Smith A. // Curr. Biol. 2007. V. 17. № 24. P. 1035–1036.
41. Germana J. // Integr. Physiol. Behav. Sci. 1996. V. 31. № 3. P. 210–218.
42. Scarr S., McCartney K. // Child. Dev. 1983. V. 54. № 2. P. 424–435.
43. Lobashev M.E. // Researches on genetics. V. 1. L.: LSU, 1961. P. 3–11.
44. Fraga M.F., Esteller M. // Trends Genet. 2007. V. 23. № 8. P. 413–418.
45. Poulsen P., Esteller M., Vaag A., Fraga M.F. // Pediatr. Res. 2007. V. 61. P. 38–42.
46. Mattick J.S. // J. Exp. Biol. 2007. V. 210. P. 1526–1547.
47. Mercer T.R., Dinger M.E., Mariani J., Kosik K.S., Mehler M.F., Mattick J.S. // Neuroscientist. 2008. V. 14. № 5. P. 434–445.
48. Savvateeva-Popova E., Popov A., Grossman A., Nikitina E., Medvedeva A., Molotkov D., Kamyshev N., Pyatkov K., Zatsepina O., Schostak N., et al. // J. Neural. Transm. 2008. V. 115. № 12. P. 1629–1642.
49. Schratt G.M., Tuebing F., Nigh E.A., Kane C.G., Sabatini M.E., Kiebler M., Greenberg M.E. // Nature. 2006. V. 439. № 7074. P. 283–289.
50. Lippman Z., Martienssen R. // Nature. 2004. V. 431. № 7006. P. 364–370.
51. Savvateeva E.V., Kamyshev N.G., Rosenblum S.R. // DAS USSR. 1978. V. 240. P. 1443–1445.
52. Savvateeva E.V., Kamyshev N.G. // Pharmacology, Biochemistry & Behavior. 1981. V. 14. P. 603–611.
53. Savvateeva-Popova E.V., Peresleny A.I., Scharagina L.M., Tokmacheva E.V., Medvedeva A.V., Kamyshev N.G., Popov A.V., Ozersky P.V., Baricheva E.M., Karagodin D., et al. // J. Evol. Biochem. Physiol. 2002. V. 38. № 6. P. 706–733.
54. Savvateeva-Popova E.V., Peresleni A.I., Sharagina L.M., Medvedeva A.V., Korochkina S.E., Grigorieva I.V., Dyuzhikova N.A., Popov A.V., BarichevaE.M., Karagodin D., et al. // Rus. J. of Genet. 2004. V. 40. № 6. P. 605–624.
55. Medvedeva A.V., Molotkov D.A., Nikitina E.A., Popov A.V., Karagodin D.A., Baricheva E.M., Savvateeva-Popova E.V. // Rus. J. of Genet. 2008. V. 44. № 6. P. 771–783.
56. Kamyshev N.G., Iliadi K.G., Bragina J.V. // Learn. & Mem. 1999. V. 6. P. 1–20.
57. Medvedeva A.V., Zhuravlev A.V., Savvateeva-Popova E.V. // Horizons in Neuroscience Research. 2010. V. 1. Ch. 4. P. 161–193.

# Molecular Mechanism of Global Genome Nucleotide Excision Repair

I. O. Petruseva[1], A. N. Evdokimov[1,2], O. I. Lavrik[1,2,3*]
[1]Institute of Chemical Biology and Fundamental Medicine, Siberian Branch of the Russian Academy of Sciences, prosp. Akad. Lavrentyeva, 8, 630090, Novosibirsk, Russia
[2]Altai State University, Ministry of Education and Science of the Russian Federation, prosp. Lenina, 61, 656049, Barnaul, Russia
[3]Novosibirsk State University, Ministry of Education and Science of the Russian Federation, Pirogova Str., 2, 630090, Novosibirsk, Russia
*E-mail: lavrik@niboch.nsc.ru
Received 31.10.2013


**ABSTRACT** **Nucleotide excision repair (NER) is a multistep process that recognizes and eliminates a wide spectrum of damage causing significant distortions in the DNA structure, such as UV-induced damage and bulky chemical adducts. The consequences of defective NER are apparent in the clinical symptoms of individuals affected by three disorders associated with reduced NER capacities: xeroderma pigmentosum (XP), Cockayne syndrome (CS), and trichothiodystrophy (TTD). These disorders have in common increased sensitivity to UV irradiation, greatly elevated cancer incidence (XP), and multi-system immunological and neurological disorders. The eucaryotic NER system eliminates DNA damage by the excision of 24–32 nt single-strand oligonucleotides from a damaged strand, followed by restoration of an intact double helix by DNA repair synthesis and DNA ligation. About 30 core polypeptides are involved in the entire repair process. NER consists of two pathways distinct in initial damage sensor proteins: transcription-coupled repair (TC-NER) and global genome repair (GG-NER). The article reviews current knowledge on the molecular mechanisms underlying damage recognition and its elimination from mammalian DNA.**
**KEYWORDS** **nucleotide excision repair; repair factors; molecular mechanisms of damage recognition and elimination.**

## INTRODUCTION

Nucleotide excision repair (NER) is one of the principal ways in which cells are protected against various, structurally and chemically different, DNA lesions. The most common lesions are bulky covalent adducts, which are formed by nitrogenous bases affected by UV light, ionizing irradiation, electrophilic chemical mutagens, some drugs, and chemically active endogenous metabolites, including reactive oxygen and nitrogen species [1]. In higher eukaryotic cells, NER excises 24-32-nt DNA fragments containing a damaged link with extreme accuracy. Reparative synthesis using an undamaged strand as a template, followed by ligation of the single-strand break that emerged as a result of the damage, is the final stage of DNA repair. Currently available information on the main genes inactivated in NER-defective cells and on the protein factors and enzymes encoded by these genes indicates that the process involves the coordinated action of approximately 30 proteins that successively form complexes with variable compositions on the DNA [1–3]. NER consists of two pathways distinct in terms of initial damage recognition. Global genome nucleotide excision repair (GG-NER) detects and eliminates bulky damages in the entire genome, including the untranscribed regions and silent chromatin, while transcription-coupled nucleotide excision repair (TC-NER) operates when damage to a transcribed DNA strand limits transcription activity. TC-NER is activated by the stopping of RNA polymerase II at the damaged sites of a transcribed strand, while GG-NER is controlled by XPC, a specialized protein factor that reveals the damage. A schematic GG-NER process is presented in *Fig. 1*; information on the main proteins participating in the process is presented in Table.

Distortions in NER activity can result in UV-sensitive and high-carcinogenic pathologies, xeroderma pigmentosum (XP), the Cockayne syndrome (CS), and trichothiodystrophy (TTD), as well as some neurodegenerative manifestations [4–6].

Xeroderma pigmentosum has provided the names of some of the genes that cause (when being mutated or distorted) the symptoms associated with the disease and the proteins coded by these genes (XPA–XPE factors). XP is a syndrome characterized by photosensitiv-

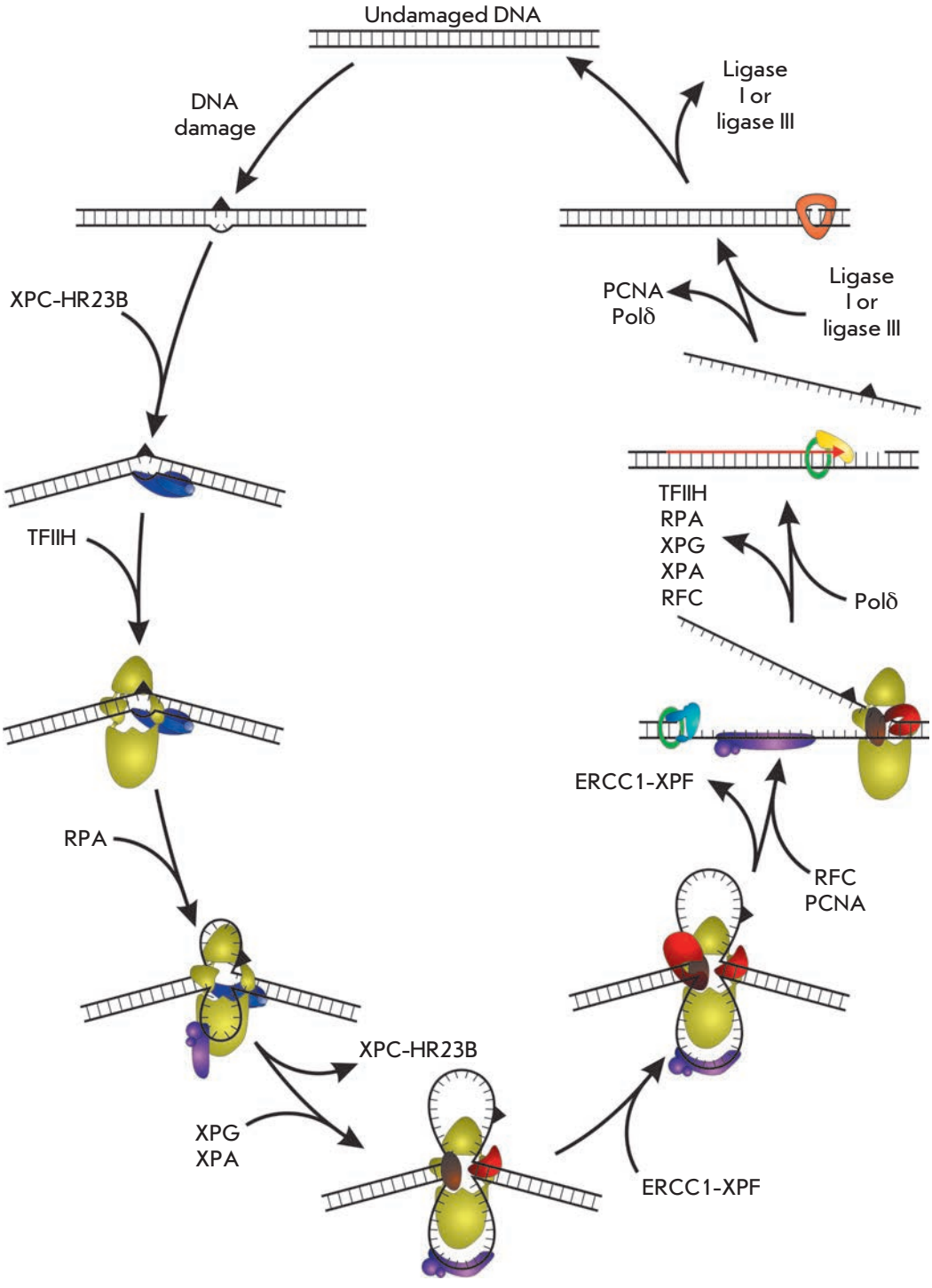


Fig. 1. Scheme of global genome excision repair for nucleotides

ity, skin atrophy, hyperpigmentation and a high rate of sunlight-induced skin cancer. The risk of internal tumors in XP patients is at least 1,000-fold higher [6, 7]. Moreover, the disease is often associated with neurologic disorders. Various XP symptoms, typical of seniors, indicate premature aging caused by the accumulation of non-repaired bulky DNA damage, including several oxidative ones [8–10].

## DAMAGE RECOGNITION

Damage recognition is the crucial step of NER initiation; it determines the rate of DNA repair [1, 2, 11]. A distorted regular structure of double-stranded DNA (dsDNA) and alteration of its stability are common signs conditioning the initial recognition of damage by the repair systems. Chemical modifications of nitrogenous bases are the elements most often eliminated by

NER proteins and their functions

| Factor | Subunit | Gene | Weight, cDNA / (size, a.a.r.) | Function within NER | Interaction with other factors |
|---|---|---|---|---|---|
| XPC | HR23B | *hhr23b* | 43 / (409) | Recognition of a distorted DNA structure | TFIIH<br>XPA<br>DDB |
| | XPC | *xpc* | 125 / (940) | | |
| | CEN2 | *cen2* | 20 / (172) | | |
| DDB | DDB1 | *ddb1* | 127 / (1140) | Recognition of damage, interaction with chromatin | XPC<br>RPA |
| | DDB2 | *ddb2* | 48 / (428) | | |
| XPA | XPA | *xpa* | 31 / (273) | Structural function, binding to a damaged strand | XPA<br>RPA<br>TFIIH<br>ERCC1 |
| RPA | RPA70 | *rpa1* | 68 / (616) | Binding to single-stranded DNA | XPA<br>XPG<br>PCNA/RFC |
| | RPA32 | *rpa2* | 30 / (270) | | |
| | RPA14 | *rpa3* | 14 / (121) | | |
| TFIIH | XPB | *xpb* | 89 / (782) | ATPase, minor helicase activity 3'→5'- DNA-helicase | XPA<br>XPC<br>XPF<br>XPG |
| | XPD | *xpd* | 87 / (760) | ATP-dependent 5'→3'-DNA-helicase; testing of modification presence | |
| | p62 | *gtf2h1* | 62 / (548) | Core subunit, stimulates XPB | |
| | p44 | *gtf2h2* | 44 / (395) | Core subunit, stimulates XPD | |
| | p34 | *gtf2h3* | 34 / (308) | DNA binding | |
| | p52 | *gtf2h4* | 52 / (462) | Regulatory subunit for ATPase activity of XPB functioning in TFIIH complex | |
| | p8 | *gtf2h5 (ttda)* | 8 / (71) | Interaction with P52, stimulation of ATPase activity of XPB | |
| | Mat1 | *mnat1* | 36 / (309) | Member of the CAK complex | |
| | Cdk7 | *cdk7* | 39 / (346) | Phosphorylates RNA-polymerase II and other substrates | |
| | ЦиклинН | *ccnh* | 38 / (323) | Regulation of cell cycle | |
| XPF | ERCC1 | *ercc1* | 33 / (297) | Endonuclease, catalyzes formation of single-strand break in DNA on the 5' side of the damage | XPA<br>TFIIH |
| | XPF | *xpf* | 103 / (905) | | |
| XPG | XPG | *xpg* | 133 / (1186) | Endonuclease, catalyzes formation of single-strand break in DNA on the 3' side of the damage | TFIIH<br>RPA<br>PCNA |
| RFC | RFC1 | *rfc1* | 128 / (1148) | ATP-dependent connection of PCNA | PCNA<br>RPA |
| | RFC2 | *rfc2* | 39 / (354) | | |
| | RFC3 | *rfc3* | 41 / (356) | | |
| | RFC4 | *rfc4* | 40 / (363) | | |
| | RFC5 | *rfc5* | 38 / (340) | | |
| PCNA | PCNA | *pcna* | 3X37 / (3X261) | Factor ensuring processivity of DNA polymerases | RFC<br>XPG<br>Polδ |
| Polδ | p125 | *p125* | 124 / (1107) | DNA polymerase | PCNA |
| | p66 | *p66* | 51 / (466) | | |
| | p50 | *p50* | 51 / (469) | | |
| | p12 | *p12* | 12 / (107) | | |
| Polε | p261 | *p261* | 261 / (2286) | DNA polymerase | PCNA |
| | p59 | *p59* | 60 / (527) | | |
| | p17 | *p17* | 17 / (147) | | |
| | p12 | *p12* | 12 / (117) | | |
| Ligase I | Ligase I | *ligI* | 102 / (919) | Ligation of a single-strand break | |
| Ligase III | Ligase III | *ligIII* | 103 / (862) | | |

the base excision repair (BER) system. Pyrimidine photodimers, platinum adducts, protein-DNA cross-links, modifications caused by DNA interaction with active derivatives of benzo[a]pyrene, benzo[c]anthracene, acetylaminofluorene, along with other bulky adducts, which cause more substantial distortions in the regular structure of double-stranded DNA than BER repairable damages, are the most typical NER substrates [12]. However, most of NER substrates cannot cause as dramatic structural and thermodynamic alterations of dsDNA as double-strand breaks and interstrand cross-links. Therefore, the detection of these damages is particularly challenging for a cell, which can be solved only through highly sensitive recognition. In contrast to BER, where a damaged base is simultaneously recognized and eliminated by a single specialized glycosylase, spezialized groups of proteins are responsible in NER for each of the processes. In eukaryotic NER universal sensor proteins perform the initial recognition of the total range of bulky damages. In the case of TC-NER, it is transcribing RNA polymerase II stopped by damage; in GG-NER, these are complexes of the XPC factor and DDB1-DDB2 heterodimer (XPE factor) enhancing the repair of UV damage [1, 2]. In general, NER recognition of damage is a multistep process involving several proteins that form near damaged complexes of variable compositions. The process is completed by the formation of a preincision complex ready to eliminate a damaged DNA fragment by specialized NER endonucleases [1, 2].

Complementary interaction of nitrogen bases is the main factor ensuring the stability of a regular helical structure of double-stranded DNA. Bulky damage causes distortion in base-pairing and occurrence of a single-stranded character in a dsDNA molecule. Undamaged DNA is not a static molecule, either. DNA strands are in continuous heat motion, causing small, rapid alterations of the distances separating the complementary bases. However, these pico- and nanosecond fluctuations existing in the undamaged DNA may be too short in order to be recognized by repair factors. Molecular modeling shows that introduction of bulky damage into DNA can give rise to more considerable and long-lived "openings" in the double helix [13, 14]. For example, such fluctuations in the DNA structure occur near the cyclobutane pyrimidine dimer 25-fold as often as those in an undamaged duplex. Moreover, the fluctuation's amplitude increases crucially due to a disturbed interaction between the complementary DNA strands. The dynamic changes that follow nucleobase damage mostly cause fluctuations in an undamaged strand fragment that is complementary to the one containing the lesion, while the damaged DNA fragment is less flexible [15, 16]. These fluctuations may mediate the recruitment of the repair factors that recognize damage at the initial stages. Results of experiments (in particular, the analysis of specific excision efficiency using model DNAs with various structures, which became the grounds for formulating the concept of the bipartite recognition process in NER) point to the important role of the intact DNA strand in the recognition process [15, 16]. NER proteins from a cellular extract can initiate the repair process only when the model DNA is characterized both by a chemical modification and distortions in the secondary structure. Thus, a fragment containing the C4'-pivaloyl adduct of deoxyribose, a bulky but not distorting structure of the regular DNA duplex, was excised only when it was located in an artificialy short site of a pairing distortion. The sites of modification-free uncoupled bases cannot act as substrates for specific excision; neither can structures containing a chemical modification opposite to the loop formed by an unmodified strand [16].

Numerous studies have been devoted to the search for the proteins responsible for initial damage recognition and recruitment of the following NER factors. Although a number of facts point to the key role of XPC in the initiation of NER [17–19], the results of the evaluation of their affinity to damaged DNA and analysis of the specificity to a damaged substrate have provided opportunity to consider the XPA factor and its complexes with RPA and XPC as a damage sensor [20–23]. Confocal microscopy using fluorescent proteins has shown that XPC can be immobilized near UV damages in the absence of XPA (XPA-deficient cells), while in XPC-deficient cells, XPA is not bound to the damaged DNA sites [3, 18]. The results of biochemical studies have shown that XPC is required for the recruitment of other factors into the GG-NER process [17, 19, and 24]. Various approaches that have included visualization methods allowing to track fluorescent protein movements within chromatin in a living cell have been applied to clarify the mechanism whereby XPC recognizes the damage against a background of an excess of intact DNA. FRAP/FLIP (fluorescence recovery after photobleaching/fluorescence loss in photobleaching). It was shown that the dynamics of the movement and intranuclear localization mode of GFP-XPC differ from the dynamics and other NER factors localization (GFP-XPA, TFIIH-GFP). XPC permanently scans the genome DNA in search of damage. The scanning mode is association-dissociation with the formation of a plethora of short-lived complexes. More stable XPC-DNA complexes are formed when XPC collides with damaged sites, following which the recruitment of other NER factors to the damaged site occurs. In addition, XPC is permanently exported from the nucleus and imported back. Such XPC exchange in the absence of damage maintains the

stationary level of its nuclear concentration, preventing redundant DNA probing that may interfere with other processes of nucleic metabolism. Under any effects on cells resulting in DNA damage, the rate of XPC transport to the cell decreases and XPC accumulates in the nucleus, which facilitates the rapid response of the repair system to genotoxic affection. This effect is maximally pronounced when NER-repaired damage arises. The XPC nucleus-cytoplasmic exchange is delayed for 6–8 h, exceeding markedly the time of the XPC presence in NER complexes. Some authors [25] regard the slow repair of some types of UV damage as the reason behind such a prolonged XPC exchange stop. XPC needs heterodimer UV-DDB as a partner protein to recognize UV damage efficiently [26–29].

The molecular basis of XPC-DNA interaction is now being actively examined. A detailed understanding of the mechanism of initial recognition of a DNA substrate by a sensor protein conditions the understanding of the interplay between the damaged structure and its rate of excision from the DNA, as well as the way by which factor XPC discriminates damaged nucleotides against a background of a substantial excess of undamaged DNA. The X-ray diffraction analysis of Rad4, a yeast ortholog of XPC, provided considerable progress in the study of the structure of a sensor protein-damaged DNA complex. The analysis of the structure of the crystallized complex of truncated Rad4 (a.a.r. 123–632) + Rad23 protein + heteroduplex containing the cyclobutane-pyrimidine dimer has shown that a large (transglutaminase, TGD) Rad4 domain with one β-hairpin from domain 1 (BHD1) forms a C-shaped structure by coming into contact with 11 nucleotides of the undamaged dsDNA on the 3' side of the damage. Another portion of Rad4 is composed of the hairpin domains BHD2 and BHD3 that mainly form van der Waals contacts with the DNA substrate near the damage site. The long β-hairpin emerging from BHD3 is inserted into the double helix, causing the DNA backbone to bend. As a result, both the cross-linked pyrimidines and the opposite bases of the undamaged strand are displaced from the helix. The protein does not come into contact with the damage directly, interacting with two adjacent bases and two bases opposite CPDs. Each adjasent undamaged base is clamped between residues of aromatic amino acids from the BHD2/BHD3 motif [30]. This is a typical mode of interaction between the OB-subdomain (a structural unit present in proteins with increased affinity to single-stranded DNA) and ssDNA [31]. The image of Rad4 matches well our understanding of the way XPC interacts with a damaged DNA based on the data on this protein structure and the results of biochemical examinations. The analysis by atomic force microscopy has shown that XPC binding results in the bending of the DNA-duplex backbone and formation of a ~140–130° angle [32]. As shown by permanganate footprinting the emerging bend of the helix axis of damaged DNA is followed by partial melting of the duplex (by approximately 4–7 nucleotides) [33]. The similarity between the schemes of location of the RAD4 and XPC factors on damaged DNA is confirmed by the results of photo-induced cross-linking of these proteins with DNA containing a bulky modification [34]. This pattern of XPC-DNA interaction, the strategy of indirect check for the presence of structural lesions, resulting in an increased level of fluctuations in the undamaged strand, underlies the incredibly wide substrate specificity of the GG-NER pathway. The transglutaminase domain and a domain structurally similar to the OB-subdomain of factor RPA were found in human XPC; the domains interact with ssDNA with the use of an aromatic damage sensor, a pair of aminoacid residues, Trp690, and Phe733 [35–37].

FRAP experiments using XPC forms truncated both at the N- and C-ends have revealed the XPC fragment mainly responsible for the recognition of damaged DNA. The fragment comprising, in fact, only 15% of the full-size XPC (a minimal sensor) appears to be capable of UV damage recognition in live cells. The minimal sensor fragment prefers heteroduplexes and single-stranded oligonucleotides; it recognizes damage due to its affinity to the regions with distorted hydrogen bonds. The fragment consists of BHD1, BHD2, and a short (25 amino acid residues) motif separating the BHD2 and BHD3 domains and is folded to form a structure known as a β-turn. Specific features of the β-turn determine the operational efficiency of a minimum damage sensor [38, 39]. This short polypeptide fragment can either be attracted to or repulsed by DNA; due to this feature, an XPC is capable of dynamic interaction with DNA within the genome. Damage recognition is facilitated in this case, providing the DNA-scanning molecules of the sensor protein with sufficient mobility. The truncated C-terminal XPC containing a β-turn keeps some residual repair activity found using the cell reactivation method. A photobleaching assay of protein motion dynamics proves increased XPC mobility in the nuclei of living cells [24]. The same approach demonstrates that rapid post-UV-immobilization of XPC occurs only in the nuclei of cells containing XPC mutants with an intact β-turn. Especially remarcable is the fact that the polypeptide fragment including BHD1 and BHD2 also acts as a minimal sensor only if an intact β-turn is presented. Biochemical experiments show that the XPC nuclear mobility determined by the structural element results from the repulsion of a protein molecule from an undamaged dsDNA. Finally, the dynamic role of a β-turn within a full-size XPC was confirmed by

the results of site-directed mutagenesis when glutamic acid was replaced with lysine. This charge inversion was supposed to reduce the strength of electrostatic repulsion between a negatively charged lateral chain of a protein and the phosphates within the DNA backbone. As was assumed, the charge inversion increased the affinity of mutant XPC molecules to undamaged DNA, reducing their mobility within the nucleus and decreasing the activity of the GG-NER pathway. Thus, the β-turn plays a crucial role in the regulation of the dynamics of XPC–normal DNA duplex interaction. This subdomain, due to its ability to repulse DNA, facilitates damage recognition, providing sufficient mobility to the XPC molecules that search for genome damage [24, 35–38]. When XPC binds to the abnormally oscillating region of a native strand in a way that excludes direct contacts with the damage, the nucleoprotein intermediates formed upon initial screening can be converted into a strong recognition complex [29, 36–39].

Within a cell, XPC exists as the heterotrimeric complex XPC-HR23B-Cen2 [1, 2, 18]. HR23B stabilizes the complex, protects it against proteasome degradation, and stimulates the DNA-binding activity of XPC. The recombinant heterodimer XPC-HR23B is a stable complex that interacts *in vitro* with damage of various types and is widely used for the NER reaction in a reconstituted system [18, 40, 41]. The interplay between XPC-HR23B and damaged DNA was analyzed using affinity modification. DNA duplexes of various structures containing bulky modifications, including photoactive fluorochloroazide pyridyl damage, were used as probes. Some model duplexes contained analogs of undamaged strands created with the use of photo reagents with a zero linker length: nucleotide links with 4-thio- and 5-iodo-modified bases [34, 42–44]; some duplexes included a platinum adduct [45]. A large XPC subunit was the only modification target in all cases. The second high-molecular weight nucleoprotein adduct with a lower electrophoretic activity appeared as a result of photo-induced cross-linking with other amino acid residues of the DNA-binding XPC subunit [44]. Moreover, the product of XPC-HR23B protein-protein cross-links emerging after hard (254 nm) and long-term (60 min) UV irradiation and revealed by Western blotting does not contain a radioactive label and can be formed independently of the presence of a DNA probe [45]. The HR23B subunit of the complex does not come into contact with DNA directly; this was shown by the absence of products of its photo-induced cross-linking with analogues of a damaged DNA. Quite recently, confocal microscopy showed that HR23B, in contrast to XPC, is not immobilized on the damaged DNA of a cell and is released from the complex after XPC binding [46].

The roles played by centrin-2 in the XPC complex have not been completely clarified, though the presence of the protein is known to increase the stability, control affinity/selectivity of DNA binding by the XPC-HR23B dimer. Also Cen2 interaction with the C-end fragment of XPC can regulate the recruitment of TFIIH [35].

Binding of TFIIH to the nucleoprotein complex formed by damaged DNA and XPC triggers the verification of the damaged DNA as a NER substrate; that is, the presence of a bulky chemical modification in the discovered XPC DNA site with a distorted regular structure.

## DAMAGE VERIFICATION AND ASSEMBLY OF THE DAMAGED FRAGMENT OF A COMPLEX READY FOR EXCISION

The TFIIH factor is a multisubunit complex composed of two helicases, XPB and XPD; enzymatic activity-free proteins, p62, p52, p44, p34 and p8; and the complex of CDK-activating kinase, CAK (cyclin H, Cdk7, and Mat1). In a 3D model of human TFIIH, established according to the results of an electron microscopic analysis, the core proteins form a slightly elongated ring-shaped structure (16 × 12.5 × 7.5 nm) with a hole of a diameter sufficient to enclose a double-stranded DNA helix (2.6–3.4 nm) [47]. A structure formed by core proteins via XPD contacts with the CAK subcomplex, forming a bulge on the external side of the ring. The smallest p8 subunit (TTDA) is also included into the core composition. XPC-dependent recruitment of TFIIH to the damage is mainly controlled by direct contact of XPC with the XPB and p62 subunit (*Fig. 2*). The TFIIH annular structure encompasses the dsDNA on the 5' side of the damage, releasing a kinase subcomplex. Uncoiling of a DNA double helix around the damage catalyzed by two specialized helicases, XPB (3'→5') and XPD (5'→3'), is the most obvious result of TFIIH binding. It is followed by the formation of an approximately 27 nucleotide-long (22 nucleotides on the 5' side of the damage and 5 nucleotides – on the 3' side) asymmetrical region of separated strands. This stage requires the energy of ATP hydrolysis [48-51]. The mechanism of formation of single-stranded DNA regions around the damage and checking for modification presence become clearer thanks to the data on the structure of the XPB and XPD factors, obtained in the study of the crystal structure of protein analogues of archaea [52-54], and the analysis of the structure of the C-terminal fragment of human XPB [53]. Analysis of the structure of *Archaeoglobus fulgidus* XPB crystals showed that the protein contains two helicase domains, HD1 and HD2, including seven helicase motifs. Two new structural motifs, RED in HD1, consisting of three

charged amino acid residues – Arg, Glu, and Asp – and a thumb-like motif (ThM) in HD2, similar to that found in T7-DNA polymerase. Each analog of the human XPD from three archaeal species (*Thermoplasma acidophilum*, *Sulfolobus tokodaii*, and *S. acidocaldarius*) contains four domains, including HD1, HD2, Arch-domain, and the unique 4FeS-domain comprising the Fe-4S-claster, which was found for the first time in the helicase structure [54–56]. The details of XPD–DNA interaction and structure of the established complexes have been actively examined using the models of recombinant archaeal helicases. The established model of XPD–DNA interaction supposes that ssDNA is bound in a groove between the Arch and HD2 domains and passes through a hole (a pore) in a globule with a diameter sufficient for free helicase motion along the DNA. Bulky adducts repaired by the NER pathway might block XPD translocation along the ssDNA located in such a way. This idea is in accordance with earlier data on the inhibiting activity of a yeast XPD analog, rad3 helicase, as it interacts with a bulky damage [57]. An XPD analog from *Ferroplasma acidarmanus*, which acts in the form of a monomer but is structurally similar to the human protein, helicase was shown to be stopped by damage in the strand along which it translocates in the 5'→3' direction. In contrast to the inhibited helicase activity, the ATPase activity of a damage-bound XPD is preserved and even increases. Moreover, when a complementary 3'→5' strand contains CPD, the enzyme dissociates from the substrate [58]. The data on the crystal structures of archaeal XPD homologs supports the idea that the presence of a modification in DNA is finally verified when a base binds to the pocket located on the XPD surface. The pocket is located near the tunnel within the protein structure used to thread a DNA strand [54, 56, 58]. Examination of the interactions between mutant human XPD proteins and DNA containing UV damage definitely confirmed the idea that the XPD subunit of TFIIH checks for the presence of damage. The mutations were inserted into the protein region located in the site of the DNA-binding channel-pore transition (a.a.r. Y192A and R196E). The amino acid residues directly involved in the helicase and ATPase activity were unaffected. The mutant proteins retained their ability to uncoil DNA but could not distinguish between damaged and undamaged DNAs; when these residues were replaced, the XPD ability to form protein complexes (stable recognition intermediates) decreased. Thus, it was demonstrated that these amino acid residues are part of a polypeptide fragment forming a sensor pocket of human XPD. The pocket location coincides with that in its archaeal homolog from *T. acidophilum* [59]. In contrast to XPD, the XPB factor moving along the DNA in 3'→5' is more likely to exhibit

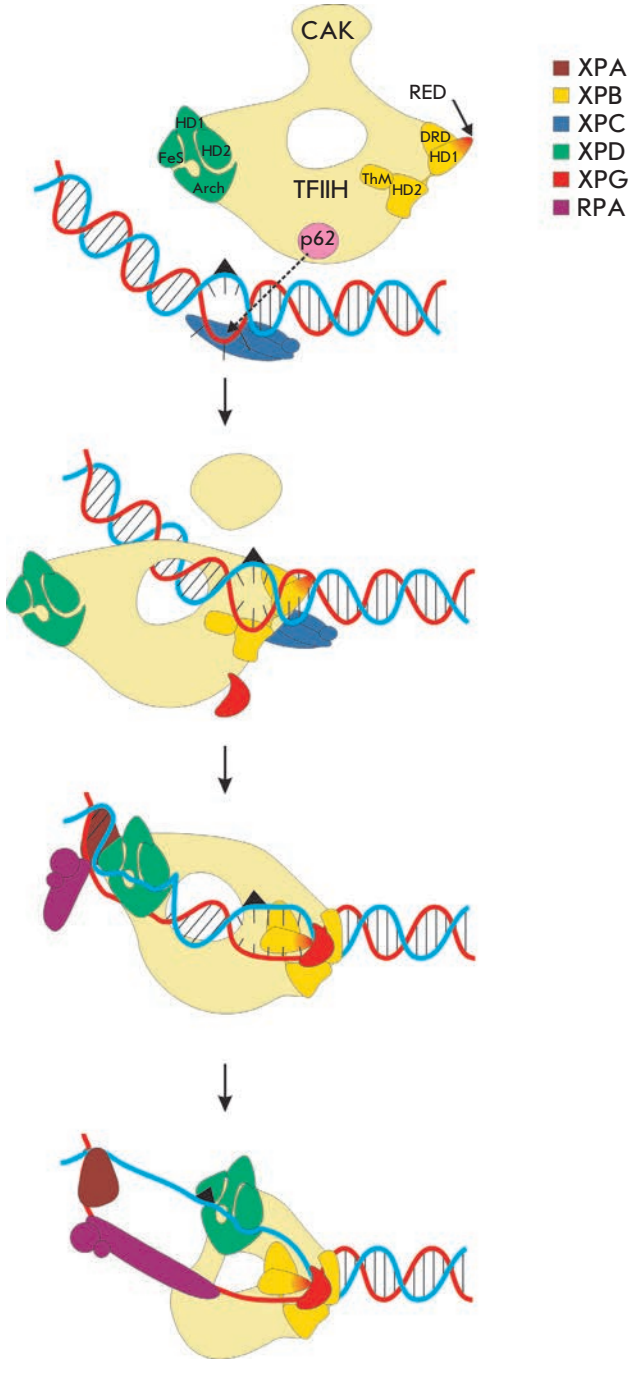


Fig. 2. Scheme of the two-step process of damage recognition

ATPase properties than helicase activity. New motifs, RED (in HD1) and Thumb (in HD2), were for the first time revealed in helicase domains [52–55]. The XPB activity is stimulated by the TFIIH p52 subunit [60]. XPB is the first to bind to a bent DNA–XPC complex. XPC interacts with a small region of a destabilized undamaged dsDNA strand (approximately 5 nucleotides from 3'-side), rotates one of the two helicase domains by 170°,

entraining DNA, brings together the helicase domains 1 and 2 connected by a flexible unstructured fragment acting as a hinge, and forms a site of ATP binding. Composed of charged amino acids the RED motif of XPB is subsequently inserted between the dsDNA strands and untwists it by approximately 5 nucleotides in the 3'→5' direction. A preliminary fixation of TFIIH on DNA occurs. A TFIIH ring is inclined with respect to the axis of the DNA helix. XPD acquires the possibility to come into contact with the site of the damaged strand (~22 nucleotides towards the 5' direction of the damage) and unwinds DNA in the 5'→3' direction when moving along the strand due to the ATP hydrolysis energy and forming an asymmetric bubble. XPD stopes as it encounters a damage site. XPD, together with TFIIH, becomes immobilized on DNA; this situation is typical of bulky modifications [50, 60, 61].

After the status of damaged DNA as a NER substrate is confirmed by the emergence of long-lived TFIIH-including an open nucleoprotein structure the next step of repair starts. A more stable and extended preincision complex is formed; the RPA and XPA factors join the complex. The interactions of RPA and XPA with the TFIIH subunits coordinate the involvement of these proteins in the complex.

RPA is a three-subunit protein factor with very high affinity to single-stranded DNA that participates in many processes of DNA metabolism and is presented in a cell by a large copy number [62]. RPA is required to form the preincision complex and during the following excision of the damaged DNA fragment [1]. Five DNA-binding domains located in the p70 and p32 subunits of RPA have different affinities for substrate, so RPA can form with ssDNA complexes of different architecture and stability. These domains interact with DNA in a polar manner (in 5'→3' direction) [63, 64]. In the preincision complex, RPA occupies approximately 30 nucleotides of the undamaged strand opposite to the damage-containing site, thus protecting DNA from illegitimate degradation and facilitating accurate positioning of XPG and ERCC1-XPF endonucleases.

XPA, similar to XPC, possesses increased affinity for DNA with a specific secondary structure (in particular, to helix kinks induced by a bulky damage): thus XPA (or its complex with RPA) was considered as a candidate damage sensor or a protein controlling the presence of a modification [1, 65, 66]. However, in contrast to XPC, the XPA factor preferably interacts with a damaged strand and has a much lower affinity for the DNA analogs of NER substrates and intermediates [65, 66]. A small XPA functioning in a cell in monomeric form has a rather complex domain structure. Analysis of the NMR spectra of the DNA-binding XPA fragment formed by the amino acid residues 98–219 revealed a positively charged groove consisting of approximately 60 a.a.r. on the protein surface near the C-end of the DNA-binding domain. The geometric parameters of the groove allow it to bind both to single- and double-stranded DNAs [67, 68]. A zinc finger containing an acid subdomain (a.a.r. 105–129) and a C-end subdomain (a.a.r. 138–209) can be distinguished in the structure of the DNA-binding fragment of XPA. The zinc finger motif does not participate in the DNA binding; it is required for interaction with RPA [67]. The domains of specific XPA interaction with a number of core NER polypeptides, RPA70, RPA32 (N-terminal and central XPA fragments), ERCC1 (a short region adjacent to the XPA N-terminal fragment), and TFIIH (the XPA C-terminal fragment) were identified using site-directed mutagenesis. XPA-RPA interaction promotes a more efficient binding of both factors to DNA [65, 66, 69], while interaction with a complex formed on the DNA opened around a lesion promotes high selectivity. These XPA properties are the results of structural features allowing for easy changes in conformation and providing efficient interaction with the damaged DNA during the formation of the preincision complex. XPA is currently regarded as a sensor of an anomalous electrostatic potential occurring at the kinks of the negatively charged sugar phosphate DNA backbone. The amino acid residues crucial for efficient XPA functioning were determined by studying the interplay between a series of mutant XPA forms and modified DNAs through gel retardation and photo-induced cross-linking to DNA containing an aryl azide modification [70]. A region of damaged DNA strand that is in contact with XPA was identified using affinity modification. The result of the experiments with a series of probes containing photoactive 5-J-dU and damage-mimicking bulky modification based on fluorescein in various mutual locations shows that most XPA-DNA contacts are located near the ssDNA/dsDNA junction on the 5' side of the damage [69]. The ability of XPA to specifically interact with DNA, as well as with many NER proteins (RPA, ERCC1-XPF, TFIIH, XPC), determines its considerable structural and functional role in the assembly of a complex ready for double incision [71–74].

## ELIMINATION OF A DAMAGED FRAGMENT FROM THE DNA

The XPG factor acting as a 3'-endonuclease during repair is recruited to a damaged region independently of XPA and RPA, through its interaction with TFIIH [74–76]. XPG-DNA binding and simultaneous release of XPC are the final stage of formation of the complex ready for excision on the DNA. At this step, XPG performs a structural function by stabilizing the open complex; it exhibits no endonuclease activity. ssDNA/dsD-

NA transition on the 3' side of the damage determines the type of XPG interaction with DNA substrates during NER. Various footprinting and gel-retardation techniques show that XPG, together with other members of the flap-endonuclease-1 family, interacts with the double-stranded region of model structures through non-specific contacts with the phosphodiester backbone (*Fig. 3*). These contacts encompass approximately 12 nucleotides of both strands and are located on the external side of the B-DNA helix. The additional non-specific XPG contacts in single-stranded fragments of model substrates (three contacts with the phosphodiester backbone in a damaged strand and contacts of unknown type with an undamaged strand) poorly affect the binding. At that, the presence of a single-stranded fragment of a damaged strand near the protein binding site is a prerequisite of the demonstration of XPG endonuclease activity [77, 78].

Factor XPF is a structure-specific endonuclease that catalyses incision of DNA at the site of the ssDNA / dsDNA junction on the 5' side of the damage and functions in NER within a heterodimer with the ERCC1 protein. An obligate ERCC1-XPF heterodimer is involved into the complex through the ERCC1-XPA interaction and breaks the damaged strand on the 5' side of the damaged site. Identified several domains involved in the functioning of ERCC1-XPF [79–83]. Both subunits contain a helix-hairpin-helix (HhH) motif required for the formation of a heterodimer near the C-ends [84]. An active center of XPF is a conservative nuclease domain adjacent to the HhH domain [79]. The central ERCC1 domain is structurally homologous with the nuclease XPF domain; however, instead of the active site with acidic residues, a groove, containing the basic and aromatic amino acid residues, exists in this domain. This fragment interacts with XPA, connecting ERCC1-XPF to other NER machineries [81, 83]. Individual recombinant XPF domains and the data on archaeal XPF proteins demonstrate that these five domains participate in the interaction with DNA [79–81]. Mass spectrometry, NMR spectroscopy, and *in vitro* analysis of the protein-DNA binding allowed to determine the structure of the complex of the C-terminal HhH domain of the XPF protein with ssDNA in a solution [78]. A stable complex with ssDNA forms an HhH homodimer. At that, DNA is twisted around a protein in a way providing protein-DNA interaction along the phosphate backbone of a molecule. A positively charged fragment in the second helix of one of the HhH motifs comes into contact with the phosphate backbone of ssDNA. These data, along with data in a previous publication [85], allow to construct a model of the ERCC1-XPF complex. This model explains the positioning of endonuclease at the site of the ssDNA /dsDNA junction on the 5' side of the dam-

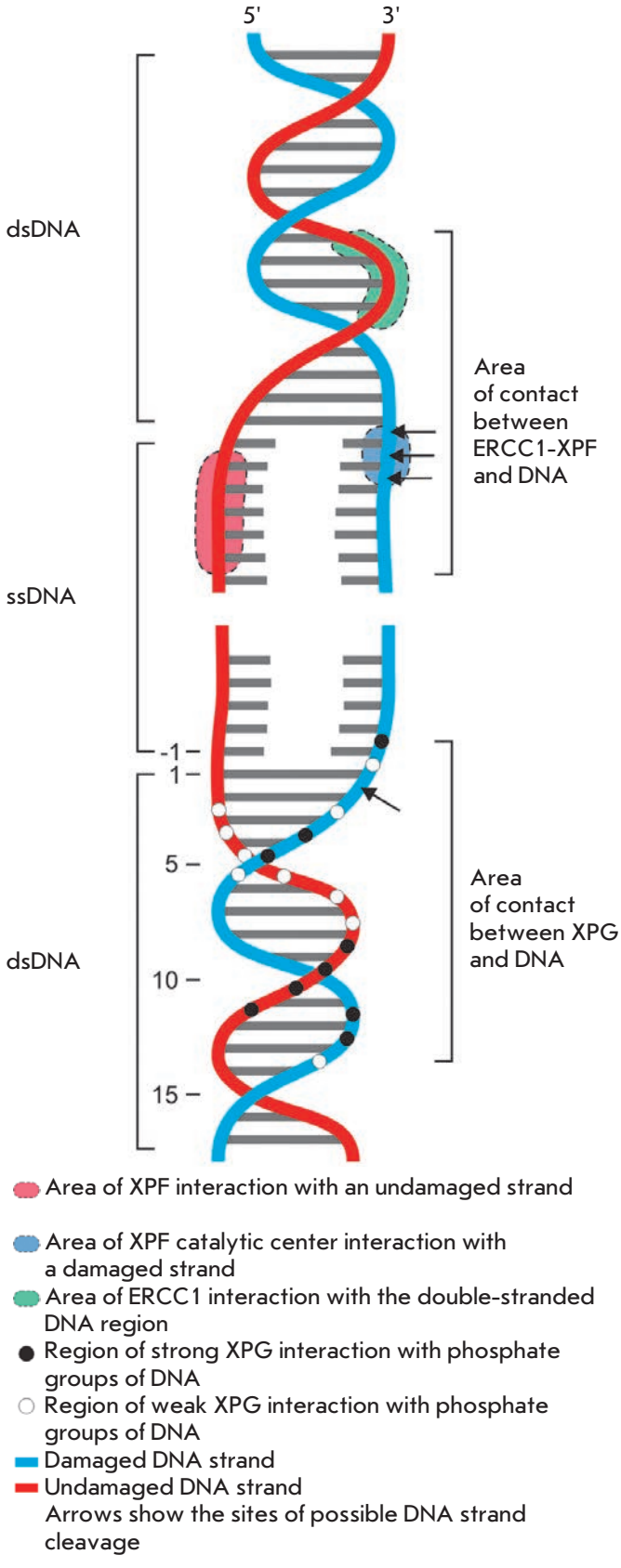


Fig. 3. Schematic representation of the XPF-ERCC1 and XPG contacts with DNA in the damage-containing region

age. According to the model, the ERCC1 HhH domain interacts with a double-stranded portion of DNA. The nuclease domain of XPF comes into contact with the damaged DNA strand, while the XPF and ERCC1 HhH domains come into contact with the undamaged strand (*Fig. 3*).

The role of the C-terminal DNA-binding domains in the interaction between heterodimer and DNA substrates was examined through a mutation analysis within full-size ERCC1-XPF. Mutations in one domain considerably reduced the activity of the NER pathway neither *in vitro* nor *in vivo*. Functioning of the NER pathway is disturbed when mutations are inserted into several domains, and the significance of separate domains is hierarchic [84]. In the presence of catalytically inactive XPG, ERCC1-XPF catalyzes 5'-incision (15–25 nucleotides away from the damage) and forms an unbound 3'-hydroxyl group required for the initiation of the repair synthesis and emergence of the mobile single-stranded fragment containing the damage. The changes in the structure of the protein-nucleic complex allow an XPG to exhibit catalytic activity [78]. 3'-incision of DNA (3–9 nucleotides from damage) completes the process of damaged site excision. In the structure of XPG, after excision while remaining bound to the DNA, there are motifs that provide specific interaction with PCNA (nuclear antigen of proliferative cells) for some time after excision. XPG might facilitate efficiency and processivity in the repair synthesis [1, 2].

## REPAIR SYNTHESIS

Repair synthesis and DNA strand ligation are performed by the enzymes and protein factors that also participate in DNA replication. The DNA polymerase δ or ε and factors RFC, PCNA, and RPA are needed for DNA synthesis. An RFC complex consisting of five different subunits facilitates ATP-dependent PCNA loading onto DNA near the 3'-end of the DNA fragment flanking a gap resulting from excision. PCNA is a homotrimeric complex that forms a ring-shaped structure sliding along DNA and interacting with DNA polymerases, thus facilitating the processivity of the enzymes [1].

## CONCLUSION

A NER process is controlled by multiple weak interactions between proteins and DNA substrates, along with protein-protein interactions in nucleoprotein complexes. In a eukaryotic cell after stable XPC/DNA complex formation during the initial recognition of the damage, NER is actually performed by reparasome, a complex of variable composition and architecture consisting of a large number of subunits. Individual subunits of the complex have no sufficient affinity and selectivity to the substrate (DNA containing bulky damage). The situation changes when specific protein complexes are established at the damage site. The NER proteins of these complexes are joined by the DNA processing. A total of 18 polypeptides must be accurately positioned within two or three DNA turns when a stable structure ready for damage removal is formed and excision starts. The structure of NER-associated proteins provides the possibility of contact with the DNA substrate and of dynamic specific protein-protein interactions. The changes in interactions performed by the same protein are one of the mechanisms that regulate the repair process and fine-tune the complexes, providing high-precision nucleotide excision repair. The study of the composition and architecture of nucleoprotein NER complexes both *in vitro* and *in vivo* requires the use of a broad range of methods and model systems of different complexity. ●

*This study was supported by the Russian Foundation for Basic Research (grant N 12-04-00487a), Russian Academy of Sciences (Program of Fundamental Studies "Molecular and Cell Biology"), and the Ministry of Education and Science of the Russian Federation (NSh-420.2014.4 and support for laboratory of O.I. Lavrik in Novosibirsk State University).*

REFERENCES

1. Gillet L.C., Schärer O.D. // Chem. Rev. 2006. V. 106. № 2. P. 253–276.
2. Sugasawa K. // Mutat. Res. 2010. V. 685. № 1. P. 29–37.
3. Volker M., Mone M.J., Karmakar P., van Hoffen A., Schul W., Vermeulen W., Hoeijmakers J.H., van Driel R., van Zeeland A.A., Mullenders L.H. // Mol. Cell. 2001. V. 8. № 1. P. 213–224.
4. Lehmann A.R. // Biochimie. 2003. V. 85. P. 1101–1111.
5. Hanawalt P.C., Spivak G. // Nat. Rev. Mol. Cell Biol. 2008. V. 9. № 11. P. 958–970.
6. Friedberg E.C. // Nat. Rev. Cancer. 2001. V. 1. P. 22–33.
7. Hoeijmakers J.H. // Nature. 2001. V. 411. № 6835. P. 366–374.
8. Kuraoka I., Bender C., Romieu A., Cadet J., Wood R.D., Lindahl T. // Proc. Natl. Acad. Sci. USA. 2000. V. 97. № 8. P. 3832–3837.
9. D'Errico M., Parlanti E., Teson M., de Jesus B.M., Degan P., Calcagnile A., Jaruga P., Bjoras M., Crescenzi M., Pedrini A.M., et al. // EMBO J. 2006. V. 25. № 18. P. 4305–4315.
10. Johnson K.A., Fink S.P., Marnett L.J. // J. Biol. Chem. 1997. V. 272. № 17. P. 11434–11438.
11. Luijsterburg M.S., Bornstaedt G., von Gourdin A.M., Politi A.Z., Moné M.J., Warmerdam D.O., Goedhart J., Vermeulen W., van Driel R., Höfer T. // J. Cell Biol. 2010. V. 189. № 17. P. 445–463.
12. Svilar D., Goellner E.M., Almeida K.H., Sobol R.W. // Antioxid. Redox Signal. 2011. V. 14. № 12. P. 2491–2507.

13. Yang W. // Cell Research. 2008. V. 18. № 1. P. 184–197.
14. Isaacs R.J., Spielmann H.P. // DNA Repair (Amst.). 2004. V. 3. № 5. P. 455–464.
15. Hess M.T., Schwitter U., Petretta M., Giese B., Naegeli H. // Proc. Natl. Acad. Sci. USA. 1997. V. 94. № 13. P. 6664–6669.
16. Buterin T., Meyer C., Giese B., Naegeli H. // Chem. Biol. 2005. V. 12. № 8. P. 913–922.
17. Sugasawa K., Ng J., Masutani C., Iwai S., van der Spek P., Eker A., Hanaoka F., Bootsma D., Hoeijmakers Jan H.J. // Mol. Cell. 1998. V. 2. № 2. P. 223–232.
18. Rademakers S., Volker M., Hoogstraten D., Nigg A.L., Moné M.J., van Zeeland A.A., Hoeijmakers J.H., Houtsmuller A.B., Vermeulen W. // Mol. Cell Biol. 2003. V. 23. № 16. P. 5755–5767.
19. Sugasawa K., Shimuzu Y., Shigenori I., Iwai S., Hanaoka F. // DNA Repair. 2002. V. 12. № 1. P. 95–107.
20. Nocentini S., Coin F., Saijo M., Tanaka K., Egly J.M. // J. Biol. Chem. 1997. V. 272. № 37. P. 22991–22994.
21. Missura M., Buterin T., Hindges R., Hübscher U., Kaspárková J., Brabec V., Naegeli H. // EMBO J. 2001. V. 20. № 13. P. 3554–3564.
22. Hermanson-Miller I.L., Turchi J.J. // Biochemistry. 2002. V. 41. № 7. P. 2402–2408.
23. Thoma B.S., Wakasugi M., Christensen J., Reddy M.C., Vasquez K.M. // Nucl. Acids Res. 2005. V. 33. № 9. P. 2993–3001.
24. Sugasawa K., Okamoto T., Shimizu Y., Masutani C., Iwai S., Hanaoka F. // Genes Dev. 2001. V. 15. № 5. P. 507–521.
25. Hoogstraten D., Bergink S., Ng J., Verbiest V.H., Luijsterburg M.S., Geverts B., Raams A., Dinant C., Hoeijmakers J.H., Vermeulen W., Houtsmuller A.B. // J. Cell Sci. 2008. V. 121. № 16. P. 2850–2859.
26. Reardon J.T., Sancar A. // Genes Dev. 2003. V. 17. № 20. P. 2539–2551.
27. Fitch M.E., Nakajima S., Yasui A., Ford J.M. // J. Biol. Chem. 2003. V. 278. № 47. P. 46906–46910.
28. Sugasawa K., Okuda Y., Saijo M., Nishi R., Matsuda N., Chu G., Mori T., Iwai S., Tanaka K., Hanaoka F. // Cell. 2005. V. 121. № 3. P. 387–400.
29. Scrima A., Konícková R., Czyzewski B.K., Kawasaki Y., Jeffrey P.D., Groisman R., Nakatani Y., Iwai S., Pavletich N.P., Thomä N.H. // Cell. 2008. V. 135. № 7. P. 1213–1223.
30. Min J.H., Pavletich N.P. // Nature. 2007. V. 449. № 7162. P. 570–575.
31. Murzin A.G. // EMBO J. 1993. V. 12. № 3. P. 861–867.
32. Janićijević A., Sugasawa K., Shimizu Y., Hanaoka F., Wijgers N., Djurica M., Hoeijmakers J.H., Wyman C. // DNA Repair (Amst.). 2003. V. 2. № 3. P. 325–336.
33. Mocquet V., Kropachev K., Kolbanovskiy M., Kolbanovskiy A., Tapias A., Cai Y., Broyde S., Geacintov N.E., Egly J.M. // EMBO J. 2007. V. 26. № 12. P. 2923–2932.
34. Krasikova Y.S., Rechkunova N.I., Maltseva E.A., Pestryakov P.E., Petruseva I.O., Sugasawa K., Chen X., Min J.H., Lavrik O.I. // J. Biol. Chem. 2013. V. 288. № 15. P. 10936–10947.
35. Bunick C.G., Miller M.R., Fuller B.E., Fanning E., Chazin W.J. // Biochemistry. 2006. V. 45. № 50. P. 14965–14979.
36. Maillard O., Solyom S., Naegeli H. // PLoS Biol. 2007. V. 5. № 4. e79.
37. Camenisch U., Trutlein D., Clement F.C., Fei J., Leitenstorfer A., Ferrando-May E., Naegeli H. // EMBO J. 2009. V. 28. № 16. P. 2387–2399.
38. Clement F.C., Camenisch U., Fei J., Kaczmarek N., Mathieu N., Naegeli H. // Mutat. Res. 2010. V. 685. № 1. P. 21–28.
39. Sugasawa K., Akagi J., Nishi R., Iwai S., Hanaoka F. // Mol. Cell. 2009. V. 36. № 4. P. 642–653.
40. Araki M., Masutani C., Takemura M., Uchida A., Sugasawa K., Kondoh J., Ohkuma Y., Hanaoka F. // J. Biol. Chem. 2001. V. 276. № 22. P. 18665–18672.
41. Nishi R., Okuda Y., Watanabe E., Mori T., Iwai S., Masutani C., Sugasawa K., Hanaoka F. // Mol. Cell Biol. 2005. V. 25. № 13. P. 5664–5674.
42. Maltseva E.A., Rechkunova N.I., Gillet L.C., Petruseva I.O., Schärer O.D., Lavrik O.I. // Biochim. Biophys. Acta. 2007. V. 1770. № 5. P. 781–789.
43. Maltseva E.A., Rechkunova N.I., Petruseva I.O., Vermeulen W., Schärer O.D., Lavrik O.I. // Bioorg. Chem. 2008. V. 36. № 2. P. 77–84.
44. Evdokimov A.N., Petruseva I.O., Pestryakov P.E., Lavrik O.I. // Biochemistry (Moscow). 2011. V. 76. № 1. P. 188–200.
45. Neher T.M., Rechkunova N.I., Lavrik O.I., Turchi J.J. // Biochemistry. 2010. V. 49. № 4. P. 669–678.
46. Bergink S., Toussaint W., Luijsterburg M.S., Dinant C., Alekseev S., Hoeijmakers J.H., Dantuma N.P., Houtsmuller A.B., Vermeulen W. // J. Cell Biol. 2012. V. 196. № 6. P. 681–688.
47. Schultz P., Fribourg S., Poterszman A., Mallouh V., Moras D., Egly J.M. // Cell. 2000. V. 102. № 5. 599–606.
48. Araújo S.J., Nigg E.A., Wood R.D. // Mol. Cell Biol. 2001. V. 21. № 7. P. 2281–2291.
49. Oksenych V., de Jesus B.B., Zhovmer A., Egly J.M., Coin F. // EMBO J. 2009. V. 28. № 19. P. 2971–2980.
50. Egly J.M., Coin F. // DNA Repair. 2011. V. 10. № 7. P. 714–721.
51. Compe E., Egly J.M. // Nat. Rev. Mol. Cell Biol. 2012. V. 13. № 6. P. 343–354.
52. Fan L., Arvai A.S., Cooper P.K., Iwai S., Hanaoka F., Tainer J.A. // Mol. Cell. 2006. V. 22. № 1. P. 27–37.
53. Hilario E., Li Y., Nobumori Y., Liu X., Fan L. // Acta Crystallogr. D Biol. Crystallogr. 2013. V. 69. № 2. P. 237–246.
54. Wolski S.C., Kuper J., Hazelmann P., Truglio J.J., Croteau D.L., van Houten B., Kisker C. // PLoS Biol. 2008. V. 6. № 6. e149.
55. Fan L., Fuss J.O., Cheng Q.J., Arvai A.S., Hammel M., Roberts V.A., Cooper P.K., Tainer J.A. // Cell. 2008. V. 133. № 5. P. 789–800.
56. Kuper J., Wolski S.C., Michels G., Kisker C. // EMBO J. 2012. V. 31. № 2. P. 494–502.
57. Naegeli H., Modrich P., Friedberg E.C. // J. Biol. Chem. 1993. V. 268. № 14. P. 10386–10392.
58. Mathieu N., Kaczmarek N., Naegeli H. // Proc. Natl. Acad. Sci. USA. 2010. V. 107. № 41. P. 17545–17550.
59. Mathieu N., Kaczmarek N., Rüthemann P., Luch A., Naegeli H. // Curr. Biol. 2013. V. 23. № 3. P. 204–212.
60. Oksenych V., Coin F. // Cell Cycle. 2010. V. 9. № 1. P. 90–96.
61. Fan L. How two helicases work together within the TFIIH complex, a perspective from structural studies of XPB and XPD helicases. Berlin-Heidelberg: Higher Education Press and Springer-Verlag, 2013. V. 1. 6 p.
62. Fanning E., Klimovic V., Nager A.R. // Nucl. Acids Res. 2006. V. 34. № 15. P. 4126–4137.
63. De Laat W.L., Appeldoorn E., Sugasawa K., Weterings E., Jaspers N.G.J., Hoeijmakers J. // Genes Dev. 1998. V. 12. № 16. P. 2598–2609.
64. Kolpashchikov D.M., Khodyreva S.N., Khlimankov D.Y., Wold M.S., Favre A., Lavrik O.I. // Nucl. Acids Res. 2001. V. 29. № 2. P. 373–379.
65. Hey T., Lipps G., Krauss G. // Biochemistry. 2001. V. 40. № 9. P. 2901–2910.
66. Patrick S.M., Turchi J.J. // J. Biol. Chem. 2002. V. 277. № 18. P. 16096–17101.

67. Ikegami T., Kuraoka I., Saijo M., Kodo N., Kyogoku Y., Morikawa K., Tanaka K., Shirakawa M. // Nat. Struct. Biol. 1998. V. 5. № 8. P. 701–706.
68. Buchko G.W., Ni S., Thrall B.D., Kennedy M.A. // Nucl. Acids Res. 1998. V. 26. № 11. P. 2779–2788.
69. Krasikova Y.S., Rechkunova N.I., Maltseva E.A., Petruseva I.O., Lavrik O.I. // Nucl. Acids Res. 2010. V. 38. № 22. P. 8083–8094.
70. Camenisch U., Dip R., Vitanescu M., Naegeli H. // DNA Repair (Amst.). 2007. V. 6. № 12. P. 1819–1828.
71. Missura M., Buterin T., Hindges R., Hübscher U., Kaspárková J., Brabec V., Naegeli H. // EMBO J. 2001. V. 20. № 13. P. 3554–3564.
72. Thoma B.S., Vasquez K.M. // Mol. Carcinog. 2003. V. 38. № 1. P. 1–13.
73. Iakoucheva L.M., Walker R.K., van Houten B., Ackerman E.J. // Biochemistry. 2002. V. 41. № 2. P. 131–143.
74. Park C.H., Sancar A. // Proc. Natl. Acad. Sci. USA. 1994. V. 91. № 11. P. 5017–5021.
75. Riedl T., Hanaoka F., Egly J.M. // EMBO J. 2003. V. 22. № 19. P. 5293–5303.
76. Zotter A., Luijsterburg M.S., Warmerdam D.O., Ibrahim S., Nigg A., van Cappellen W.A., Hoeijmakers J.H., van Driel R., Vermeulen W., Houtsmuller A.B. // Mol. Cell Biol. 2006. V. 23. № 23. P. 8868–8879.
77. Hohl M., Thorel F., Clarkson S.G., Schärer O.D. // J. Biol. Chem. 2003. V. 278. P. 19500–19508.
78. Hohl M., Dunand-Sauthier I., Staresincic L., Jaquier-Gubler P., Thorel F., Modesti M., Clarkson S.G., Schärer O.D. // Nucl. Acids Res. 2007. V. 35. № 9. P. 3053–3063.
79. Enzlin J.H., Schärer O.D. // EMBO J. 2002. V. 21. P. 2045–2053.
80. Tsodikov O.V., Enzlin J.H., Schärer O.D., Ellenberger T. // Proc. Natl. Acad. Sci. USA. 2005. V. 102. № 32. P. 11236–11241.
81. Tsodikov O.V., Ivanov D., Orelli B., Staresincic L., Shoshani I., Oberman R., Schärer O.D., Wagner G., Ellenberger T. // EMBO J. 2007. V. 26. № 22. P. 4768–4776.
82. Tripsianes K., Folkers G., Ab E., Das D., Odijk H., Jaspers N.G., Hoeijmakers J.H., Kaptein R., Boelens R. // Structure. 2005. V. 13. № 12. P. 1849–1858.
83. Tripsianes K., Folkers G.E., Zheng C., Das D., Grinstead J.S., Kaptein R., Boelens R. // Nucl. Acids Res. 2007. V. 35. № 17. P. 5789–5798.
84. Das D., Folkers G.E., van Dijk M., Jaspers N.G.J., Hoeijmakers J.H.J., Kaptein R., Boelens R. // Structure. 2012. V. 20. № 4. P. 667–675.
85. Su Y., Orelli B., Madireddy A., Niedernhofer L.J., Schärer O.D. // J. Biol. Chem. 2012. V. 287. № 26. P. 21846–21855.

# "Green" Nanotechnologies: Synthesis of Metal Nanoparticles Using Plants

V. V. Makarov[1,2], A. J. Love[3], O. V. Sinitsyna[2,6], S. S. Makarova[2,5], I. V. Yaminsky[2,4], M. E. Taliansky[2,3], N. O. Kalinina[1,2*]

[1]Belozersky Institute of Physico-Chemical Biology, Lomonosov Moscow State University, Leninskie Gory 1, Bldg. 40, 119991, Moscow, Russia

[2]Advanced Technologies Center, 4-5-47 Stroiteley Str., 119311, Moscow, Russia

[3]The James Hutton Institute, Invergowrie, Dundee, DD2 5DA, Scotland, UK

[4]Department of Physics, Lomonosov Moscow State University, Leninskie Gory 1, Bldg. 2, 119991, Moscow, Russia

[5] Department of Biology, Lomonosov Moscow State University, Leninskie Gory 1, Bldg. 12, 119991, Moscow, Russia

[6]Nesmeyanov Institute of Organoelement Compounds, Russian Academy of Sciences, Vavilova Str. 28, 119991, Moscow, Russia

*E-mail: kalinina@genebee.msu.ru

Received 03.09.2013



**ABSTRACT** **While metal nanoparticles are being increasingly used in many sectors of the economy, there is growing interest in the biological and environmental safety of their production. The main methods for nanoparticle production are chemical and physical approaches that are often costly and potentially harmful to the environment. The present review is devoted to the possibility of metal nanoparticle synthesis using plant extracts. This approach has been actively pursued in recent years as an alternative, efficient, inexpensive, and environmentally safe method for producing nanoparticles with specified properties. This review provides a detailed analysis of the various factors affecting the morphology, size, and yield of metal nanoparticles. The main focus is on the role of the natural plant biomolecules involved in the bioreduction of metal salts during the nanoparticle synthesis. Examples of effective use of exogenous biomatrices (peptides, proteins, and viral particles) to obtain nanoparticles in plant extracts are discussed.**

**KEYWORDS** **biomatrices; bioreduction; metal nanoparticles; plant metabolites; plant extracts.**

## INTRODUCTION

The widespread practical application of metal nanoparticles (particles less than 100 nm) is attributable to a number of their unique properties [1–4]. Different physical and chemical processes are currently widely used to synthesize metal nanoparticles, which allow one to obtain particles with the desired characteristics [5–8]. However, these production methods are usually expensive, labor-intensive, and are potentially hazardous to the environment and living organisms [9, 10]. Thus, there is an obvious need for an alternative, cost-effective and at the same time safe and environmentally sound method of nanoparticle production [11–13]. During the past decade, it has been demonstrated that many biological systems, including plants and algae [14], diatoms [15, 16], bacteria [17], yeast [18], fungi [19], and human cells [20] can transform inorganic metal ions into metal nanoparticles via the reductive capacities of the proteins and metabolites present in these organisms. It is significant that the nanoparticle production using plants described in the present review displays important advantages over other biological systems. The low cost of cultivation, short production time, safety, and the ability to up production volumes make plants an attractive platform for nanoparticle synthesis [21].

## PLANTS AS BIOREACTORS FOR THE SYNTHESIS OF METAL NANOPARTICLES

It has long been known that plants are able to reduce metal ions both on their surface and in various organs and tissues remote from the ion penetration site. In this regard, plants (especially those which have very strong metal ion hyperaccumulating and reductive capacity) have been used for extracting precious metals from land which would be economically unjustifiable to mine; an approach known as phytomining. The metals accumulated by the plants can be recovered after harvesting via sintering and smelting methods. Inter-

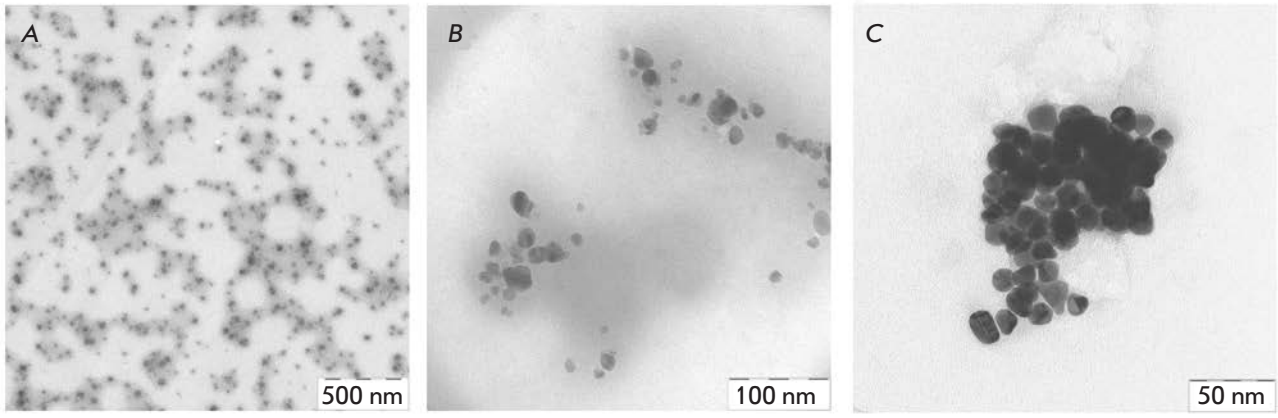


Fig. 1. Electron micrographs of the iron (A), silver (B), and gold (C) nanoparticles synthesized in extracts of *N. benthamiana* at room temperature

estingly, study of the metal bioaccumulation process in plants has revealed that metals are usually deposited in the form of nanoparticles. For example, *Brassica juncea* (mustard greens) and *Medicago sativa* (alfalfa) accumulate 50 nm silver nanoparticles to a high level (13.6% of their own weight) when grown on silver nitrate as a substrate [22]. In addition, gold icosahedra of 4 nm in size were detected in *M. sativa* [23], and semi-spherical copper particles with a size of 2 nm were observed in *Iris pseudacorus* (yellow iris) [24] grown on substrates containing salts of the respective metals. Whole plants can obviously be used to produce metal nanoparticles. However, there exists certain limitations that should be taken into account upon industrial application of this technology. Firstly, the size and shape of nanoparticles vary depending on their localization in the plant, which may depend on differences in the content of metal ions in various tissues and the subsequent possibility of nanoparticle movement and penetration. These factors could influence the level of metal deposition around already existing nanoparticles, and also the prospect of new nucleation events (initiation of nanoparticle formation) [23]. The heterogeneity of the size and morphology of nanoparticles produced in whole plants may hinder their use in applications where specific, finely tuned sizes and shapes are required; thus illustrating the inability to tailor the whole plant synthesized nanoparticles to market requirements. Moreover, efficient extraction, isolation and purification of nanoparticles from plant material is a difficult and problematic procedure, with a low recovery.

In this regard, *in vitro* approaches have actively been developed in recent years, in which plant extracts are used for the bioreduction of metal ions to form nanoparticles. These approaches provide a more flexible control over the size and shape of the nanoparticles (for example, by changing the medium pH and reaction temperature), as well as facilitating easy purification. Significantly, this process occurs much faster than the synthesis of nanoparticles in whole plants, because the reaction proceeds almost instantaneously, without the delay required for the uptake and diffusion of metal ions throughout the plant. This *in vitro* approach has been demonstrated using extracts from a variety of different plant species in combination with a variety of acids and salts of metals, such as copper, gold, silver, platinum, iron, and many others [22, 25–27].

For example, extracts of *Pelargonium graveolens* (rose geranium) have been used to reduce gold ions into 20–40 nm decahedral icosahedral shaped nanoparticles and stabilize them [28], whereas gold nanospheres and nanotriangles 0.05–18 μm in size have been synthesized in extracts from *Cymbopogon flexuosus* (lemon grass) [29]. The *Azadirachta indica* (neem, Indian lilac) extract was used to reduce tetrachloroauric acid ($HAuCl_4$) to flat gold triangles and hexagons with a size of 50–100 nm [30]. In that study, it was also demonstrated that the *A. indica* juice can reduce silver nitrate to polydispersed spherical nanoparticles with a size of 5–25 nm [30]. The leaf extract of *Aloe barbadensis* (aloe vera) was used to produce cubic $In_2O_3$ particles 5–50 nm in size [31]. It has been demonstrated using FTIR spectroscopy that plant metabolites such as sugars, terpenoids, polyphenols, alkaloids, phenolic acids, and proteins play an important role in the reduction of metal ions into nanoparticles and in supporting their subsequent stability [29, 30, 32–34]. It has been suggested that control over the size and

morphology of nanostructures may be connected to the interaction of these biomolecules with metal ions [30]. Various plants differ in the concentration and composition of these biologically active components. This may partly explain the morphological diversity of the described nanoparticles: triangles, hexagons, pentagons, cubes, spheres, ellipsoids, nanowires, and nanorods. The diversity in the morphology and size of nanoparticles synthesized from a variety of metal ions in extracts of various plants has been described in detail in the reviews [11, 35]. As an example, *Fig. 1* shows images of the iron, silver and gold nanoparticles produced in *Nicotiana benthamiana* extracts.

## THE ROLE OF PLANT METABOLITES IN THE BINDING AND REDUCTION OF METAL IONS

As mentioned above, various plant metabolites, including terpenoids, polyphenols, sugars, alkaloids, phenolic acids, and proteins, play an important role in the bioreduction of metal ions, yielding nanoparticles. Examples of the main types of compounds capable of reducing metal ions are shown in *Fig. 2*.

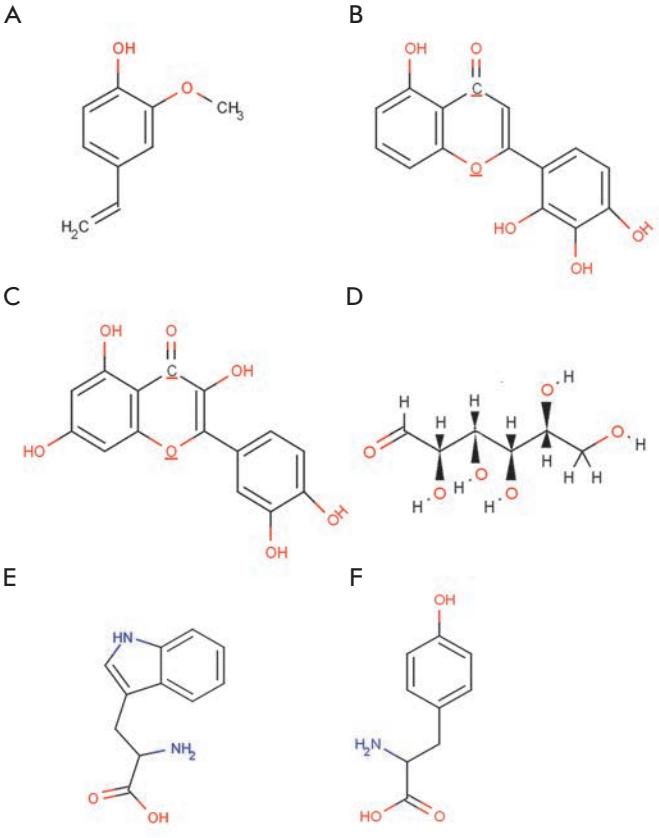


Fig. 2. The main types of plant metabolites involved in the synthesis of metal nanoparticles: A – terpenoids (eugenol); B,C – flavonoids (luteolin, quertcetin); D – a reducing hexose with the open chain form; E,F – amino acids (tryptophan (E) and tyrosine (F))

Using FTIR spectroscopy of nanoparticles synthesized in plants/plant extracts, it has been demonstrated that terpenoids are often associated with nanoparticles. Terpenoids are a class of diverse organic polymers synthesized in plants from five-carbon isoprene units, which display strong antioxidant activity. Shankar *et al.* [29] initially suggested that terpenoids play a key role in the transformation of silver ions into nanoparticles in reactions using extracts from geranium leaves. Eugenol, the main terpenoid of *Cinnamomum zeylanisum* (cinnamon) extracts, was found to play the principal role in the bioreduction of $HAuCl_4$ and $AgNO_3$ to nanoparticles [36]. Based on the FTIR spectroscopy data, it was suggested [36] that dissociation of a proton of the eugenol OH-group results in the formation of resonance structures capable of further oxidation. This process is accompanied by the active reduction of metal ions, followed by nanoparticle formation.

Flavonoids are a large group of polyphenolic compounds that comprise several classes: anthocyanins, isoflavonoids, flavonols, chalcones, flavones, and flavanones, which can actively chelate and reduce metal ions into nanoparticles. Flavonoids contain various functional groups capable of nanoparticle formation. It has been postulated that the tautomeric transformations of flavonoids from the enol-form to the keto-form may release a reactive hydrogen atom that can reduce metal ions to form nanoparticles. For example, it is believed that in the case of *Ocimum basilicum* (sweet basil) extracts it is the transformation of flavonoids luteolin and rosmarinic acid from the enol- to the keto-form that plays a key role in the formation of silver nanoparticles from Ag ions [37]. Moreover, the internal mechanism of the conversion of ketones to carboxylic acids in flavonoids is likely to be involved in $Au_3^+$ ion reduction. Interestingly, some flavonoids are able to chelate metal ions with their carbonyl groups or π-electrons. For example, quercetin is a flavonoid with very strong chelating activity, because it can chelate at three positions involving the carbonyl and hydroxyls at the C3 and C5 positions and the catechol group at the C3' and C4' site. These groups chelate various metal ions such as $Fe^{2+}$, $Fe^{3+}$, $Cu^{2+}$, $Zn^{2+}$, $Al^{3+}$, $Cr^{3+}$, $Pb^{2+}$, and $Co^{2+}$. The presence of such mechanisms may indeed explain the ability of flavonoids to be adsorbed onto the surface of a nascent nanoparticle. This probably means that they are involved in the stages of initiation of nanoparticle formation (nucleation) and further aggregation, in addition to the bioreduction stage. Moreover, isolated flavonoids and flavonoid glycosides have the ability to induce the formation of metal nanoparticles. For exam-

ple, apiin (apigenin glycoside) was extracted from *Lawsonia inermis* (lawsonite thornless, henna) and used for the synthesis of anisotropic gold and quasi-spherical silver nanoparticles with an average size of 21–30 nm [38]. A FTIR analysis revealed that apiin was attached to the nanoparticles through a carbonyl group.

There are data according to which the sugars present in plant extracts can also induce the formation of metal nanoparticles. It is known that monosaccharides such as glucose (linear and containing an aldehyde group) can act as reducing agents. Monosaccharides containing a keto-group, e.g. fructose, can act as antioxidants only when they have undergone a series of tautomeric transformations from a ketone to an aldehyde. Moreover, the reducing ability of disaccharides and polysaccharides depends on the ability of any of their individual monosaccharide components to adopt an open chain form within an oligomer and, hence, to provide access (of a metal ion) to an aldehyde group. For example, the disaccharides maltose and lactose have reducing ability, since at least one of their monomers can assume an open chain form. Sucrose, in contrast, has no ability to reduce metal ions, because glucose and fructose monomers are linked in such a way that the open chain form is not available. It was found [39] that glucose is capable of participating in the synthesis of metal nanoparticles of various morphologies, whereas fructose mediates the synthesis of monodispersed nanoparticles of gold and silver. Glucose was also noted [39] to be a stronger reducing agent than fructose, because the antioxidant potential of fructose is limited by the kinetics of tautomeric shifts (as discussed above). It was shown [39] that sucrose is unable to reduce silver nitrate or palladium chloride into nanoparticles. However, when these metal salts were replaced by tetrachloroauric and tetrachloroplatinic acids, nanoparticles were formed in the presence of sucrose, which is likely due to the acidic hydrolysis of sucrose into free glucose and fructose, which have an open chain-form structure. It is currently believed that the sugar aldehyde group is oxidized into a carboxyl group via the nucleophilic addition of OH-, which in turn leads to the reduction of metal ions and to the synthesis of nanoparticles. A similar mechanism was proposed for the bioreduction of gold ions using the magnolia vine extract [29].

FTIR analysis of nanoparticles synthesized in plants or plant extracts revealed that nascent nanoparticles are very frequently found in association with proteins [40]. Amino acids were found to differ in their ability to bind metal ions and to reduce them. For example, as Gruen observed [41], amino acids such as lysine, cysteine, arginine, and methionine are capable of binding silver ions. Other studies have shown that aspartate can reduce tetrachloroauric acid to form nanoparticles, although valine and lysine do not possess this ability [42]. Tan *et al.* [43] recently analyzed all of the 20 natural α-amino acids to determine their potential for reduction or binding of metal ions. They established that tryptophan is the strongest reducing agent for Au ions, whereas histidine is one of the strongest binding agents for Au ions. Amino acids can bind to metal ions through the amino and carbonyl groups of the main chain or through side chains, such as the carboxyl groups of aspartic and glutamic acid or a nitrogen atom of the imidazole ring of histidine. Other side chains binding metal ions include the thiol (cysteine), thioether (methionine), hydroxyl (serine, threonine, and tyrosine), and carbonyl groups (asparagine and glutamine) [44]. A study of the ability to reduce metal ions indicated that the hydroxyl groups of tyrosine and carbonyl groups of glutamine and asparagine are involved in the reduction process of Ag ions. Side thiol groups (e.g. of cysteine) and amino groups are also responsible for the reduction of metal ions.

After amino acids are linked to the peptide chain, their individual ability to bind and reduce metal ions may change. For example, the formation of the peptide backbone changes the functionality of the R-carbon of carboxylic acids and amines of some amino acid residues since they move to a form inaccessible for interaction with metal ions. However, free side chains of amino acids can still participate in the binding and reduction of metal ions. The suitability of side chains for this interaction may change depending on the amino acid sequence, which could affect the accessibility of individual groups. The work by Tan *et al.* [43] explained in detail how the amino acid sequence may affect the protein's ability to chelate and/or reduce metal ions. It was found that synthesized peptides, composed of amino acids capable of effective binding of metal ions, and of amino acids possessing high reducing activity, had lower reduction parameters than expected. It was suggested that the strong sequestration of metal ions to the peptide was inhibitory to their subsequent reduction by reducing amino acids. It was also found that peptides containing amino acids that weakly bind metal ions such as leucine, phenylalanine, and proline were ineffective in reducing tetrachloroauric acid anions, probably because of their inability to retain metal ions close to the reduction sites. It was assumed [44] that protein molecules facilitating the formation of nanoparticles from metal ions display high reducing activity and high potential for attracting metal ions to the regions of a molecule that are responsible for reduction, but that their chelating activity is not excessive. The paper also demonstrated that the amino acid sequence of a protein can greatly affect the size, morphology, and amount of nascent nanoparticles. For example, a synthetic peptide

GASLWWSEKL rapidly reduces metal ions to form a large amount of small nanoparticles less than 10 nm in size, whereas replacement of N-and C-terminal amino acid residues in a peptide (SEKLWWGASL) leads to a slower reduction reaction that results in the formation of larger nanospheres and nanotriangles about 40 nm in size. These data indicate that the peptides and proteins present in plant extracts probably play a very important role in determining the shape of nanoparticles and affect the overall yield of nanoparticles.

On the whole, the mechanism of metal nanoparticle synthesis in plants and plant extracts includes three main phases: 1) the activation phase during which the reduction of metal ions and nucleation of the reduced metal atoms occur; 2) the growth phase during which the small adjacent nanoparticles spontaneously coalesce into particles of a larger size (direct formation of nanoparticles by means of heterogeneous nucleation and growth, and further metal ion reduction; a process referred to as Ostwald ripening), which is accompanied by an increase in the thermodynamic stability of nanoparticles; and 3) the process termination phase determining the final shape of the nanoparticles [44, 45]. The process of nanoparticle formation is shown schematically in *Fig. 3*. As the duration of the growth phase increases, nanoparticles aggregate to form nanotubes, nanoprisms, nanohexahedrons, and a variety of other irregularly shaped nanoparticles, as well [44, 46]. In the termination phase, nanoparticles acquire the most energetically favorable conformation, with this process being strongly influenced by the ability of a plant extract to stabilize metal nanoparticles. For example, nanotriangles have a very high surface energy, which makes them less stable, and if the stability of nanoparticles is not supported in given extracts, then the nanotriangles will acquire a more stable morphology, such as a truncated triangle, in order to minimize the Gibbs free energy.

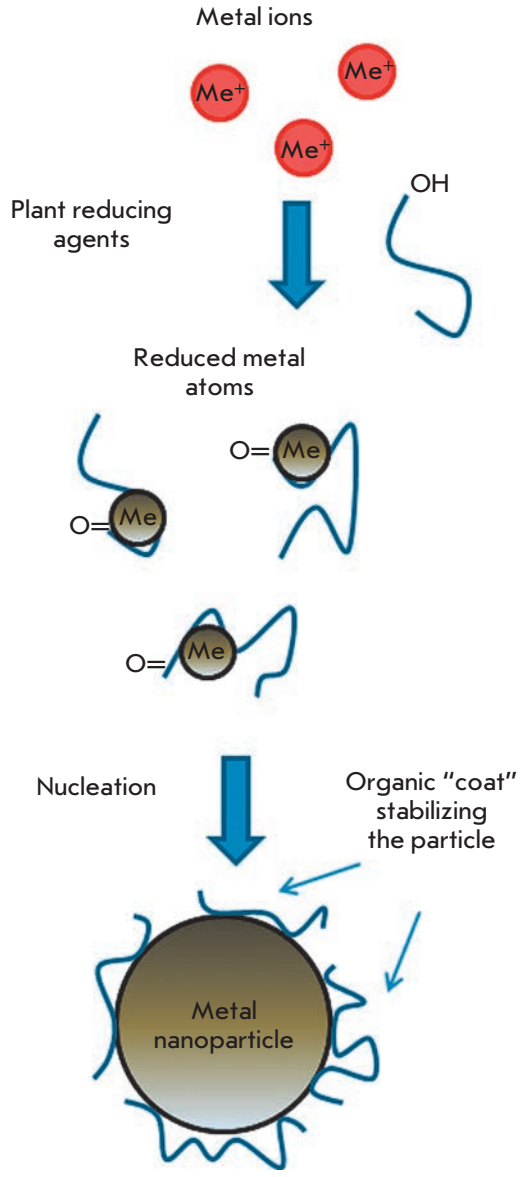


Fig. 3. A schematic representation of metal nanoparticle synthesis in a plant extract. The metal ions bind to the reducing metabolites and stabilizing agents and are reduced to metal atoms. The resulting complex of the metal ion and metabolite interacts with similar complexes forming a small metal nanoparticle. Next, growth and coalescence of separate small particles into larger ones occur through the coarsening process. This process continues until the particles assume a stable shape and size

## OTHER FACTORS AFFECTING THE FORMATION OF METAL NANOPARTICLES IN PLANTS

Therefore, the reduction process of metal ions with the formation of nanoparticles is affected by a large number of factors; besides the nature of a plant extract containing active biomolecules in different combinations and concentrations (the effects of which are described above), these include the reaction mixture pH, incubation temperature, reaction time, concentration, and electrochemical potential of a metal ion [11, 35, 47, 48].

The pH value of a plant extract exerts great influence on the formation of nanoparticles [49–52]. A change in pH results in a charge change in the natural phytochemicals contained in an extract, which affects their ability to bind and reduce metal cations and anions in the course of nanoparticle synthesis, and this in turn may affect the shape, size, and yield of nanoparticles. For example, in the *Avena sativa* (common oat) extract more numerous small-sized gold nanoparticles were formed at pH 3.0 and 4.0, whereas more aggre-

gated particles were observed at pH 2.0. Therefore, it has been suggested that nanoparticle aggregation is dominant over the process of reduction and primary nucleation of reduced atoms at very acidic pH values. This may perhaps be related to the fact that a larger number of functional groups that bind and nucleate tetrachloroauric acid ions become accessible at pH 3.0 and 4.0 than at pH 2.0. At pH 2.0 the most accessible metal ions are apparently involved in a smaller number of nucleation events, which leads to agglomeration of the metal [52]. In contrast, it was demonstrated using extracts from pears that hexagonal and triangular gold nanoplates are formed at alkaline pH values, whereas nanoparticles do not form at acidic pHs [50]. In the case of silver ions (1+) and the tuber powder of *Curcuma longa* (turmeric), a substantially larger number of silver nanoparticles are synthesized at alkaline pHs, at which extracts may contain more negatively charged functional groups capable of efficient binding and reduction of silver ions [52].

Temperature is another important factor affecting the formation of nanoparticles in plant extracts [53–57]. In general, temperature elevation increases the reaction rate and efficiency of nanoparticle synthesis. It was found that in alfalfa plants (*M. sativa*) triangular silver nanoparticles formed only at temperatures above 30 °C [54]. Furthermore, experiments on the synthesis of silver nanoparticles in lemon verbena extracts (*Aloysia citrodora*) demonstrated that increasing the reaction temperature is accompanied by an increase in the efficiency of the silver ion reduction [56]. Moreover, crystal particles are formed much more frequently at high temperatures than at room temperature. It is assumed that elevating the temperature increases the nucleation rate. In experiments with *Cassia fistula* (golden shower tree) extracts, it was found that temperature may also affect the structural form of the synthesized nanoparticles; silver nanoribbons are mainly formed at room temperature, whereas spherical nanoparticles predominate at temperatures above 60 °C [55]. In this case it is believed that higher temperatures alter the interaction of phytochemicals with the nanoparticle surface, thereby inhibiting incorporation of adjacent nanoparticles into the structure of nanoribbons. Furthermore, in some situations higher temperatures may facilitate the nucleation process to the detriment of the secondary reduction process and further condensation of a metal on the surface of nascent nanoparticles. This phenomenon is believed to explain the formation of the spherical gold nanoparticles in *Nyctanthes arbortristis* (jasmine night) alcoholic extracts at 80 °C in contrast to the nanoparticles of different morphology and "nanocolors" formed at room temperature [57].

Due to the limited ability of plants to reduce metal ions, the efficiency of metal nanoparticle synthesis also depends on the electrochemical potential of an ion [35]. Thus, the ability of a plant extract to effectively reduce metal ions may be significantly higher in the case of ions having a large positive electrochemical potential (for example, $Ag^+$) than in the case of ions with a low electrochemical potential such as ($[Ag(S_2O_3)_2]^{3-}$) [35].

As discussed above, the proteins that are present in a plant extract may significantly affect the formation of nanoparticles. The approaches that have recently been used for the "green" synthesis of metal nanoparticles combine the use of plant extracts with the exogenous supplementation of the *in vitro* reactions with biomatrices: peptides, and proteins, whose amino acid sequence and structure are optimized for the efficient production of nanoparticles. The phage display method is used for the search for peptides with the appropriate characteristics. Tryptophan and amino acids such as tyrosine, arginine, and lysine possess superior ability to reduce metal ions. However, a polypeptide composed only of tryptophan residues is much less effective than a mixture of tryptophan molecules interspersed with other amino acids at forming nanoparticles, likely due to strong binding of the reduced ion, which in turn is inhibitory to further reduction. In turn, peptides that consist of different amino acids (for example, RWRWRWRWR) capable of strongly binding metal ions are also poorly suited as a biomatrix for the synthesis of nanoparticles due to entropic effects. Peptides comprising amino acids that weakly bind tetrachloroauric acid ions, such as glutamic or aspartic acids, are also inefficient in the synthesis of nanoparticles because of rapid dissociation of the peptide - metal ion complex. Therefore, the most suitable peptides for the formation of metal nanoparticles are those in which reducing and strongly binding amino acid residues (e.g., tryptophan) alternate with weakly binding amino acids that act as an up-regulator. The next important stage in the formation of metal nanoparticles is the agglomeration of reduced metal atoms to nanoparticles. This process depends on many factors and determines a number of the properties of a nascent nanoparticle such as its size or shape. At the beginning of the process, small particles of the reduced metal are formed on the surface of a peptide biomatrix that are further redistributed into larger nanoparticles during Ostwald ripening (coarsening). It has been shown that the faster and more efficient nanoparticle formation is, the more isotropic and smaller nanoparticles are produced, since the coarsening effectiveness is time-dependent. For example, it was possible to vary the shape and size of produced nanoparticles by altering the amino acid sequence and thus the reaction kinetics of nanoparticle formation.

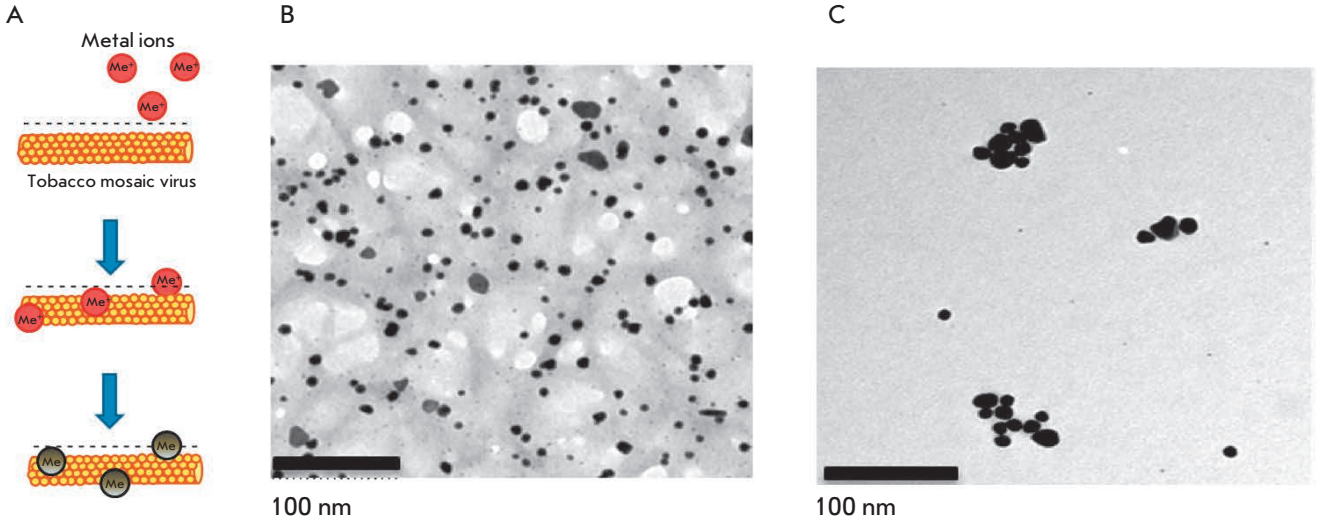


Fig. 4. Formation of nanoparticles in plant extracts using biomatrices. A — A scheme of nanoparticle formation in the presence of the tobacco mosaic virus (TMV) as a biomatrix. Metal ions interacting with negatively charged groups on the TMV surface are reduced upon addition of a plant extract. The regular positioning of TMV active groups significantly increases the number of effective events of initiation, which increases the output of metal nanoparticles 3–5-fold. B,C – electron micrographs of gold nanoparticles produced in *N. benthamiana* extracts in the presence (B) and in the absence (C) of TMV particles

The identified patterns also hold for macromolecular biomatrices, such as viruses and virus-like particles. In one of the first studies carried out using this approach, a plant RNA virus with helical symmetry (tobacco mosaic virus (TMV) with a length of 300 nm and a width of 18 nm) or icosahedral particles of the non-infectious bovine papilloma virus (particles with a diameter of 55 nm obtained by self-assembly of the viral envelope protein expressed in plants) were added to silver or gold salts before adding *N. benthamiana* or barley extracts [58,59]. In the presence of virus/virus-like particles at low concentrations, a decrease in the size of nanoparticles and a 4- to 5-fold increase in their number was observed compared to samples containing no virus (*Fig. 4B,C*) [58,59]. Interestingly, the amount of formed nanoparticles was significantly less at a high TMV concentration, but viral particles were metallized (*Fig. 5*). Amino acid side chains capable of chelating and reducing metal ions are exposed on the inner and outer surfaces of the TMV and on the outer surface of bovine papilloma virus particles. For example, carboxyl and hydroxyl groups are accessible on the TMV outer surface as part of the exposed peptide segments of the surface loop and C-terminal region, while amino acid amino groups are accessible in the TMV inner channel [60]. Carbonyl, hydroxyl, and carboxyl groups are accessible on the surface of bovine papilloma virus particles [58]. Another important factor allowing viruses

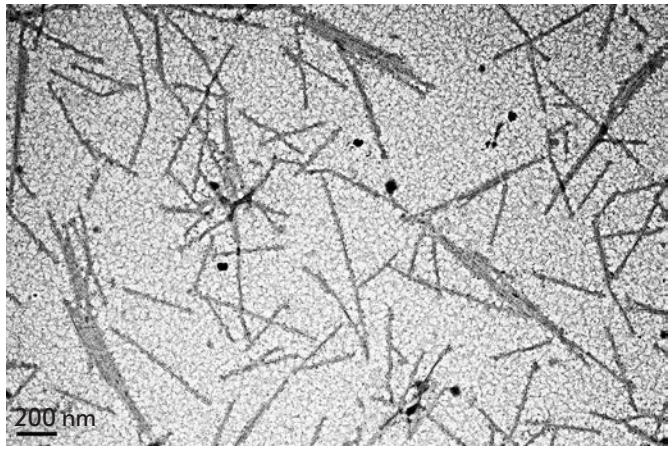


Fig. 5. Micrograph of the metallized tobacco mosaic virus obtained by transmission electron microscopy

and virus-like particles to be considered as effective biomatrices for nanoparticle synthesis is the mutual spatial orientation of active peptide groups due to the structural regularity of these biomatrices. This can lead to significant acceleration of the synthesis reaction and, consequently, to an increasing yield of nanoparticles. The surface of a viral particle consists of dense arrays of appropriately packed capsid proteins (a single TMV particle consists of 2,130 molecules of the capsid pro-

tein and a bovine papilloma virus particle consists of 360 molecules of the capsid protein) that form a highly reactive quasiregular surface capable of interacting with metal ions. At low virus concentrations in a reaction mixture, metal ions are believed to react with amino acid residues in the molecules of the viral capsid protein that initiates the nucleation process. Preformed nucleation centers undergo a significantly more rapid reduction upon addition of a plant extract. The presence of a virus in a reaction mixture probably inhibits aggregation by increasing the number of nucleation sites, which reduces the accumulation of metal ions around a smaller number of points. At increased virus concentrations, the elevated number and concentration of clustered active amino acid residues in a small space enhances the binding and reduction of metal ions in the vicinity of the virus surface; effectively decreasing the development of free nucleation centers and inhibition of metal nanoparticle formation outside viral clusters ("free" nanoparticles). Subsequent addition of plant extracts quickly reduces metal ions chelated by viral particles, which leads to metallization of viral particles (e.g., to the formation of nanowires in the case of TMV) but decreased rate of formation of "free" nanoparticles.

## PROSPECTIVE APPLICATION OF NANOPARTICLES SYNTHESIZED IN PLANTS

The diversity of plant extracts and types of metal salts, the ability to alter the composition of a reaction mixture and reaction conditions through changes in the temperature, pH, and inclusion of additives of biological origin (biomatrices), allow one to produce nanoparticles of various metals with a defined size and shape. Despite the fact that "green" synthesis of nanoparticles using plant material is of considerable interest, it is worth studying the equivalence of these nanoparticles with nanoparticles produced through physical and chemical methods, especially with regard to their potential applications and production scalability. For example, it is well-known that traditional physicochemically synthesized metal nanoparticles have been used in cancer therapy, the targeted delivery of drugs, molecular imaging, wastewater treatment, catalysis, biosensor development, fuel elements, coatings, cosmetics and as antiseptics. Nanoparticles produced in plants/plant extracts have been tested so far only in a small number of practical applications. For example, silver nanoparticles produced using the *Tridax procumbens* (tridax daisy) extract display, similar to their equivalents obtained using chemical or physical methods, strong antimicrobial activity against *Escherichia coli*, *Shigella dysenteriae*, and *Vibrio cholera* [61]. Silver nanoparticles obtained using *Pinus thunbergii* (Japanese black pine) cone extracts exhibit antibacterial activity against various Gram-positive and Gram-negative agricultural pathogens, such as *Pseudomonas syringae*, *Xanthomonas oryzae*, *Burkholderia glumae*, and *Bacillus thuringiensis* [62]. Silver nanoparticles synthesized in plants display significant cytotoxic activity against various tumor cell lines. Silver nanoparticles synthesized in *Iresine herbstii* (Herbst's bloodleaf) were found to inhibit the survival and growth of HeLa cell lines, and silver nanoparticles produced using *Euphorbia nivulia* (leafy milk hedge) latex extracts are toxic to the A549 cell line of human lung cancer [63]. Silver nanoparticles synthesized in *Nerium oleander* (oleander) display strong larvicidal activity against larvae of the malaria vector *Anopheles stephensi* [64].

In perspective, functionalization of these particles with antibodies or peptides is intended for targeted action in certain tissues of the body in order to achieve greater efficiency and reduce side effects. *Cyamopsis tetragonoloba* (cluster bean) extracts were used recently to produce composite silver nanoparticles that can act as a biosensor to determine ammonia, with possible applications in agriculture and biomedicine. Depending on the ammonia concentration, the distance between the nanoparticles inside the nanocomposite changes, which affects its optical properties [65]. Platinum nanoparticles obtained using *Ocimum sanctum* (Holy basil) extracts were shown to possess a catalytic activity and may be used in the production of hydrogen fuel elements [66]. Catalytic activity is also ascribed to gold nanoparticles obtained in *Sesbania drummondii* (rattlebush) that may participate in the reduction of aromatic nitro compounds; for example, convert highly toxic 4-nitrophenol to 2-amino-phenol, which suggests their possible involvement in waste decontamination.

These examples are not an exhaustive list of all the data on the application of "green" nanoparticles: however, they provide strong evidence of a possible practical application of nanoparticles synthesized using plants/plant extracts. The main question that needs to be answered is whether the biological and physicochemical characteristics of nanoparticles of plant "origin" differ from the characteristics of their existing prototypes and to what extent these differences affect efficiency in nanoparticle application for specific practical problems. It is significant to note that nanoparticles synthesized in plant extracts already have a functionalized surface that can contain (depending on reaction conditions) the organic ligands, proteins, polysaccharides, and polyatomic alcohols that are absent in nanoparticles synthesized using physical and chemical methods. The presence of these biological components promotes, as is known, an increase in the stability of the particles and may also facilitate, if necessary, the

subsequent attachment of functional molecules, such as antibodies or DNA, to nanoparticles [67].

## CONCLUSIONS

Obviously, the synthesis of metal nanoparticles in plant extracts (plant biomasses), despite obvious limitations, has a significant potential and a number of substantial advantages relative to traditional methods of nanoparticle synthesis. However, to compete cost-effectively with nanoparticles obtained through physical and chemical methods, it is necessary to scale these methods of nanoparticle production using plant material and to develop schemes for keeping expenses in check during their synthesis. Continuous methods for the synthesis of nanoparticles have so far been used only in small-scale production. When using chemical synthesis, the prime cost of nanoparticles is mainly determined by the cost of the metal salts and reducing agents. In the case of "green" synthesis, the bulk of the costs will be determined only by the cost of the metal salts, because plant wastes from the food industry can serve as reducing agents. Moreover, it is possible to envision companies involved in the food industry and interested in the recycling of waste to partially pay for nanoparticle production. This fact further emphasizes the environmental advantages of "green" synthesis over traditional methods of nanoparticle production. ●

*This work was supported by the Ministry of Education and Science of the Russian Federation, the Federal Target-Oriented Program "Scientific and Scientific-pedagogical Personnel of Innovative Russia", the event 1.5, Agreement № 14.U02.21.1235. A.J.L. and M.T. were supported by funding from Scottish Government Rural and Environmental Science and Analytical Services Division and the work of V.V.M was funded by the Grant of the President of the Russian Federation for supporting of young scientists MK-2072.2014.4*

REFERENCES:

1. Roco M.C. // Curr. Opin. Biotechnol. 2003. V. 14. P. 337–346.
2. Zhang L., Gu F.X., Chan J.M., Wang A.Z., Langer R.S., Farokhzad O.C. // Clin. Pharmacol. Ther. 2008. V. 83. P. 761–780.
3. Daniel M.C., Astruc D. // Chem. Rev. 2004. V. 104. P. 293–346.
4. Wong T.S., Schwaneberg U. // Curr. Opin. Biotechnol. 2003. V. 14. P. 590–596.
5. Eds., Fendler J.H. Nanoparticles and nanostructured films: Preparation, characterization and applications. John Wiley & Son. 1998. 463 p.
6. Tsuji M., Hashimoto M., Nishizawa Y., Tsuji T. // Chem. Lett. 2003. V. 32. P. 1114–1115.
7. Kundu S., Maheshwari V., Saraf R. // Nanotechnology. 2008. V. 19. № 6. 065604.
8. Okitsu K., Mizukoshi Y., Yamamoto T.A., Maeda Y., Nagata Y. // Lett. Materials. 2007. V. 61. P. 3429–3431.
9. Narayanan K.B., Sakthivel N. // Adv. Colloid. Interface. Sci. 2010. V. 22. № 156. P. 1–13.
10. Gan P.P., Ng S.H., Huang Y., Li S.F. // Bioresour. Technol. 2012. V. 113 P. 132–135.
11. Raveendran P., Fu J., Wallen S.L. // Am. Chem. Soc. 2003. V. 125. № 46. P. 13940–13941.
12. Sharma H.S., Ali S.F., Hussain S.M., Schlager J.J., Sharma A. // J. Nanosci. Nanotechnol. 2009. V. 9. № 8. P. 5055–5072.
13. Narayanan S., Sathy B.N., Mony U., Koyakutty M., Nair S.V., Menon D. // ACS. Appl. Mater. Interfaces. 2012. V.4. № 1. P. 251–260.
14. Govindaraju K., Khaleel Basha S., Ganesh Kumar V., Singaravelu G. // J. Materials Sci. 2008. V. 43. P. 5115–5122.
15. Scarano G., Morelli E. // Biometals. 2002. V. 15. № 2. P. 145–151.
16. Scarano G., Morelli E. // Plant Sc. 2003. V. 165. P. 803–810.
17. Lengke M.F., Fleet M.E., Southam G. // Langmuir. 2007. V. 23. № 5. P. 2694–2699.
18. Kowshik M., Deshmukh N., Vogel W., Urban J., Kulkarni S.K., Paknikar K.M. // Biotechnol. Bioeng. 2002. V. 78. № 5. P. 583–588.
19. Rautaray D., Ahmad A., Sastry M. // J. Am. Chem. Soc. 2003. V. 125. № 48. P. 14656–14657.
20.Anshup A., Venkataraman J.S., Subramaniam C., Kumar R.R., Priya S., Kumar T.R., Omkumar R.V., John A., Pradeep T. // Langmuir. 2005. V. 21. № 25. P. 11562–11567.
21. Njagi E.C., Huang H., Stafford L., Genuino H., Galindo H.M., Collins J.B., Hoag G.E., Suib S.L. // Langmuir. 2011. V. 27. № 1. P. 264–271.
22. Harris A.T., Bali R. // J. Nanoparticle Res. 2008. V. 10. P. 691–695.
23. Gardea-Torresdey J.L., Parsons J., Gomez E., Peralta-Videa J., Troiani H., Santiago P., Yacaman M. // Nano Lett. 2002. V. 2. P. 397–401.
24. Manceau A., Nagy K.L., Marcus M.A., Lanson M., Geoffroy N., Jacquet T., Kirpichtchikova T. // Environ. Sci. Technol. 2008. V. 42. № 5. P. 1766–1772.
25. Ghosh S., Patil S., Ahire M., Kitture R., Gurav D.D., Jabgunde A.M., Kale S., Pardesi K., Shinde V., Bellare J. // J. Nanobiotechnology. 2012. V. 10. P. 17.
26. Khan M., Adil S.F., Tahir M.N., Tremel W., Alkhathlan H.Z., Al-Warthan A., Siddiqui M.R. // Int. J. Nanomedicine. 2013. V. 8. P. 1507–1516.
27. Rai M., Yadav A. // IET Nanobiotechnol. 2013. V. 7. № 3. P. 117–124.
28. Shiv Shankar S., Ahmad A., Sastry M. // Biotechnol. Prog. 2003. V. 19. P. 1627–1631.
29. Shiv Shankar S., Ahmad A., Pasricha R., Sastry M. J. // Mater. Chem., 2003. V. 13. P. 1822–1846.
30. Shiv Shankar S., Rai A., Ahmad A., Sastry M. // J. Colloid. Interface. Sci. 2004. V. 275. P. 496–502.
31. Maensiri S., Laokul P., Klinkaewnarong J., Prokha S., Promark V., Seraphin S. // Optoelectronics and Advanced Materials. 2008. V. 2. P. 161–165.
32. Vilchis-Nestor A.R., Sánchez-Mendieta V., Camacho-López M.A., Gómez-Espinosa R.M., Arenas-Alatorre J.A. // Mater. Lett. 2008. V. 62. P. 3103–3105.
33. Song J.Y., Kwon E.Y., Kim B.S. // Bioprocess. Biosyst. Eng. 2010. V. 33. P. 159–164.

34. Song J.Y., Kim B.S. // Bioprocess. Biosyst. Eng. 2009. V. 32. № 1. P. 79–84.
35. Haverkamp R., Marshall A. // J. Nanoparticle. Res. 2009. V. 11. № 6. P. 1453–1464.
36. Singh A., Talat M., Singh D., Srivastava O.N. // J. Nanoparticle Res. 2010. V. 12. P. 1667–1675.
37. Ahmad N., Sharma S., Alam M.K., Singh V.N., Shamsi S.F., Mehta B.R., Fatma A. // Colloids Surf. B. Biointerfaces. 2010 V. 81. P. 81–86.
38. Kasthuri J., Veerapandian S., Rajendiran N. // Colloids Surf. B. Biointerfaces. 2009. V. 68. P. 55–60.
39. Panigrahi S., Kundu S., Ghosh S., Nath S., Pal T. // J. Nanoparticle Res. 2004. V. 6. № 4. P. 411–414.
40. Zayed M.F., Eisa W.H., Shabaka A.A. // Spectrochim. Acta. A. Mol. Biomol. Spectrosc. 2012. V. 98. P. 423–428.
41. Gruen L.C. // Biochim. Biophys. Acta. 1975. V. 386. P. 270–274.
42. Saikat Mandal P., Selvakannan R., Phadtare S., Renu P., Sastry M. // J. Chem. Sci. 2002. V. 114. P. 513–520.
43. Tan Y.N., Lee J.Y., Wang D.I //. J. Am. Chem. Soc. 2010. V. 132. № 16. P. 5677–5686.
44. Glusker J., Katz A., Bock C. // Rigaku J. 1999. V. 16. № 2. P. 8–16.
45. Si S., Mandal T.K. // Chemistry. 2007. V. 13. № 11. P. 3160–3168.
46. Kim J., Rheem Y., Yoo B., Chong Y., Bozhilov K.N., Kim D., Sadowsky M.J., Hur H.G., Myung N.V. // Acta. Biomater. 2010. V. 6. № 7. P. 2681–2689.
47. Selvakannan P., Mandal S., Phadtare S., Gole A., Pasricha R., Adyanthaya S.D., Sastry M. // J. Colloid. Interface. Sci. 2004. V. 269. № 1. P. 97–102.
48. Willett R.L., Baldwin K.W., West K.W., Pfeiffer L.N. // Proc. Natl. Acad. Sci. 2005. V. 102. № 22. P. 7817–7822.
49. Gan P.P., Li S.F. // Rev. Environ. Sci. Biotechnol. 2012. V. 11. P. 169–206.
50. Ghodake G.S., Deshpande N.G., Lee Y.P., Jin E.S. // Colloids Surf. B: Biointerfaces. 2010. V. 75. P. 584–589.
51. Armendariz V., Herrera I., Peralta-Videa J.R., Jose-Yacaman M., Troiani H., Santiago P., Gardea-Torresdey J.L. // J. Nanopart. Res. 2004. V. 6. № 4. P. 377–382.
52. Sathishkumar M., Sneha K., Yun Y.S. // Bioresour. Technol. 2010. V. 101. № 20. P. 7958–7965.
53. Bankar A., Joshi B., Ravi Kumar A., Zinjarde S. // Colloids Surf. B: Biointerfaces. 2010. V. 80. P. 45–50.
54. Lukman A.I., Gong B., Marjo C.E., Roessner U., Harris A.T. // J. Colloid. Interface. Sci. 2010. V. 353. P. 433–444.
55. Lin L., Wang W., Huang J., Li Q., Sun D., Yang X., Wang H., He N., Wang Y. // Chem. Eng. J. 2010. V. 162. P. 852–858.
56. Cruz D., Fale′ P.L., Mourato A., Vaz P.D., Luisa Serralheiro M., Lino A.R.L. // Colloids Surf. B: Biointerfaces. 2010. V. 81. P. 67–73.
57. Das R.K., Gogoi N., Bora U. // Bioprocess. Biosyst. Eng. 2011. V. 34. № 5. P. 615–619.
58. Love A.J., Makarov V.V., Yaminsky I.V., Kalinina N.O., Taliansky M.E. // Virology. 2014. V. 449. P. 133–139.
59. Love A.J., Chapman S.N., Shaw J., Taliansky M.E. // Nanoparticles. 2013. International Patent Application No. PCT/GB2013/052473.
60. Namba K., Pattanayek R., Stubbs G. // J. Mol. Biol. 1989. V. 208. P. 307–325.
61. Dhanalakshmi T., Rajendran S. // Arch. Appl. Sci. Res. 2012. V. 4. P. 1289–1293.
62. Velmurugan P., Lee S.M., Iydroose M., Lee K.J., Oh B.T. // Appl. Microbiol. Biotechnol. 2013. V. 7. P. 361–368.
63. Valodkar M., Rathore P.S., Jadeja R.N., Thounaojam M., Devkar R.V., Thakore S. // J. Hazard. Mater. 2012. V. 201. P. 244–249.
64. Suganya A., Murugan K., Kovendan K., Mahesh Kumar P., Hwang J.S. // Parasitol. Res. 2013. V. 112. P. 1385–1397.
65. Pandey G., Madhuri S., Mandloi A.K. // Pl. Arch. 2012. V. 12. P. 1–4.
66. Soundarrajan C., Sankari A., Dhandapani P., Maruthamuthu S., Ravichandran S., Sozhan G., Palaniswamy N. // Bioprocess. Biosyst. Eng. 2012. V. 35. P. 827–833.
67. Sintubin L., Verstraete W., Boon N. // Biotechnol. Bioeng. 2012. V. 109. P. 2422–2436.

# Generation of iPS Cells from Human Hair Follice Dermal Papilla Cells

I. A. Muchkaeva[1,2], E. B. Dashinimaev[1,2], A. S. Artyuhov[2], E. P. Myagkova[1,2], E. A. Vorotelyak[1,2], Y. Y. Yegorov[3], K. S. Vishnyakova[3], I. E. Kravchenko[3,4], P. M. Chumakov[3,4], V. V. Terskikh[1], and A. V. Vasiliev[1]

[1] Koltsov Institute of Developmental Biology, Russian Academy of Sciences, Vavilova str., 26, 117808, Moscow, Russia

[2] Pirogov Russian National Research Medical University, Ostrovitianov str., 1, 117997, Moscow, Russia

[3] Engelhardt Institute of Molecular Biology, Russian Academy of Sciences, Vaviolva str., 32, 119991, Moscow, Russia

[4] Shemyakin and Ovchinnikov Instituse of Bioorganic Chemistry, Russian Academy of Sciences, Miklukho-Maklay str., 16/10, 117997, Moscow, Russia

E-mail: izomerizaciya@list.ru

Received 02.08.2013



**ABSTRACT** **Dermal papilla (DP) cells are unique regional stem cells of the skin that induce formation of a hair follicle and its regeneration cycle. DP are multipotent stem cells; therefore we supposed that the efficiency of DPC reprogramming could exceed that of dermal fibroblasts reprogramming. We generated induced pluripotent stem cells from human DP cells using lentiviral transfection with Oct4, Sox2, Klf4, and c-Myc, and cultivation of cells both in a medium supplemented with valproic acid and at a physiological level of oxygen (5%). The efficiency of DP cells reprogramming was ~0.03%, while the efficiency of dermal fibroblast reprogramming under the same conditions was ~0.01%. Therefore, we demonstrated the suitability of DP cells as an alternative source of iPS cells.**

**KEYWORDS** **Hair follicle dermal papilla (DP) cells, induced pluripotent stem (iPS) cells, reprogramming.**

**ABBREVIATIONS** **AP – alkaline phosphatase, BSA – bovine serum albumin, DMEM/F12 – Dulbecco's Modified Eagle Medium: Ham's Nutrient Mixture F-12, DP – dermal papilla, ES cells (ESCs) – embryonic stem cells, FBS – fetal bovine serum, iDP cells (iDPCs) - iPS from DP cells, iPS cells (iPSCs) – induced pluripotent stem cells, PBS – phosphate buffered saline, PFA – paraformaldehyde, PSCs – pluripotent stem cells.**

## INTRODUCTION

The generation of induced pluripotent stem (iPS) cells , which are of significant interest in medicine and developmental biology, is one of the topical problems of stem cell research. Advanced cell technologies allow one to generate various iPS cell lines that can be used to model diseases and test new drugs. Developing iPSC-based therapy is associated with the generation of products for replacement enzyme therapy and, further, for cell transplantology.

Hair follicle dermal papilla cells are regional stem cells of the skin and a unique subject for study. They play the key role in the morphogenesis of a hair follicle and its growth cycle. Reorganization of hair is a result of a series of inductive interactions between skin epithelial and mesenchymal cells during the growth cycle of a hair follicle. Back in 1967, Oliver demonstrated that DP cells can induce the generation of hair follicles [1]. DP cells of scalp hair originate from the neural crest; DP cells of the dorsal side of the body are derivatives of the somite dermatome, while DP cells of the visceral body side originate from the splanchnotom visceral layer. It is well known that the WNT, BMP, and FGF signal paths act in intact DP cells [2]; their activation promotes maintenance of the inductive properties of cultured DP cells. The most commonly tested markers of dermal papilla include alkaline phosphatase (AP), versican, CD133 (in mice), Noggin, and Lef1. ALP is probably the most accurate marker of DP cells. Maximum expression of this enzyme is observed during early anagen. ALP is considered to be an indicator of the DP induction potential. Versican is an extracellular matrix proteoglycan synthesized during the anagen. A number of proteins, including the aforementioned ones, very often cannot be detected during DP cell passage, and the induction potential of DP cells disappears with time.

By the time we started our study, no data or publications devoted to the reprogramming of DP cells of the human hair follicle were available. A number of authors have assumed that successful reprogramming of

somatic cells to a pluripotent state is impossible without induced expression of the four pluripotency transcription factors Oct4, Sox2, Klf4, and c-Myc [3–5]. Higgins *et al.* [6] demonstrated that Klf4 and c-Myc begin to be expressed in cultured cells, while they cannot be detected in intact DP. In contrast, another reprogramming factor, Sox2, is synthesized in intact DP but not in culture [7]. However, two years earlier, in 2010, the same authors had denied the fact that Sox2 synthesizes in human DP cells [6]. With allowance for these facts, we set out to use DP cells as an alternative source of iPS cells and to analyze their reprogramming efficiency. We assumed that at least two (Klf4 and c-Myc), or even three (Sox2, Klf4, and c-Myc), reprogramming factors may be synthesized in non-reprogrammed DP cells, this promoting cell transition to the pluripotent state. The cells were cultured in a medium supplemented with valproic acid [8] and at a physiological oxygen level (5%) [9] to increase reprogramming efficiency. Therefore, our study was aimed at generating iPS cells from human DP cells under set conditions and at comprehensively characterizing the generated iDP cells.

## EXPERIMENTAL

### Cell cultures

The following cell cultures were used in the study: human hair follicle dermal papilla (DPC) cells; hESMK05 human embryonic stem cells, kindly provided by M.A. Lagarkova (Vavilov Institute of General Genetics, Russian Academy of Sciences), and primary mouse embryonic fibroblasts (MEFs).

DP cells were isolated according to our own procedure [10] and cultured in AmnioMAX II (Gibco) supplemented with penicillin (50 U/ml) and streptomycin (50 μg/ml) (Paneco). The medium was changed every 3–4 days. As soon as a cell layer reached the subconfluent state, the cells were passed at a 1 : 3 ratio. hESMK05 and reprogrammed iPS cells were cultured in mTeSR™ 1 (STEMCELL Technologies) at 37°C, 5% $CO_2$ and 5% $O_2$. PSCs were passed either mechanically, with a plastic tipped pipette, or by incubation in a 1 mg/ml dispase solution (STEMCELL Technologies) on a cultural substrate Matrigel, a mixture of extracellular matrix proteins and proteoglycans (BD Biosciences); the medium was changed daily.

### Generation of iDP cell clones

DP cells of the third passage (0.5 mln per a 30–60 mm Petri dish) were infected with lentiviral vectors carrying the pluripotency genes (*Oct4, Sox2, Klf4*, and *c-Myc*) in the DP cells culture medium supplemented with 5 μg/ml Polybrene (Sigma) at 37°C, 5% $CO_2$, and 5% $O_2$ overnight. Through the first seven days, the medium was supplemented with small molecule compounds enhancing reprogramming efficiency, 2 mM valproic acid (Sigma) and 50 μg/mL ascorbic acid (Sigma), and changed every other day. On day 8, the reprogramming medium was replaced with the medium for pluripotent stem cells, mTeSR™ 1 (STEMCELL Technologies), and was further changed daily. Cells in their first passages were mechanically plated onto mitotically inactive MEFs and, with the beginning of colony contacting, onto Matrigel-coated plastic dishes (BD Biosciences). The aforementioned additives were discontinued from the first cell passage onto 100 mm Petri dishes. Within 2–3 weeks after passing, iPSC clones were selected according to a PSC-surface marker, Tra-1-60, using vital immunolabeling and mechanical selection of positive clones.

### Alkaline phosphatase activity assay

The activity of AP was assayed using an NBT/BCID kit (Roche), according to the manufacturer's protocol.

### Immunocytochemistry and flow cytometry

For immunofluorescent assay, the cells were fixed in a 4% paraformaldehyde solution. The cells were incubated with primary antibodies (see the Table) in PBS with either 1% BSA (Helicon) or 5% FBS (BioWest) at 4°C overnight, and then with the secondary antibodies, Alexa Fluor 488, Alexa Fluor 594, or Texas Red, at the ambient temperature for 60 min. Nuclei were counterstained with 4,6-diamidino-2-phenylindole (DAPI) in PBS (Vector Laboratories) at the ambient temperature for 10 minutes. The specimens were analyzed on an Olympus IX51 fluorescent microscope (Olympus) and a Coolpix 8700 digital camera (Nicon). Cells expressing PSC surface antigens were quantified on a Cell Lab Quanta™ SC flow cytometer (Beckman Coulter). Three replicates of a sample, at least 30,000 cells each, were analyzed.

### Telomerase activity test

Cell telomerase activity was assayed using the TRAPEZE® XL Telomerase Detection Kit (Millipore) and Encyclo polymerase (Evrogen) as a PCR enzyme.

### RT-PCR gene expression assay

Total RNA was isolated with the use of Quick-RNA™ MiniPrep (Zymo Research) according to the manufacturer's protocol, slightly modified. Reverse transcription (RT) was performed using the RT-PCR kit and oligo(dT)15-primers (Sileks). Primers were selected according to Ohnuki *et al.* [11] from the primer bank http://pga.mgh.harvard.edu/primerbank/index.html. PCR was performed using a ScreenMix-HX (Evrogen) and a Bio-Rad amplifier. PCR products were separated by electrophoresis in 2% agarose gel in a Tris-

List of used antibodies

| Antibodies (antigens) | Manufacturer | Antibody producer | Working dilution |
|---|---|---|---|
| Oct4 | Millipore (MAB4401) | Mouse | 1 : 200 |
| Sox2 | Cell Signalling (#3579) | Rabbit | 1 : 250 |
| Nanog | Abcam (ab80892) | Rabbit | 1 : 400 |
| SSEA3 | STEMCELL Technologies (#01553) | Rat | 1 : 100 |
| SSEA4 | Abcam (ab16286) | Mouse | 1 : 250 |
| Tra-1-60 | Abcam (ab16288) | Mouse | 1 : 100 |
| Tra-1-81 | STEMCELL Technologies(#01556) | Mouse | 1:300 |
| Desmin | Abcam (ab15200) | Rabbit | 1 : 200 |
| Nestin | Millipore (MAB5326) | Mouse | 1 : 200 |
| Doublecortin | Abcam (ab77450) | Rabbit | 1 : 200 |
| β-III-tubulin | Millipore (MAB1637) | Mouse | 1 : 100 |
| Neuron-specific enolase | DakoCytomation (M087329) | Mouse | 1 : 200 |
| Vimentin | Abcam (ab8978) | Mouse | 1 : 200 |
| Pan-cytokeratin | Santa-Cruz (sc-81714) | Mouse | 1 : 20–1 : 50 |
| Osteopontin | Millipore (MAB3057) | Rat | 1 : 350 |
| Osteonectin | Millipore (AB1858) | Rabbit | 1 : 500 |
| Hnf4α | Santa-Cruz (sc-8987) | Rabbit | 1 : 50 |
| Foxa2 | Millipore (#07-633) | Mouse | 1 : 100 |
| Alpha-fetoprotein | R&D Systems (MAB1368) | Mouse | 1 : 200 |
| Albumin | R&D Systems (MAB1455) | Mouse | 1 : 250 |
| CK8 | Millipore (04-588) | Rabbit | 1 : 200 |
| CK18 | Millipore (MAB3234) | Mouse | 1 : 100 |
| Alexa Fluor 488 | Molecular Probes (# A-11029, A-21206, A-21208) | Goat, donkey | 1 : 500 |
| Alexa Fluor 594 | Molecular Probes (# A-11032) | Goat | 1 : 500 |

acetate buffer and visualized using a UV gel analyzer (BioRad).

### Real-time PCR gene expression assay

Real-time PCR was performed using HS-SYBR (Evrogen), and cDNA generated with reverse transcription was analyzed as follows: cDNA (from 15 ng of RNA) and 10 μg of each primer selected from the primer banks http://pga.mgh.harvard.edu/primerbank/index.html and http://medgen. ugent.be/rtprimerdb were used for each reaction; cDNAs diluted 4-, 16-, 64-, and 256-fold in three replicates were used to build a calibration curve. Amplification was performed according to the following program: 95˚C – 10 min, followed by 40 two-stage cycles: 95˚C – 15 s, 60˚C – 1 min in a 7500 Real-Time PCR System (Applied Biosystems). A melting profile of the reaction products was constructed after 40 cycles and used to analyze reaction specificity and by-products.

### Generation, culturing, and analysis of embryoid bodies (EBs)

EBs were generated by culturing in either a AggreWell™ (STEMCELL Technologies) or DMEM/F12 (Gibco) medium supplemented with a 20% KSR serum substitute (Gibco); 1× NEAA (Gibco); 1× GlutaMAX (Gibco); penicillin (50 U/ml), and streptomycin (50 μg/ml, Paneco). Each embryoid body was formed in a hanging drop and grown in the suspended state in Ultra Low Adhesion Plates (Corning), preventing cell-plastic attachment. The medium was changed daily. EBs were fixed in 3% paraformaldehyde, incubated in a 15% sucrose solution, embedded into Tissue-Tek® OCT™ Compound (Sakura)б and frozen in liquid nitrogen. Next, 7.5 μm thick sections were cut with a cryotome (CM1900) and layered onto positively charged microscope slides. Non-specific binding was blocked in PBS with a 1% BSA solution. Further, the samples were prepared as aforesaid.

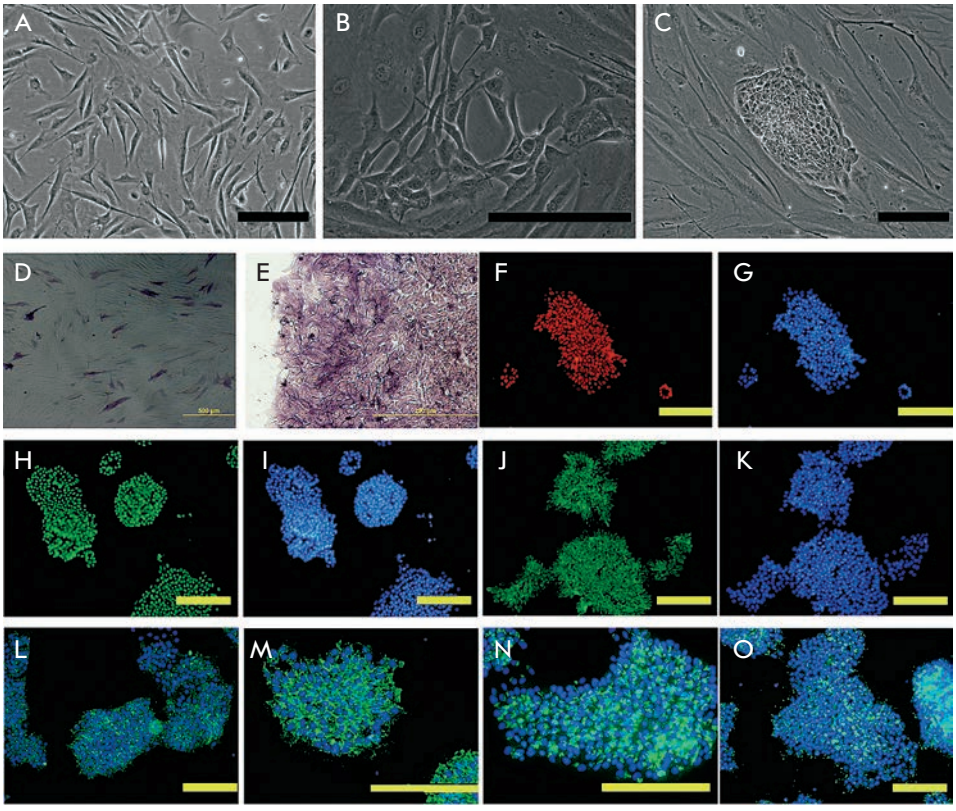


Fig. 1. Generation of human iDP cells. Morphology of cultured DP cells before reprogramming factors infection (A) and emergence of first reprogrammed clones on the 8th day after infection (B) and 11th day after infection (C). Expression of alkaline phosphatase in non-reprogrammed (passage 6) DP cells (D) and in generated (passage 6) iDP cells (E). Immunofluorescent detection of nucleus proteins: Oct4(F), Sox2 (G), and Nanog (H), and surface antigens: SSEA3 (L), SSEA4(M), Tra- 1 -60 (N), and Tra -1-81 (O) in iDP cells. G, I, K, L-O - nuclei are counterstained with DAPI (blue). Scale bars = 200 μm. (G, I, K – the same visual fiels as F, H, J respectively)

### Directed *in vitro* iPSC differentiation

Both pieces of embryoid bodies and undifferentiated cells (clusters occupying 10–20% of the cultural dish surface) were used for differentiation. Immunocytochemical staining was used to identify differentiation. Osteogenic differentiation was induced by cell culturing in a medium containing DMEM/F12 (Gibco), 10% FBS (Gibco), 2 mM glutamine (Paneco), 10 ng/ml hepatocyte growth factor (HGF, Invitrogen), 10 ng/mL epidermal growth factor (EGF, PeproTech), 20 ng/ml bone morphogenetic protein 2 (BMP2, R&D), and 0.03 mM nicotinamide. In case of support-grown cells forming ESC-type colonies, the entodermal differentiation program was induced by supplementing the medium with activin A (R&D) at a 100 ng/ml concentration during the first 2–3 days (no activin A was required for differentiation from EBs). After discontinuation of activin A, the medium was supplemented with 30 ng/ml of fibroblast growth factor 4 (FGF4, Invitrogen). As soon as the cell layers reached 80% confluence, FGF4 and BMP2 were removed from the medium and the cells were further cultivated with oncostatin M (10 ng/ml, R&D) and dexamethasone (0.1 μM, Sigma-Aldrich) for 5–7 days. After passaging, 1× B27 (Gibco) was added to the medium for the next 7–10 days. To induce neural differentiation, 20 ng/mL of both Noggin (Invitrogen) and fibroblast growth factor 2 (FGF2, PeproTech) were added to DMEM/F12 (Gibco) with 3% FBS (Gibco), 1×X NEAA (Gibco), 1× GlutaMAX (Gibco), penicillin (50 U/ml), and streptomycin (50 μg/ml) (Paneco) for seven days. The cells were then cultivated with 1× B27 (Gibco); seven days later, 10 ng/ml of both the neurotrophic growth factor (BDNF, PeproTech) and nerve growth factor β (NGFβ, PeproTech) were added and the cells were cultivated for the next 7–14 days.

### Karyotyping

To prepare chromosome plates, colcemid (Colcemid, Gibco) was added to the culture medium. After colcemid incubation, the cells were kept in a hypotonic solution (60 mM KCl) and fixed in methanol: ice acetic acid (3 : 1) cooled to –20°C. The resulting suspension was dropped onto microscopic slides from a height of approximately 10 cm and the fixator was fired on the glass. For the differentiated staining, the chromosome plates were processed with fluorescent dyes DAPI and 7-aminoactinomycin D (7-AAD).

### Teratoma formation test

The pluripotent state of induced cells was assayed using the standard *in vivo* teratoma formation test. Approximately $5\times10^6$ undifferentiated cells were injected

subcutaneously to Nude immunodeficient mice. After tumor formation, the mouse was euthanized; the tumor was cut out and fixed; histologic and immunohistologic samples were prepared.

## RESULTS AND DISCUSSION

iPS and ES cells share a number of morphological and metabolic parameters. The study compares the generated iPS and human ES cells (hESMK05).

### Transfection, isolation, and cultivation of iDP cells

The early stages of reprogramming include changes in cell dimensions and shape, as well as organization of the cytoskeleton and receptors. The emergence of cells visually distinct from the initial culture can be a signal of the onset of a reprogramming process in the transfected cells. We used a histone deacetylase inhibitor, valproic acid [8], along with incubation of the cells in 5% oxygen to enhance reprogramming efficiency. We observed the emergence of the first cell colonies with an altered morphology on the 8$^{th}$ day after lentiviral transfection of DP cell culture (*Fig. 1B*), which points to one of the reprogramming parameters, mesenchyme-epithelial transition [12]. At this moment, the reprogramming medium was replaced with mTesr1 to maintain the undifferentiated state. The colonies increased in size and new colonies emerged with time. Virtually all colonies had an ESC-like morphology and distinct shapes. The morphological parameters of all the generated clones were virtually identical. The high nucleus-to-cytoplasm ratio was typical of the cells forming these colonies (same as that for ESCs) (*Fig. 1C*).

Only a small number of morphologically similar transformed colonies travel all through reprogramming to the pluripotent state; therefore, discriminating between the totally and partially reprogrammed clones became our next challenge. The morphological similarity of the separated clones to PSCs is a common parameter used to separate reprogrammed cells from the pool of non-reprogrammed ones. AP is one of the pluripotent state markers; hence, assay of its expression is the common first stage leading to further cloning of AP positive colonies [13, 14]. However, expression of AP is typical of intact DP cells [15], and the positive signal raised a question as to whether the AP expression resulted from cell reprogramming or from the integrity of the maternal cells parameters. Therefore, we considered selection of the clones according to this parameter to be unreasonable. To simplify the separation of totally reprogrammed iPS cells, we performed vital immunolabeling against the surface antigen Tra-1-60, one of the markers of pluripotent cells [16], on the 21$^{st}$ day after transfection with the reprogramming factors, and then we manually selected Tra-1-60- positive colonies. We preferred the Tra-1-60 staining bearing two facts in mind: that reprogramming is a multistage process, and that this marker emerges at the later stages of acquiring pluripotency. The colonies were transferred onto a cultural plastic coated with a feeder layer of mitotically inactivated MEFs. The cells were subsequently passed onto the Matrigel-coated plastic.

### Verification of the undifferentiated state of the generated iPS cells

AP, a marker of pluripotent and stem cells, is expressed in intact DP cells and indicates the induction capacity of DP. However, a number of proteins typical of intact DP cells, including AP, become virtually undetectable with time, and DP cells lose their induction potential [17]. Researchers consider the loss of own parameters and acquisition of interfollicular fibroblast signs a result of the absence of the microenvironment that is native to a natural DP cell culture. We detected AP expression in the isolated clones of the reprogrammed cells at the sixth passage (three passages before transfection with the *Oct4, Sox2, Klf4,* and *c-Myc* and three passages after transfection) (*Fig. 1E*), while only single cells of the initial DP culture expressed AP at the same passage (*Fig. 1D)*. AP expression mainly attests to the reprogramming process taking place in cells but not always shows the totally reprogrammed state. We noticed the formation of colonies positive towards this marker, which did not become genuine iPS cells. They either could fail to totally reprogram or were rapidly undifferentiated after becoming pluripotent (and we did not manage to register this moment).

The isolated colonies were AP positive during continuous cultivation, as well. With the use of immucytochemical staining, we found that the examined clones of reprogrammed cells expressed the pluripotency transcription factors Oct4, Sox2, and Nanog (*Fig. 1 F–K*), along with the surface antigens SSEA-3, SSEA-4, Tra-1-60, and Tra-1-81 (*Fig. 1 L–O*). We selected one iDP cell clone positive towards all the listed markers, for further study.

However, the results of immunocytochemical staining do not show the quantitative parameters of the generated iDP. Therefore, we used flow cytometry to determine the iPS cell percentage in a culture expressing the above-mentioned surface pluripotency markers (*Fig. 2A*). Virtually all iDP cells (99.28%) were SSEA4-positive; 78.36% of iDP cells expressed Tra-1-60; 67.39% expressed Tra-1-81, and more than half of the iDP cell population (53.94%) were SSEA3-positive. The data show that not all cells of the clone express the pluripotency antigens SSEA3, SSEA4, Tra-1-60, and Tra-1-81; however, the share of these cells is considerable (53–99%). The selected iDP cells express SSEA3, SSEA4,

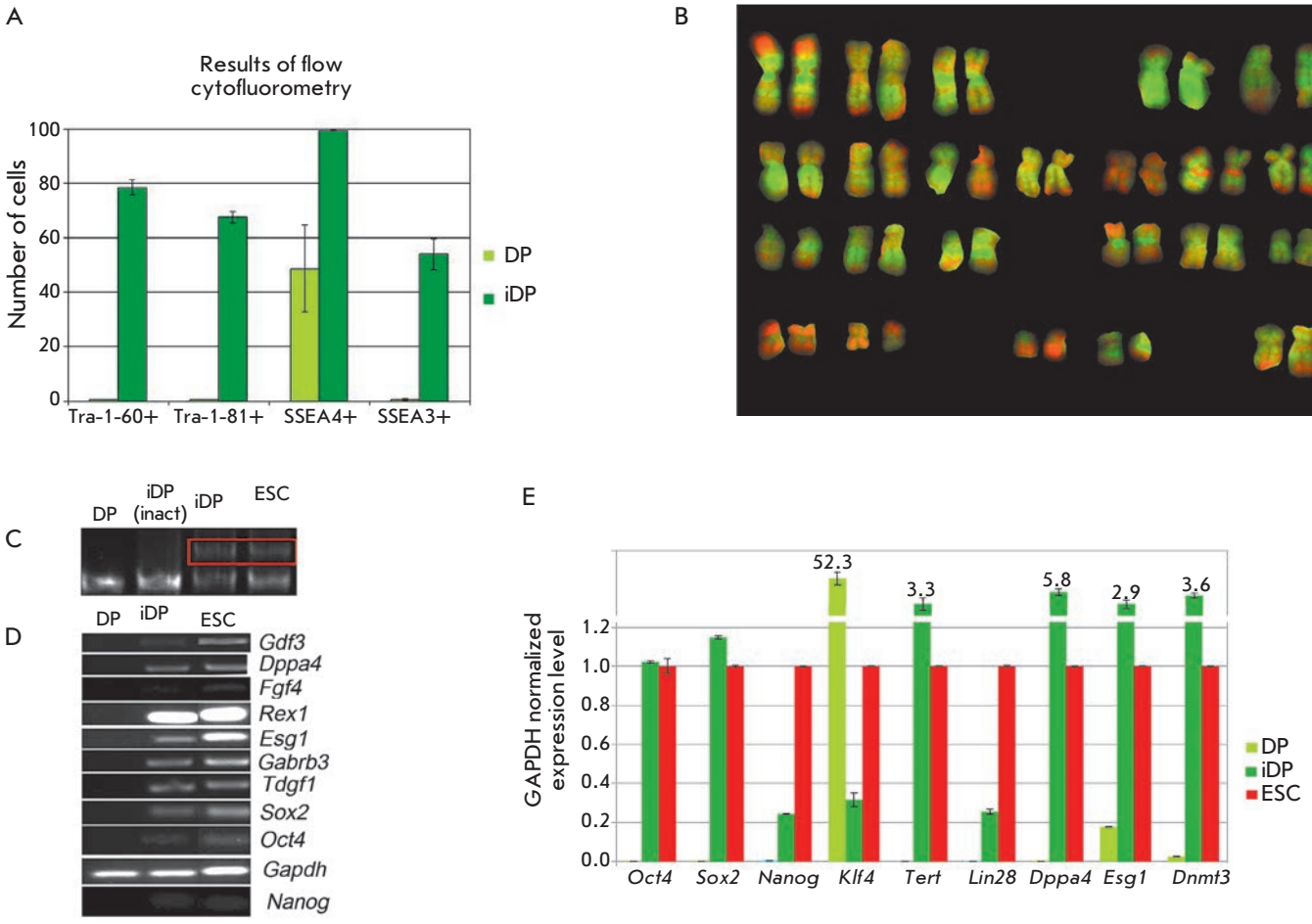


Fig. 2. Ratio of untreated (DP) to reprogrammed (iDP) cells expressing pluripotency markers, *Tra-1 -60* , *Tra-1-81* , *SSEA3*, and *SSEA4*, according to flow cytofluorometry (A). Normal diploid karyotype (46,XX) of iDP cells. Chromosomes are stained with DAPI (green) and 7-AAD (red) (B). Telomerase reactivation in iDP cells (C). Telomerase is active in the samples, with additional bands corresponding to telomeric repeats (iDP, ESCs). Control: ES and iDP cells heated before telomerase inactivation (iDP) (inact). Telomerase of the initial iDP cell culture is inactive. Reverse transcription-PCR (RT-PCR) analysis of iDP cells (D). Expression levels of *Oct4*, *Sox2*, *Nanog*, *Tert*, *Klf4*, *Lin28*, *Dppa4*, *Dnmt3* in DP, iDP, and ES cells (E), according to real-time PCR

Tra-1-60, and Tra-1-81, which remain virtually undetected in the initial DP cells. The maternal cells do not express these pluripotency markers, and the generated iDP cells are positive towards them; therefore, it is clear that these cells undergo reprogramming.

The average doubling time of the iDP cell population determined using the least square method was 25 h. Hence, the growth kinetics of the generated iDP was similar to that of ES cell clones (the average doubling time of the ESC population was 25 h). iDP cells of the fifth passage had normal 46,XX diploid karyotype (*Fig. 2B*).

Telomerase reactivation is another criterion of cell reprogramming to pluripotency. It is common knowledge that telomerase is inactive in somatic cells, while activated in the course of reprogramming. Telomerase acts as the reverse transcriptase elongating telomeric fragments of cell DNA. The TRAP-PCR analysis showed that telomerase of the generated iDP cells is active (*Fig. 2C*), which is not surprising considering the high proliferative potential of the cells under examination. This enzyme is inactive in the initial DP culture; therefore, iDP cell telomerase was reactivated during cell reprogramming. Telomerase activity in the generated iDP cells was similar to that in ESCs.

Using RT-PCR, we detected transcripts of the genes (*Nanog*, *Oct4*, *Sox2*, *Tdgf1*, *Gabrb3*, *Esg1*, *Rex1*, *Fgf4*, *Dppa4*, and *Gdf3*) in iPSC cultures, which are active during the early development and serve as PSC markers (*Fig. 2D*). Transcripts of these genes could not be detected in the initial DP culture; therefore, the emer-

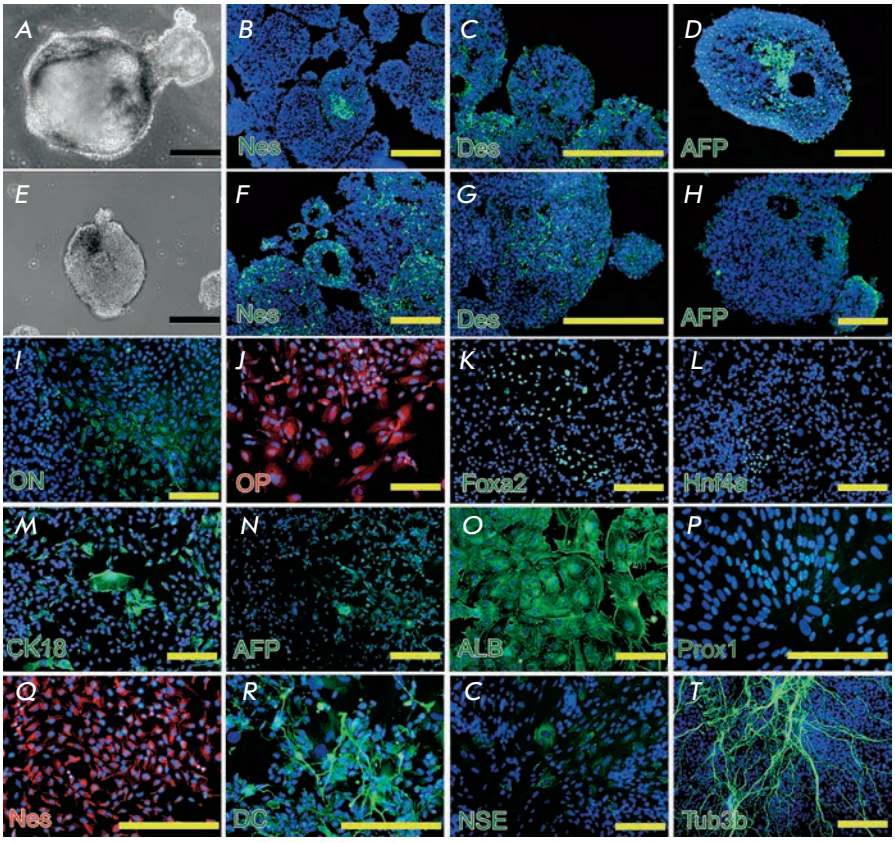


Fig. 3. iDP cells differentiation in vitro. Formation and characterization of embryoid bodies (EBs) in iDP cell cultures (A–D), and in the control, human ES cells (E–H). Morphology of EBs in iDP (A) and ES (E) cell cultures. Expression of markers of three germinal layers, nestin (Nes), desmin (Des), and alpha-fetoprotein (AFP), EBs differentiation in iDP- (B–D) and hES-derived cells (F–H) EBs. Directed differentiation of iDP cells (I–T). Expression of osteogenic differentiation markers: osteonectin (ON, I) and osteopontin (OP, J). Expression of hepatocyte differentiation markers: Foxa2 (K), Hnf4α (L), cytokeratin18 (CK18, M), alpha-fetoprotein (AFP, N), and albumin (ALB, O). Expression of neuronal differentiation markers Prox1 (P), nestin (Nes, Q) doublecortin (DC, R), neuron-specific enolase (NSE, S), and β-III- tubulin (Tub3b, T). Scale bars = 200 μm

gence of positive signals in iDP cells indicates their activation in the course of reprogramming. Most likely, Oct4, Sox2, and Nanog activate other genes of early development. Our results confirm the key role of the above-mentioned factors in reprogramming.

We used real-time PCR to detect specific details of the culture (*Fig. 2E*) and succeeded in detecting some details in the examined cultures. However, the expression levels of virtually all the examined genes were similar in iDP and ES cells, while distinct from the expression profile in non-reprogrammed cells.

Therefore, the generated reprogrammed cells meet the criteria of undifferentiated state according to the analyzed parameters. Their further characterization required determining their differentiation potential.

### Determination of iDP cell differentiation potential

We used iDP cells to generate embryoid bodies, which are similar to the early stages of embryogenesis in a laboratory environment (*Fig. 3A*). EB are self-organizing round aggregates with an internal cavity. We detected ectodermal (nestin), mesodermal (desmin), and entodermal (alphafetoprotein, AFP) proteins both in the iDP- and ESC-generated EBs (*Figs. 3B–D*).

PSCs can be used to examine early development processes and directed differentiation of cells into a particular tissue due to their ability to differentiate under laboratory conditions. We determined the conditions for iPS cell differentiation into the ecto- (neuronal differentiation), meso- (osteogenic differentiation), and entodermal (hepatic differentiation) directions.

### Osteogenic differentiation

Two or three weeks after induction of osteogenic differentiation of iDP cells, we detected extracellular matrix proteins, osteopontin (*Fig. 3J*) and osteonectin (*Fig. 3I*), which are regarded as osteoblast markers and participate in bone mineralization.

### Hepatic differentiation

Hepatic differentiation was performed during 3–5 weeks; the onset of the expression of nuclear transcription factors, Foxa2 (a marker of the definitive entoderm) and Hnf4α (a marker of extraembryonic entoderm) in iDP cells, was observed within this period. Cells positive for these factors were located by groups, approximately 50–100 cells each (*Fig. 3K, L*). Expression of two proteins emerged: alphafetoprotein (AFP)

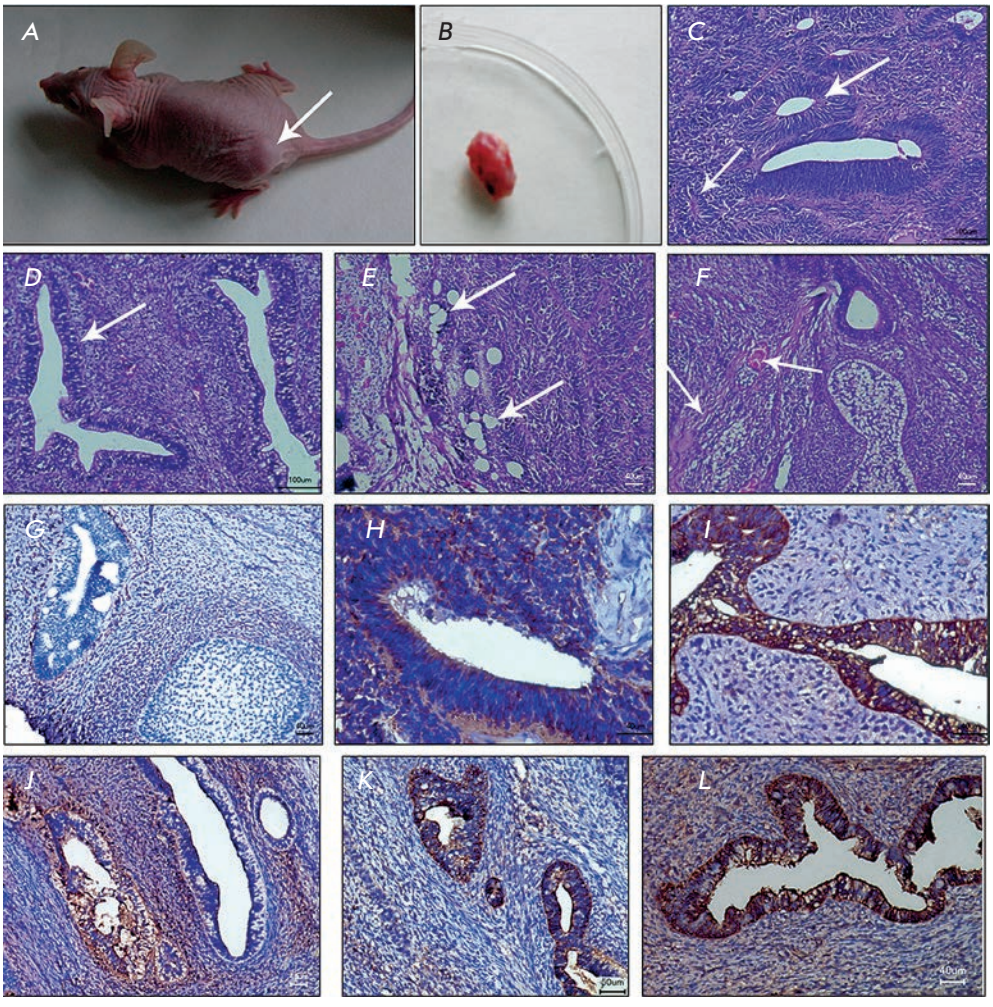


Fig. 4. Formation of teratoma from iDP cells. The recipient mouse (A) with teratoma (arrow) and the resected teratoma (B) six weeks after subcutaneous injection of iDP cells. Histological sections of hematoxylin and eosin-stained teratomas (C–F): neuroglia (neuroepithelial tubules and rosettes, arrows) (C); glandular epithelium (D), mesenchyme (adipose cells, arrows in D; fibers of loose connective tissue and vessels, arrows in F) (E, F); stained with antibodies against: vimentin (G), nestin (H) , pan CK (I) CK8 (J), CK18 (K) and AFP (L)

that points to hepatoblast committing of the cells and epithelial marker cytokeratine 18 (CK18), indicating a higher differentiated state of the cells (*Fig. 3M,N*). After the differentiation, albumin expression, typical of mature hepatocytes, begins in the cells (*Fig. 3O*).

### Neuronal differentiation

Neuronal differentiation was performed during 3–5 weeks. Immunocytochemical staining showed that neuronal differentiated iPD cells expressed Prox1 (*Fig. 3P*), which may play the pivotal role in CNS development, participating in the regulation of the expression and development of post-mitotic undifferentiated neuron precursors. Neuronal iDP cells were positive for nestin, a marker of neural stem cells, (NSC) (*Fig. 3Q*) and doublecortin (DC), a marker of immature neurons (*Fig. 3R*); they also formed plexus of cells with long processes positive towards βIII tubulin, a marker of mature neurons (*Fig. 3T*), and were positively stained towards neuron-specific enolase (NSE) (*Fig. 3S*).

### *In vivo* differentiation of iPSCs

The ability of cells to form teratoma in thymus-free mice is one of the reliable tests that confirm their pluripotency. Teratoma is a tumor consisting of several types of tissues, usually derivatives of three germinal layers, not typical of organs or anatomical areas where the tumor develops. Data on the efficiency of teratoma formation with respect to a site of undifferentiated PSCs injection are rather ambiguous. Thus, Prokhorova *et al.* [18] reported the site-specificity of teratomas formed from the same cells, while other authors found no difference between the efficiency of the teratoma test at injection of PSCs into different areas of the recipient's body [19]. We chose the least laborious technique of iDP cell subcutaneous injection into the back and posterior limb of a mouse. Within 3–6 weeks after the injection of undifferentiated iDP cells, a teratoma started to form at the injection site (*Fig. 4 A,B*). Histologically, this was immature teratoma, containing structures of ecto-, meso-, and entoderm origin. The

mesenchymal tissues observed in histological specimens had abundant capillaries, with expanded lumens in some of them, and fibers of loose connective tissue between them (*Fig. 4F*). Moreover, it contained large cells with foam cytoplasm, a potential indicator of adipose tissue forming in the teratoma (*Fig. 4E*). Vast areas of glandular epithelium (*Fig. 4D*), along with fragments of immature nerve tissue, consisting of small hyperchromatic cells with a narrow cytoplasm rim could be observed in the specimen. Structures resembling primitive neuroectodermal rosettes and tubules were found, as well (*Fig. 4C*). The authenticity of teratoma generation from iDP cells was confirmed by immunohistochemical analysis. Vimentin-rich sites located within inter-canal tissues were detected in the specimens (*Fig. 4G*). Nestin was found in structures resembling neuroectodermal rosettes and tubules (*Fig. 4H)*. We observed a large number of glandular structures in which pan-cytokeratin, cytokeratins 8 and 18, along with alphafetoprotein, were expressed (*Figs. 4 I–L*).

The reprogramming efficiency reported in [6] was ~0.02% vs. ~0.03% in our study. Most probably, this difference is insignificant and is related to the different techniques used in different laboratories. However, the result of our study might point to the positive effect of culturing conditions (low oxygen content and valproic acid supplementation) on the efficiency of reprogramming; this is quite possible, because Higgins *et al.* [6] did not mention the use of these components in their experiments. Thus, the results of these two studies are comparable and complement each other.

Considering the neural crest origin of the used DP cells, further study of the generated iDP cell line, including its epigenetic parameters and tendencies towards spontaneous *in vitro* neuronal differentiation, comparatively with iPS cell lines originated from other sources is of interest. ●

*This research was supported by the Ministry of Education and Science of the Russian Federation: Government Contract N 8796 dated October 4, 2012 (SPECIALISTS 1.2.2), Government Contract N 16.740.11.0637 dated July 2, 2011 (SPECIALISTS 1.3.1), and Government Contract N 14.512.11.0040 dated April 3, 2013 (Technologies and Developments).*

REFERENCES

1. Oliver R.F. // J. Embryol. Exp. Morphol. 1967. V. 18. № 1. P. 43–51.
2. Ohuama M., Kobayashi T., Sasaki T., Shimizu A., Amagai M. // J. Cell Sci. 2012. V. 125. № Pt17. P. 4114–4125.
3. Shutova M.V., A.N. Bogomazova, M.A. Lagarkova, S.L. Kiselev // ActaNaturae. 2009. V. 1. № 2. P. 104–106.
4. Takahashi K., Yamanaka S. // Cell. 2006. V. 126. № 4. P. 663–676.
5. Liskovykh M. A., Chuykin I. A., Ranjan A., Safina D. A., Tolkunova E. N., Minina Yu. M., Zhdanova N. S., Dyban P. A., Mullins J., Kostyleva E. I. et al. // Tsitologiya. 2011. V. 53. № 12. P. 927–934.
6. Higgins C., Ito M., Inoue K., Richardson G., Jahoda K., Cristiano A. // Exp. Dermatol. 2010. V. 19. № 6. P. 568.
7. Higgins C., Ito M., Inoue K., Richardson G., Jahoda K., Cristiano A. // J. Invest. Dermatol. 2012. V. 136. № 6. P. 1725–1727.
8. Medvedev S.P., Grigor'eva E.V., Shevchenko A.I., Malakhova A.A., Dementyeva E.V., Shilov A.A., Pokushalov E.A., Zaidman A.M., Aleksandrova M.A., Plotnikov E.Y. et. al. // Stem Cells Dev. 2011. V. 20. № 6. P. 1099–1112.
9. Warren L., Manos P.D., Ahfeldt T., Loh Y.H., Li H., Lau F., Ebina W., Mandal P.K., Smith Z.D., Meissner A. et al. // Cell Stem Cell. 2010. V. 7. № 5. P. 618–630.
10. Chermnykh E. S., Radyukhina N. V., Rutkevich P. N., Shevelyov A. Y., Vlasik T. N., Vorotelyak E. A., Vasiliev A. V., Terskikh V. V. // Tsitologiya. V. 52. № 3. P. 219–224.
11. Ohnuki M., Takahashi K., Yamanaka S. Generation and Characterization of Human Indused Pluripotent Stem Cells. Curr. Protoc. Stem Cell Biol. 2009. Chapter 4:Unit 4A.2. doi: 10.1002/9780470151808.sc04a02s9.
12. Li R., Liang J., Ni S., Zhou T., Qing X., Li H., He W., Chen J., Li F., Zhuang Q., et. al. // Cell Stem Cell. 2010. 7 № 1. P. 51–63.
13. Kim D., Kim C.H., Moon J.I., Chung Y.G., Chang M.Y., Han B.S., Ko S., Yang E., Cha K.Y., Lanza R. et. al. // Cell Stem Cell. 2009. V. 4. № 6. P. 472–476.
14. Marchetto M.C., Yeo G.W., Kainohana O., Marsala M., Gage F.H., Muotri A.R. // PLoS One. 2009. V. 4. № 9. e7076.
15. Gnedeva K.Y. // Candidate Thesis, M., 2012.
16. Yehezkel S., Rebibo-Sabbah A., Segev Y., Tzukerman M., Shaked R., Huber I., Gepstein L., Skorecki K., Selig S. // Epigenetics. 2011. V. 6. № 1. P. 63–75.
17. Rendl M., Polak L., Fuchs E. // Genes Develop.2008. V. 22. № 4. P. 543–557.
18. Prokhorova, T.A., L.M. Harkness, U. Frandsen, N. Ditzel, H. D. Schroder, J.S. Burns, M. Kassem. // Stem Cells Dev. 2009. V. 18. № 1. P. 47–54.
19. Zhang W.Y., de Almeida P.E., Wu J.C. // 2012. Teratoma formation: A tool for monitoring pluripotency in stem cell research. StemBook [Internet], doi/10.3824/stembook.1.53.1. http://www.stembook.org.

# Patient-Specific Induced Pluripotent Stem Cells for SOD1-Associated Amyotrophic Lateral Sclerosis Pathogenesis Studies

I. V. Chestkov[1]*, E. A. Vasilieva[1], S. N. Illarioshkin[2], M. A. Lagarkova[1], S. L. Kiselev[1]
[1]Vavilov Institute of General Genetics RAS, Gubkina Str., 3, Moscow, Russia, 119991
[2]Research Center of Neurology RAMS, Volokolamskoye shosse, 80, Moscow, Russia, 125367
*E-mail: ichestkov@vigg.ru
Received 09.09.2013


**ABSTRACT** **The genetic reprogramming technology allows one to generate pluripotent stem cells for individual patients. These cells, called induced pluripotent stem cells (iPSCs), can be an unlimited source of specialized cell types for the body. Thus, autologous somatic cell replacement therapy becomes possible, as well as the generation of *in vitro* cell models for studying the mechanisms of disease pathogenesis and drug discovery. Amyotrophic lateral sclerosis (ALS) is an incurable neurodegenerative disorder that leads to a loss of upper and lower motor neurons. About 10% of cases are genetically inherited, and the most common familial form of ALS is associated with mutations in the *SOD1* gene. We used the reprogramming technology to generate induced pluripotent stem cells with patients with familial ALS. Patient-specific iPS cells were obtained by both integration and transgene-free delivery methods of reprogramming transcription factors. These iPS cells have the properties of pluripotent cells and are capable of direct differentiation into motor neurons.**
**KEYWORDS** **induced pluripotent stem cells; amyotrophic lateral sclerosis; differentiation; motor neurons.**
**ABBREVIATIONS** **ALS – amyotrophic lateral sclerosis; DAPI – 4',6-diamidino-2-phenylindole; CCS – copper chaperone for superoxide dismutase; ChAT – choline acetyltransferase; ESCs – embryonic stem cells; GFAP – glial fibrillary acidic protein; iPSCs – induced pluripotent stem cells; hSOD1 – human superoxide dismutase 1.**

## INTRODUCTION

Amyotrophic lateral sclerosis (ALS, also known as the motor neuron disease (MND), Charcot disease or Lou Gehrig's disease) is an adult-onset progressive neurodegenerative disease that involves selective death of motor neurons in the brain and spinal cord. Gradual muscle de-innervation is observed during disease progression, and the death usually occurs from respiratory muscle failure. There is no effective early diagnosis of ALS and, therefore, patients live no more than 5 years after the manifestation of the first symptoms. Most cases of ALS (about 90%) are not genetically inherited and are known as sporadic ALS. The most common case of familial ALS (ALS1, 20% of all ALS patients) is associated with autosomal dominant mutations in the Cu/Zn superoxide dismutase (*SOD1*) gene. Over 170 mutations in the *SOD1* gene have been characterized in ALS patients (ALSoD database, June 28, 2013).

However, the relationship between the genetic defect and the loss of motor neurons has not yet been established. Generation of transgenic mice with the mutant human *SOD1* allele made it possible to reproduce the basic symptoms of neurodegeneration in ALS and test several hypotheses on the basis of disease pathogenesis. It was shown that the toxic effect of *SOD1* on motor neurons is not associated with impairment or loss of its enzyme activity. Similar symptoms of ALS, including the loss of close synaptic contacts between motor neurons [1], disruption of the mitochondrial function [2], and activation of glial cells [3], have been confirmed in *SOD1*-trangenic mouse models expressing both dismutase-active ($hSOD1^{G37R}$ [4], $hSOD1^{G93A}$ [5]), and non-active ($hSOD1^{G85}R$ [6], $hSOD1^{G127X}$ [7]) mutants. Moreover, homozygous *SOD1*−deficient mice showed no symptoms of neurodegenerative disorders [8].

The catalytic activity of SOD1 depends on the presence of a copper ion in the active site of the enzyme. In its free state, this metal ion exhibits extreme reactivity and toxicity; therefore, inefficient delivery of copper into the active site of SOD1 or its binding violation due to conformational changes in the enzyme (due to mutations) may prove the reason behind intracellular disorders and the death of motor neurons. However, removal of the copper chaperone of SOD1 (CCS) [9] or introduction of mutations in the copper-binding site of

the enzyme [10] failed to reduce the selective toxicity to motor neurons in mice.

Nevertheless, conformational changes and the toxicity of mutant SOD1 are currently considered as the main cause of ALS. The loss of copper and zinc ions in the active protein site or the disruption of intramolecular disulfide bonds, leads to dissociation of native SOD1 homodimer into monomers and subsequent formation of protein aggregates, the presence of which is a characteristic of typical ALS [11]. Furthermore, the presence of SOD1-protein aggregates in a sporadic ALS patient's motor neurons suggests that aberrant oligomerization of SOD1 is a common feature of ALS, regardless of genotype [12]. The conformational theory is supported by the fact that there are forms of the disease with different manifestation and progression rates that are dependent on the type of mutation in the *SOD1* gene.

It should be noted that the death of motor neurons in ALS may be not an autonomous cell process, since the expression of *SOD1* mutants selectively in motor neurons does not lead to neurodegeneration in transgenic mice [13], while a toxic effect has been shown for astrocytes [14] and microglial cells [3].

However, the results obtained in transgenic animals cannot always be directly transferred to humans. Systems overexpressing the mutant *SOD1* gene may fail to reproduce the molecular basis of the disease progression. Besides, the study of human ALS is limited by the inaccessibility of affected tissues. The cell reprogramming technology allows the reprogramming of any somatic patient's cells, for instance, skin fibroblasts [15] endothelial cells [16, 17], to the pluripotent state. These induced pluripotent stem cells (iPSCs) display all the characteristics of embryonic stem cells (ESCs), including the unlimited proliferative potential and the ability to differentiate into all cell types of the body.

In this article, we obtained iPS cells from patients with familial forms of *SOD1*-mediated ALS by reprogramming primary skin fibroblasts using ectopic expression of four transcription factors Oct3/4, Sox2, c-Myc, and Klf4. These iPSC lines have been characterized, and the protocol of their differentiation into motor neurons has been developed.

## EXPERIMENTAL

### Primary Fibroblast Culture

Skin biopsies were plated under glass coverslips in Petri dishes (Greiner Bio-One) coated with 0.1% gelatin (Sigma) and cultured in Dulbecco's modified Eagle medium (DMEM) (PanEco) supplemented with 10% fetal bovine serum (FBS) (Hyclone), 1% nonessential amino acids (Invitrogen), 2 mM L-glutamine (Invitrogen), 50 units/mL penicillin and 50 μg/mL streptomycin (PanEco), and 4 ng/ml hrbFGF (PeproTech) (fibroblast medium). At approximately day 14$^{th}$ the confluent cell monolayer was formed, and cells were passaged with 0.25% trypsin (Hyclone). For cryoconservation, fibroblast cells were frozen in DMEM with 20% FBS and 10% dimethyl sulfoxide (DMSO).

### Cell Culture

Primary dermal fibroblasts were cultured as described above. Phoenix retroviral packaging cells were cultured in DMEM with 5 % heat-inactivated (56°C) fetal bovine serum, 2 mM L-glutamine, 50 units/mL penicillin and 50 μg/mL streptomycin in Petri dishes coated with 0.1% gelatin. iPS cell lines were cultured in mTeSR1 medium (STEMCELL Technologies) in Petri dishes coated with Matrigel (BD). All cell lines were incubated at 5% $CO_2$ and 37°C.

### Recombinant Lentiviruses Production

For the production of recombinant lentiviruses, a Phoenix packaging cell line was transfected with the lentiviral vectors encoding the reprogramming factors LeGO-hOct3/4, LeGO-hSox2, LeGO-hKlf4, LeGO-hc-Myc as previously described [18].

### Transfection of Fibroblasts and iPS Cells Generation

Fibroblasts were reprogrammed by the non-integrating method using a CytoTune-iPS Sendai Reprogramming Kit (Invitrogen) according to the manufacturer's instructions.

To reprogram the cells by recombinant lentivirus particles, the fibroblasts at passage 1-2 were seeded at a density of 1 x $10^5$ per well of a 6-well plate (Greiner Bio-One) and incubated overnight in the fibroblast medium. The next day, the fibroblast medium was replaced with the fresh medium containing 8 mg/mL of polybrene (Sigma) and incubated for an hour. Then, the cells were incubated with virus-containing supernatants (MOI 5 for each lentivirus). The medium was changed every other day. Five days after transfection, the cells were passaged with 0.25% trypsin to mitomycin C-treated (10 μg/ml, Sigma) mouse embryonic fibroblasts (MEF) on 100-mm Petri dishes coated with 0.1 % gelatin. On the sixth day, the fibroblast medium was replaced with the human ESCs culture medium of the following composition: DMEM/F12 (1:1) (PanEco), 20% Knockout Serum Replacement (KO SR, Invitrogen), 1% nonessential amino acids, 1 mM L-glutamine, 50 units/ml penicillin, 50 μg/ml streptomycin, 0.1 mM beta-mercaptoethanol (Sigma), 4 ng/ml hrbFGF containing 1 μM BIX-01294, inhibitor of histone methyltransferase G9a (Sigma), and 1 μM valproic acid, histone deacetylase (HDAC) inhibitor (Sigma). The medium was changed every day. BIX-01294 and valproic acid were added to the me-

dium for 7 days. Clones which were morphologically indistinguishable from ES cells were manually selected and cultivated in a mTeSR1 medium in Matrigel-covered cell culture dishes.

### Visualization of endogenous alkaline phosphatase activity

The culture medium was aspirated, and the cells were washed twice with a buffer solution containing 100 mM Tris-HCl, 100 mM NaCl, 5 mM MgCl2, and 0.05% Tween-20, pH 9.5. Then, the buffer was aspirated and the working solution supplemented with 0.02% BCIP, 0.03% NBT in 0.1 M TBS (Tris-Buffered Saline), pH 9.5, was added. The cells were incubated for 30 min at room temperature, washed twice with the buffer solution, and positively stained clones were counted by light microscopy.

### Karyotyping and immunostaining

Metaphase Chromosome Spread Preparations of iPSC lines and the immunostaining of cells were performed as previously described [17].

The following primary antibodies were used: mouse monoclonal antibody against SSEA-4 (1:100), TRA-1-60 (1:100), TRA-1-81 (1:50) (Cell Signaling Technology), HB9 (1:50, Developmental Hybridoma Bank or DSHB), βIII-tubulin, GFAP (1:500, Abcam), and vimentin (1:200, Daco); rabbit monoclonal antibody against Nanog (1:200), Oct4 (1:300), Sox2 (1:400) (Cell Signaling Technology), rabbit polyclonal antibody against ChAT, beta-tubulin, GFAP (1:500, Abcam), alpha-fetoprotein (1:400, Dako). The secondary antibodies included Alexa Fluor 555 goat anti-rabbit IgG (1:700, Invitrogen) and Alexa Fluor 488 goat anti-mouse IgG (1:500, Invitrogen).

The nuclei were counterstained with DAPI. The preparations were analyzed with an Axio Imager A1 epi-fluorescence microscope (Carl Zeiss). Pseudo color images of the micro-objects were obtained using the AxioVision software (Carl Zeiss).

### Formation of the embryoid bodies and their differentiation *in vitro*

Spontaneous differentiation of pluripotent cells was induced as previously described [18].

### Neuronal differentiation

The differentiation protocol, with some modifications, was used [19] to prepare motor neurons *in vitro*. Embryoid bodies were prepared using an AggreWell 400 Plate (STEMCELL Technologies) in DMEM/F12 medium supplemented with 5% KO SR, 1% nonessential amino acids, 2 mM L-glutamine, 50 units/ ml penicillin, 50 μg/ml streptomycin, 0.1 mM beta-mercaptoethanol, 200 ng/ml recombinant human Noggin protein (Biological Industries), and 2 μM SB431542 (Stemgent) for 12 days. Afterwards, embryoid bodies were cultured for a additional 10 days in Neurobasal Medium (Gibco) with 2 mM L-glutamine, B27 (Gibco), 1 μM retinoic acid, 200 ng/ml recombinant human Sonic hedgehog (PeproTech), 10 ng hrbFGF, and then transferred to Matrigel-coated Petri dishes with Neurobasal Medium containing 2 mM L-glutamine, 10 ng/ml BDNF, and 10 ng/ml GDNF (all from PeproTech) and cultured for another 14 days. Adherent cell colonies were treated with Accutase (Sigma) to dissociate them into single cells and cultured in Matrigel-coated Petri dishes for 5 days, after which the immunostaining was performed.

The directed differentiation of iPS cells into functional astrocytes was performed as described above [20].

## RESULTS AND DISCUSSION

### Genetic reprogramming of the skin fibroblasts of patients with familial ALS

Skin biopsies of patients with ALS-characterized forms were provided by the Research Center of Neurology, RAMS. Homogeneous cultures of primary skin fibroblasts were obtained from these biopsy materials. The migration of fibroblasts occurred within two weeks prior to the formation of the first cell monolayer. No later than after 1–2 passages, the primary fibroblasts were transfected using lentiviral or recombinant Sendai virus-based delivery systems by four transcription factors: Oct3/4, Sox2, c-Myc, and Klf4. To increase efficiency of reprogramming, a methyltransferase inhibitor (BIX-01294) [21] and a histone deacetylase inhibitor (valproic acid) [22] were added to the culture medium. The induction of pluripotency in somatic cells is accompanied by a cascade of epigenetic events, including methylation of the gene promoters expressed in the differentiated cell types, hypomethylation of promoters and activation of pluripotency genes, as well as global chromatin changes and reactivation of a somatically silenced X chromosome [17]. Starting on day 11 after transduction, compact colonies, consisting of actively growing cells with an increased nucleus/cytoplasm ratio compared to the primary fibroblast culture (*Fig. 1A, B*), were formed. Since these cell colonies were morphologically similar to ESCs, we held the mechanical selection of individual colonies to produce stable iPSC lines (*Fig. 1C*). Staining for alkaline phosphatase (whose activity is elevated in pluripotent cells [23]) showed that the reprogramming efficiency increased 10-fold when the lentiviral gene delivery system was used (0.77 ± 0.025%), as compared with the recombinant Sendai virus delivery technique (0.083 ± 0.006%) (*Fig. 1D, E, F*). Moreover, the stabilization of the pluripotent state using the Sendai virus-based method in the ob-

Table. Comparison of short tandem repeat (STR) profiles for the primary skin fibroblasts (PSF) of patients with familial ALS and isolated iPSC lines

| STR-marker | PSF1 | iPSC1.2 | PSF2 | iPSC2.2 |
|---|---|---|---|---|
| AMEL | X Y | X Y | X X | X X |
| CSF1PO | 10 14 | 10 14 | 10 12 | 10 12 |
| D10S1248 | 13 14 | 13 14 | 14 15 | 14 15 |
| D12S391 | 16 23 | 16 23 | 20 23 | 20 23 |
| D13S317 | 11 12 | 11 12 | 11 11 | 11 11 |
| D16S539 | 12 12 | 12 12 | 11 13 | 11 13 |
| D18S51 | 15 15 | 15 15 | 13 14 | 13 14 |
| D1S1656 | 13 17.3 | 13 17.3 | 12 16.3 | 12 16.3 |
| D22S1045 | 15 16 | 15 16 | 15 16 | 15 16 |
| D2S441 | 10 13 | 10 13 | 11 14 | 11 14 |
| D3S1358 | 15 16 | 15 16 | 17 18 | 17 18 |
| D5S818 | 11 11 | 11 11 | 12 13 | 12 13 |
| D7S820 | 9 11 | 9 11 | 10 12 | 10 12 |
| D8S1179 | 13 14 | 13 14 | 14 15 | 14 15 |
| FGA | 21 23 | 21 23 | 21 21 | 21 21 |
| SE33 | 16 30.2 | 16 30.2 | 26.2 26.2 | 26.2 26.2 |
| TH01 | 9 9.3 | 9 9.3 | 6 9.3 | 6 9.3 |
| TPOX | 9 11 | 9 11 | 8 8 | 8 8 |
| vWA | 17 18 | 17 18 | 17 18 | 17 18 |

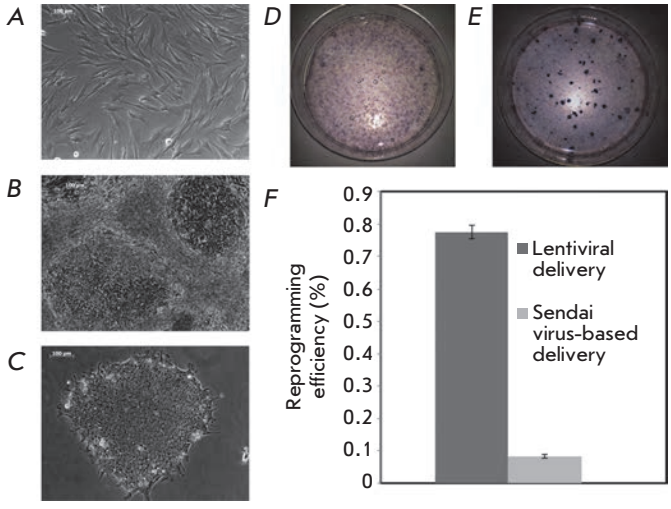


Fig. 1. Generation of stable iPSC lines from the primary skin fibroblasts of patients with familial ALS. A – primary culture of skin fibroblasts; B – formation of iPS cell colonies after introduction of reprogramming genes (day 15); C – mechanically picked iPSC colony in feeder-free culture conditions; D, E – visualization of iPS colonies obtained with lentiviral (D) and Sendai virus-based systems (E) by alkaline phosphatase staining; F – comparison of the efficiency of two reprogramming systems

tained transgene-free iPSC lines occurred gradually, over several passages, and it was accompanied by a high percentage of spontaneously differentiated cells (data not shown). Nevertheless, the use of the transgene-free delivery method allowed us to obtain genetically unmodified pluripotent stem cells for each patient. That is very important both for cell replacement therapy and for studying disease pathogenesis, since transgene integration into active chromatin sites may lead to changes in gene expression.

### Characteristics of patient-specific iPSC lines

According to immunocytochemistry results, iPSC lines expressed both ESC-specific surface antigens (SSEA-4, TRA-1-60, TRA-1-81) and the nuclear transcription factors associated with pluripotency (Nanog, Oct4, Sox2) (*Fig. 2A-I*). The GTG-banding of iPSC lines revealed no changes in the number and structure of chromosomes during reprogramming (*Fig. 2J*). In order to determine the ability of iPS cells to differentiate into all three germ layers, the analyzed lines were placed in the suspension culture, where they formed embryoid bodies. On day 14 after cultivation, embryoid bodies were transferred to gelatin-coated culture dishes for adhesion and following cell migration. The adherent cells showed various types of morphologies; immunocytochemistry revealed cells positive for βIII-tubulin (a marker of ectoderm), vimentin (mesoderm), and α-fetoprotein (AFP, endoderm) (*Fig. 3*).

To confirm the fact that isolated iPSCs were derived from the patient's skin fibroblasts, we checked their short tandem repeat (STR) profiles. We found that the patterns of 18 STRs (*Table*) were completely matched between isolated iPSCs and primary skin fibroblasts. Additionally, *SOD1* gene mutations different for each patient were detected in iPS cell lines (*Fig. 2K, L*).

Thus, according to cell morphology, pluripotency markers expression and the ability to differentiate into derivatives of three germ layers, the iPS cells derived from the fibroblasts of the patients with SOD1-associated ALS were pluripotent cells.

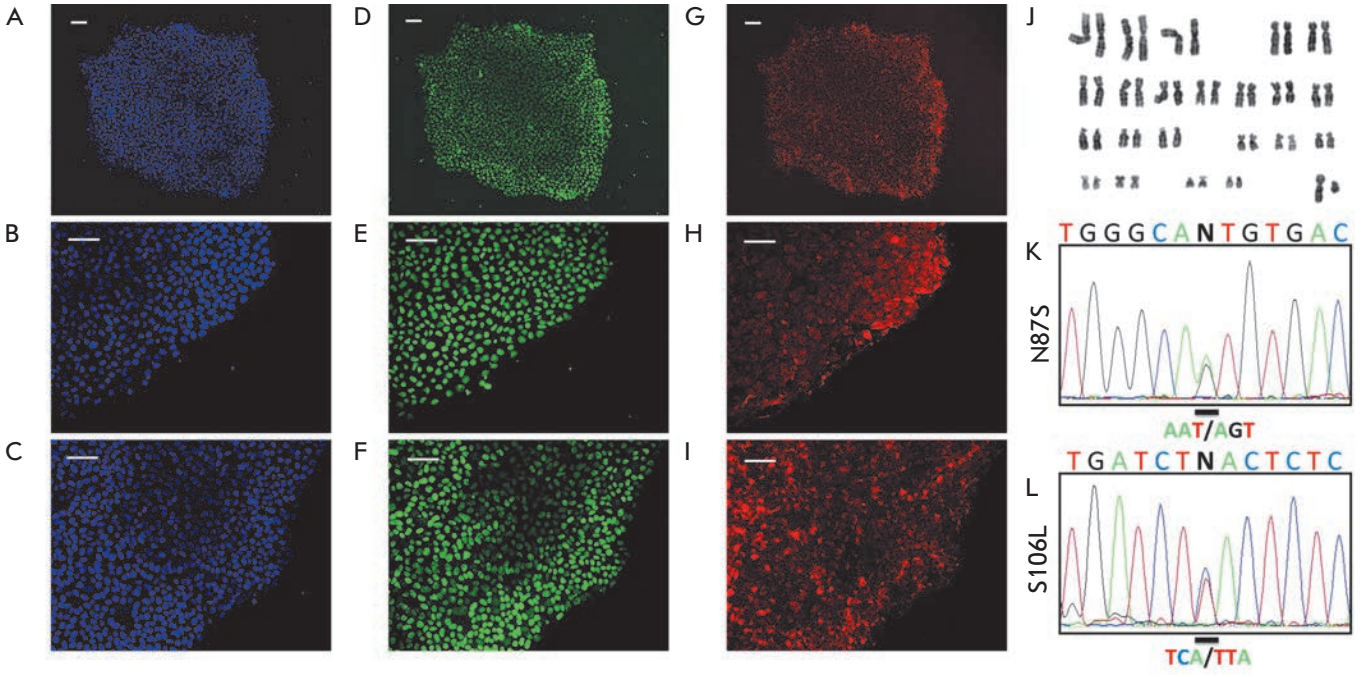


Fig. 2. Characterization of patient-specific iPS lines. A–I – immunofluorescent analysis of the expression of pluripotency markers, including the transcription factors Oct3/4 (D), Sox2 (E), Nanog (F), and surface antigens SSEA4 (G), Tra-1-60 (H), Tra-1-81 (I). DAPI staining indicating the total cell count per field (A, B, C); J – karyotype of iPSC lines, GTG-banding; K, L – nucleotide sequences with mutations in the *SOD1* gene

## Generation of motor neurons from the SOD1 mutant of iPS cells

As previously reported, the death of motor neurons in ALS patients might be a non-cell-autonomous process but depends on the cellular microenvironment [3, 14]. Therefore, our next aim was to develop protocols for the differentiation of iPSCs into motor neurons and astrocytes. Previously, it was shown *in vivo* that during development, motor neurons are forming by the exposure of rostral neural progenitors to two consecutive signals: retinoic acid (caudalization) and Sonic hedgehog (ventralization) [24]. These rostral neural progenitors were obtained from embryoid bodies suspension by inhibiting the Smad signaling pathway. The direct differentiation of iPSCs into motor neurons was performed 12 days later by adding retinoic acid (RA) and recombinant Sonic hedgehog (Shh) to the culture medium. After dissociation of neurospheres to single-cell suspension, neuronal precursors were transferred on Matrigel-coated dishes and cultivated as an adherent culture. These cells express the common neuronal marker βIII-tubulin, proving that the obtained cells are of neuronal origin (*Fig. 4A–C*). In the last step, maturation of motor neurons occurred under the influence of neurotrophic growth factors, such as the brain-derived neurotrophic factor (BDNF) and glial cell line-derived neurotrophic factor (GDNF). Immunocytochemical staining of these cultures showed that βIII-tubulin-positive neurons co-expressed markers such as Hb9 (MNX1, motor neuron-specific transcription factor) and ChAT (choline acetyltransferase) (*Fig. 4D–I*). Thus, patient-specific iPSC lines are capable of

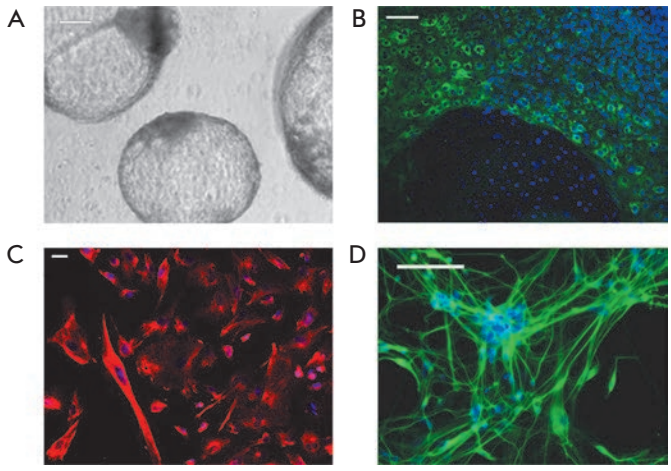


Fig. 3. Spontaneous differentiation of iPS cells into three germ layers. A – representative image of embryoid bodies; B, C, D – immunocytochemical staining of α-fetoprotein (B), vimentin (C), βIII-tubulin (D). Cell nuclei stained with DAPI (blue)

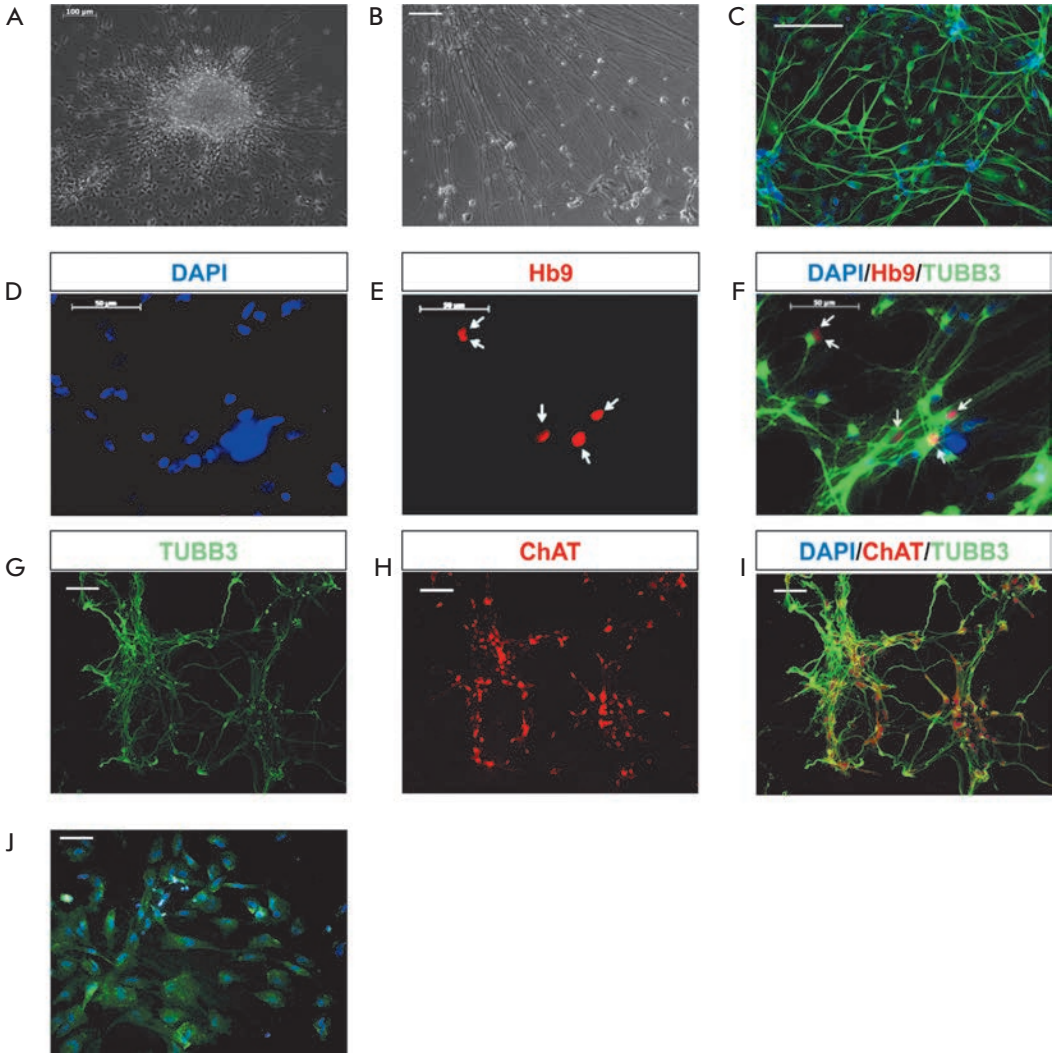


Fig. 4. Neuronal differentiation of ALS patient-specific iPS cells. A, B – representative images of differentiated neuron-like cells; C – immunocytochemical staining of βIII-tubulin-positive cells; D–I – cells stained for the motor neuron markers Hb9 (E, F) and ChAT (H, I); J – detection of GFAP in iPSC-derived astrocytes. Cell nuclei stained with DAPI (blue)

direct differentiation into motor neurons, which are affected during ALS.

Additionally, when using iPSC lines for astroglial differentiation, we identified the cells expressing a specific astrocyte marker (GFAP) (*Fig. 4J*); their toxic effect was displayed in ALS pathology.

Thus, patient-specific iPS lines have an advantage over other published models [25], since these cells are genetically identical to primary patient cells and, potentially, might most accurately reproduce the molecular events taking place in the development of ALS. In addition, cultivation of these iPSC lines under specified conditions (such as the presence of the mTeSR1 medium) allows us to maintain their pluripotent state for a stable and unlimited production of motor neurons.

## CONCLUSIONS

We have obtained iPSC lines from patients with SOD1-associated ALS. The reprogramming efficiency with the lentiviral gene delivery system was at least 10-fold higher than that with the recombinant Sendai virus-based system. These iPSC lines with mutations in the *SOD1* gene are pluripotent and capable of directed differentiation into motor neurons. ●

*This work was supported by the Russian Foundation for Basic Research (grant № 12-04-32018).*

REFERENCES

1. Frey D., Schneider C., Xu L., Borg J., Spooren W., Caroni P. // J. Neurosci. 2000. V. 20. P. 2534–2542.
2. Liu J., Lillo C., Jonsson P.A., Vande Velde C., Ward C.M., Miller T.M., Subramaniam J.R., Rothstein J.D., Marklund S., Andersen P.M., et al. // Neuron. 2004. V. 43. P. 5–17.
3. Boillee S., Yamanaka K., Lobsiger C.S., Copeland N.G., Jenkins N.A., Kassiotis G., Kollias G., Cleveland D.W. // Science. 2006. V. 312. P. 1389–1392.
4. Wong P.C., Pardo C.A., Borchelt D.R., Lee M.K., Copeland N.G., Jenkins N.A., Sisodia S.S., Cleveland D.W., Price D.L. // Neuron. 1995. V. 14. P. 1105–1116.

5. Howland D.S., Liu J., She Y., Goad B., Maragakis N.J., Kim B., Erickson J., Kulik J., DeVito L., Psaltis G., et al. // Proc. Natl. Acad. Sci. USA. 2002. V. 99. P. 1604–1609.
6. Bruijn L.I., Becher M.W., Lee M.K., Anderson K.L., Jenkins N.A., Copeland N.G., Sisodia S.S., Rothstein J.D., Borchelt D.R., Price D.L., et al. // Neuron. 1997. V. 18. P. 327–338.
7. Jonsson P.A., Ernhill K., Andersen P.M., Bergemalm D., Brannstrom T., Gredal O., Nilsson P., Marklund S.L. // Brain. 2004. V. 127. P. 73–88.
8. Reaume A.G., Elliott J.L., Hoffman E.K., Kowall N.W., Ferrante R.J., Siwek D.R., Wilcox H.M., Flood D.G., Beal M.F., Brown R.H. Jr., et al. // Nat. Genet. 1996. V. 13. P. 43–47.
9. Subramaniam J.R., Lyons W.E., Liu J., Bartnikas T.B., Rothstein J., Price D.L., Cleveland D.W., Gitlin J.D., Wong P.C. // Nat. Neurosci. 2002. V. 5. № 4. P. 301-307.
10. Wang J., Slunt H., Gonzales V., Fromholt D., Coonfield M., Copeland N.G., Jenkins N.A., Borchelt D.R. // Hum. Mol. Genet. 2003. V. 12. P. 2753–2764.
11. Kabashi E., Valdmanis P.N., Dion P., Rouleau G.A. // Ann. Neurol. 2007. V. 62. № 6. P. 553-559.
12. Gruzman A., Wood W.L., Alpert E., Prasad M.D., Miller R.G., Rothstein J.D., Bowser R., Hamilton R., Wood T.D., Cleveland D.W., et al. // Proc. Natl. Acad. Sci. USA. 2007. V. 104. P. 12524-12529.
13. Pramatarova A., Laganiere J., Roussel J., Brisebois K., Rouleauet G.A. // J. Neurosci. 2001. V. 21. P. 3369–3374.
14. Nagai M., Re D.B., Nagata T., Chalazonitis A., Jessell T.M., Wichterle H., Przedborski S. // Nat. Neurosci. 2007. V. 10. P. 615– 622.
15. Takahashi K., Tanabe K., Ohnuki M., Narita M., Ichisaka T., Tomoda K., Yamanaka S. // Cell. 2007. V. 131. № 5. P. 861-872.
16. Shutova M.V., Bogomazova A.N., Lagarkova M.A., Kiselev S.L. // Acta Naturae. 2009. V. 1. № 2. P. 91-92.
17. Lagarkova M.A., Shutova M.V., Bogomazova A.N., Vassina E.M., Glazov E.A., Zhang P., Rizvanov A.A., Chestkov I.V., Kiselev S.L. // Cell Cycle. 2010. V. 9. 937–946.
18. Shutova M.V., Chestkov I.V., Bogomazova A.N., Lagarkova M.A., Kiselev S.L. // Springer Protocols Handbook ser. 2012. P. 133–149.
19. Egawa N., Kitaoka S., Tsukita K., Naitoh M., Takahashi K., Yamamoto T., Adachi F., Kondo T., Okita K., Asaka I., et al. // Sci. Transl. Med. 2012. V. 4. № 145. P. 145.
20. Krencik R., Zhang S.C. // Nat. Protoc. 2011. V. 6. № 11. 1710-1717.
21. Shi Y., Desponts C., Do J.T., Hahm H.S., Scholer H.R., Ding S. // Cell Stem Cell. 2008. V. 3. P. 568–574.
22. Huangfu D., Maehr R., Guo W., Eijkelenboom A., Snitow M., Chen A.E., Melton D.A. // Nat. Biotechnol. 2008. V. 26. P. 795–797.
23. Hanna J., Markoulaki S., Schorderet P., Carey B.W., Beard C., Wernig M., Creyghton M.P., Steine E.J., Cassady J. P., Foreman R., et al. // Cell. 2008. V. 133. № 2. P. 250-264.
24. Wichterle H., Lieberam I., Porter J.A., Jessell T.M. // Cell. 2002. V. 110. № 3. P. 385-397.
25. Dimos J.T., Rodolfa K.T., Niakan K.K., Weisenthal L.M., Mitsumoto H., Chung W., Croft G.F., Saphier G., Leibel R., Goland R., et al. // Science. 2008. V. 321. № 5893. P. 1218-1221.

# Fusion to the Lysosome Targeting Signal of the Invariant Chain Alters the Processing and Enhances the Immunogenicity of HIV-1 Reverse Transcriptase

E. S. Starodubova[1,2*], M. G. Isaguliants[2,3], Y. V. Kuzmenko[1], A. A. Latanova[1], O. A. Krotova[1,2], V. L. Karpov[1]

[1]Engelhardt Institute of Molecular Biology Russian Academy of Sciences, Vaviolva str., 32, 119991, Moscow, Russia

[2]D.I. Ivanovsky Institute of Virology, Ministry of Health of the Russian Federation, 123098, Moscow, Russia

[3]Department of Microbiology, Tumor and Cell Biology, Karolinska Institutet, 17177, Stockholm, Sweden

*E-mail: estarodubova@yandex.ru

Received 24.07.2013



**ABSTRACT** **Intracellular processing of the antigen encoded by a DNA vaccine is one of the key steps in generating an immune response. Immunization with DNA constructs targeted to the endosomal-lysosomal compartments and to the MHC class II pathway can elicit a strong immune response. Herein, the weakly immunogenic reverse transcriptase of HIV-1 was fused to the minimal lysosomal targeting motif of the human MHC class II invariant chain. The motif fused to the N-terminus shifted the enzyme intracellular localization and accelerated its degradation. Degradation of the chimeric protein occurred predominantly in the lysosomal compartment. BALB/c mice immunized with the plasmid encoding the chimeric protein demonstrated an enhanced immune response, in the form of an increased antigen-specific production of Th1 cytokines, INF-γ and IL-2, by mouse splenocytes. Moreover, the majority of the splenocytes secreted both cytokines; i.e., were polyfunctional. These findings suggest that retargeting of the antigen to the lysosomes enhances the immune response to DNA vaccine candidates with low intrinsic immunogenicity.**

**KEYWORDS** **reverse transcriptase; invariant chain; antigen processing; DNA immunization; T-helper immune response.**

**ABBREVIATIONS** **HIV – Human immunodeficiency virus; MHC – major histocompatibility complex; ER – endoplasmic reticulum; Ii – MHC class II-associated invariant chain; IFN-γ – interferon-gamma; IL-2 – Interleukin 2; RT – reverse transcriptase.**

## INTRODUCTION

DNA vaccine-encoded antigens are synthesized in the cellular cytoplasm, processed mainly by proteasomes, and presented on the cell membrane through MHC class I molecules that are recognized by cytotoxic CD8+ T-lymphocytes [1]. At the same time, plasmid DNA-injected mice require MHC class II-dependent activation of CD4+ T-cells to mount a strong immune response [2, 3]. There are now techniques for enhancing the efficacy of DNA vaccines aimed at increasing CD4+ T-cell involvement in the antigen-driven immune response [4, 5]. One of such techniques is based on an enhanced presentation of the plasmid-encoded antigens in the context of MHC class II molecules. The antigenic peptides to be presented on the MHC class II molecules are generated through the lysosomal proteolysis [6]. Antigen presentation by MHC class II molecules can be artificially enhanced by incorporation into the antigen of the lysosomal targeting motives [7].

MHC class II molecules are transported to the lysosomes in association with the invariant chain (Ii) bearing the lysosome-targeting sequence at the N-terminus [6]. The signal peptide is located at the N-terminus (amino acid residues 1–30), with Leu7, Ile8, Pro15, Met16, and Leu17 being the most important residues in the functional context [8–10]. It has been shown that fusion of pro-

teins with this signal sequence promotes their transport to the lysosomes [11–15]. In this work, we constructed a plasmid encoding HIV-1 reverse transcriptase (RT) of HIV-1 fused to the human MHC class II invariant chain in order to alter RT processing and enhance its immunogenicity, which was reported to be poor [16, 17]. The incorporation of the invariant chain motif shifted the localization of RT towards the lysosomal compartment and increased the rate of its degradation by lysosomal proteases, which led to the augmentation of the immunogenicity of the RT gene in mice.

## EXPERIMENTAL

### Cloning of DNA constructs

Plasmid pKCMV2RT encoding the HIV-1 HXB2 Reverse Transcriptase (RT) was generated by recloning the *RT* gene from pCMVRT into the pKCMV plasmid vector using *SalI* and *EcoRI* restriction sites [18] [19]. RT-encoding fragment contained in pCMVRT was amplified by PCR with Pfu-polymerase (Fermentas, Lithuania) using the following primers: RT-SalI-BsiWI-F (5'-tcaggtcgactgaacgtacgatgcccattagccctattg-3') and RT-BamHI-EcoRI-R (5'-agtagaattcatgtggatccctagagcactttcctgattccagc-3').

Plasmid pKCMV2RT-Ii encoding RT fused N-terminally to the human MHC class II invariant chain was designed step-wise from pKCMV2RT. For this, the nucleotide sequence of the human MHC class II invariant chain motif (NM_001025159.1) was generated using synthetic oligonucleotides (Sintol, Russia). The first step involved annealing of the oligonucleotides IC_1–45 (corresponding to the positions 1 to 45 of the invariant chain gene (5'-atggatgaccagcgcgaccttatctccaacaatgagcaactgccc-3')), IC_46–90 (phosphorylated at the 5'-end and corresponding to the positions 46–90 (5'-atgctgggcc ggcgccctggggccccggagagcaagtgcagccgc-3')) and IC-mid (corresponding to the positions 37 to 71 of the reverse sequence (5'-ggcgccggcccagcatgggcagttgctcattgttg-3')), followed by ligation of a single-stranded break between IC_1–45 and IC_46–90. In the second step, the double-stranded fragment served as a template for PCR. PCR was carried out with Pfu polymerase and IC-F (5'-atccgtcgacatggatgaccagcgcgacc-3') and IC-R (5'-tgcgcgtacggcggctgcacttgctctc-3') primers bearing the SalI and BsiWI restriction sites, respectively. Finally, the amplified PCR fragment was cloned into pKCMV2RT at the 5'-end of the *RT* gene, using the SalI and BsiWI sites. This produced an in-frame fusion between Ii and RT. The nucleotide sequence of the cloned fragment was verified by DNA sequencing.

The plasmids used to immunize animals were purified using Plasmid EndoFree kits (QIAGEN, Germany) following the manufacturer's instructions.

### Preparation and transfection of cell cultures

Cervical adenocarcinoma cells (HeLa) were cultured in a DMEM medium (PanEko, Russia) containing 10% fetal bovine serum and a mixture of 100 U/ml penicillin and 100 μl/ml streptomycin. Cells were transfected with plasmids using Lipofectamine LTX (Invitrogen, USA) according to the manufacturer's manual.

### Quantification of the fusion protein in the transfected cells

The level of expression of RT variants in the transfected cells were evaluated by immunoblotting. Two days posttransfection, the cells were lysed in a RIPA buffer (10 mm Tris-HCl pH 7.5, 150 mM NaCl, 1% sodium deoxycholate, 1% Triton X-100, 0.1% SDS, 1 mM EDTA). Lysates normalized to the protein content were run on a 10% polyacrylamide gel (PAGE) under denaturing conditions and transferred onto the nitrocellulose membrane (BioRad, USA). To block nonspecific binding sites, the membranes were incubated overnight at 4°C in a PBS-T buffer (80 mM $Na_2HPO_4$, 20 mM $NaH_2PO_4$, 100 mM NaCl, 0.1% Tween-20) supplemented with 5% non-fat milk, followed by incubation with rabbit anti-RT polyclonal antibodies diluted a 1/5000 [20] followed by incubation with the horseradish peroxidase-conjugated goat anti-rabbit IgG antibodies (Jackson, USA) diluted 1/5000. Further, the blots were stripped and re-probed with mouse anti-beta-actin monoclonal antibodies (Sigma, USA) diluted 1/5000 followed by the horseradish peroxidase-conjugated goat anti-mouse antibodies (Jackson, USA) diluted 1/5000. Specific bands on the blots were visualized using a chemiluminescence detection kit (ECL™ plus; Amersham Pharmacia Biotech., USA); the emission from the blots was registered on X-ray films (Fuji Film, Japan). The films were scanned, and the signals were quantified with the ImageJ software (http://rsb.info.nih.gov/ij).

### Half-life of the fusion protein in transfected cells

The half-life of the fusion protein was evaluated by cycloheximide chase assay as described [21]; the technique had been previously used to estimate the half-life of RT [22]. Two days posttransfection, the cells were mixed with cycloheximide (Sigma, USA) at 100 μg/ml and incubated for 0, 2 and 4 h. After incubation, cells were lysed, lysates were normalized with respect to the protein content and resolved by electrophoresis in 10% SDS-PAAG followed by Western blotting (see section above). The RT content was quantified as described above.

The half-life of RT was determined using the standard half-life equation $N = N_0 \times 2^{t/T}$, where $N_0$ is the initial protein quantity, $N$ is the amount of protein at time $t$, and $T$ is the half-life of the protein.

### Inhibition of proteasomal and lysosomal proteolysis in cell culture

The proteasomal inhibitors MG132 and epoxomicin (Calbiochem, USA) were used at concentrations of 5 and 0.1 μM, respectively. The activity of the lysosomal proteases was inhibited by chloroquine (Sigma, USA) at a concentration of 100 μM. Inhibitors were added to the cell culture 24 h posttransfection. The cells were co-cultured with inhibitors for an additional 18 h and then lysed and tested for the presence of the target proteins by immunoblotting.

### Immunostaining of cells

HeLa cells were grown and transfected on 20 × 20 mm glass cover slips in 6-well plates. At day 2 posttransfection, the cells were fixed with a mixture of acetone-methanol (1 : 1) for 1 h at −20°C. Fixed cells were incubated in a PBS buffer for 30 min at room temperature, followed by sequential incubations with rabbit anti-RT polyclonal antibodies [20] diluted 1/100, swine anti-rabbit IG antibodies conjugated to TRITC (Dako, Denmark) diluted 1/50, and anti-human lysosomal-associated membrane protein 1 monoclonal antibodies (LAMP1, also known as CD107a) conjugated to FITC (BD Pharmingen, USA) diluted 1/50. All antibodies were diluted in PBS containing 0.5% Tween-20 and 2% bovine serum albumin (BSA). After each incubation, cells were washed three times with PBS. Finally, nuclei were stained for 1 min with 150 mM DAPI (4,6-Diamidino-2-phenylindole, dihydrochloride; Invitrogen, USA). The cover slips were mounted on the glass slides in Vectashield (Vector Laboratories, USA) and viewed under a Leica TCS5 laser confocal microscope (Leica, Germany).

### DNA immunization of mice

Immunization was performed in BALB/c female mice (8-weeks; Charles River Laboratories, Sandhofer, Germany). Groups of 3-4 mice received plasmids encoding RT-Ii, or RT, or the empty vector. Each mouse received two injections of 10 μg plasmid DNA in 20 μl PBS. Plasmids were injected intradermally with an insulin syringe at the left and right sides of the back near the base of the tail, followed by electroporation of the injected area using DermaVax (Celectis, France) as described [23]. Six days following the first injection, 50 μg of the same plasmid in PBS was administered intramuscularly into the tibialis anterior of the hind limb. At day 28, mice were bled from the tail vein, euthanized and spleens were collected. The immunization experiment was repeated twice.

### FluoroSpot

The spleens of immunized mice were homogenized individually, and splenocytes were recovered [24]. Splenocytes were incubated in RPMI containing protein RT (12.5 μg/ml) [25, 26], or peptides representing RT amino acids (aa) 375–389 (ITTESIVIWGKTPKF) or aa 528–543 (KEKVYLAWVPAHKGIG) at 10 mg/ml. Stimulation with concanavalin A (ConA; 5 μg/ml) served as a positive, and with medium alone, as a negative control. After a 20-h incubation with specific and control antigens, splenocytes were assessed for the level of production of IFN-γ and IL-2. Cytokine secretion was analyzed with the FluoroSpot technique using FluoroSpot plates and a Dual IFN-γ/IL-2 FluoroSpot kit (Mabtech, Sweden) following the manufacturer's instructions. Cytokine-secreting cells were counted on an AID ELISpot reader (Autoimmun Diagnostika GmbH, Germany).

## RESULTS

### Accumulation and cellular localization of the chimeric reverse transcriptase with an in-built fragment of the MHC class II *invariant chain*

To change the processing of HIV-1 reverse transcriptase, we constructed a plasmid encoding a fusion protein composed of the RT sequence N-terminally fused to the lysosome-targeting signal of the invariant chain (Ii) of human MHC class II, which promotes its transport to the lysosomes through the endoplasmic reticulum (ER). To accomplish this, we designed a pKCMV2RT-Ii plasmid carrying the *RT* gene with the 5'-end insert of the nucleotide sequence encoding the 30-amino acid signal sequence of Ii. HeLa cells transfected with this plasmid expressed a 68–70kDa protein consistent with the expected molecular mass of RT-Ii chimera (*Fig. 1, lane 3*).

We had previously shown that in cells transfected with the plasmid encoding reverse transcriptase the encoded protein is uniformly distributed throughout the cytoplasm [27]. In this study, immunostaining of HeLa cells transfected with the plasmid encoding the RT-Ii chimera demonstrated a shift from the diffuse to a vesicular pattern (*Fig. 2*). Such a vesicular pattern is indicative of the invariant chain on the way to the endosomal-lysosomal compartment [28]. Co-staining of the transfected cells with anti-RT antibodies and antibodies against the lysosomal-associated membrane protein 1 (LAMP1, CD107a) restricted to the endosomal-lysosomal compartment revealed almost full overlap of the signals (*Fig. 2, field 4*). These findings suggest the invariant chain-driven transport of RT to the lysosomes.

### Incorporation of the invariant chain sequence alters the degradation of RT

Targeting of reverse transcriptase into lysosomes changes its degradation rate as well as the range of proteases involved in RT degradation. We have previously

shown that RT has a half-life of 18 h [29, 30]. The half-life of the RT-Ii chimera assessed after the translation arrest reduced to 4.5 h (*Fig. 3*). Thus, the fusion of RT to the Ii signal sequence caused a four-fold decrease in the protein half-life.

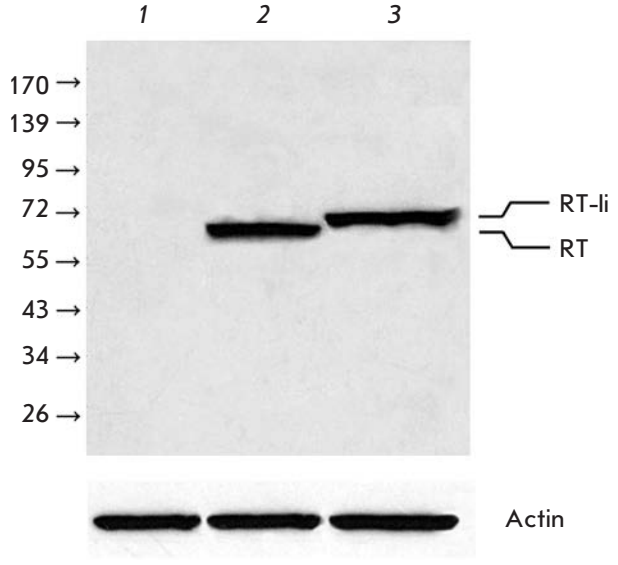


Fig. 1. Accumulation of RT and RT-Ii in HeLa cells. Immunoblotting of the lysates of: non-transfected cells (*1*); cells transfected with pKCMV2RT (*2*) or pKCMV2RT-Ii (*3*). Blots were stained with anti-RT polyclonal antibodies. To normalize the signal to the total protein content of the loaded samples, the membranes were stripped and re-probed with anti-actin antibodies. Position of the protein molecular mass standards (in kDa) is indicated to the left

The role of proteasomal and lysosomal pathways in the processing of the RT-Ii chimera was examined using specific inhibitors. The in-put of proteasome into RT-Ii degradation was assessed with the help of MG132 and epoxomicin; and of lysosome, with the help of chloroquine. The transfected Hela cells were co-cultured with the inhibitors for 18 h and then subjected to immunoblotting to evaluate the accumulation of the protein in comparison with that in the untreated cells (*Fig. 4*). Lysosomal inhibitor chloroquine had no effect on the accumulation of RT but increased the amount of RT-Ii in the cells by more than six-fold (*Fig. 4*). At the same time, RT-Ii, in contrast to RT, appeared to be insensitive to the proteasomal inhibitors (*Fig. 4*).

### Introduction of the lysosomal targeting signal enhances the immunogenicity of RT

BALB/c mice were primed by the intradermal injection of the RT-Ii encoding plasmid, followed by electroporation. Five days after the first injection, they received a boost with the same plasmid by the intramuscular route. The control mice received either a plasmid encoding the parental *RT* gene, or an empty vector. The immune response was assessed by the capacity of murine splenocytes to produce IFN-γ and IL-2 after *in vitro* stimulation with the protein RT or RT-derived peptide representing its immunodominant epitopes at amino acid residues 375–389 and 528–543 [31, 32]. IFN-γ, IL-2, or IFN-γ / IL-2 producing cells were identified with the Fluorospot assay (*Fig. 5*). A specific production of IFN-γ and IL-2 in response to stimulation with the protein or peptide was observed only in mice immunized with the plasmid encoding the RT-Ii chimera. Most of the cells producing IFN-γ also produced IL-2, which demonstrated their polyfunctionality. No

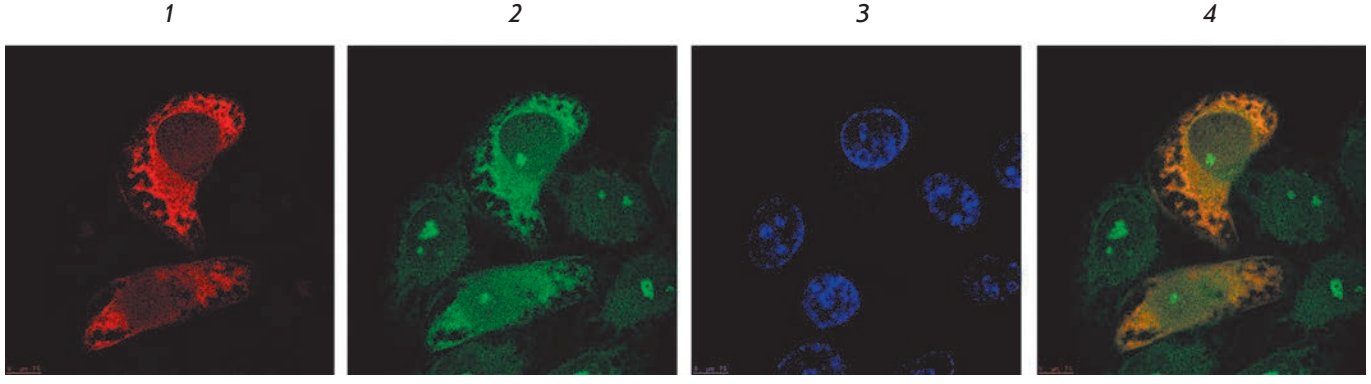


Fig. 2. Intracellular localization of the chimeric RT-Ii. HeLa cells were transfected with the pKCMV2RT-Ii plasmid, fixed and stained with anti-RT polyclonal antibodies and secondary TRITC-conjugated antibodies (*1*), anti-human CD107a monoclonal antibodies conjugated to FITC (*2*), or DAPI (*3*). Superposition of images demonstrating RT-specific and CD107a-specific stainings (*4*)

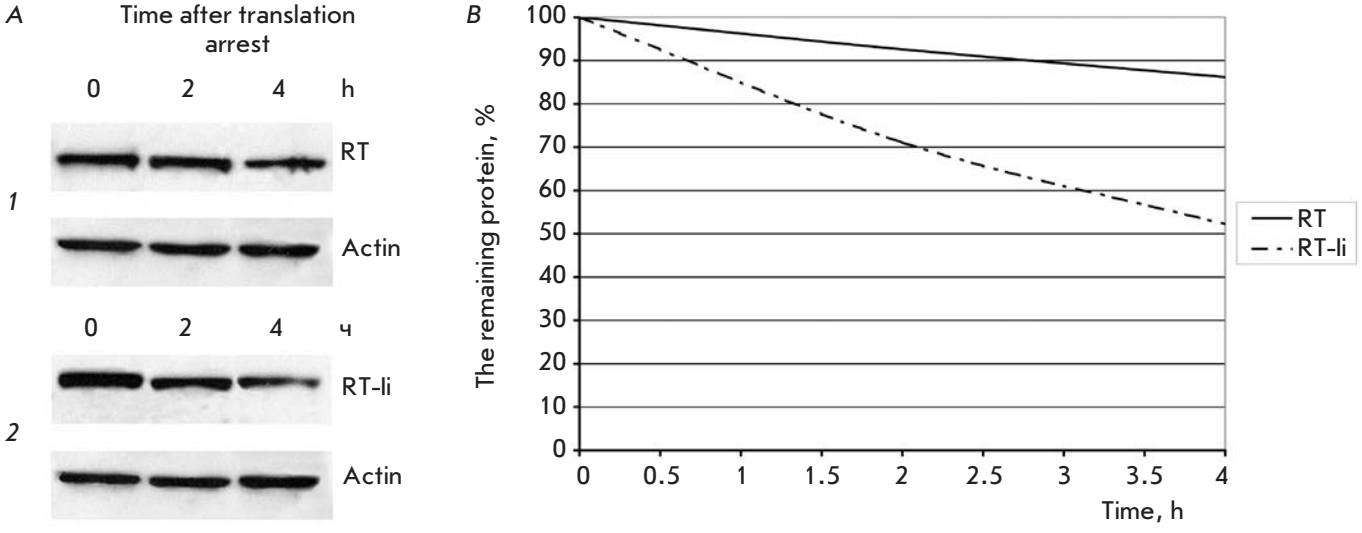


Fig. 3. Comparison of RT and RT-li degradation in the expressing cells. *A* – Immunoblotting of HeLa cells transfected with pKCMV2RT (*1*) and pKCMV2RT-li (*2*) sampled at the given time-points after the addition of cycloheximide (100 μg/ml). Blots were stained with anti-RT polyclonal antibodies. To normalize the signal to the total protein content of the loaded samples, the membranes were stripped and re-probed with anti-actin antibodies. *B* – The kinetics of degradation of RT and RT-li

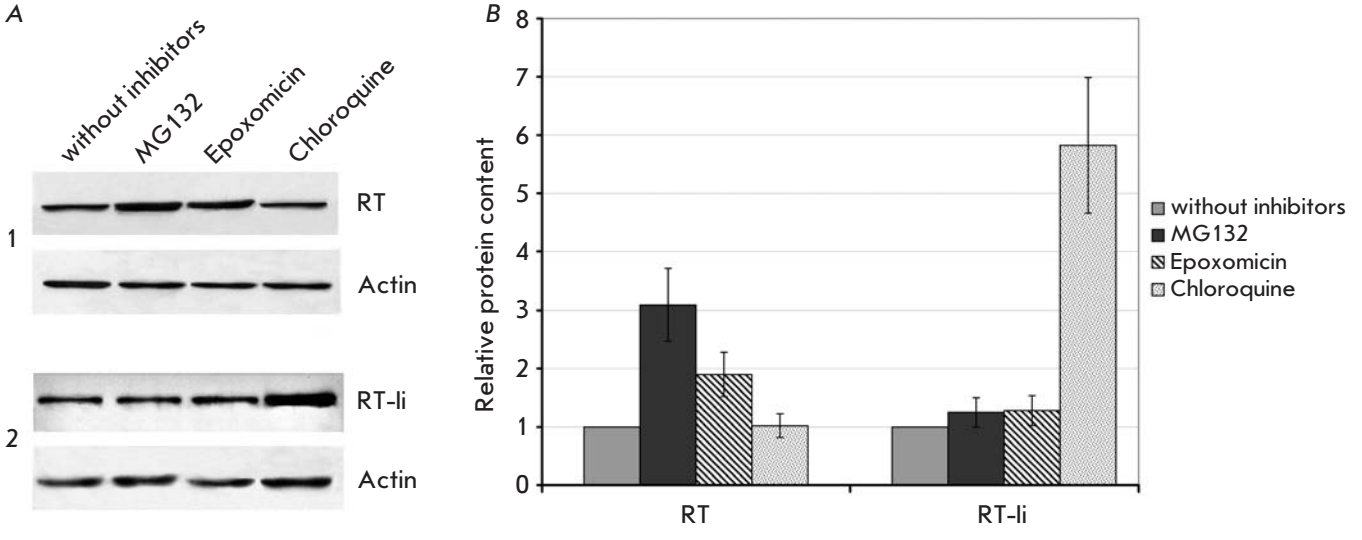


Fig. 4. Accumulation of RT and RT-li following treatment of expressing cells with proteasomal and lysosomal inhibitors. *A* – immunoblotting of HeLa cells transfected with pKCMV2RT (*1*) and pKCMV2RT-li (*2*), after co-culturing for 18 h with MG132 (5 μM), epoximicine (0.1 μM), chloroquine (100 μM), or in the medium alone. Blots were stained with anti-RT antibodies. To normalize the signal to the total protein content of the loaded samples, the membranes were stripped and re-probed with anti-actin antibodies. *B* – The diagram showing the relative content of RT in cells treated with the proteasomal or lysosomal inhibitors as compared to the untreated cells

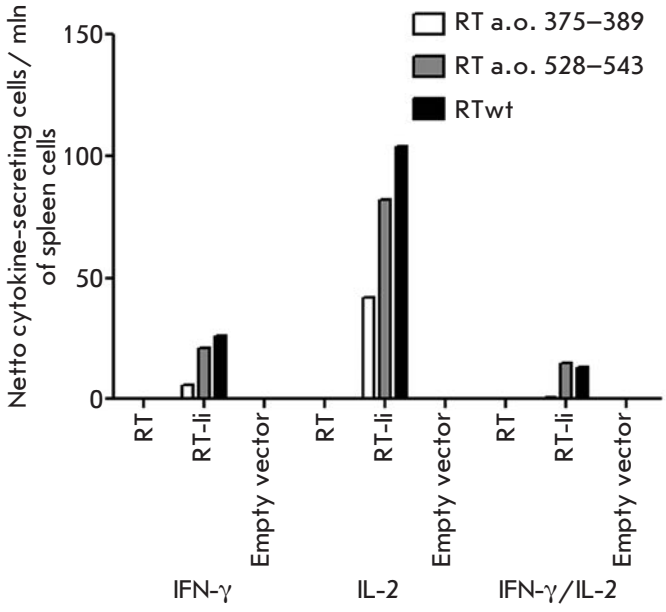


Fig. 5. Immune response of mice immunized with the plasmids encoding RT and RT-Ii. Mice were immunized with the plasmids pKCMV2RT and pKCMV2RT-Ii, encoding RT and RT-Ii, respectively, or an empty vector. After completion of immunization, mice were sacrificed, and their splenocytes were harvested and stimulated with reverse transcriptase (RTwt) or RT-derived peptides (RT 375–389 or RT 528–543). The number of splenocytes producing IFN-γ and IL-2 in response to specific antigen stimulation was assessed by FluoroSpot assay as the average number of signal-forming units (sfu) per mln cells with the background secretion in the media subtracted

specific cytokine production was observed in mice receiving the RT gene or the empty vector (*Fig. 5*).

## DISCUSSION

CD4+ T-cells play an important role in mounting a potent immune response, stimulating both the cellular-(Th1-type CD4+ T-cells) and humoral-(Th2-type) mediated immunity. CD4+ T-cells are activated after recognition by their receptors of the complexes of antigen-derived peptides with the MHC class II molecules on the surface of antigen-presenting cells [33]. Peptides bound by MHC class II molecules mainly originate from the exogenous proteins that are taken up by endocytosis and transported to lysosomes [34]. However, there are mechanisms that load MHC class II molecules with peptides derived from the self-proteins. These peptides are generated by the processing of the proteins associated with the lysosomes [35, 36]. Based on these findings, we attempted to fuse our antigen with a natural signal sequence targeting proteins to the lysosome and thus re-direct it into the lysosomal compartment for processing and presentation in complex with MHC class II molecules [7].

Attempts to re-route antigens to enhanced presentation by MHC class II molecules have been made, which employed the sorting signal of LAMP-1 [37] and the AP3-binding motif of LIMP II [38]. Studies of the immunogenicity of such chimeras delivered into animals as DNA vaccines showed their capacity to elicit stronger immune responses than the parental immunogens [24, 39, 40]. Immunization by genes encoding lysosomal-targeted fusion proteins led to both an enhanced production by B cells of the protective antibodies, and an enhanced cytolytic activity. Also, in most cases, the longevity of the immune response induced by the lysosome-targeted antigen exceeded the longevity of the response to the parental antigen [7].

Fusion of the invariant chain to recombinant antigens demonstrated the potential to increase both the immunogenicity and the duration of a protective immune response to the prototype DNA vaccines in laboratory animals. DNA constructs encoding a chimera composed of Ii and the lymphocytic choriomeningitis virus glycoprotein showed an enhanced capacity to activate both CD4+ and CD8+ T-cells [12]. Single administration of this plasmid to mice conferred protection against a lethal challenge with this virus [12]. The efficacy of such treatment was also reported in DNA immunization of large animals, which permitted construction of a DNA vaccine encoding a chimeric protein composed of the *Anaplasma marginale* major surface protein and the bovine invariant chain fragment [13]. A single injection of this DNA construct into calves elicited production of IgG antibodies against *Anaplasma* and increased the proliferation of CD4+ T-cells, accompanied with antigen specific-secretion of IFN-γ. This DNA immunization proved to be sufficient to mount immune memory for a rapid recall response upon antigen re-exposure [13].

In this work, we designed a DNA construct encoding the HIV-1 subtype B reverse transcriptase N-terminally fused to the lysosomal targeting signal of the human MHC class II invariant chain. The chimeric protein was shown to accumulate in the vesicular compartments such as ER, Golgi apparatus, and endosomal/lysosomal compartment. The introduction of the Ii signal resulted in a significant (four-fold) decrease of the half-life of the chimeric protein as compared to the parental RT. Proteasome inhibitors had no effect on the cellular accumulation of the chimera. At the same time, treatment of cells expressing RT-Ii with the lysosomal inhibitor led to a significant accumulation of the chimeric protein. Overall, the attachment to RT of the lysosomal

targeting signal of human MHC class II invariant chain induced a shift from the proteasomal to the lysosomal route of degradation.

Mice immunized with the plasmid encoding the chimera mounted antigen-specific IFN-γ and IL-2 responses, whereas the parental RT was nonimmunogenic. Thus, insertion of the fragment encoding the lysosomal targeting sequence of the invariant chain allowed us to overcome the poor immunogenicity of the *RT* gene immunogen.

Of note, most of the splenocytes of the RT-Ii immunized mice were able to secret both IFN-γ and IL-2. IFN-γ secretion is an important parameter that demonstrates an onset of the protetive immune response against viral infection. IL-2 plays an essential role in the expansion of the memory T-cells critical for long-term protective immunity [41]. Most of the epitope-specific cytotoxic lymphocytes produce IFN-γ; a proportion of these cells secretes also IL-2 and/or TNF-α, i.e. are polyfunctional [42]. These cells are required for an efficient control of the infections, as well as for the generation of a protective response following vaccination [43, 44]. The approach to DNA-vaccine design utilized herein ensures the generation of a polyfunctional immune response, allowing to build such a response against vaccine candidates with intrinsically poor immunogenicity.

## CONCLUSIONS

Fusion to a sequence of the human invariant chain carrying the lysosomal targeting signal was used to improve the immunogenic performance of a prototype DNA-vaccine based on HIV-1 reverse transcriptase. The lysosome-targeting sequence inserted at the N-terminus of HIV-1 RT changed both its cellular localization and the degradation pathway. This modification allowed to overcome the poor immunogenicity of reverse transcriptase as DNA-immunogen, generating a potent antigen-specific immune response in mice. The improved HIV-1 RT-based DNA construct could be included into multi-gene DNA vaccines against HIV-1 to enhance their efficacy. ●

*This work was supported by the Russian Foundation for Basic Research (grant № 11-04-01569-a).*

REFERENCES

1. Gurunathan S., Klinman D.M., Seder R.A. // Annu. Rev. Immunol. 2000. V. 18. P. 927–974.
2. Chan K., Lee D.J., Schubert A., Tang C.M., Crain B., Schoenberger S.P., Corr M. // J. Immunol. 2001. V. 166. P. 3061–3066.
3. Maecker H.T., Umetsu D.T., DeKruyff R.H., Levy S. // J. Immunol. 1998. V. 161. P. 6532–6536.
4. Almeida R.R., Rosa D.S., Ribeiro S.P., Santana V.C., Kallas E.G., Sidney J., Sette A., Kalil J., Cunha-Neto E. // PLoS One. 2012. V. 7. P. e45267.
5. Hutnick N.A., Myles D.J., Bian C.B., Muthumani K., Weiner D.B. // Curr. Opin. Virol. 2011. V. 1. P. 233–240.
6. Neefjes J., Jongsma M.L., Paul P., Bakke O. // Nat. Rev. Immunol. 2011. V. 11. P. 823–836.
7. Starodubova E.S., Isaguliants M.G., Karpov V.L. // Acta Naturae. 2010. V. 2. № 1 (4), P. 53–60.
8. Bremnes B., Madsen T., Gedde-Dahl M., Bakke O. // J. Cell Sci. 1994. V. 107. P. 2021–2032.
9. Odorizzi C.G., Trowbridge I.S., Xue L., Hopkins C.R., Davis C.D., Collawn J.F. // J. Cell Biol. 1994. V. 126. P. 317–330.
10. Pieters J., Bakke O., Dobberstein B. // J. Cell Sci. 1993. V. 106. Pt 3. P. 831–846.
11. Diebold S.S., Cotten M., Koch N., Zenke M. // Gene Ther. 2001. V. 8. P. 487–493.
12. Holst P.J., Sorensen M.R., Mandrup Jensen C.M., Orskov C., Thomsen A.R., Christensen J.P. // J. Immunol. 2008. V. 180. P. 3339–3346.
13. Mwangi W., Brown W.C., Splitter G.A., Davies C.J., Howard C.J., Hope J.C., Aida Y., Zhuang Y., Hunter B.J., Palmer G.H. // Clin. Vaccine Immunol. 2007. V. 14. P. 304–311.
14. Rowe H.M., Lopes L., Ikeda Y., Bailey R., Barde I., Zenke M., Chain B.M., Collins M.K. // Mol. Ther. 2006. V. 13. P. 310–319.
15. Sponaas A., Carstens C., Koch N. // Gene Ther. 1999. V. 6. P. 1826–1834.
16. Brave A., Hallengard D., Malm M., Blazevic V., Rollman E., Stanescu I., Krohn K. // Vaccine. 2009. V. 27. P. 184–186.
17. Sandstrom E., Nilsson C., Hejdeman B., Brave A., Bratt G., Robb M., Cox J., Vancott T., Marovich M., Stout R., et al. // J. Infect. Dis. 2008. V. 198. P. 1482–1490.
18. Isaguliants M.G., Petrakova N.N., Zuber B., Pokrovskaya K., Gizatullin R., Kostyuk D.A., Kjerrstrom A., Winberg G., Kochetkov S.N., Hinkula J., et al. // Intervirology. 2000. V. 43. P. 288–293.
19. Isaguliants M.G., Pokrovskaya K., Kashuba V.I., Pokholok D., Hinkula J., Wahren B., Kochetkov S.N. // FEBS Lett. 1999. V. 447. P. 232–236.
20. Isaguliants M.G., Gudima S.O., Ivanova O.V., Levi M., Hinkula J., Garaev M.M., Kochetkov S.N., Wahren B. // AIDS Res. Hum. Retroviruses. 2000. V. 16. P. 1269–1280.
21. Zhou P. // Methods Mol. Biol. 2004. V. 284. P. 67–77.
22. Starodubova E.S., Isaguliants M.G., Karpov V.L. // Mol. Biol. (Moskow). 2006. V. 40. P. 885–890.
23. Roos A.K., Eriksson F., Walters D.C., Pisa P., King A.D. // Mol. Ther. 2009. V. 17. P. 1637–1642.
24. Starodubova E., Boberg A., Ivanov A., Latyshev O., Petrakova N., Kuzmenko Y., Litvina M., Chernousov A., Kochetkov S., Karpov V., et al. // Vaccine. 2010. V. 28. P. 1975–1986.
25. Rechinskii V.O., Barbashov S.F., Degtiarev I.L., Vorob'ev S.M., Liakhov D.L., Kostiuk D.A., Starov A.I., Matsevich G.R., Kochetkov S.N. // Mol. Biol. (Mosk). 1991. V. 25. P. 1248–1257.
26. Ivanov A.V., Korovina A.N., Tunitskaya V.L., Kostyuk D.A., Rechinsky V.O., Kukhanova M.K., Kochetkov S.N. // Protein Expr. Purif. 2006. V. 48. P. 14–23.
27. Starodubova E.S., Boberg A., Litvina M., Morozov A., Petrakova N.V., Timofeev A., Latyshev O., Tunitskaya V.,

Wahren B., Isaguliants M.G., et al. // Vaccine. 2008. V. 28. P. 1975-1986.
28. Lamb C.A., Yewdell J.W., Bennink J.R., Cresswell P. // Proc. Natl. Acad. Sci. USA. 1991. V. 88. P. 5998–6002.
29. Isaguliants M.G., Belikov S.V., Starodubova E.S., Gizatullin R.Z., Rollman E., Zuber B., Zuber A.K., Grishchenko O.I., Rytting A.S., Kallander C.F., et al. // AIDS Res. Hum. Retroviruses. 2004. V. 20. P. 191–201.
30. Starodubova E., Boberg A., Kashuba E.V., Wahren B., Karpov V., Isaguliants M. // Vaccine. 2006. V. 24. P. 4541–4547.
31. Borg J.P., Ihlenfeldt H.G., Jung G., Haas G., Pierres M. // Eur. J. Immunol. 1994. V. 24. P. 1496–1502.
32. Restle T., Pawlita M., Sczakiel G., Muller B., Goody R.S. // J. Biol. Chem. 1992. V. 267. P. 14654–14661.
33. Prlic M., Williams M.A., Bevan M.J. // Curr. Opin. Immunol. 2007. V. 19. P. 315–319.
34. Watts C. // Annu. Rev. Immunol. 1997. V. 15. P. 821–850.
35. Robinson J.H., Delvig A.A. // Immunology. 2002. V. 105. P. 252–262.
36. Van Bergen J., Ossendorp F., Jordens R., Mommaas A.M., Drijfhout J.W., Koning F. // Immunol. Rev. 1999. V. 172. P. 87–96.
37. Wu T.C., Guarnieri F.G., Staveley-O'Carroll K.F., Viscidi R.P., Levitsky H.I., Hedrick L., Cho K.R., August J.T., Pardoll D.M. // Proc. Natl. Acad. Sci. USA. 1995. V. 92. P. 11671–11675.
38. Gupta S.N., Kloster M.M., Rodionov D.G., Bakke O. // Eur. J. Cell. Biol. 2006. V. 85. P. 457–467.
39. Goldoni A.L., Maciel M., Jr., Rigato P.O., Piubelli O., de Brito C.A., Melo A., Marques E.T., August J.T., Duarte A.J., Sato M.N. // Immunobiology. 2011. V. 216. P. 505–512.
40. Valentin A., Chikhlikar P., Patel V., Rosati M., Maciel M., Chang K.H., Silvera P., Felber B.K., Pavlakis G.N., August J.T., et al. // Vaccine. 2009. V. 27. P. 4840–4849.
41. Williams M.A., Tyznik A.J., Bevan M.J. // Nature. 2006. V. 441. P. 890–893.
42. Belz G.T., Xie W., Doherty P.C. // J. Immunol. 2001. V. 166. P. 4627–4633.
43. Darrah P.A., Patel D.T., De Luca P.M., Lindsay R.W., Davey D.F., Flynn B.J., Hoff S.T., Andersen P., Reed S.G., Morris S.L., et al. // Nat. Med. 2007. V. 13. P. 843–850.
44. Forbes E.K., Sander C., Ronan E.O., McShane H., Hill A.V., Beverley P.C., Tchilian E.Z. // J. Immunol. 2008. V. 181. P. 4955–4964.

# The Role of Dihydroorotate Dehydrogenase in Apoptosis Induction in Response to Inhibition of the Mitochondrial Respiratory Chain Complex III

A. A. Khutornenko[1], A. A. Dalina[3], B. V. Chernyak[1], P. M. Chumakov[3], A. G. Evstafieva[1, 2*]
[1]Belozersky Institute of Physico-Chemical Biology, Lomonosov Moscow State University, Leninskie Gory, 1, Bld. 40, 119991, Moscow, Russia
[2]Department of Bioengineering and Bioinformatics, Lomonosov Moscow State University, Leninskie Gory, 1, Bld. 73, 119991, Moscow, Russia
[3]Engelhardt Institute of Molecular Biology, Russian Academy of Sciences, Vavilova Str., 32, 119991, Moscow, Russia.
*E-mail: evstaf@genebee.msu.ru
Received 12.08.2013


**ABSTRACT** **A mechanism for the induction of programmed cell death (apoptosis) upon dysfunction of the mitochondrial respiratory chain has been studied. Previously, we had found that inhibition of mitochondrial cytochrome *bc*1, a component of the electron transport chain complex III, leads to activation of tumor suppressor p53, followed by apoptosis induction. The mitochondrial respiratory chain is coupled to the *de novo* pyrimidine biosynthesis pathway via the mitochondrial enzyme dihydroorotate dehydrogenase (DHODH). The p53 activation induced in response to the inhibition of the electron transport chain complex III has been shown to be triggered by the impairment of the *de novo* pyrimidine biosynthesis due to the suppression of DHODH. However, it remained unclear whether the suppression of the DHODH function is the main cause of the observed apoptotic cell death. Here, we show that apoptosis in human colon carcinoma cells induced by the mitochondrial respiratory chain complex III inhibition can be prevented by supplementation with uridine or orotate (products of the reaction catalyzed by DHODH) rather than with dihydroorotate (a DHODH substrate). We conclude that apoptosis is induced in response to the impairment of the *de novo* pyrimidine biosynthesis caused by the inhibition of DHODH. The conclusion is supported by the experiment showing that downregulation of DHODH by RNA interference leads to accumulation of the p53 tumor suppressor and to apoptotic cell death.**
**KEYWORDS** **apoptosis; p53 tumor suppressor; mitochondrial respiratory chain; dihydroorotate dehydrogenase; *de novo* pyrimidine biosynthesis.**
**ABBREVIATIONS** **MRC – mitochondrial respiratory chain; DHODH - dihydroorotate dehydrogenase; shRNA – short hairpin RNA; SDS – sodium dodecyl sulfate; PAAG – polyacrylamide gel; PrI – propidium iodide; FITC – fluorescein isothiocyanate.**

## INTRODUCTION

Mitochondria play a central role in homeostasis in eukaryotic cells. They both supply the cell with energy by means of oxidative phosphorylation and act as important mediators of programmed cell death, as well as of the intracellular signaling cascades mediated by calcium ions and reactive oxygen species [1]. The mitochondrial respiratory chain (MRC) consists of multicomponent I-IV protein complexes integrated into the inner mitochondrial membrane, which catalyze electron transfer from NADH to molecular oxygen. This leads to the generation of the electrochemical proton gradient through the inner mitochondrial membrane, which is the driving force behind ATP synthesis by means of ATP synthase (complex V).

Many human diseases are associated with mitochondrial dysfunctions; moreover, the so-called "mitochondrial diseases" are usually caused by respiratory chain defects in these organelles [2]. Mitochondrial dysfunctions are involved in the aging process [3]. With age,

the number of mutations in mammalian mitochondrial DNA increases and respiratory chain dysfunction is observed. Cells with defects in the MRC are prone to apoptosis, and the increased cell loss is an important consequence of mitochondrial dysfunctions. In this paper we address the mechanism of apoptotic program activation upon MRC dysfunction.

The tumor suppressor p53 is a key regulatory protein that in many cases determines cell behavior in different types of stress: whether cell-cycle arrest occurs, accompanied by damage repair, or mechanisms of programmed cell death are activated, which are aimed at deleting cells with unrepairable damage [4]. Previously, we had found that the inhibition of the MRC complex III leads to an increase in the level of p53 and its activity, as well as to the activation of programmed death of human cancer cells [5]. The p53 activation appeared to be caused not by the inhibition of the MRC itself, but by the dysfunction of complex III (complex of cytochrome *bc*1) that transfers electrons from reduced ubiquinone (ubiquinol) to cytochrome *c*. One of the most important metabolic pathways in the cell, the *de novo* pyrimidine biosynthesis is coupled with the MRC [6]. The only mitochondrial enzyme of this pathway is dihydroorotate dehydrogenase (DHODH), which oxidizes dihydroorotate to orotate and uses ubiquinone as an electron acceptor [6]. The dysfunction of MRC complex III results in the transition of ubiquinone to the reduced state, which in turn may inhibit the DHODH function and lead to impairment of pyrimidine biosynthesis. Indeed, we demonstrated that an increase in the level and activity of p53 upon inhibition of the MRC complex III is due to the impairment of the DHODH function and *de novo* pyrimidine biosynthesis [5]. However, it remained unclear whether the suppression of the DHODH function is the main reason behind the activation of the cell apoptotic program upon inhibition of MRC complex III.

In this paper, we have demonstrated that impairment of the DHODH function and, as a consequence, of *de novo* pyrimidine biosynthesis induces apoptosis in human colon cancer cells upon inhibition of MRC complex III.

## EXPERIMENTAL

### Conditions for cell culturing and treatment

RKO and HCT116 human colon cancer cells were grown on a DMEM medium supplemented with 10% fetal bovine serum (HyClone) at 37 $^0$C and 5% $CO_2$ to 50–70% confluency. Then, the cells were incubated for 12 h to determine the p53 level and for 20–26 h to analyze apoptosis in the presence of 200 nM myxothiazol (Sigma-Aldrich Inc.). In some experiments, the medium was supplemented with uridine to a final concentration of 50 μg/ml; orotate or dihydroorotate (Sigma-Aldrich Inc.) to a final concentration of 1 mM.

### Evaluation of apoptosis by flow cytometry

The cells were detached from the scaffold by tryptic cleavage, washed with phosphate-buffered saline (PBS, 0.14 M NaCl; 2.7 mM KCl; 10 mM $Na_2HPO_4$; 1.8 mM $KH_2PO_4$, pH 7.3), and suspended in 100 μl of a Annexin buffer (10 mM HEPES; 140 mM NaCl; 2.5 mM $CaCl_2$, pH 7.4). Then the cells were supplemented with 7.5 μl of Annexin V conjugated to FITC (Invitrogen) and with propidium iodide (Clontech) to a final concentration of 100 μg/ml and incubated in the dark for 15 min. Thereafter, another 500 μl of the Annexin buffer was added; the cell suspension was filtered through a 30 μm filter and analyzed on a Partec PASIII flow cytometer.

### Immunoblotting

The cells were lysed in a RLB buffer (Promega Inc.). Equal amounts of protein extracts (50–100 μg) were fractionated by electrophoresis in 12% SDS-PAGE; electrotransfer of the proteins onto a nitrocellulose membrane and treatment of the membrane were performed as previously described [7]. The membrane was incubated with mouse monoclonal antibodies to DHODH (ab54621, Abcam), to p53 (DO-1), or to actin (G-2) (Santa Cruz Biotechnology Inc.) diluted at a ratio of 1 : 500 with a TBST buffer (20 mM Tris-HCl, pH 7.5; 140 mM NaCl; 0.05% Tween-20) for 2 h. To control loading, the membranes were incubated with actin antibodies. Detection was performed using secondary sheep anti-mouse antibodies conjugated to horseradish peroxidase (GE Healthcare) and enhanced chemiluminescence according to the standard technique (Western Lightning Chemiluminescence Reagent, Perkin Elmer Life Sciences).

### Preparation of cell lines with a reduced DHODH level

Lentiviral vectors based on the pLKO.1-puro plasmid (Sigma-Aldrich Inc.) contained the genes of short hairpin RNAs to DHODH with the following sequences: si21 – CCGGTCCGGGATTTATCAACTCAAACTCGAGTTTGA GTTGATAAATCCCGGATTTTT, si32 – CCGGCGGACTTTATAAGATGGGCTTCTCGA GAAGCCCATCTTATAAAGTCCG TTTTT.

For each lentiviral vector, pLKO-si21 and pLKO-si32, viral stocks were obtained. For this purpose, HEK293T human embryonic kidney cells on 10-cm Petri dishes were transfected with the corresponding lentiviral vector and a set of packaging plasmids [8] using LipofectAMIN 2000 (Invitrogen) according to the manufacturer's procedure. A mixture of four plasmids was used: the 3 μg lentiviral vector, 12 μg plasmid

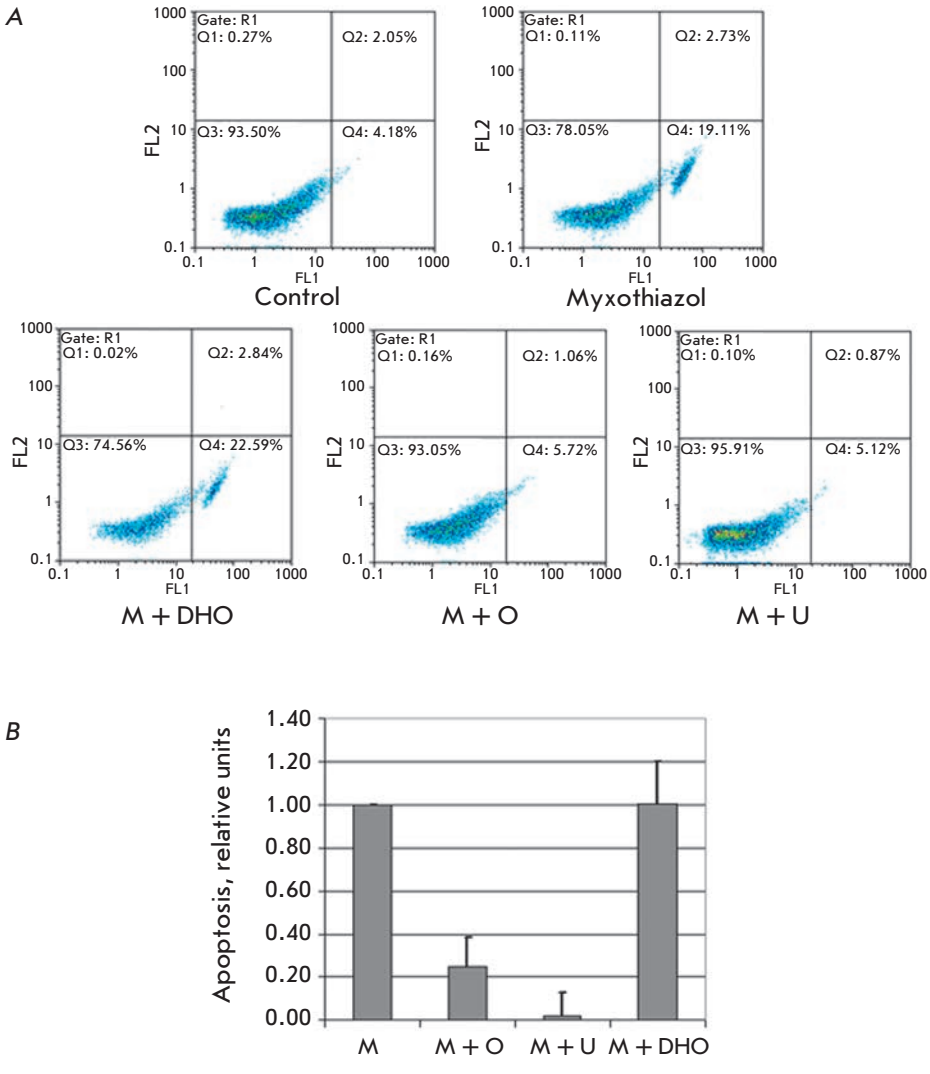


Fig. 1. Uridine and orotate, but not dihydroorotate, protect RKO cells against myxothiazol-induced apoptosis. The apoptosis level of RKO cells stained with FITC-Annexin V and PrI was determined by flow cytometry. *A* – a representative 2D diagram of cell distribution over the fluorescence intensity in FL2 (PrI) and FL1 (FITC-Annexin V) channels. Cells were analyzed 26 h after treatment with 200 nM myxothiazol (Myxothiazol, M) only or along with 1 mM dihydroorotate (M + DHO), 1 mM orotate (M + O), and 1 mM uridine (M + U). The control is untreated cells. *B* — Statistical analysis of the results. Percentage of apoptotic (AnnexinV-positive, PrI-negative) cells in each sample after subtraction of control values was normalized to the percentage of cells in which apoptosis was induced by myxothiazol without additives. The diagram shows the mean values of the relative apoptosis level and SDs of three independent experiments

pRev2 expressing the protein Rev, 6 μg plasmid pGag1 expressing the proteins Pol and Gag, and 3 μg plasmid pVSV-G expressing glycoprotein G of the vesicular stomatitis virus (a total of 24 μg DNA). The plasmid mixture, diluted with the DMEM medium, was mixed with the diluted LipofectAMIN 2000 (60 μL), stirred vigorously, incubated for 20 min at room temperature, and pipetted into a plate with the cells. On the next day, the medium was replaced with 10 ml of DMEM containing 2% fetal bovine serum.

The secreted viral particles were harvested 2 days after transfection: 10 ml of the medium from the transfected cells was filtered through a low protein binding filter (Durapore membrane, Millex-HV, Millipore) with 0.45 μm pores; 1 ml aliquots were stored at −70 °C.

RKO cells were infected with viral particles carrying two different variants of the gene of short hairpin RNA to DHODH (si32 and si21), as well as with control viruses containing no short hairpin RNA (pLS-Lpw). For this purpose, cells grown on 35-mm plates were supplemented with 1 ml of viral particles diluted in 1 ml of a fresh medium and 5–8 μg of polybrene (Hexadimethrine bromide, Sigma-Aldrich Inc.). The cells were grown in the presence of uridine (50 μg/ml). Three days later, puromycin was added (1 μg/ml) and the selection was conducted for 3 more days. The cells were lysed; the DHODH level was determined using immunoblotting.

## RESULTS

### The role of the impairment of pyrimidine biosynthesis in apoptosis induction upon the inhibition of the mitochondrial respiratory chain complex III

We have shown that the action of the MRC complex III inhibitors leads to growth arrest in a number of cell lines of epithelial tumors and to their massive death. A cytometric analysis of RKO human colon cancer cells

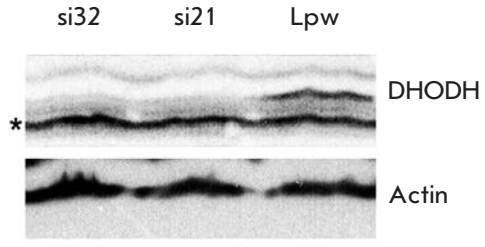


Fig. 2. Efficiency of DHODH-specific RNA interference. Western blot analysis of DHODH levels in the lysates of RKO cells infected with pLKO-si21 (si21), or with pLKO-si32 (si32), or with the empty vector pLS-Lpw (Lpw). The upper panel shows the reaction with DHODH antibodies, the lower panel shows the reaction with β-actin antibodies used as a loading control. The asterisk (*) denotes a nonspecific band, which can also serve as a sample loading control


Fig. 3. DHODH interference in RKO cells results in p53 induction similarly to the effect of myxothiazol, the inhibitor of the MRC complex III. Western blot analysis of p53 levels in RKO cells infected with pLKO-si21 (si21), or with pLKO-si32 (si32), or with the empty vector pLS-Lpw (Lpw). Cells were cultured in the absence of uridine for 24 h. For comparison, the right panel shows the Western blot analysis of p53 levels in RKO cells untreated (C) or treated with 200 nM myxothiazol (M) for 12 h. Upper panel –with p53 antibodies; lower panel – with β-actin antibodies

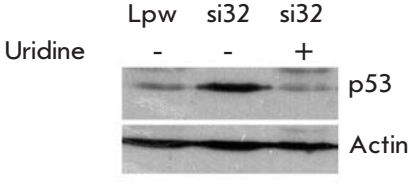


Fig. 4. Uridine prevents p53 induction in cells with DHODH knockdown. Western blot analysis of p53 levels in RKO cells infected with pLKO-si32 (si32) or with the empty vector pLS-Lpw (Lpw). Cells were cultured in the absence (–) or in the presence (+) of uridine for 24 h. Upper panel – with p53 antibodies; lower panel – with β-actin antibodies

treated with myxothiazol, an inhibitor of MRC complex III, and stained with FITC-Annexin V and propidium iodide (PrI) revealed a significant population of apoptotic cells (*Fig. 1*). In general, three cell populations were observed: normal cells (Annexin V-negative, PrI-negative), apoptotic cells (Annexin V-positive, PrI-negative, approximately 20% of all cells), and a third small population of dead cells (Annexin V-positive, PrI-positive, whose fraction was approximately 3%). The size of the third population was bigger when cells were collected not only from the scaffold, but from the medium as well (data not shown), and these cells were considered as necrotic or late-apoptotic.

Since the mitochondrial respiratory chain is functionally coupled with the *de novo* pyrimidine biosynthesis pathway via the dihydroorotate dehydrogenase inserted in the mitochondrial membrane [6], we decided to test how replenishment of the pyrimidine pool affects myxothiazol-induced apoptosis. For this purpose, a cytometric analysis was performed after treatment of RKO cells with myxothiazol in the presence of uridine. Uridine, a precursor of both uridylic and cytidylic nucleotides, appeared to almost completely prevent the accumulation of apoptotic Annexin V-positive, PrI-negative cells caused by treatment with myxothiazol (*Fig. 1*). This indicates that the reason for apoptosis induction is impairment of the *de novo* pyrimidine biosynthesis, presumably due to DHODH inhibition.

To directly assess the role of DHODH, RKO cells were treated with myxothiazol in the presence of a substrate or a product of the DHODH-catalyzed reaction; the apoptosis level was analyzed by flow cytometry. Dihydroorotate (a DHODH substrate) had no effect on myxothiazol-induced apoptosis (*Fig. 1*), but orotate (a product of the DHODH-catalyzed reaction) substantially prevented it (the number of apoptotic cells was 4 times lower than upon apoptosis induction by myxothiazol (*Fig. 1*).

Similar results were obtained for the other human colon cancer cell line, HCT116 (not shown).

The obtained data suggest that apoptosis induction upon inhibition of MRC complex III is, to a great extent, due to the DHODH inhibition and impairment of the *de novo* pyrimidine biosynthesis. For more confidence in this molecular mechanism, it was decided to conduct the reverse experiment and to check whether dysfunction of DHODH causes apoptotic cell death similarly to the inhibition of MRC complex III.

### The effect of dihydroorotate dehydrogenase knockdown on tumor suppressor p53 and programmed cell death

Does dysfunction of DHODH really cause apoptotic cell death similarly to the inhibition of the MRC complex III?

To find out, it was decided to prepare a RKO cell line with DHODH expression suppressed by RNA interference. The lentiviral system was used for effective delivery of a cassette expressing short interfering RNAs. RKO cells were infected with the lentiviral particles carrying two different variants of the gene of short hairpin RNA to DHODH (si32 and si21) and also with the control viruses, which did not contain these genes (pLS-Lpw) and were grown in the presence of uridine. The cells with expression cassettes integrated into the chromosome were selected using puromycin and lysed; the DHODH level was determined using immunoblotting (*Fig. 2*).

Thus, the DHODH level in cells expressing two different short hairpin RNAs to DHODH was found to be significantly lower than in cells infected with viral particles on the basis of the "empty" vector (*Fig. 2*).

Previously, we had shown that the inhibition of MRC complex III leads to activation of the tumor suppressor p53 due to the dysfunction of DHODH [5]. To determine whether DHODH knockdown causes accumulation of p53, immunoblotting was used to compare the p53 level in the control cells and the cells with RNA interference specific to DHODH, cultured in the absence of an external uridine source. The p53 level in the cells with DHODH knockdown appeared to increase in the same way as the inhibition of the MRC complex III (*Fig. 3*).

Uridine prevented the accumulation of p53 in cells with RNA interference specific to DHODH (*Fig. 4*). Consequently, impairment of the *de novo* pyrimidine biosynthesis can be considered as the most likely cause of the increased p53 level in these cells.

Further, a cytometric analysis was performed for FITC-Annexin V and propidium iodide-stained cells with RNA interference specific to DHODH, which were cultured in the absence of an external uridine source. It turned out that an increase in the fraction of apoptotic Annexin V-positive, PrI-negative cells is the functional consequence of the suppression of DHODH expression and stabilization of p53 (*Fig. 5*). Adding uridine to the growth medium reduced the percentage of apoptotic cells to the reference level, which proves the specificity of the observed effect.

Thus, it was demonstrated by suppressing DHODH expression using the RNA interference method that both the dysfunction of DHODH and the inhibition of MRC complex III lead to elevation of the intracellular level of tumor suppressor p53 and to an increase in the level of programmed cell death (apoptosis). These results support our model, according to which apoptosis induction upon inhibition of the MRC complex III, as well as activation and stabilization of p53, occurs due to DHODH inhibition and impairment of *de novo* pyrimidine biosynthesis.

## DISCUSSION

Mitochondria are the "power stations" of the cell and, simultaneously, mediators of a number of regulatory pathways, including apoptosis induction [1]. Previously, we had demonstrated that the inhibition of the MRC complex III leads to the activation of tumor suppressor p53 and to the triggering of the cell death program [5]. The activation of p53 turned out to be caused not

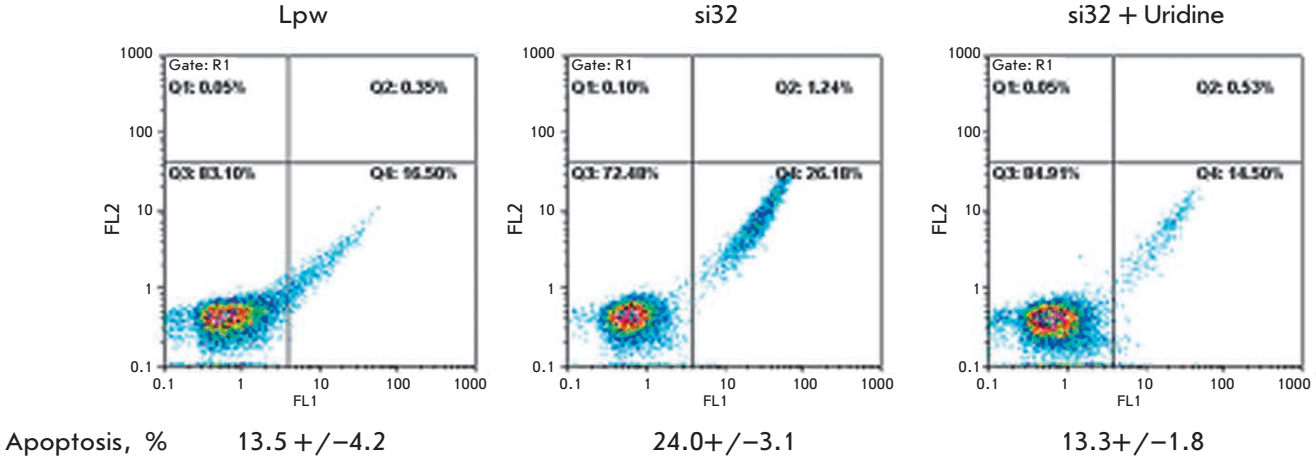


Fig. 5. Uridine protects RCO cells with DHODH knockdown against apoptosis. The apoptosis level of RKO cells, either control (Lpw) or with DHODH-specific RNA interference, cultured in the absence of an external uridine source (si32) or in the presence of uridine (si32 + uridine), was measured by flow cytometry. Cells were stained with FITC-Annexin V and propidium iodide (PrI). Results are presented as a 2D diagram of cell distribution over the fluorescence intensity in the FL2 (PrI) and FL1 (FITC-Annexin V) channels. The bottom panel shows the percentage of apoptotic (AnnexinV-positive, PrI-negative) cells (the mean value +/– SD of three independent experiments)

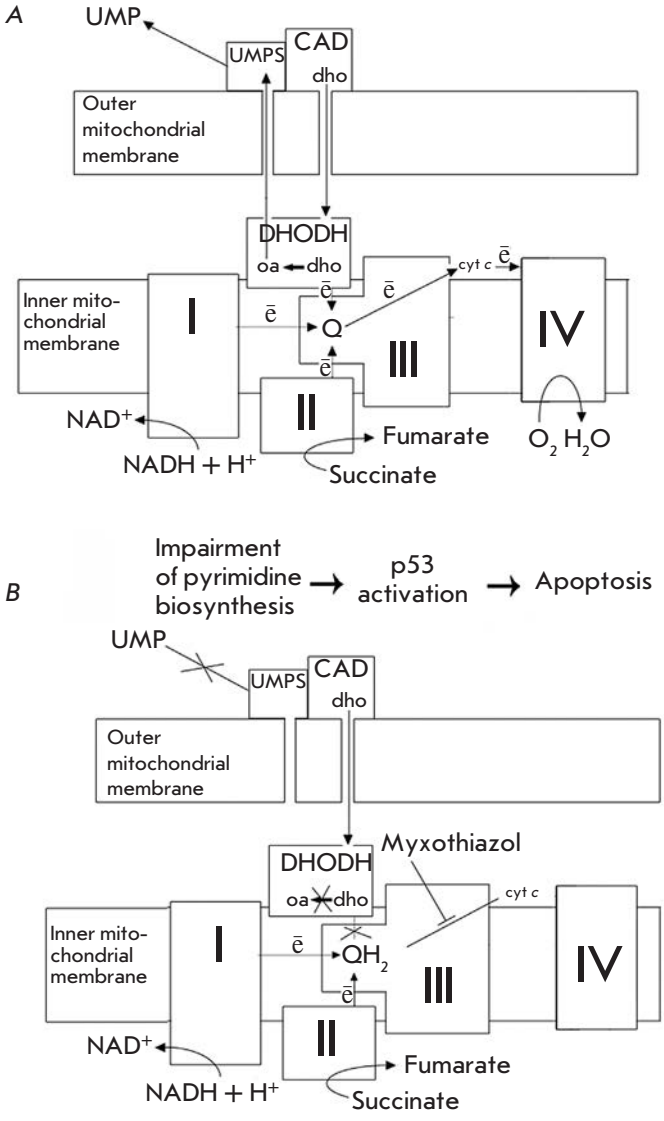


Fig. 6. A model explaining the proposed mechanism of induction of p53-dependent apoptosis in response to MRC complex III inhibition. I, II, III, IV – the MRC complexes; Q – ubiquinone; QH2 – ubiquinol; cyt *c* – cytochrome *c*; DHODH – dihydroorotate dehydrogenase; dho – dihydroorotate; oa – orotate; UMPS – uridine monophosphate synthase, UMP – uridine monophosphate, CAD – multifunction enzyme that initiates the *de novo* pyrimidine biosynthesis, OMM and IMM – outer and inner mitochondrial membranes: electrons are shown as *e*. *A* –untreated cells, *B* – after treatment with myxothiazol. Explanations are provided in the text

by the electron transport chain inhibition itself, but by the dysfunction of the cytochrome *bc*1 complex. It was demonstrated that this occurs due to the inhibition of dihydroorotate dehydrogenase, the only mitochondrial enzyme of the *de novo* pyrimidine biosynthesis pathway. However, it remained unknown whether the inhibition of DHODH was the exclusive cause behind the triggering of programmed cell death upon inhibition of the MRC complex III.

DHODH is a flavoprotein inserted in the inner mitochondrial membrane. DHODH oxidizes dihydroorotate to orotate and uses ubiquinone as an electron acceptor [6]. This paper demonstrates that apoptotic cell death induced by myxothiazol (an inhibitor of the MRC complex III) is fully prevented by uridine (a precursor of uridylic and cytidylic nucleotide biosynthesis) and to a large extent by orotat (a product of the reaction catalyzed by dihydroorotate dehydrogenase). Meanwhile, dihydroorotate, a DHODH substrate, does not possess this property. These data suggest that apoptotic cell death upon inhibition of the MRC complex III is in reality caused by the inhibition of DHODH, the mitochondrial enzyme of the *de novo* pyrimidine biosynthesis pathway. This conclusion is confirmed by the results of experiments on the suppression of DHODH expression using RNA interference. DHODH knockdown turned out to result in the accumulation of tumor suppressor p53 and acceleration of apoptosis.

*Figure 6* provides a tentative diagram of the events resulting in apoptosis upon inhibition of the MRC complex III. Under normal conditions, ubiquinone accepts electrons from complex I, complex II, and dihydroorotate dehydrogenase. At that, ubiquinone is reduced to ubiquinol, which then donates electrons to cytochrome *c* through complex III (*Fig. 6A*). Myxothiazol-induced inhibition of MRC complex III blocks ubiquinol oxidation; ubiquinone passes to the completely reduced state and loses its ability to accept electrons during dihydroorotate oxidation. This leads to dysfunction of DHODH and, as a consequence, to impairment of *de novo* pyrimidine biosynthesis, stabilization and activation of tumor suppressor p53, and induction of programmed cell death (*Fig. 6B*). The significance of ubiquinone regeneration within the respiratory chain for *de novo* pyrimidine biosynthesis is confirmed by the fact that, as recently established, the malaria parasite *Plasmodium falciparum* apparently maintains the active mitochondrial electron transport chain exclusively for this purpose [9].

The results are in good agreement with data indicating that the DHODH inhibitor leflunomide/teriflunomide induces apoptosis in a number of human cancer cell lines [10–12]. However, according to [12], transformed keratinocytes with the mutant p53 gene, which lack transcriptionally active p53, are more sensitive to apoptosis induced by teriflunomide than normal keratinocytes with wild-type p53. In normal human epidermal keratinocytes (NHEK) a long-term exposure to teriflunomide was shown to induce cell cycle arrest at

Go/G1 due to an induction of the p53 regulated gene CDKN1A encoding the cyclin-dependent kinase inhibitor p21. The response apparently reflects a cytoprotective role for p53 against teriflunomide-induced apoptosis [12]. Treatment of human fibroblasts with PALA, another inhibitor of pyrimidine biosynthesis (N-phosphonacetyl-L-aspartate, transcarbamylase inhibitor), led to reversible cell cycle arrest, survival of cells expressing transcriptionally active p53, and apoptotic cell death in the absence of p53 [13–15]. It is assumed that under conditions of suppressed pyrimidine biosynthesis, the cytoprotective properties of p53 (promoting the survival of normal cells with wild-type p53 and death of cancer cells with inactivated p53) may be used for anti-tumor therapy employing the proper inhibitors [12].

In contrast to the published data [12–15], the present work demonstrates that the suppression of DHODH activity and impairment of *de novo* pyrimidine biosynthesis lead to apoptosis induction in human colon cancer cells expressing transcriptionally active p53. Moreover, we had previously shown that HCT116 $p53^{-/-}$ cells (cells lacking p53) demonstrate significant suppression of apoptosis compared to wild-type HCT116 cells [5]. Hence, in the studied tumor cells, p53 does not perform the cytoprotective function, but instead it promotes apoptosis induction upon impairment of *de novo* pyrimidine biosynthesis. The discrepancy between our results and the results of [12–15] may be due to tissue-specific variations and requires further study.

Our findings, as one of the consequences, suggest a possible application of inhibitors of pyrimidine biosynthesis in malignant human colon tumors expressing wild-type p53.

## CONCLUSION

The mechanism of programmed cell death activation upon dysfunction of the mitochondrial respiratory chain has been investigated. It has been demonstrated that dysfunction of the mitochondrial enzyme dihydroorotate dehydrogenase, leading to blockage of the *de novo* pyrimidine biosynthesis pathway, activation of tumor suppressor p53 and, as a result, induction of p53-dependent apoptosis is the reason behind apoptosis induction in human colon cancer cells upon inhibition of the mitochondrial respiratory chain complex III.

The results disagree with the previously published data, according to which tumor suppressor p53 in human keratinocytes and fibroblasts plays the cytoprotective role and protects cells against apoptosis induced by inhibitors of pyrimidine biosynthesis. We have demonstrated that suppression of DHODH activity and impairment of *de novo* pyrimidine biosynthesis induce apoptosis in human colon cancer cells expressing transcriptionally active p53. In the studied cell lines, p53, in contrast, promoted apoptosis induction upon impairment of *de novo* pyrimidine biosynthesis. The discrepancy between our results and previously published results may be due to tissue-specific variations and requires further study. The findings suggest a possible application of inhibitors of pyrimidine biosynthesis in human colon tumors expressing wild-type p53. ●

*This work was supported by the Russian Foundation for Basic Research (grants № 12-04-01444, 12-04-00538, and 12-04-32131-mol_a) and by the Federal Program "Research and Scientific-Pedagogical Personnel of Innovative Russia" (State contract P334, 2010-2012).*

REFERENCES

1. McBride H.M., Neuspiel M., Wasiak S. // Curr. Biol. 2006. Vol.16. № 5. P. 551–560.
2. Meunier B., Fisher N., Ransac S., Mazat J.P., Brasseur G. // Biochim. Biophys. Acta. 2013. V. 1827. № 11–12, P. 1346–1361.
3. Trifunovic A., Larsson N.-G. // J. Intern. Med. 2008. V. 263. № 2. P.167–178.
4. Chumakov P.M. // Biochemistry (Mosc). 2007. V. 72. № 13. P.1399–1421.
5. Khutornenko A.A., Roudko V.V., Chernyak B.V., Vartapetian A.B., Chumakov P.M., Evstafieva A.G. // Proc. Natl. Acad. Sci. U S A. 2010. V.107. № 29. P. 12828–12833.
6. Evans D.R., Guy H.I. // J. Biol. Chem. 2004. V. 279. № 32. P. 33035–33038.
7. Sukhacheva E.A., Evstafieva A.G., Fateeva T.V., Shakulov V.R., Efimova N.A., Karapetian R.N., Rubtsov Y.P., Vartapetian A.B. // J. Immunol. Methods. 2002. V. 266. №1–2. P. 185–196.
8. Guryanova O.A., Makhanov M., Chenchik A.A., Chumakov P.M., Frolova E.I. // Mol. Biol. (Mosk). 2006. V. 40. № 3. P. 396–405.
9. Painter H.J., Morrisey J.M., Mather M.W., Vaidya A.B. // Nature. 2007. V. 446. № 1. P. 88–91.
10. Baumann P., Mandl-Weber S., Völkl A., Adam C., Bumeder I., Oduncu F., Schmidmaier R. // Mol. Cancer Ther. 2009. V. 8. № 3. P. 366–375.
11. Hail N.Jr., Chen P., Bushman L.R. // Neoplasia. 2010. V. 12. № 4. P. 464–475.
12. Hail N.Jr, Chen P., Kepa J.J., Bushman L.R. // Apoptosis. 2012. V. 17. № 2. P. 258–268.
13. Agarwal M.L., Agarwal A., Taylor W.R., Chernova O., Sharma Y., Stark G.R. // Proc. Natl. Acad. Sci. U S A. 1998. V. 95. № 25. P. 14775–14780.
14. Agarwal M.K., Hastak K., Jackson M.W., Breit S.N., Stark G.R., Agarwal M.L. // Proc. Natl. Acad. Sci. U S A. 2006. V. 103. № 44. P. 16278–16283.
15. Hastak K., Paul R.K., Agarwal M.K., Thakur V.S., Amin A.R., Agrawal S., Sramkoski R.M., Jacobberger J.W., Jackson M.W., Stark G.R., Agarwal M.L. // Proc. Natl. Acad. Sci. USA. 2008. V. 105. № 17. P. 6314–6319.

# Protective Immune Response against *Bacillus anthracis* Induced by Intranasal Introduction of a Recombinant Adenovirus Expressing the Protective Antigen Fused to the Fc-fragment of IgG2a

D. N. Shcherbinin[1]*, I. B. Esmagambetov[1], A. N. Noskov[1], Yu. O. Selyaninov[2], I. L. Tutykhina[1], M. M. Shmarov[1], D. Yu. Logunov[1], B. S. Naroditskiy[1], A. L. Gintsburg[1]

[1]Gamaleya Research Institute for Epidemiology and Microbiology, Ministry of Public Health of the Russian Federation, Gamaleya Street 18, 123098, Moscow, Russia

[2]National Research Institute for Veterinary Virology and Microbiology of Russia, Russian Academy of Agricultural Sciences, 601120, Pokrov, Vladimir region, Russia

*E-mail: dim284@inbox.ru

Received 13.08.2013



**ABSTRACT** **Anthrax is a particularly dangerous infectious disease that affects humans and livestock. It is characterized by intoxication, serosanguineous skin lesions, development of lymph nodes and internal organs, and may manifest itsself in either a cutaneous or septic form. The pathogenic agent is Bacillus anthracis, a gram-positive, endospore-forming, rod-shaped aerobic bacterium. Efficacious vaccines that can rapidly induce a long-term immune response are required to prevent anthrax infection in humans. In this study, we designed three recombinant human adenovirus serotype-5-based vectors containing various modifications of the fourth domain of the B. anthracis protective antigen (PA). Three PA modifications were constructed: a secretable form (Ad-sPA), a non-secretable form (Ad-cPA), and a form with the protective antigen fused to the Fc fragment of immunoglobulin G2a (Ad-PA-Fc). All these forms exhibited protective properties against Bacillus anthracis. The highest level of protection was induced by the Ad-PA-Fc recombinant adenovirus. Our findings indicate that the introduction of the Fc antibody fragment into the protective antigen significantly improves the protective properties of the Ad-PA-Fc adenovirus against B. anthracis.**

**KEYWORDS** *Bacillus anthracis*, **immunization, protective antigen, recombinant adenovirus.**

**ABBREVIATIONS** **Ad – adenovirus; PFU – plaque-forming unit; PA – protective antigen; Fc – Fc-fragment of IgG2a; IFA – incomplete Freund's adjuvant; PBS – phosphate-buffered saline.**

## INTRODUCTION

*Bacillus anthracis* is a gram-positive, endospore-forming, rod-shaped aerobic bacterium that causes a dangerous infectious disease that affects susceptible animals and humans. Human anthrax cases are reported every year in many countries. Anthrax spores penetrate the body and are absorbed by macrophages, which, in turn, migrate to the local lymph nodes [1]. Inside the macrophages, the spores evolve into a vegetative form, which causes progression of the generalized infection. Due to the *B. anthracis* pathogenicity, anthrax often becomes an acute, highly lethal disease, unless preventive and curative interventions are undertaken on time [2–5].

Even today, the problem of anthrax prevention remains important, because of the yearly sporadic disease outbreaks with lethal outcomes in humans [6, 7]. In Russia, a vaccine containing the acapsular strain STI-1 is used for anthrax prevention. However, the live spore vaccine STI-1 has a number of disadvantages, including the need for annual re-vaccinations, reactogenicity, and absence of a strong immunity against certain field isolates circulating in Russia [8–12]. The chemical vaccine used in the USA is not an ideal option, as it requires six-dose vaccination series over 18 months to develop a strong immunity, which causes allergization of the re-vaccinated organism. Taking this factor into account, the issue of further exploring g anthrax

vaccines remains important both in the medical and veterinary practice: therefore, the search for means of specific anthrax prophylaxis continues.

One of the first attempts to use the adenoviral vector to immunize laboratory animals against *B. anthracis* was undertaken by a U.S. research group led by M.J. McConnell [13]. The researchers achieved expression of the secretable modification of the fourth domain of the protective antigen using the recombinant adenoviral vector and demonstrated that a single immunization of experimental animals with subsequent introduction of a lethal dose of the anthrax toxin provided 67% protection to Balb/c mice. These data indicated for the first time that adenoviral vectors carrying genes of the main protective antigen determinants could be successfully used for immunization against anthrax.

We generated recombinant adenoviruses capable of inducing a specific immune response against *B. anthracis*. The construct contained an insertion encoding a fusion protein consisting of the fourth domain of the protective antigen (PA) and the Fc-fragment of IgG2a. Two recombinant adenoviruses were genetically engineered as controls. The above-mentioned adenoviruses carried secretable and non-secretable modifications of the PA fourth domain. All three variants showed immunogenic and protective properties, inducing the synthesis of specific antibodies against *B. anthracis*. However, a recombinant adenovirus containing the insertion encoding the fusion protein (Ad-PA-Fc) demonstrated the highest level of protection in comparison with the controls Ad-sPA and Ad-cPA.

## EXPERIMENTAL

### Generation of recombinant adenoviruses

The codons in the gene encoding the protective antigen were optimized by *in silico* analysis. The two most frequent amino acid triplets were used to modify the codons in the PA-Fc gene to be expressed in *Mus musculus* cells. The most frequent codons of *M. musculus* were defined in accordance with the following database: http://www.kazusa.or.jp/codon/. The modified nucleic acid sequence encoding the fourth domain of PA fused to the Fc-fragment of antibody was synthesized by ZAO Eurogen and delivered to us in the form of a pAtlas-PA-Fc plasmid.

The NotI- and HindIII sites of the PA-Fc fragment were cloned into the shuttle vector pShuttle-CMV in order to obtain the shuttle plasmid pShuttle-CMV-PA-Fc. After that, the plasmids pShuttle-sPA and pShuttle-CMV-cPA were retrieved via restriction and subsequent ligation. pShuttle-CMV-sPA was obtained via the splitting of pShuttle-CMV-PA-Fc with XhoI restriction endonuclease, followed by ligation of the sticky ends. The corresponding C-end XhoI restriction site sat in the sequence TAACTCGAGTAAAAGCTT in such a way that after the Fc-fragment restriction a new termination codon appeared. pShuttle-cPA was retrieved from the pShuttle-CMV-sPA plasmid by deleting the site containing the leader sequence peptide tpa using the NotI and NdeI restriction endonucleases.

The method of homologous recombination was used to generate the replication-defective adenoviruses Ad-PA-Fc, Ad-cPA, Ad-sPA. For this purpose, the plasmids pShuttle-CMV-PA-Fc, pShuttle-CMV-cPA, and pShuttle-CMV-sPA were linearized by PmeI, mixed with the pAd-Easy (Adenoviral vector system, Stratogen), and then cotransformated into *E. coli* (BJ5183 strain). The obtained recombinant clones were used to extract plasmid DNA, whose molecular weight was later assessed. The *E. coli* of the DH5alpha strain were transformed with plasmids larger than 20 kbp due to the fact that this strain, unlike BJ5183, allows one to produce preparative amounts of the recombinant plasmids. The purified plasmid clones were analyzed both by splitting with the HindIII restriction endonuclease and PCR.

At the next step, we studied the infectivity of the described plasmids to permissive cells. Cells of the 293 line were transfected with the plasmids pAd-PA-Fc, pAd-sPA, and pAd-cPA, all linearized by PacI-sites. Transfection was performed in a 24-well plate using Lipofectamine 2000 (Invitrogen). Ten days after the transfection, the cells were collected and subjected to a freeze-thaw cycle; the obtained lysate containing recombinant adenoviruses was used to infect 293 cells in a 35-mm dish. After 5 days, specific lysis caused by the cytopathic effect of the recombinant viruses was detected. The lysate was used to extract DNA and perform an analysiss with PCR. The cell lysate was demonstrated to contain DNA of the recombinant human adenovirus serotype 5 carrying insertions that encode the protective antigen.

### Virus accumulation

To accumulate recombinant adenoviruses serotype 5, we used a culture of 293 cells. A cell monolayer with a confluence of 50–70% was infected with the lysate of 293 cells, which, in turn, had been previously infected with recombinant Ad with a concentration of $10^7$ PFU per 15-cm plate. After 48 h, we collected the infected cells, concentrated them by low-speed centrifugation, suspended them in a buffer (0.01 M TrisHCl pH 8.0, 0.01 M NaCl, 5 мМ EDTA), and disrupted them by triple freezing-thawing. The obtained suspension was centrifuged at 2000 rpm over 10 min at +4°C; the pellet was removed. The supernatant recombinant adenoviruses were purified via cesium chloride equilibrium density

gradient centrifugation. As a result, we obtained 3 recombinant human adenoviruses serotype 5 carrying different insertions: Ad-cPA, Ad-sPA, and Ad-PA-Fc. Dilution of the recombinant adenovirus product was estimated by means of the plaque-forming method using HEK-293 cells.

### Expression of the recombinant proteins-based adenovirus vector

Expression of three recombinant proteins containing the *B. anthracis* protective antigen was analyzed by Western blotting with monoclonal antibodies. A specimen of the protective antigen purchased from Calbiochem (176908-100UG) was used as a positive control. A549 cells were transduced with recombinant adenoviruses; after 48 h, expression of the protective antigen in the supernatant and lysed cell pellet was assessed. To analyze the Fc-domain of the antibody within the fusion protein, we resorted to Western blotting with anti-species antibodies against mice IgG, conjugated to horseradish peroxidase (Amersham).

### Production of the protective antigen in *E. coli*

A plasmid carrying the gene of the receptor domain was designed with the use of the commercial vectors pUC19 and pET28b (Novagen). We used total DNA extracted from the *B. anthracis* strain 71/1 as a matrix. The cloning was performed with NdeI and EcoRI as restriction sites. The forward and the reverse primers used for PAGR4 were GAGATCATATGGTTGGGGCGGATGAG and ATCTCGAATTCTTATCCTATCTCATAGCC, respectively. PCR fragments were extracted using kits (GE, Inc.) in accordance with their specifications. Fragments obtained after the restriction by NdeI and EcoRI sites (Fermentas) were subcloned into the pUC19 vector (*E. coli* JM109 was a recipient), and then into the pET28b vector. To extract the recombinant proteins, *E. coli* BL21 were transformed with the designed vectors. The bacterial culture grew first in a LB medium until $OD_{600}$ = 0.6–0.8, then for 3.5–4 h with IPTG (Sigma) at a concentration of 10 mM. After that, we centrifuged the bacterial mass for 15 min at 8000 *g* and then re-suspended the bacterial pellet in PBS. Subsequently, we sonicated the cells (in 3 steps, 30 s each, by an MSE disintegrator (England)) and extracted inclusion bodies by centrifugation for 40 min at 20000 *g*. The obtained pellet of inclusion bodies was dissolved in a 8-M urea solution; recombinant proteins were extracted according to a specification to Ni-NTA-sepharose (Invitrogen), using thrombin (Sigma).

### Immunogenicity

Immunogenicity of the recombinant adenoviruses encoding *B. anthracis* antigens was assessed in mice. Balb/c mice were immunized with recombinant adenoviruses twice within an interval of 2 weeks. A native protective antigen fused to an incomplete Freund's adjuvant was employed as the positive control and administered by subcutaneous injection. A recombinant adenovirus without the antigen (Ad-null) served as the negative control. Recombinant adenoviruses were administered intranasally at a dose of $4.6 \times 10^9$ PFU/mouse and in a volume of 100 μl. Two weeks following the second immunization, we drew blood samples, extracted serum, and performed its examination for antibodies.

### Immunization

The recombinant adenoviruses were introduced into the experimental animals intranasally at a dose of $15 \times 10^9$ PFU/mice. The protective antigen with the Freund's adjuvant was injected subcutaneously at a dose of 8–10 μg.

### Experimental animals

We used female Balb/c mice with a weight of 20 g.

### Challenge

To assess the protective ability of the potential genetic vaccine, the immunized animals were infected by means of intraperitoneal inoculation of the test culture at a dose of 4 $LD_{50}$. An acapsular strain *Sterne B. anthracis* was employed as an infectious agent. Both the experimental and control groups of animals were monitored for 10 days following the infection. All experiments involving animals were carried out at the National Research Institute for Veterinary Virology and Microbiology of Russia, Russian Academy of Agricultural Sciences (RAAS).

### Statistical analysis

The statistical analysis of the results was performed in Statistica 6.0. The results of the comparison of the experimental and the control group were considered statistically reliable at $p<0.05$. The survival rate was evaluated using the Mann–Whitney U-test.

## RESULTS AND DISCUSSION

### Design of the recombinant adenoviruses

The amino acid and nucleotide sequences of the fourth domain of the PA antigen were derived from UniProtKB/Swiss-Prot P13423 and GenBank M22589.1. Analysis of the PA codons of *B. anthracis* showed that many codons did not suit well for expression in eukaryotic cells. The most frequent codons of *B. anthracis* and *M. musculus* were defined according to the codon usage database http://www.kazusa.or.jp/codon/. In

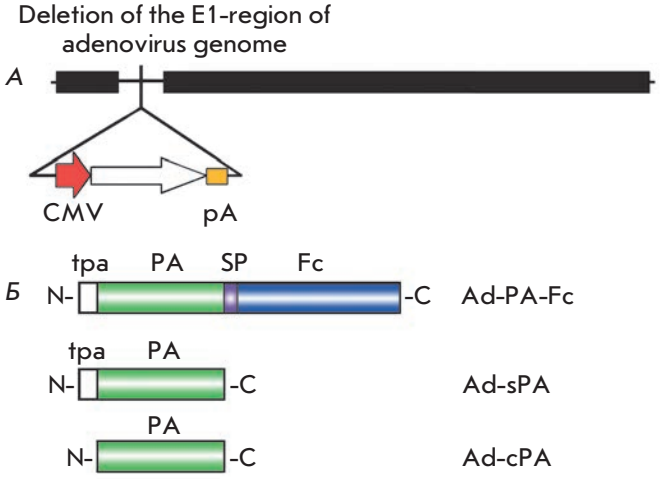


Fig. 1. Layout of the recombinant adenovirus genome carrying the protective antigen of *B. anthracis*. *A* – human recombinant adenovirus serotype 5 genome. Expression cassette is inserted into where the E1 region was deleted. CMV – cytomegalovirus promoter; pA – polyadenylation signal. *B* – antigen schematic structure; tpa – tissue plasminogen activator, PA – protective antigen, SP – glycine serine spacer, Fc –Fc-fragment of the IgG2a antibody

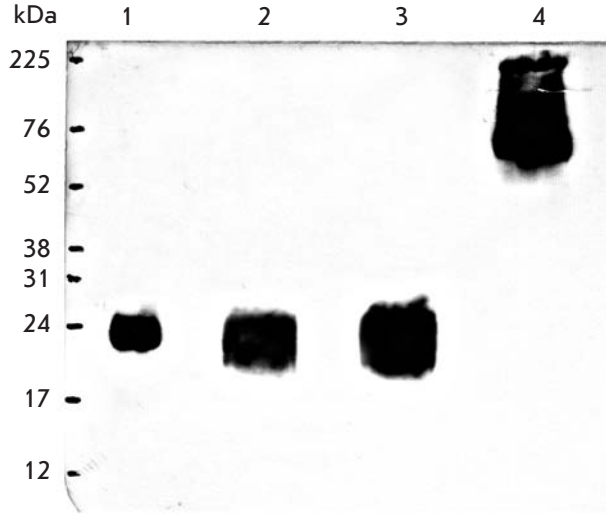


Fig. 2. Results of PA detection carried out by means of Western blotting. 1 – purified fourth domain of the receptor antigen produced in *E. coli*; 2 – lysate of the cells infected with Ad-cPA; 3 – supernatant of the cells transduced with Ad-sPA; 4 – supernatant of the cells transduced with Ad-PA-Fc

order to achieve a high rate of protein production, the codons were optimized to be translatable in the *M. musculus* cells. The amino acids and nucleotide sequences of the Fc-fragment of IgG2a were obtained from UniProtKB/Swiss-Prot P01863 and GenBank V00798.1. A 12-membered glycine-serine spacer was inserted between the PA antigen and Fc-fragment of the antibody (*Fig. 1*). Three shuttle vectors were designed on the basis of one pShuttle-CMV-PA-Fc plasmid with a number of fragments consecutively deleted.

### Properties of *in vitro* synthesized Ad-cPA, Ad-sPA, and Ad-PA-Fc

In order to obtain data on the expression and secretion of PA as part of a recombinant adenovirus, A549 cells were retransduced with three adenovirus constructs. The fourth domain of PA, produced in E. coli, was employed as the positive control. After 48 h of incubation, we assessed the presence of the fourth domain of PA in both the supernatant and pellet left after the infected cells (*Fig. 2*). The supernatant of the cells transduced with the recombinant adenoviruses Ad-sPA and Ad-PA-Fc (*lanes 3*, *4*), as well as the lysed cells transduced with the recombinant adenovirus Ad-cPA (*lane 2*), contained the mentioned domain. The purified PA fourth domain synthesized in *E. coli* also showed a positive result (*lane 1*).

### Immune response induced by the recombinant adenoviruses Ad-cPA, Ad-sPA, and Ad-PA-Fc *in vivo*

The immune response to the PA fourth domain expressed as part of the recombinant adenoviruses was studied on Balb/c mice. The mice were immunized twice within an interval of 2 weeks. Ten days following the second immunization, mouse blood was examined for specific antibodies against the PA in the serum by means of ELISA (*Fig. 3*). An unexpected result was that the blood serum of mice infected with Ad-cPA revealed a high level of specific antibodies similar to that observed in the mice immunized with the PA fused to the incomplete Freund's adjuvant. The blood serum of mice infected with Ad-sPA and Ad-PA-Fc demonstrated almost the same concentration of specific PA antibodies, which was lower than that for Ad-cPA.

### Defining subclasses of the specific IgG

The sera obtained at the previous step were also tested for subclasses of the specific IgG to the PA-antigen (*Fig. 4*). It was demonstrated that all recombinant adenoviruses induced a high-level production of IgG2a and IgG1 (*Fig. 4A, B*). The blood serum of the mice immunized with Ad-cPA and Ad-Fc-PA contained antibodies of the IgG2b subclass (*Fig. 4D*). None of the mice groups, including that of the positive control, revealed IgG3 in their blood serum (*Fig. 4C*). It is inter-

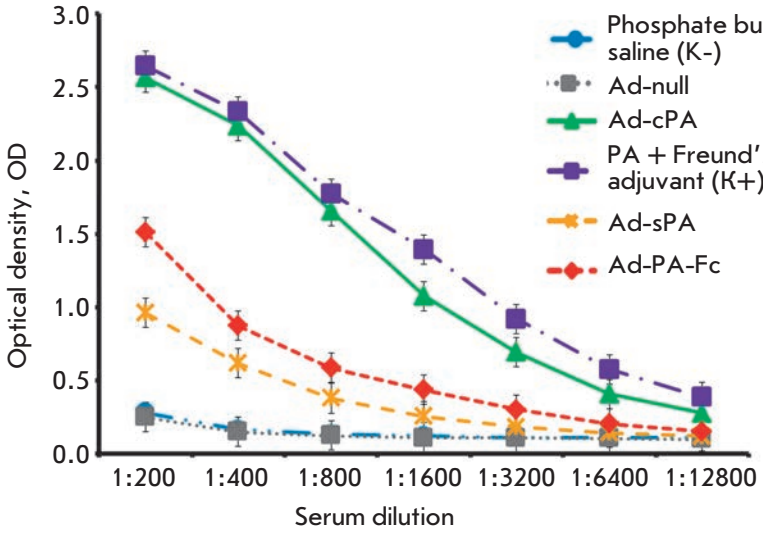


Fig. 3. Results of anti-PA antibodies in the blood serum of mice immunized with recombinant adenoviruses by ELISA. Ad-PA-Fc – recombinant adenovirus containing the PA fused to the Fc-fragment of IgG2a; Ad-cPA – recombinant adenovirus containing a non-secretable form of PA; Ad-sPA – recombinant adenovirus containing the secretable form of PA. Positive control – the PA protein fused to an incomplete Freund's adjuvant. Negative control – phosphate buffered saline (PBS)

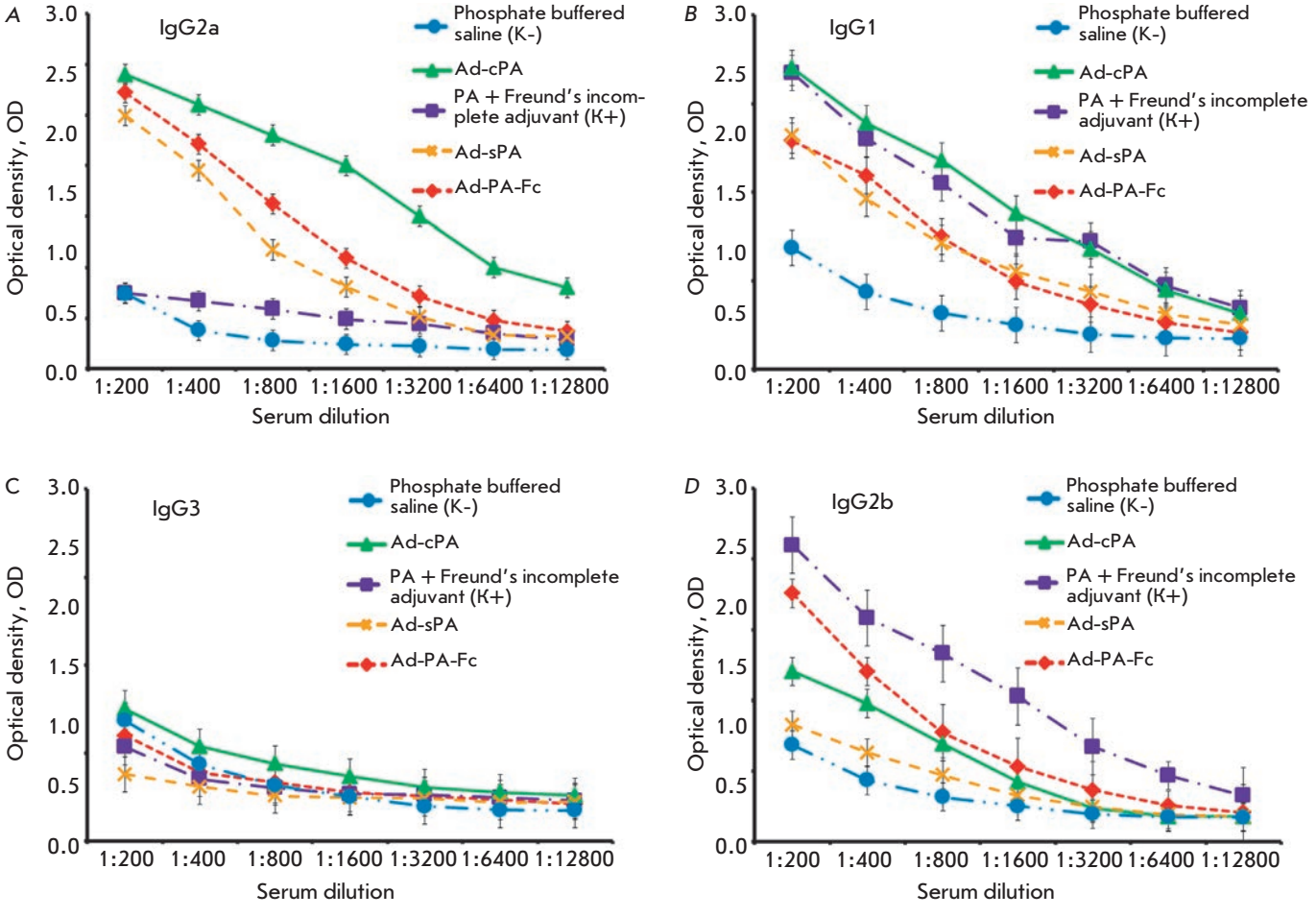


Fig. 4. Results of detection of the specific IgG against the protective antigen by ELISA in the blood serum of mice immunized with Ad-cPA, Ad-sPA, and Ad-Fc-PA. A – amount of IgG2a; B – IgG1; C – IgG3; D – IgG2b. Ad-PA-Fc – recombinant adenovirus containing the protective antigen fused to the Fc-fragment of IgG2a; Ad-cPA – recombinant adenovirus containing a non-secretable form of PA; Ad-sPA – recombinant adenovirus containing a secretable form of PA. Positive control – PA protein fused to a incomplete Freund's adjuvant. Negative control – phosphate buffered saline (PBS)

Table 1. Protective ability of genetic vaccines based on the recombinant adenoviruses in Balb/c inbred white mice as a model

| Group of animals | Immunizing product | Balb/c mice | Survived | Died | Protection, % |
|---|---|---|---|---|---|
| 1 | PA + IFA | 10 | 3 | 7 | 30 |
| 2 | Ad-PA-Fc | 10 | 9 | 1 | 90 |
| 3 | Ad-cPA | 10 | 8 | 2 | 80 |
| 4 | Ad-sPA | 10 | 8 | 2 | 80 |
| 5 | Ad-null | 10 | 2 | 8 | 20 |

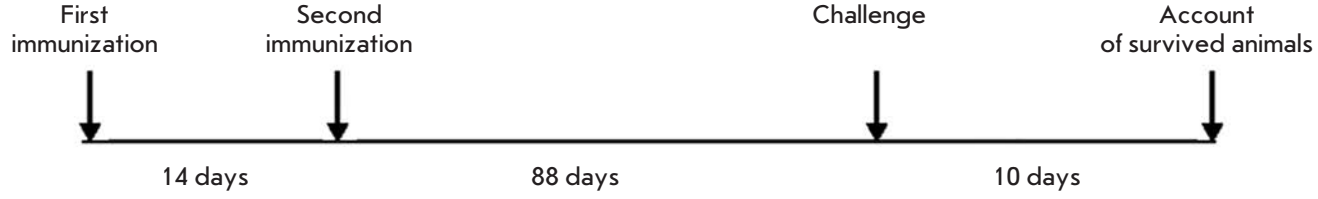


Fig. 5. Schematic view of the protection of immunized animals against *B. anthracis*. Recombinant adenoviruses were administered intranasally at a dose of 4.6 × 109 PFU/mouse, in a volume of 100 µl. Native PA protein with an incomplete Freund's adjuvant was employed as a positive control

esting to mention that immunization with the PA fused to the incomplete Freund's adjuvant failed to induce the production of IgG2a, but it triggered that of IgG2b and IgG1 subclasses.

### Examination of the protective abilities of the recombinant adenoviruses by the control challenge

To assess the protective ability of the humoral immune response induced by the designed recombinant adenoviruses, we infected the immunized mice with a lethal dose of the *B. anthracis, Sterne* strain (4 $LD_{50}$). In a week, 80% of the control group animals vaccinated with the recombinant adenovirus without insertion (Ad-null) died. All the constructs with the protective antigen provided protection against *B. anthracis* in 80–90% of the animals (*Table 1*).

The duration of a strong immunity against anthrax was preliminary estimated as follows (*Fig. 5*). Balb/c mice were immunized with the recombinant adenoviruses at a dose of $4.6 \times 10^9$ PFU/mouse within an interval of two weeks. Eighty-eight days later, they were infected with *B. anthracis* of the *Sterne* strain (4 $LD_{50}$). *Table 2* shows that after the introduction of *B. anthracis* of the *Sterne* strain, 90–100% of the mice vaccinated with the recombinant adenoviruses survived. Mice immunized with Ad-PA-Fc demonstrated a stronger immunity than those immunized with Ad-sPA and Ad-cPA. Moreover, animals immunized with Ad-sPA and Ad-cPA lost weight and showed signs of sickness, unlike those immunized with Ad-PA-Fc.

## DISCUSSION

In 2003 Y. Tan designed the first recombinant adenovirus serotype 5 encoding a protective antigen modified to be expressed in human cells [14]. It was demonstrated that intramuscular introduction of $10^9$ viral particles induced the production of anti-PA-antibodies in an amount 2.7 times higher than that produced upon immunization with the subunit human vaccine used in the USA. It is remarkable that the recombinant adenovirus induced a faster humoral immune response than the subunit vaccine. When immunization was followed by administration of the anthrax toxin, mice immunized with the recombinant adenovirus demonstrated immunity in 75% of cases, whereas the subunit vaccine provided protection only in 25% of cases.

In 2005, the same authors performed an analogous study for the recombinant adenovirus serotype 7 [15]. They demonstrated that the preexisting immune response to adenovirus serotype 5 in mice can be overridden by an adenovirus of a different type and that this allows one to protect animals from a lethal dose of the anthrax toxin.

A similar feature is that not the entire amino acid sequence of the PA was employed as an antigen, but only its fourth domain. The reason behind this was

Table 2. Protective ability of genetic vaccines based on the recombinant adenoviruses in Balb/c inbred white mice as a model

| Group of animals | Immunizing product | Balb/c mice | Survived | Died | Protection, % |
|---|---|---|---|---|---|
| 1 | Ad-PA-Fc | 9 | 9 | 0 | 100 |
| 2 | PA + IFA | 9 | 9 | 0 | 100 |
| 3 | Ad-sPA | 9 | 8 | 1 | 89 |
| 4 | Ad-cPA | 9 | 8 | 1 | 89 |
| 5 | Ad-null | 9 | 1 | 8 | 11.1 |
| 6 | PBS | 9 | 1 | 8 | 11.1 |

that the mentioned domain was essential for binding the cell receptor: so, one could achieve a protective immune response by blocking the domain with antibodies. For example, Z. Yu *et al.* designed two plasmids carrying codes of secretable and non-secretable forms of the PA fourth domain [16]. After the immunization of animals with these plasmids, an increase in the IFN-γ level was observed along with the secretion of anti-PA-antibodies. The authors of another study, J. McConnell *et al.* [13], achieved expression of the PA fourth domain encoded by the adenoviral vector. At a single immunization with subsequent introduction of a lethal dose of the anthrax toxin, experimental animals demonstrated immune protection in 67% of cases. The next study by the same authors was devoted to the protective effect of the recombinant adenovirus in mice infected with a lethal dose of the vaccine strain 34F2 [17]. They resorted to prime-boost immunization. Priming with plasmid DNA followed by boosting with the recombinant adenovirus, as well as priming with recombinant adenovirus followed by boosting with the recombinant adenovirus, fully protected mice against *B. anthracis*. These results indicate that vaccination with the recombinant adenovirus protects against anthrax infection, and that this approach can be effective in immunization against bacterial and viral pathogens.

The remarkable feature of our study was that we demonstrated that dimerization of the protective antigen with the Fc-fragment of the antibody increases the immunogenicity of the former and the ability of the above-mentioned fragment to bind specifically to macrophages through Fc-receptors and activate the complement system via the classical pathway.

The dimer-forming ability allows two antigen determinants to reside in the same particle, which increases the immunogenicity of the fusion protein [18, 19]. Activation of multichain immune recognition receptors (MIRR receptors) is probably a mechanism inducing the increase in immunogenicity. When ligands bind, MIRR receptors transduce the signal via ITAMs, whose activation leads to the merging of immune complexes and to the merging of endosomes with MHCII-containing vesicles [20, 21].

On the other hand, if the unit of the fusion protein capable of oligomerization or the antigen itself can interact with the pattern recognition receptor, this helps increase immunogenicity up to a maximum and to avoid additional adjuvants [18]. As a result, the protein capable of oligomerzation acts as a "molecular adjuvant." In our study, we added the Fc-fragment of IgG2a of *M. musculus* to the protective antigen in the fusion protein. The Fc-fragment of the antibody can activate the classical pathway of the complement system, whose pattern recognition receptors (PR) deliver an essential co-stimulatory signal [22]. The combined actions of MIRR and PR receptors in the same cell result in the presentation of the antigen peptides to helper T lymphocytes, which can assist both T- and B-cells. Possibly, this is the reason as to why the above-mentioned recombinant adenovirus carrying PA-Fc provides a stronger protection than Ad-sPA and Ad-cPA (see *Table 1*).

Another aspect that is important to mention is the use of an adenovirus vector as a carrier of the synthesized gene. Due to the fact that the gene is synthesized inside the cells transduced with the recombinant adenovirus, some antigen molecules undergo processing and peptide presentation, together with MHC I molecules. The complexes that are formed on activated cells induce cytotoxic T-lyphocytes, which aid in the protection against intracellular pathogens, including *B. anthracis* [14, 15, 23]. In our study, in order to estimate the activity of cytotoxic T-lymphocytes, we designed the recombinant adenovirus Ad-cPA carrying a non-secretable modification of the protective antigen and showed it to protect 89% of experimental animals (*Table 2*). On the other hand, the secretable form of the protective antigen (Ad-sPA) provided almost

the same level of protection without "molecular adjuvants." Thus, the results we obtained fully correlate with those obtained by other groups of researchers [16]. We assume that the use of the recombinant adenoviral vectors Ad-sPA and Ad-cPA helps to induce antigen-specific cytotoxic T-lymphocytes.

In the present study we resorted to the intranasal introduction of adenoviral vectors, because it is this particular way of delivering recombinant adenoviruses that helps to override the preexisting immune response to the vector [24]. Intranasal introduction has a number of advantages in comparison with other ways: it is a needle-free, non-invasive and painless procedure that requires no medical staff and can be performed by the vaccinated individuals themselves. In addition, the data obtained by J. Zhang *et al.* [24] demonstrated that a single intranasal immunization with a recombinant adenoviral vector carrying the gene of the protective antigen protects mice against *B. anthracis* on condition of preexisting immune response to the adenoviral vector.

It is interesting to note that immunization with recombinant adenoviruses induces IgG to belong to the same class as the protective antigen. Our experiments revealed antibodies belonging to the subclasses that are produced at an immune response of the Th1 type (characterized by the highest level of IgG2a antibodies), whereas when an incomplete Freund's adjuvant is used, an immune response of the Th2 type (characterized by the highest level of IgG2b antibodies) is induced. One may assume that this was the reason as to why mice immunized with the recombinant adenoviruses during the first experiment were better protected than those from the positive control group (*Fig. 4*) (*Table 1*). Our results correlate with the data of Y. Tan *et al.* [14], who demonstrated an analogous profile of the antibody subclasses upon adenoviral immunization. A remarkable distinction of our study was the total absence of IgG3, whereas Y. Tan's group detected the above-mentioned subclass, even though in a lesser amount than that of other IgG.

It is remarkable that there can be two classes of antibodies produced in response to the *B. anthracis* protective antigen. The first type of antibodies are able to bind single molecules of the protective antigen and neutralize them, i.e., to sterically block protein-protein interactions between the PA molecules. Antibodies of the second type interact only with the oligomeric complexes of the protective antigen and change their structure in such a way that those are no longer able to interact with the receptors on the cell surface [25]. This means that antibodies of the second type are produced only in the presence of oligomerized molecules of the antigen, a complex of which threads through the membranes of eukaryotic cells. Since the fourth domain of PA resides on the C-end of the protein, and in our construct (PA-Fc) it resides on the N-end (to provide the Fc-fragment of the antibody with a higher functional activity), we designed a recombinant adenovirus carrying the Fc-fragment at the N-end of the protein and the fourth domain of PA – at the C-end of the protein. The designed recombinant adenovirus (Ad-Fc-PA) was studied in the described experiments. It was shown that it exhibited the same immunogenic and protective properties as the recombinant adenovirus Ad-PA-Fc (data are not presented).

## CONCLUSIONS

We have shown that immunization with the recombinant adenovirus protects against the acapsular strain of *B. anthracis*. Ad-PA-Fc carrying the Fc-fragment of the antibody fused to the protective antigen provides a higher level of protection compared to Ad-sPA and Ad-cPA. Besides, immunization with Ad-PA-Fc can confer full immunity to mice during the following three months. Our plans for the future are to experiment on guinea pigs with sporules of endospore-forming strains of *B. anthracis*. ●

REFERENCES

1. Guichard A., Nizet V., Bier E. // Microbes Infect. 2012. V. 14. № 2. P. 97–118.
2. Brachman P.S. // Ann. N.Y. Acad. Sci. 1980. № 353. P. 83–93.
3. Davies J.C.A. // Central African J. Med. 1982. № 28. P. 291–298.
4. Davies J.C.A. // Central African J. Med. 1983. № 29. P. 8–12.
5. Davies J.C.A. // Central African J. Med. 1985. № 31. P. 176–180.
6. Metcalfe N. // Occup. Med. 2004. V. 54. № 7. P. 489–493.
7. Meaney-Delman D., Zotti M.E., Rasmussen S.A., Strasser S., Shadomy S., Turcios-Ruiz R.M., Wendel G.D., Treadwell T.A., Jamieson D.J., Gladus M.A., et al. // Obstet. Gynecol. Dec. 2012. V. 120. № 6. P. 1439–1449.
8. Ipatenko N.G., Gavrilov V.A., Manichev A.A., Bastarov S.I., Salenko L.S., Yakovleva T.N., Stepanova V.V., Shmorgun B.I., Kiselev Yu.T., Sayitkhulov B.S. // Veterinary. 1995. № 5. C. 27–30.
9. Auerbach S., Wright G.G. // J. Immunol. 1955. V. 75. № 2. P. 129–133.
10. Broster M.G., Hibbs S.E. // Salisbury Med. Bull. Sp. Suppl. 1990. № 68. P. 91–92.
11. Little S.F., Knudson G.B., Neidhardt F.C. // Ann. Meet. Amer. Soc. Microbiol. 1984. P. 46.
12. Ward M.K., McGann V.G., Hogge A.L., Huff M.L., Kanode R.G., Roberts E.O. // J. Infect. Dis. 1965. № 115. P. 59–67.
13. McConnell M.J., Hanna P.C., Imperiale M.J. // Infect. Immun. 2006. V. 74. № 2. P. 1009–1015.
14. Tan Y., Hackett N.R., Boyer J.L., Crystal R.G. // Hum. Gene. Ther. 2003. V. 14. № 17. P. 1673–1682.

15. Hashimoto M., Boyer J.L., Hackett N.R., Wilson J.M., Crystal R.G. // Infect. Immun. 2005. V. 73. № 10. P. 6885–6891.
16. Yu Y.Z., Li N., Wang W.B., Wang S., Ma Y., Yu W.Y., Sun Z.W. // Vaccine. 2010. V. 28. № 47. P. 7529–7535.
17. McConnell M.J., Hanna P.C., Imperiale M.J. // Mol. Ther. 2007. V. 15. № 1. P. 203–210.
18. Shcherbinin D. N., Shmarov M.M., Naroditsky B.S., Rubakova E.I., Kondrateva T.K. // Tuberculosis and lung diseases. 2010. V. 87. № 10. P. 50–53.
19. Shcherbinin D. N., Tutyhina I.L., Logunov D.U.,Shmarov M.M., Apt A.S., Kondrateva T.K. Naroditsky B.S. //Med. immunol. 2010. V. 13. № 4–5. P. 347.
20. Sigalov A.B. // Adv. Exp. Med. Biol. 2008. № 640. P. 121–163.
21. Graham D.B., Akilesh H.M., Gmyrek G.B., Piccio L., Gilfillan S., Sim J., Belizaire R., Carrero J.A., Wang Y., Blaufuss G.S., et al. // Blood. 2010. V. 116. № 17. P. 3208–3218.
22. Walport M.J. // N. Engl. J. Med. 2001. V. 344. № 14. P. 1058–1066.
23. Tutykhina I.L., Logunov D.Y., Shcherbinin D.N., Shmarov M.M., Tukhvatulin A.I., Naroditsky B.S., Gintsburg A.L. // J. Mol. Med. 2011. V. 89. № 4. P. 331–341.
24. Zhang J., Jex E., Feng T., Sivko G.S., Baillie L.W., Goldman S., van Kampen K.R., Tang D.C. // Clin. Vaccine Immunol. 2013. V. 20. № 1. P. 1–8.
25. Radjainia M., Hyun J.K., Leysath C.E., Leppla S.H., Mitra A.K. // Proc. Natl. Acad. Sci. USA. 2010. V. 107. № 32. P. 14070–14074.

# Development of Immunoassays Using Interferometric Real-Time Registration of Their Kinetics

A. V. Orlov[1,2], A. G. Burenin[1,2], V. O. Shipunova[2], A. A. Lizunova[2], B. G. Gorshkov[1], P. I. Nikitin[1*]
[1]Prokhorov General Physics Institute, Russian Academy of Sciences, Vavilov Str., 38, 119991, Moscow, Russia
[2] Moscow Institute of Physics and Technology, Institutskiy per., 9, 141700, Moscow Region, Dolgoprudny, Russia
*E-mail: nikitin@kapella.gpi.ru
Received 15.05.2013


**ABSTRACT** **A method for effective development of solid-phase immunoassays on a glass surface and for optimization of related protocols by highly sensitive quantitative monitoring of each assay step has been proposed and experimentally implemented. The method is based on the spectral correlation interferometry (SCI) that allows real-time measuring of the thickness of a biomolecular layer bound to the recognition molecular receptors on the sensor chip surface. The method is realized with compact 3-channel SCI-biosensors that employ as the sensor chips standard cover glass slips without deposition of any additional films. Different schemes for antibody immobilization on a glass surface have been experimentally compared and optimized toward a higher sorption capacity of the sensor chips. Comparative characterization of the kinetics of each immunoassay stage has been implemented with the optimized protocols: i) covalent immobilization of antibody on an epoxylated surface and ii) biotinylated antibody sorption on a biotinylated surface via a high-affinity biotin-streptavidin bond. We have shown that magnetic nanoparticles employed as labels with model detection of cardiac troponin I further amplify the SCI signal, resulting in 100-fold improvement of the detection limit. The developed protocols can also be used with the alternative immunoassay platforms, including the label methods based on registration of only the final assay result, which is the quantity of bound labels.**
**KEYWORDS** **Label-free biosensors, interferometry, sensor chips, surface functionalization, surface epoxylation, surface biotinylation, efficiency of biomolecular immobilization, immunoassay, magnetic nanoparticles, cardiac troponin I.**
**ABBREVIATIONS** **AR – analytical grade; APTES – (3-Aminopropyl)triethoxysilane; BSA –bovine serum albumin; cTnI – cardiac troponin I; DMF – dimethylformamide; GLYMO – (3-glycidyloxypropyl)trimethoxysilane; MNP – magnetic nanoparticles; PBS – phosphate buffered saline; SCI – spectral correlation interferometry.**

## INTRODUCTION

In recent years much attention has been focused on studies of methods for the identification of the protein markers of diseases in complex biological fluids such as blood, serum, saliva and others. The development of immunoassay methods for detection of these substances is of high importance for clinical [1] and emergency [2] diagnostics, control of treatment efficiency [3], discovery of new specific antigens as disease markers [4], drug development [5–7], etc. One of the most common immunoassay formats [8] that provides high sensitivity, accuracy, and specificity is the solid phase sandwich immunoassay [9, 10]. It is based on formation of a "capture antibody-antigen-tracer antibody" complex on the solid phase, which is possible only in the presence of the antigen under test. The result is recorded with the use of different labels (enzymatic [11], latex [12], gold [13], magnetic [14, 15] and others) conjugated with tracer antibodies either covalently or by a highly affine intermediate bond, e.g., antibody-antigen [16], biotin-streptavidin [17], or barnase-barstar [18, 19].

The key characteristics of immunoassays (detection limit, linear and dynamic range, sensitivity, and specificity) depend on the selected antibodies, mode of their immobilization on the solid phase, square of the solid phase surface, incubation time and concentration of immunoreagents, as well as on the composition of the buffer and stabilizing solutions [20]. If one uses the label-based methods, the contribution of each of

the mentioned parameters can be estimated only at the final stage of the immunoassay. Label-free optical methods can substantially increase the efficiency of development of immunoassay protocols due to real-time monitoring of all stages of the biochemical reactions and through reducing the assay duration and number of operations. The methods that employ expensive sensor chips with precisely deposited gold films [21, 22], optical dielectric films with a regulated refractive index [23], porous silicon structures with a fixed porosity depth [24] can be named among the most commonly used techniques. As a result, many methods are too costly compared to the conventional ELISA for diverse applications that require disposable consumables.

Earlier, we proposed the original methods of spectral phase [25, 26] and spectral correlation interferometry [27–29] for registration of biomolecular interactions on the surface of plane-parallel transparent plates, e.g., inexpensive glass cover slips, either without any coating or coated with thin films typical for the surface layers of biosensor chips. These methods were successfully employed for quantitative detection of conformational changes in polymers [30], identification of disease markers in blood serum [31], pyrethroids in environmental monitoring [32], and discovering the functional mechanisms of drugs [33].

This work was aimed at developing a method for optimization of sandwich-type immunoassays using real-time monitoring of each assay stage with the spectral correlation interferometry. Optimization of the magnetic immunoassay [15, 34, 35] that employs magnetic nanoparticles as labels has been performed as an experimental demonstration of the developed method.

## EXPERIMENTAL

### Reagents

A complex of subunits of the cardiac troponins I, T and C, monoclonal antibodies to cardiac troponin I (clones 19C7 and 16A11), conjugates of monoclonal antibodies to cardiac troponin I (clones 19C7 and 16A11) with biotin were kindly provided by prof. A.G. Katrukha (Immunology Group at Moscow State University, Moscow). (3-Aminopropyl)triethoxysilane, (3-glycidyloxypropyl) trimethoxysilane, and biotin N-hydroxysuccinimide ester were purchased from Sigma Aldrich (USA); commercially available nanoparticles of ~50 nm composed of several crystals of ferric oxide and covered with a polymeric coating with covalently conjugated recognition biomolecules of streptavidin or monoclonal rat anti-mouse antibodies to isotype IgG1 were obtained from Miltenyi Biotec (Germany) . Other reagents were at least of analytical grade.

### Characterization of magnetic nanoparticles (MNP)

Microphotographs of MNP were made using a JEOL JEM-2100 transmission electron microscope with an accelerating voltage of 200 kV.

### The method of spectral correlation interferometry (SCI)

The spectral correlation interferometry (SCI) method described in detail in Refs. [27-29] employs two Fabry–Pérot interferometers in an original optical setup with the use of superluminescent diode radiation. The first interferometer base (distance between the mirrors) is periodically changed by a piezoelectric driver. A transparent plane-parallel plate made, for instance, of glass or plastic without any coating or with partially transparent films deposited on its surface, serves as the second interferometer and, simultaneously, as the sensor chip. In this work, a glass cover slip with immobilized receptor molecules on its surface is used as the sensor chip. It has been shown that such slips with a thickness of 100 μm can perform as acceptable Fabry–Pérot interferometers if the size of each separate registration area is 2–8 mm. Within such a distance, the thickness variations of the standard cover slips are less than a quarter of the radiation wavelength.

The SCI method uses the interference between a reference beam reflected from the lower surface of the cover slip and a probe beam reflected from the upper glass surface with biorecognition molecules (*Fig. 1A*). During the biochemical reaction under study, biomolecules from the solution (ligands) bind to the receptor molecules on the sensor chip, thus increasing the optical path of the probe beam reflected from the "liquid-biolayer" interface. The result of interference of these two beams depends on the biological layer thickness, whose variations during the reaction are calculated using the changes in the phase of the correlation signal while scanning the base of the first interferometer.

The SCI method is realized as the Picoscope® family of devices (*Fig. 1B*), which allows real-time registration of the dynamics of the molecular reactions on the surface of the cover slips with the picometer resolution of thickness averaged over the observation spot [28]. In the used instrument realization, the sensor chip was placed inside the device and covered with a cuvette that provided three independent channels. Each channel was connected to a flow system that provided the reagent supply along the upper surface of the slip. The channel height was 0.1 mm; linear dimensions were 3.5 × 1.7 mm. The reagents were supplied at 7.5 μl/min at room temperature. The optical detection in each channel was performed using the spectrum of interfering beams reflected from the lower surface of the sensor chip in a registration spot of 1 $mm^2$ in the cen-

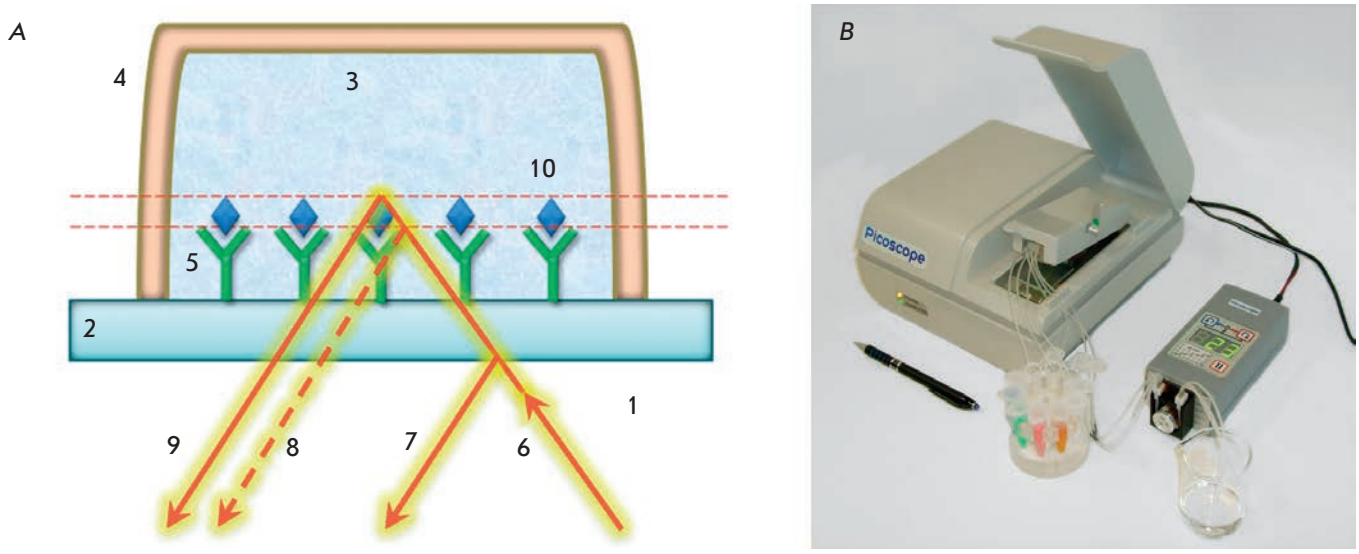


Fig. 1. The SCI principle. Changes in the optical thickness of a biolayer on a glass surface are recorded by a spectrum of interfering beams reflected from the sensor chip (A): 1 – air; 2 – microscopic glass cover slip; 3 – test solution; 4 – flow channel; 5 – receptor molecules; 6 – incident beam of superluminescent diode; 7,9 – reflected beams; 8 – position of the reflected beam before a biochemical reaction; 10 – detected biomolecules. (B): Photo of a three-channel Picoscope® biosensor

tral part of the channel. Picoscope® allows one to use the sensor chips with preliminarily immobilized antibodies [28]. In this work, the immobilization was performed directly in the flow inside the device to permit quantitative monitoring.

### Cleaning the glass slip surface

The chemical modifications of the glass surface described below were performed according to the techniques developed for the detection of the cardiac troponin concentration based on the approaches discussed in [32].

In order to clean and increase the density of hydroxyl groups on the surface, the cover slips were washed with methanol and immersed in a 1 : 3 solution of 30% hydrogen peroxide and 95% sulfuric acid for incubation for 40 min at 70°C. The slips were then washed thrice with tri-distilled water and twice with methanol. After the cleaning, the slips were immediately subjected to further chemical modification.

### Amination of the glass slips and antibody immobilization

Aminated glass slips were prepared as follows: the cleaned glass slips were immersed in a 3% APTES solution in methanol and incubated overnight at room temperature, washed thrice in isopropanol, and dried. The aminated slips were stored at room temperature until usage.

For covalent immobilization, 5 µl of the antibody (1 mg/ml) was mixed with 1 mg of 1-ethyl-3-(3-dimethylaminopropyl)carbodiimide (EDC), 2 mg N-hydroxysuccinimide (NHS) and 35 µl of a 10 mM phosphate buffer (pH 5.0), and incubated for 15 min. Next, 160 µl of phosphate buffered saline (PBS), pH 7.4, was added and the resulting solution was passed over the surface of the aminated glass slips in the flow system of the Picoscope® biosensor for 10 min.

### Epoxylation of the glass slips and antibody immobilization

The clean glass slips were immersed in a 5% GLYMO solution in methanol and incubated for 16 h at room temperature. The slips were then washed thrice in isopropanol and dried in an exsiccator for 1 h at 105°C. The slips were stored at room temperature until usage. Immobilization of antibodies was performed directly in the flow system of the device by passing the respective antibody solution of 25 µg/ml in PBS over the glass slip surface.

### Biotinylation of the glass slips and antibody immobilization

The aminated glass slips were immersed in a solution containing a 10 mM biotin N-hydroxysuccinimide ester and 500 mM triethylamine in dimethylformamide (DMF) for 2 h at room temperature. Following washing with DMF and methanol, the slips were dried and

stored at room temperature until usage. For antibody immobilization, the solutions of streptavidin and the respective biotinylated antibody both at a concentration of 25 μg/ml in PBS were consecutively passed over the glass slip surface in the flow system of the device, both processes being monitored by a sensogram that showed the thickness increase of the biomolecules on the surface.

### Carboxylation of the glass slips and antibody immobilization

The aminated glass slips were immersed in a solution containing 15 mM succinic anhydride in DMF for 2 h. After triple washing in DMF, the slips were dried and stored at room temperature until usage. Then, the slips were immersed in a mix of 10 mM EDC and 15 mM NHS in DMF for 15 min. After washing in DMF, the slips were dried. The sorption of the capture antibody at a concentration of 25 μg/ml in PBS was performed in the flow system of the device, along with control of the layer thickness averaged over the sensing area.

### Immunoassay for troponin detection

The following immunoreagent solutions in PBS (pH 7.4) were consecutively passed over the biotinylated surface of the sensor chip: 1) streptavidin – 25 μg/ml, 2) biotinylated capture antibody (clone 19C7) to troponin – 25 μg/ml, 3) a complex of subunits of the cardiac troponins I, T and C with the addition of 100 μg/ml BSA and 0.01% glycine, 4) tracer antibody (clone 16A11) to troponin – 25 μg/ml, and 5) magnetic particles with 0.1% BSA. Between the immunoreagents, PBS was passed for 3 min for washing. The immunoassay on the aminated, epoxylated, and carboxylated surfaces of the sensor chips was done in the same way but a 25 μg/ml solution of the native capture antibody (clone 19C7) to troponin was passed instead of steps 1 and 2 . The detection limit was calculated by the 2σ criterion as the minimal antigen concentration at which the recorded signal exceeded the signal of the negative control in the absence of the antigen for at least two values of the standard deviation of the signal of the negative control.

### Determination of the observed kinetic association constant

Determination of the observed kinetic association constant was based on the theoretical model of equilibrium association [36] adapted to the biosensor system in use. The values of the kinetic constants of association $k_a$ and dissociation $k_d$ as well as of the maximal signal $R_{max}$ were chosen to provide best fitting of the observed sensogram sections during passing the analyte at concentration $C$ to the approximating function:

$$R_t = Ck_aR_{max}\{1-\exp[-(Ck_a + k_d)t]\}/(Ck_a + k_d).$$

## RESULTS AND DISCUSSION

### Subject of the study

Cardiac troponin I (cTnI) was chosen as a model antigen for demonstration of the immunoassay. cTnI is a specific marker of myocardial infarction [37]. It is localized in the cardiac muscle and participates in the regulation of its contraction. Upon injury of the cardiac muscle, troponin I enters the bloodstream [38], and its presence in blood allows one to distinguish acute myocardial infarction from other diseases with similar symptoms. The normal presence of this cardiomarker in the blood of healthy donors estimated by the 99$^{th}$ percentile of the control group slightly varies between tests from different manufacturers and accounts for 0.01–0.1 ng/ml [39]. Troponin concentration starts increasing in the first hours from myocardial infarction, reaches its peak in 24–48 h, when it can exceed 1000 ng/ml [40], but then returns to a normal level after 5–14 days [41]. Moreover, this marker helps to estimate the risk of cardiovascular diseases in healthy persons, as well as complications in the postinfarction period [42]. Currently, antibodies to cTnI have been developed that demonstrate low cross-reactivity and high specificity [43], and they are commercially available. Despite a considerable number of techniques proposed for cTnI registration [44], the extremely high requirements to detection of this substance still dictate the demand for new, faster and more sensitive approaches. Therefore, the purpose of this research was creating a tool for quantitative real-time monitoring of all stages of immunoassays to accelerate and simplify the development of a wide spectrum of detection techniques.

### Comparative analysis of different schemes of antibody immobilization

The conventional method of sandwich immunoassay comprises several stages: a) antibody immobilization on the surface of a sensor chip (in commercial tests, this is usually done beforehand); b) antigen binding to the immobilized antibody; c) recognition of another epitope of the antigen by tracer antibody; d) association of labels with the tracer antibodies and detection of the labels. The assay characteristics largely depend on the surface chemistry of antibody immobilization on the solid phase. A comparative analysis of four different schemes of glass surface functionalization shown in *Fig. 2* was performed with the use of a Picoscope® biosensor.

The sensograms (dependence of the biolayer thickness on the sensor chip upon time) for the abovemen-

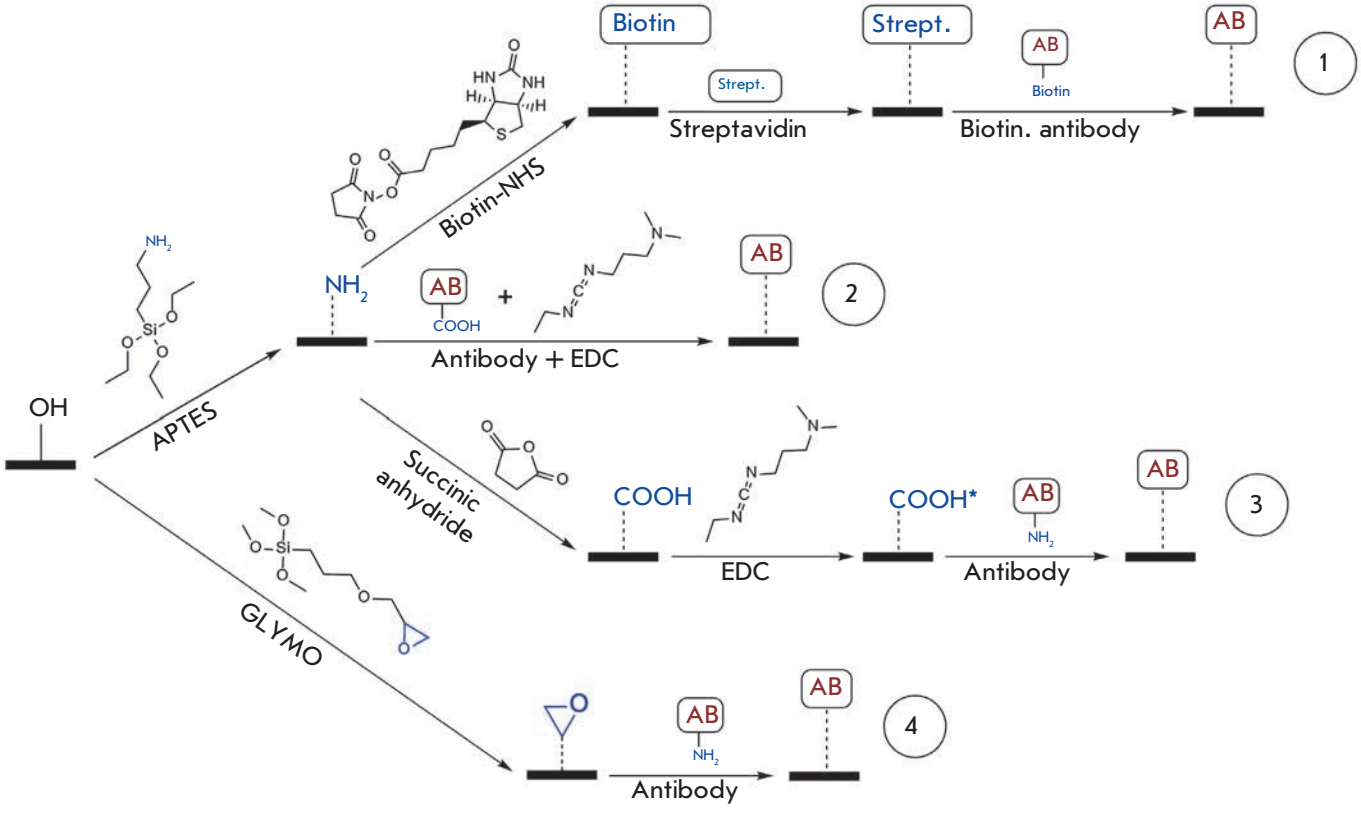


Fig. 2. Schemes of antibody immobilization on a glass surface: non-covalent sorption of biotinylated antibody on a biotinylated surface (1); covalent sorption on aminated (2), carboxylated (3) and epoxylated (4) surfaces

tioned schemes at the stage of antibody immobilization are shown in *Fig. 3*. These sensograms allow one to estimate the kinetic parameters and integral density of antibody sorption. From this figure we notice that the maximum immobilization rate and the highest sorption density for the selected conditions are achieved with schemes 2 and 4, while scheme 3 features slower sorption and lower immobilization density. These results demonstrate quantitative real-time monitoring of the antibody immobilization process with the proposed approach. Meanwhile, an unambiguous comparison of the selected schemes is beyond the scope of this work as not all the conditions have been preliminarily optimized.

It is worth noticing that the integral density of antibody sorption estimated at the immobilization stage by the change in the biolayer thickness $\Delta d_{AB}$ may differ from the density of biologically active antibodies on the solid phase surface, because the antibodies may lose their ability to bind antigen during sorption due to partial denaturation, steric inaccessibility of binding sites during the unoriented sorption, etc. As an example, the antibody inactivation may occur while using scheme 2 due to the formation of crossed peptide bonds between different molecules after incubation with carbodiimide. As it is shown below, the SCI method allows one to quantitatively estimate the loss of antibody activity under various immobilization schemes by registration of antigen binding.

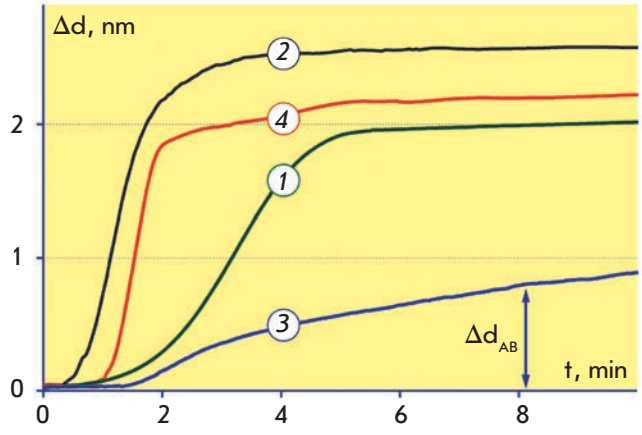


Fig. 3. Sensograms of antibody immobilization on biotinylated (1); aminated (2), carboxylated (3) and epoxylated (4) surfaces

It should be noted that schemes 2 and 3 require preliminary activation of the sensor chip surface or antibodies by carbodiimide. Besides time consumption, this activation may lead to insufficient reproducibility of the results in practical conditions when maintaining carbodiimide stability is challenging. Schemes 1 and 4 were chosen for subsequent experiments because of their efficiency and ease of use in laboratory conditions.

### Optimization of protocols for antibody immobilization

The protocols for antibody immobilization have been optimized to achieve a high sorption capacity of the sensor surface, which is an essential factor for immunoassay sensitivity. The representative sensogram shown in *Fig. 4* illustrates the consecutive changes in the biolayer thickness in response to antibody immobilization on the epoxylated surface and binding of cardiac troponin from the analyte solution containing 0.5 μg/ml cTnI. 3-min PBS washing before inlet of the analyte solution corresponds to a short horizontal fragment of the sensogram, where the biolayer thickness is virtually unchanged.

As a criterion of optimization of the antibody immobilization process, we chose the maximum change in the biolayer thickness $\Delta d_{AG}$ registered while passing 1 μg/ml antigen solution over the surface of the sensor chips prepared by both methods. The $\Delta d_{AG}$ value is proportional to the quantity of antigens bound to the antibodies immobilized on the sensor chip surface and characterizes the density of biologically active antibodies on the solid phase surface, which is a more important parameter for the assay sensitivity than the integral density of the immobilized antibodies.

For the selected schemes, we studied the dependence of antibody immobilization efficiency on the time of initial incubation of the glass slips with the surface-modifying agents (APTES and GLYMO), as well as on the volume concentration of water in the incubation solution. The latter parameter affects the ratio of surface modification rates, copolymerization of organosilanes molecules in the solution, and hydrolysis of their functional groups [45] that define the efficacy of the subsequent immobilization of antibodies: their surface density (optical thickness) and reactivity. It has been shown that the maximum increase in the antigen layer at the stage of immunoassay is achieved if the initial modification of the cover slips lasts 16 h and the volume concentration of water is 1% and 0.1% for APTES and GLYMO, respectively. To illustrate, the representative plot of the signal versus incubation time for GLYMO is shown in *Fig. 5*. One should note that the maximum biolayer thickness and, thus, the assay sensitivity were achieved if the sensor surface modification was 16 h. The shape of this experimental curve can be explained by the combined behavior of 2 competing processes: immobilization of organosilanes on the sensor chip surface and hydrolysis of the silane epoxy group.

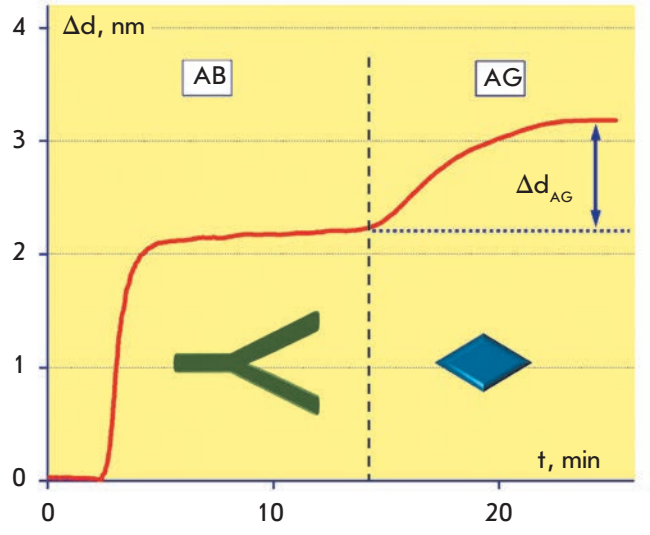


Fig. 4. Sensogram of label-free detection of 0.5 μg/ml cardiac troponin I on an epoxylated surface. PBS was passed for 3 min for washing right before the analyte solution (dashed line)

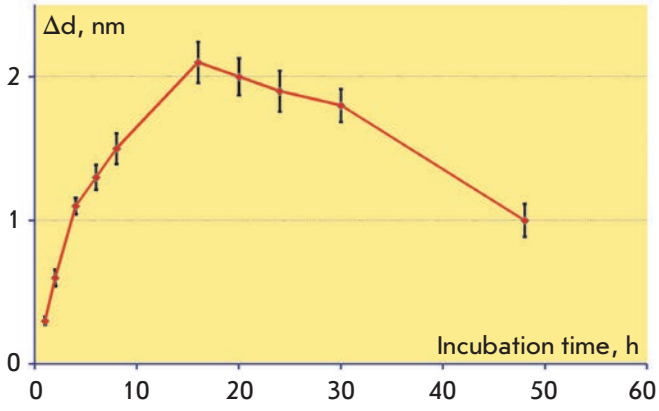


Fig 5. Dependence of the signal recorded during sorption of 1 μg/ml cardiac troponin on the duration of initial epoxylation of the sensor chips in GLYMO at a 0.1% volume concentration of water

It has been experimentally demonstrated that under optimal parameters the epoxylated and biotinylated surfaces have a virtually identical density of antibody immobilization $\Delta d_{AB}$, while the density of cTnI antigen sorption on antibody on the epoxylated surface is approximately twice as high; i.e. the proportion of active antibody molecules in that case is substantially higher.

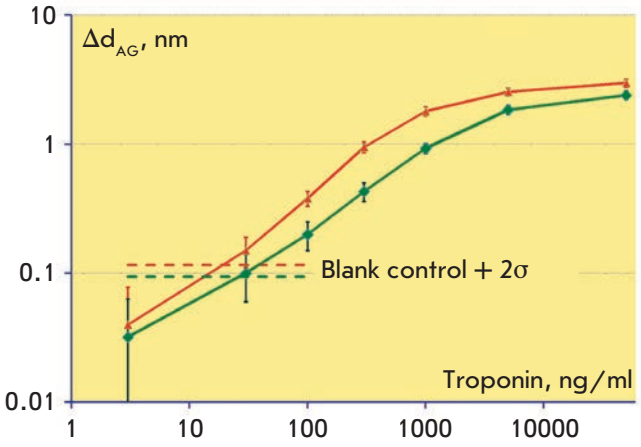


Fig. 6. Calibration curves in log-scale obtained in a label-free mode on biotinylated (*bottom green curve*) and epoxylated (*top red curve*) surfaces show the dependence of the biolayer increase $\Delta d_{AG}$ upon the cardiac troponin concentration. The horizontal dashed lines represent values that exceed the negative control values by two standard deviations of the negative control in the absence of the antigen

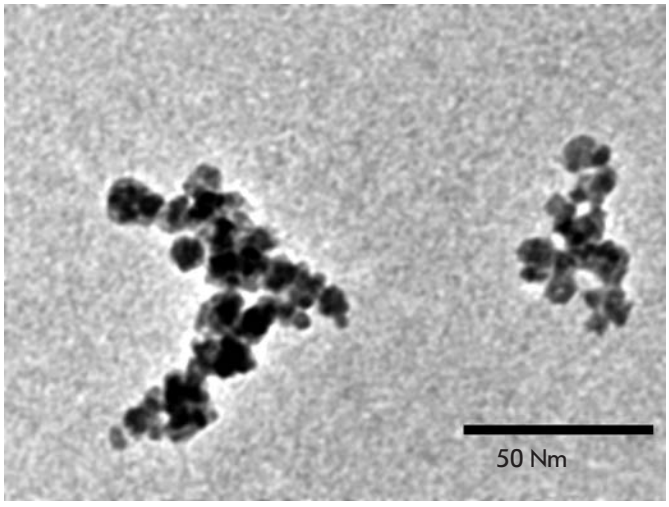


Fig. 7. TEM image of streptavidin-conjugated magnetic nanoparticles

### Calibration curves in label-free mode

Calibration curves in the label-free mode represent the dependences of the recorded signal $\Delta d_{AG}$ on the troponin concentration (*Fig. 6*). The detection limits for immobilization on the epoxylated and biotinylated surfaces of the sensor chips were 20 and 30 ng/ml, respectively. The difference in the detection limits for these schemes of antibody immobilization is due to the abovementioned experimental finding that the density of immunoactive antibodies on the epoxylated surface is on average twice higher. The dynamic range in both cases was around 2 orders of concentration magnitude, allowing one to detect troponin levels up to ~3000 ng/ml. This range permits identification of extensive myocardial infarctions but do not cover the entire clinically significant range of low concentrations of cardiac troponin.

The developed protocols of antibody immobilization, as well as the methods for quantitative assessment of immobilization efficiency, can be directly transferred to modern biosensing platforms, including those based on the detection of colored, enzyme, or fluorescent labels. It is noteworthy that Picoscope® allows deposition on the glass slips of a broad range of partially transparent films (polymeric [30], carbonic, and others) or interface layers; i.e. detecting of intermolecular interactions either directly on glass or on many other surface types commonly used in various biosensors. Thus, it is possible to simplify the development of a wide spectrum of different immunoassay types with the use of Picoscope® for the procedures proven to be labor-consuming in label-based methods; e.g., antibody screening, selection of buffer solutions, of incubation times for the reagents, and other stages of preliminary assay optimization. The results of this optimization may then be used in combination with various label-based detection methods. This points to the advantage of the SCI method over the majority of other optical label-free methods and speaks for its usage for the development of a wide range of other biosensing systems.

### Characterization and real-time monitoring of magnetic nanoparticles binding

The final stage of sandwich immunoassays is the binding of labels to the solid phase and their subsequent detection. In this work, magnetic nanoparticles were used as labels. Application of MNP in immunoassay allows to reduce the assay duration, increasing its sensitivity, enables detection in complex media and analysis of large-volume samples [35]. The representative microphotography of streptavidin-conjugated MNP obtained by a transmission electron microscope is shown in *Fig. 7*. From this figure it can be seen that the particles represent heterogeneous in size clusters consisting of several nanoparticles with a diameter of ~10 nm. This corresponds to the results of several other studies of similar particles [46]. Nevertheless, these particles show low nonspecific binding to the components of complex biological mediums (e.g., whole blood [47]) and ensure high reproducibility of immunoassay results when used as the detection labels [35].

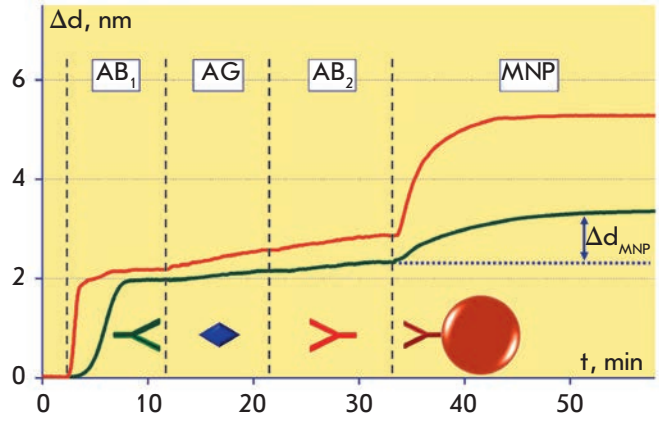


Fig. 8. Sensograms demonstrating all stages of the magnetic immunoassay on the biotinylated (*bottom green curve*) and epoxylated (*top red curve*) surfaces of the sensor chip: $AB_1$ – antibody immobilization; AG – antigen (100 ng/ml) capture by immobilized antibodies; $AB_2$ – recognition by tracer antibodies of another antigen epitope; MNP – association of magnetic nanoparticles with tracer antibodies. PBS washing was performed before each step as indicated with dotted lines

*Figure 8* shows the sensograms obtained for chips with epoxylated (upper curve) and biotinylated (lower curve) surfaces that demonstrate all stages of a magnetic sandwich immunoassay with detection of a 100 ng/ml cTnI solution. Washing by PBS implemented right before the injection of each immunoreagent corresponds to the short horizontal sections of the sensograms when the biolayer thickness remains practically unchanged. In the assay on the epoxylated chips, covalently immobilized native capture antibodies $AB_1$, biotinylated tracer antibodies $AB_2$, and MNP covered with streptavidin were used. The use of such magnetic particles together with the biotinylated sensor chips might cause high nonspecific signals due to direct binding of MNP with free biotin molecules. Therefore, $AB_1$ antibodies of the IgG2b isotype were immobilized on the biotinylated chips via streptavidin, and $AB_2$ of the IgG1 isotype were used as tracer antibodies, along with another type of magnetic particles that specifically recognize this $AB_2$ isotype.

The differences at the AG and $AB_2$ stages in the sensograms obtained for different surfaces with the same antigen concentration become more prominent at the MNP stage. *Figure 8* illustrates that the binding rate of streptavidin-conjugated MNP is higher than that of MNP covered with antibodies to the isotype of the tracer antibody. First, this can be explained by the different efficiency of antibody sorption on the sensor chip. Second, the kinetic constant of association for biotin-streptavidin is several orders of magnitude higher than that of the monoclonal antibody with antigen. This provides stronger and faster binding of MNP covered with streptavidin, compared with MNP covered with antibodies.

The obtained results allow estimation of the kinetic characteristics of interactions between biomolecules, as well as with magnetic particles. The observed kinetic association constants estimated for each assay stage by the sensograms recorded by Picoscope® are shown in the table. These values observed at the MNP stage are 2–3 orders of magnitude higher than those at the preceding stages for both schemes of antibody immobilization, despite the fact that at each subsequent assay stage, this parameter is smaller than its true value due to dissociation of the complexes formed at the previous stage. Such good kinetic characteristics of MNP binding compared to antibody and antigen molecules may be explained by MNP polyvalence. Several biorecognition biomolecules simultaneously linked to a single particle may provide a higher probability of effective collision of MNP with the sensor chip surface.

*Figure 9* shows the dependences of the biolayer increase $\Delta d_{MNP}$ upon troponin concentration at the stage of MNP passing. The detection limit on the epoxylated

Table. Dependence of the kinetic association constant observed at each stage of the magnetic immunoassay upon the surface type

| Surface type | Observed kinetic association constant, $M^{-1}s^{-1}$ | | |
|---|---|---|---|
| | AG stage | $AB_2$ stage | MNP stage |
| Epoxylated | $(6.4 \pm 1.3) \times 10^5$ | $(1.2 \pm 0.2) \times 10^5$ | $(1.6 \pm 0.2) \times 10^8$ |
| Biotinylated | $(8.2 \pm 1.9) \times 10^5$ | $(1.7 \pm 0.3) \times 10^5$ | $(6.4 \pm 1.1) \times 10^7$ |

surface calculated using the 2σ criterion was 0.1 ng/ml, which was 10 times better than the 1 ng/ml value obtained for the biotinylated surface. The dynamic range in both cases was around 3 orders of concentration magnitude. Thus, the use of MNP provides a resulting improvement of the detection limit of over 100 times as compared with label-free detection, i.e. multiple amplification of the signal is realized. The significantly greater increase in the biolayer thickness $\Delta d_{MNP}$ at the MNP stage compared to the stages of antigen and detecting antibody binding over the full range of measured cTnI concentrations is due to the fact that the nanoparticle diameter is significantly larger than the characteristic sizes of the detected biomolecules. The achieved detection limit for cardiac troponin of 0.1 ng/ml corresponds to the clinically significant threshold for the diagnostics of myocardial infarction [48]. The high sensitivity and wide dynamic range make the developed biosensor an attractive instrument with affordable consumables (disposable sensor chips) for real-time immunoassays in disease diagnostics, detection of pathogens in food, and environmental monitoring. Further studies will aim at estimating the efficiency of cTnI detection in real biological samples and validating the correlation between the obtained results and the data received by conventional methods.

Beside the dignostic significance of the developed immunoassay achieved due to the amplification of the SCI signal, our results may be of special interest for the investigation and kinetic characterization of the interactions of nanoparticles with molecules. We should note that to date the most widespread label-free biosensors that allow estimation of the kinetic parameters of nanoparticles are those based on the surface plasmon resonance (SPR) [21, 36]. These biosensors permit the study of interactions of particles with the biomolecules immobilized on the modified surface of highly conductive gold or silver films. The interface (surface) chemistry used in this case significantly differs from that used in the most widespread methods of solid-phase immunoassay. This fact complicates the transfer of the results obtained with the SPR biosensors to other platforms. As a contrast, the SCI method in combination with inexpensive, disposable sensor chips greatly enhances research opportunities for the development of various immunoassays. The methods for immunoassay optimization proposed in this work allow easy transfer of all the protocols to label-based biosensing platforms; for example, those using the highly sensitive methods of MNP detection by compact electronic devices [15], based on frequency mixing [49] under nonlinear particle remagnetization [34].

The dependence of the signal amplification efficacy on the MNP size deserves a separate study. On the one hand, bigger magnetic particles (up to several micrometers) can better amplify the signal. However, bigger particles are prone to gravity sedimentation and may cause a high nonspecific signal. Neither sedimentation nor nonspecific interaction with the surface was observed in this work while using 50 nm MNP; therefore, the use of smaller nanoparticles appears to be unreasonable.

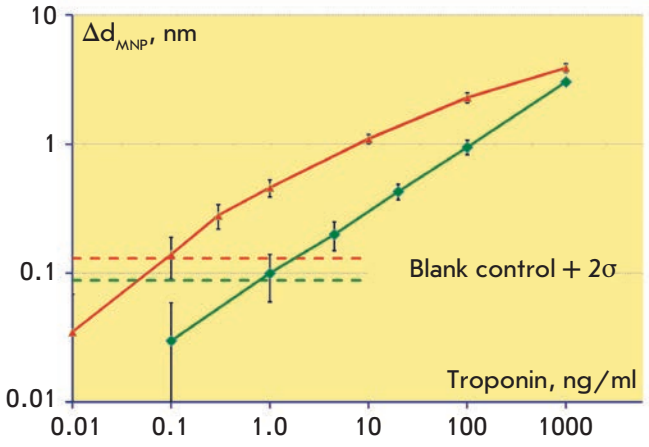


Fig. 9. Calibration curves in log-scale obtained while detection of cardiac troponin at the stage of magnetic nanoparticles passing along the biotinylated (*bottom green curve*) and epoxylated (*top red curve*) surfaces of the sensor chip. The horizontal dashed lines represent values that exceed the negative control values by two standard deviations of the negative control in the absence of the antigen

The absence of nonspecific sorption during signal amplification permits further gain in sensitivity by using several amplification steps. As an example, if a biotinylated protein with several biotinylation sites is repeatedly passed between two runs of streptavidin-conjugated MNP, it is possible to substantially increase the number of labels and, hence, the sensitivity.

In addition to low nonspecific binding, MNP possess unique properties that can be used to further develop the proposed techniques. For example, a combination of magnetic properties with optical detection allows one to realize an optomagnetic immunoassay [50]. In that assay, the duration of immunochemical reactions can be significantly reduced due to magnetic stirring by MNP, as well as by rotation of MNP chains by a magnetic field. It also permits one to enrich the sample with antigens by magnetic separation and to decrease nonspecific binding of labels with the surface by removal of the loosely bound particles by a magnetic field of the respective spatial orientation for "magnetic" washing of the labels.

## CONCLUSION

We have developed a method for magnetic immunoassay on a glass surface that allows real-time detection of each stage of the assay and usage as disposable sensor chips of inexpensive cover slips without deposition of any films . Four schemes of antibody immobilization have been tested and optimized with their efficacy assessed. As a result, high sorption capacity and proportion of active antibodies on the surface of the sensor chip have been achieved. The possibility of real-time recording of the kinetics of interactions of magnetic nanoparticles with biomolecules has been shown. It has been demonstrated that the use of magnetic nanoparticles amplifies the signal of spectral correlation interferometry, which leads to an additional 100-fold improvement of the detection limit for cardiac troponin. Thus, the developed interferometric biosensing systems may serve as effective tools for conducting the assays, as well as for a wide range of applications, including the development and optimization of immunoassay methods, quality control of immunoreagents, and control of surface sorption properties. The obtained results on the selection of schemes and optimization of antibody immobilization protocols, as well as on real-time monitoring of all immunoassay stages and kinetic characterization of nanoparticles, can be directly transferred to other biosensing platforms, including those based on various labels – magnetic, fluorescent, enzymatic, and others. The proposed biosensing technique is an economically sound alternative for immunoassays with disposable consumables for disease diagnostics, detection of pathogens in food, and environmental monitoring. ●

*The authors are grateful to prof. A.G. Katrukha from Moscow State University (Moscow) for the provided immunoreagents.*

*The work was supported by the Russian Foundation for Basic Research (grants №№10-02-01185, 11-02-01440, 11-04-12181-ofi-m 2011, 13-02-01260, 13-03-12468). This work was conducted within the scope of the "Russian Federal Targeted Programme for research and development in priority fields for the development of Russia's science and technology complex for 2007–2012" (state contract 16.512.11.2124) with the use of equipment from the Center for the Collective Use of Unique Equipment in the Nanotechnology Field at MIPT (CCU MIPT), funded by the Ministry of Education and Science of the Russian Federation.*

REFERENCES

1. Vaidya V.S., Bonventre J.V. Biomarkers: In Medicine, Drug Discovery, and Environmental Health: Wiley-Blackwell, 2010. 640 p.
2. Yanga Zh., Zhoub D.M. // Clin. Biochem. 2006. V. 39. № 8. P. 771–780.
3. Mayeux R. // NeuroRx. 2004. V. 1. № 2. P. 182–188.
4. Lundblad R.L. Development and Application of Biomarkers: CRC Press, Taylor & Francis Group, 2011. 297 p.
5. Frank. R, Hargreaves, R. // Nat. Rev. Drug. Discov. 2003. V. 2. P. 566–580.
6. Lee J.M., Han J.J., Altwerger G., Kohn E.C. // J. Proteomics. 2011. V. 74. № 12. P. 2632–2641.
7. Bleavins M.R., Carini C., Jurima-Romet M., Rahbari R. Biomarkers in Drug Development: A Handbook of Practice, Application, and Strategy: Wiley-Blackwell, 2010. 760 p.
8. Yalow R.S., Berson S.A. // Nature. 1959. V. 184. P. 1648–1649.
9. Uotila M., Ruoslathi E., Envall E. // J. Immunol. Methods. 1981. V. 42. P. 11–15.
10. Dzantiev B.B., Zherdev A.V. Problems of analytical chemistry. Biochemical methods of analysis // Ed. Dzantiev B.B. Moscow: Nauka, 2010. V. 12. P. 297–326.
11. Engvall E., Perlmann P. // Immunochemistry. 1971. V. 8. P. 871–874.
12. Plotz C.M., Singer J.M. // Am. J. Med. 1956. V. 21. № 6. P. 888–892.
13. Leuvering J.H.W., Thal P.J.H.M., Van der Waart M., Shurs A.H.W.M. // J. Immunol. Meth. 1981. V. 45. P. 183–194.
14. Laborde R., O'Farrell B. // IVD Technology. 2002. April issue. P. 36.
15. Nikitin P.I., Vetoshko P.M., Ksenevich T.I. // Sens. Lett. 2007. V. 5. № 1. P. 296–299.
16. Rosi N.L., Mirkin. C.A. // Chem. Rev. 2005. V. 105. № 4. P. 1547–1562.
17. Lei J., Ju. H. // Chem. Soc. Rev. 2012. V. 41. P. 2122–2134.
18. Aghayeva U.F., Nikitin M.P., Lukash S.V., Deyev S.M. // ACS Nano. 2013. V. 7. № 2. P. 950–961.
19. Nikitin M.P., Zdobnova T.A., Lukash S.V., Stremovskiy O.A., Deyev S.M. // Proc. of Natl. Acad. Sci. 2010. V. 107. № 13. P. 5827–5832.
20. David W. The Immunoassay Handbook. Oxford: Elsevier Ltd., 2005. P. 103–135.
21. Liedberg B., Nylander C., Lundstrom I. // Biosens. Bioelectron. 1995. V. 10. № 8. P. I–IX.
22. Cunningham B.T. Label-free optical biosensors: An introduction. In: Cooper M.A. Label-Free Biosensors: Techniques and Applications. Cambridge: Cambridge Univ. Press, 2009. P. 1–28.
23. Gauglitz G., Brecht A., Kraus G., Nahm W. // Sens. Act. B. 1993. V. 11. P. 21–27.
24. Dancil K.S., Greiner D.P., Sailor M.J. // J. Am. Chem. Soc. 1999. V. 121. P. 7925–7930.
25. Nikitin P.I., Gorshkov B.G., Valeiko M.V., Rogov S.I. // Quantum Electronics. 2000. V. 30. № 12. P. 1099–1104.
26. Nikitin P., Gorshkov B., Valeiko M., Nikitin S. // Proc. SPIE. 2001. V. 4578. P. 126–135.
27. Nikitin P.I., Valeiko M.V., Gorshkov B.G. // Sens. Act. B. 2003. V. 90. P. 46–51.
28. Nikitin P.I., Gorshkov B.G., Nikitin E.P., Ksenevich T.I. // Sens. Act. B. 2005. V. 111 –112. P. 500–504.

29. Nikitin P.I., Svetoch I.E., Nikitin M.P., Ksenevich T.I., Gorshkov B.G., Konov V.I., Aksinin V.I. // Proc. SPIE. 2007. V. 6733. P. 67331M.
30. Ivanov A.E., Solodukhina N., Wahlgren M., Nilsson L., Vikhrov A.A., Nikitin M.P., Orlov A.V., Nikitin P.I., Kuzimenkova M.V., Zubov V.P. // Macromol Biosci. 2011. V. 11. № 2. P. 275–284.
31. Diryugina E.G., Burenin A.G., Nikitin M.P., Orlov A.V., Nikitin P.I. // Proceedings of MIPT. 2012. V. 4. № 3. P. 11–17.
32. Burenin A.G., Nikitin M.P., Orlov A.V., Ksenevich T.I., Nikitin P.I. // Applied Biochemistry and Microbiology. 2013. V. 49. № 3. P. 306–311.
33. Arefieva T.I., Krasnikova T.L., Potekhina A.V., Ruleva N.U., Nikitin P.I., Ksenevich T.I., Gorshkov B.G., Sidorova M.V., Bespalova Zh.D., Kukhtina N.B., Provatorov S.I., Noeva E.A., Chazov E.I. // Inflammation Research. 2011. V. 60. № 10. P. 955–964.
34. Nikitin P.I., Vetoshko P.M., Ksenevich T.I. // J. Magn. Magn. Mater. 2007. V. 311. P. 445–449.
35. Orlov A.V., Khodakova J.A., Nikitin M.P., Shepelyakovskaya A.O., Brovko F.A., Laman A.G., Grishin E.V., Nikitin P.I. // Anal. Chem. 2013. V. 85. № 2. P. 1154–1163.
36. Appendix C. Predefined models. In: BIAevaluation 3.0 Software Handbook. Biacore AB, 1997. P. C-2–C-33.
37. Adams J.E., Bodor G.S, Davila-Roman V.G., Delmez J.A., Apple F.S., Ladenson J.H., Jaffe A.S. // Circulation. 1993. V. 88. № 1. P. 101–106.
38. Katrukha A.G., Bereznikova A.V., Esakova T.V., Pettersson K., Lovgren T., Severina M.E., Pulkki K., Vuopio-Pulkki L.M., Gusev N.B. // Clin. Chem. 1997. V. 43. № 8. P. 1379–1385.
39. Thygesen K., Mair J., Giannitsis E., Mueller C., Lindahl B., Blankenberg S., Huber K., Plebani M., Biasucci L.M., Tubaro M., et al. // Eur Heart J. 2012. V. 33. № 18. P. 2252–2257.
40. Peri. G., Introna M., Corradi. D., Iacuitti G., Signorini S., Avanzini F., Pizzetti F., Maggioni A.P., Moccetti T., Metra M., et al. // Circulation. 2000. V. 102. P. 636–641.
41. NICE clinical guideline 95. Chest pain of recent onset. Assessment and diagnosis of recent onset chest pain or discomfort of suspected cardiac origin. 2010.
42. Morrow D.A., Cannon C.P., Jesse R.L., Newby L.K., Ravkilde J., Storrow A.B., Wu A.H.B., Christenson R.H. // Clin. Chem. 2007. V. 53. P. 552–574.
43. Katrukha A.G. Antibody selection strategies in cardiac troponin assays. In: Wu A.H.B. Cardiac Markers. 2nd Ed. New York: Humana Press, 2003. P. 137–185.
44. Lemos J.A. // JAMA. 2013. V. 309. № 21. P. 2262–2269.
45. Silane Coupling Agents. Chapter 13. In: Hermanson G.T., Bioconjugate Techniques, 2nd Ed. London: Acad. Press, 2008. P. 565–567.
46. Schreiber S., Savla M., Pelekhov D.V., Iscru D.F., Selcu C., Hammel P.C., Agarwal G. // Small. 2008. V. 4. № 2. P. 270–278.
47. Martin V.M., Siewert C., Scharl A., Harms T., Heinze R., Ohl S., Radbruch A., Miltenyi S., Schmitz J. // Exp. Hematol. 1998. V. 26. P. 252–264.
48. Bingisser R., Cairns C., Christ M., Hausfater P., Lindahl B., Mair J., Panteghini M., Price C., Venge P. // A. J. of Emergency Med. 2012. V. 30. P. 1639–1649.
49. Grigirenko A.N., Nikitin P.I., Roshepkin G.V. // Journal of Experimental and Theoretical Physics. 1997. V.85. N2. P. 343–350.
50. Nikitin P., Ksenevich T., Nikitin M., Gorshkov B. // Proceedings of Ninth European Conference on Optical Chemical Sensors and Biosensors, EUROPT(R)ODE IX. Dublin, 2008. P.OA4.2.

# Composite Scaffolds Containing Silk Fibroin, Gelatin, and Hydroxyapatite for Bone Tissue Regeneration and 3D Cell Culturing

M. M. Moisenovich[1], A. Yu. Arkhipova[1], A. A. Orlova[1], M. S Drutskaya[1], S. V. Volkova[1], S. E. Zacharov[1], I. I. Agapov[2#*], Academician M. P. Kirpichnikov[1#]

[1]Biological Faculty, Moscow State University, Leninskie Gory, 1-12, 119991, Moscow, Russia

[2]Shumakov Institute of Transplantology and Artificial Organs, Federal Agency for High-Tech Medical Services, Shchukinskaya Str., 1, 113182, Moscow, Russia

[#] All authors contributed equally to the study (listed in alphabetical order)

* E-mail: igor_agapov@mail.ru

Received 01.08.2013



**ABSTRACT** **Three-dimensional (3D) silk fibroin scaffolds were modified with one of the major bone tissue derivatives (nano-hydroxyapatite) and/or a collagen derivative (gelatin). Adhesion and proliferation of mouse embryonic fibroblasts (MEF) within the scaffold were increased after modification with either nano-hydroxyapatite or gelatin. However, a significant increase in MEF adhesion and proliferation was observed when both additives were introduced into the scaffold. Such modified composite scaffolds provide a new and better platform to study wound healing, bone and other tissue regeneration, as well as artificial organ bioengineering. This system can further be applied to establish experimental models to study cell-substrate interactions, cell migration and other complex processes, which may be difficult to address using the conventional two-dimensional culture systems.**

**KEYWORDS** **adhesion; hydroxyapatite; gelatin; composite biodegradable scaffolds; proliferation; silk fibroin.**

**ABBREVIATIONS** **GFP – green fluorescent protein; RGD – the one-letter amino acid abbreviation for Arginine-Glycine-Aspartic acid; HA – hydroxyapatite; CLSM – confocal laser scanning microscopy; MEF – murine embryonic fibroblasts; SEM – scanning electron microscopy.**

## INTRODUCTION

Developing and improving the techniques for the restoration of damaged or lost organs and tissue fragments, as well as constructing artificial organs, are pressing issues in tissue engineering and regenerative medicine today. Low-immunogenicity biomaterials that can maintain cell adhesion and proliferation, and degrade to their chemical derivatives safe for the organism with time, are required for a technological breakthrough in these fields. Bacterial polyhydroxyalkanoates are an example of such advanced materials [1]. An important advantage of these materials is that they exhibit unique mechanical properties, plasticity, and tolerance to extrusion processing. Bacterial polyhydroxyalkanoates can be used to manufacture irregularly shaped items; hence, they are a rather promising material for 3D prototypes. These materials are characterized by a lower biocompatibility compared to collagen and other extracellular matrix components. However, the use of collagen is limited by its mechanical properties, while articles made of silk fibroin demonstrate a good biocompatibility, along with high mechanical resistance and elasticity. The availability of silk, its water solubility, biodegradability with the formation of amino acids, thermal resistance, the availability of easily accessible chemical groups for functional modification, radioresistance, the possibility of using gas sterilization, and suitability for composite materials are additional important benefits [2, 3]. The increasing number of publications and references on the use of fibroin for the re-generation of various organs and tissues (tendons, ligaments, cartilages, bone tissue, skin, liver, trachea, nerves, retina, tympanic membrane, and bladder) attests to the high potential of the polymer as a material for biomedicine [4].

We compared the properties of scaffolds from fibroin and recombinant spidroin in our previous studies. Those studies showed that re-generated fibroin maintains the adhesion and proliferation of fibroblasts (one of the main components involved in wound heal-

ing and tissue regeneration) to a lesser extent than the substrate formed by polymerized recombinant spidroin from *Nephila clavipes*. The reduced capability of fibroin materials to maintain cell adhesion and proliferation has the potential to cause a poorer re-generation ability compared with that of spidroin scaffolds in experiments with a bone injury model. The re-generative properties of fibroin scaffolds in these experiments were considerably improved by the use of nano-hydroxyapatite mineralization [5]. We have introduced a combination of two composite additives, nano-hydroxyapatite (a bone tissue component) and gelatin (a collagen derivative), into the formulations of fibroin scaffolds to enhance their capability to maintain the adhesion and proliferation of fibroblasts. The composite substrate formed by all three components was the optimal material that maintained MEF adhesion and proliferation.

## EXPERIMENTAL

Pods of bombycid, *Bombyx mori*, were kindly provided by V.V. Bogoslovskii, Director of the Republican Sericulture Research Station of the Russian Academy of Agricultural Sciences (Zheleznovodsk, Stavropol region). The desericinization technique was used to produce pure fibroin. Sericin and other impurities were removed from the pods by boiling in a 0.03 M $NaHCO_3$ solution (pH 8.4) for 1.5 h, followed by washing with water and drying. Natural hydroxyapatite was provided by Prof. V.V. Guzeev (Seversk Technological Institute, National Research Nuclear University MEPhI, Russia).

### Scaffold Manufacturing

To manufacture a scaffold, a weighted fibroin sample (250 mg) was dissolved in 1,000 μL of a 10% lithium chloride solution in 90% formic acid at 60–70°C for 30 min. A mixture containing fibroin (225 mg) and gelatin (25 mg) in 1,000 μL of the solution was used to form a composite scaffold with a 10% content of gelatin. The resulting solution was centrifuged at 12,100 *g* for 5 min; the supernatant was used to form scaffolds. 50 μL of the pre-heated supernatant was placed into the mold, layer-by-layer, and mixed with 100 mg of sodium chloride with different particle sizes. NaCl crystals (150–300 μm in diameter) were used as an expanding agent. A weighted sample of HA powder was mixed with expanding NaCl particles (150–300 μm in diameter) to produce composite scaffolds with a 30% HA content. The salt concentration was selected in such a manner as to form a scaffold with a complex internal porous surface free of isolated cavities. The resulting samples were dried at 75–80°C for 3 h, kept at ambient temperature for 16 h, processed with 96% ethanol for 120 min, washed in bidistilled water for 120 min, and degased and stored in 70% ethanol.

### Scanning Electron Microscopy (SEM)

Scanning electron microscopy was used to examine the structure of the scaffolds.

SEM samples were prepared by the standard procedures: fixation in glutaric aldehyde and dehydration in graded series of ethanol and acetone. The samples were then dried by the critical point method in an HCP-2 critical point dryer (Hitachi Ltd., Japan). The samples were sputter-coated with a 20 nm-thick layer of gold in an argon atmosphere with a 6 mA ion current and 0.1 mm Hg in an Ion Coater IB-3 (Eiko Engineering, Mito, Japan). A Camscan S2 microscope (Cambridge Instruments, Cambridge, UK) with a 10 nm resolution and 20 kV operating volume was used (the SEI mode) for scanning electron microscopy. The MicroCapture software (SMA, Russia) was used to capture images.

### Confocal Laser Scanning Microscopy (CLSM)

We used a confocal laser scanning system (Nikon, Japan) in which Eclipse, a clinical inverted microscope for laboratory studies, is combined with an A1 confocal module. The pinhole size, laser parameters, and analyzing filter size for all series of optical sections were chosen as recommended by the manufacturer to achieve a high resolution of the images

### Primary Cultures of the GFP Expressing Mouse Embryonic Fibroblasts

MEF cells were isolated from GFP+ embryos on the 13.5$^{th}$ day of intrauterine growth. Two C57Bl/6 females were mated with a GFP+ male for a night and checked for vaginal plugs the next morning. The moment of plug detection was considered to be the 0.5$^{th}$ day of time-dated pregnancy. The mice were euthanized on the 13.5$^{th}$ day of pregnancy. The uterus was removed; heads and internals were separated from the embryos, and GFP expression was determined using a trans-illuminator. The rest of the tissues were aseptically chopped with eye scissors, dissociated in a 0.05% trypsin/EDTA solution, and centrifuged at 1,000 rpm for 5 min. The resulting cell suspension was transferred into 25-cm$^2$ cultural flasks for adherent cell growth (Greiner). The cells were subsequently cultivated in DMEM supplemented with 4.5 g/L glucose (HyClone) and 10% fetal bovine serum (HyClone) at 37°C, 5% $CO_2$, and 95% humidity. The cells were passaged at a 1:3 ratio every three days after they reached 80-85% confluence.

The C57Bl/6 females were purchased from the Pushchino Animal Breeding Facility (BIBC RAS); and the transgene males with the expressed GFP were kindly provided by N.N. Logunova (ISTC RAMS).

## RESULTS AND DISCUSSION

We had previously formed silk fibroin scaffolds [6] and silk fibroin–HA scaffolds [5], and examined the biologi-

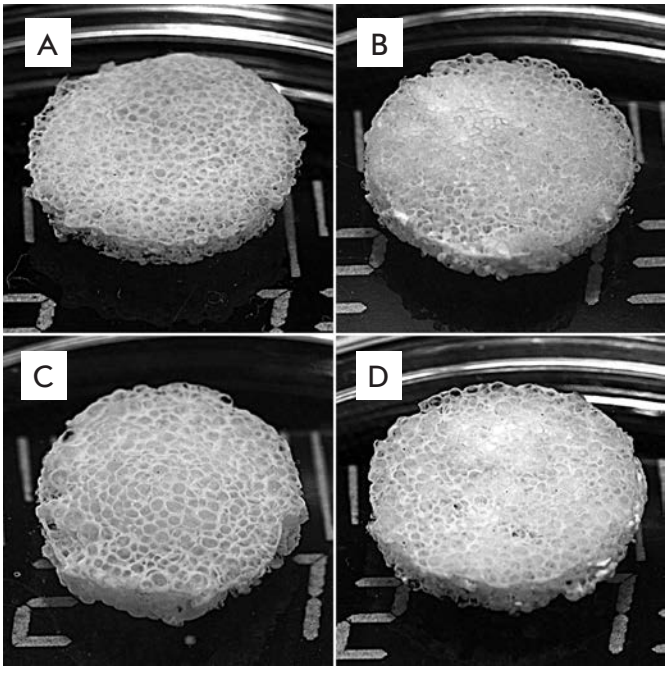


Fig. 1. Appearance of 3D porous silk fibroin (A) and composite fibroin–gelatin (B), fibroin–hydroxyapatite (C), and fibroin–gelatin–hydroxyapatite (D) scaffolds. Introduction of gelatin and hydroxyapatite into the scaffold structure does not modify its appearance

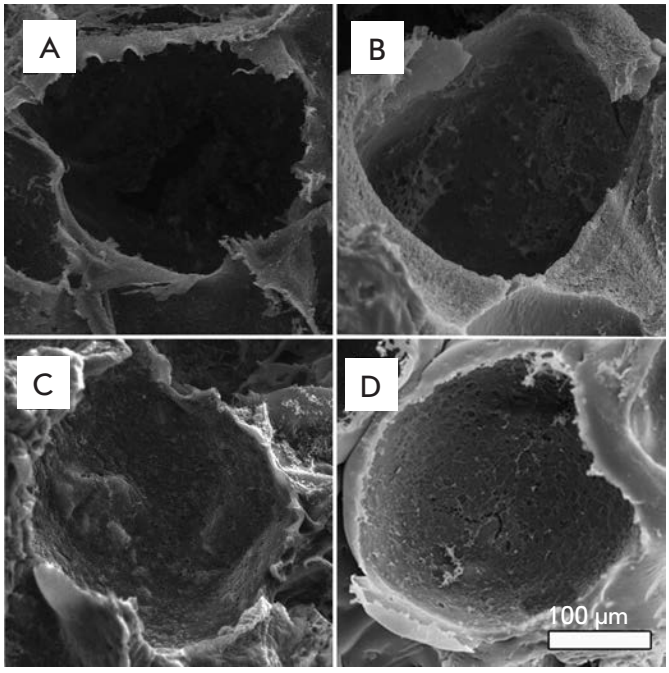


Fig. 2. Structure of 3D porous silk fibroin (A) and composite fibroin–gelatin (B), fibroin–hydroxyapatite (C), and fibroin–gelatin–hydroxyapatite (D) scaffolds. The images were recorded on a scanning electron microscope. Introduction of gelatin and hydroxyapatite into the scaffold structure does not modify the pore size and the general scaffold structure

cal properties of the pilot samples. The scaffolds possess all the characteristics needed for bone surgery; in particular, they are biocompatible, strong, and porous. The current study yielded silk fibroin scaffolds, composite silk fibroin–gelatin and silk fibroin–HA scaffolds, and composite scaffolds containing three main components: silk fibroin, gelatin, and HA (*Fig. 1*). A pore-forming agent with a preset particle diameter was selected to produce these scaffolds.

The resulting test samples could maintain their integrity and acquired the preset cylindrical shape. The composite silk fibroin–gelatin scaffolds underwent an elastic deformation under direct mechanical pressure, while the silk fibroin–HA scaffolds remained un-deformed. The pores of the scaffolds produced by leaching had sizes corresponding to the added particles of the pore-forming agent (150–300 μm).

The surface of the products was examined by scanning electron microscopy (SEM) (*Fig. 2*). The resulting scaffolds had a cellular mesh structure totally free of the pore-forming agent (its traces were never found in the material) (*Figs. 2, 3*). The permeability test with suspended colored ink particles confirmed the conjunctivity of the scaffold pores.

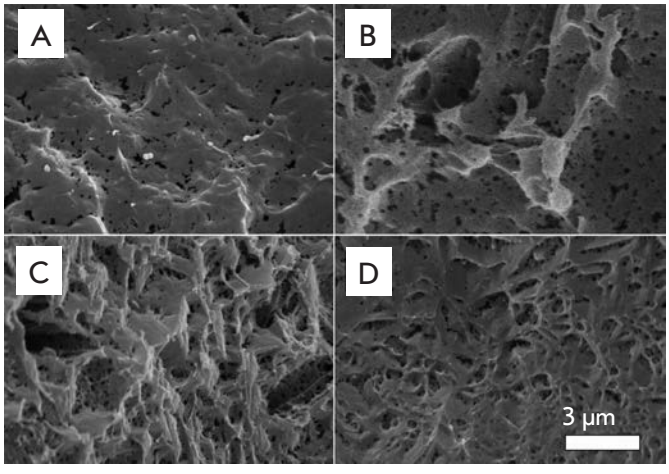


Fig. 3. Pore wall surface of silk fibroin (A) and composite fibroin–gelatin (B), fibroin–hydroxyapatite (C), and fibroin–gelatin–hydroxyapatite (D) scaffolds. The images were recorded on a scanning electron microscope. Introduction of gelatin and hydroxyapatite into the scaffold structure changes the fine architecture of the scaffolds

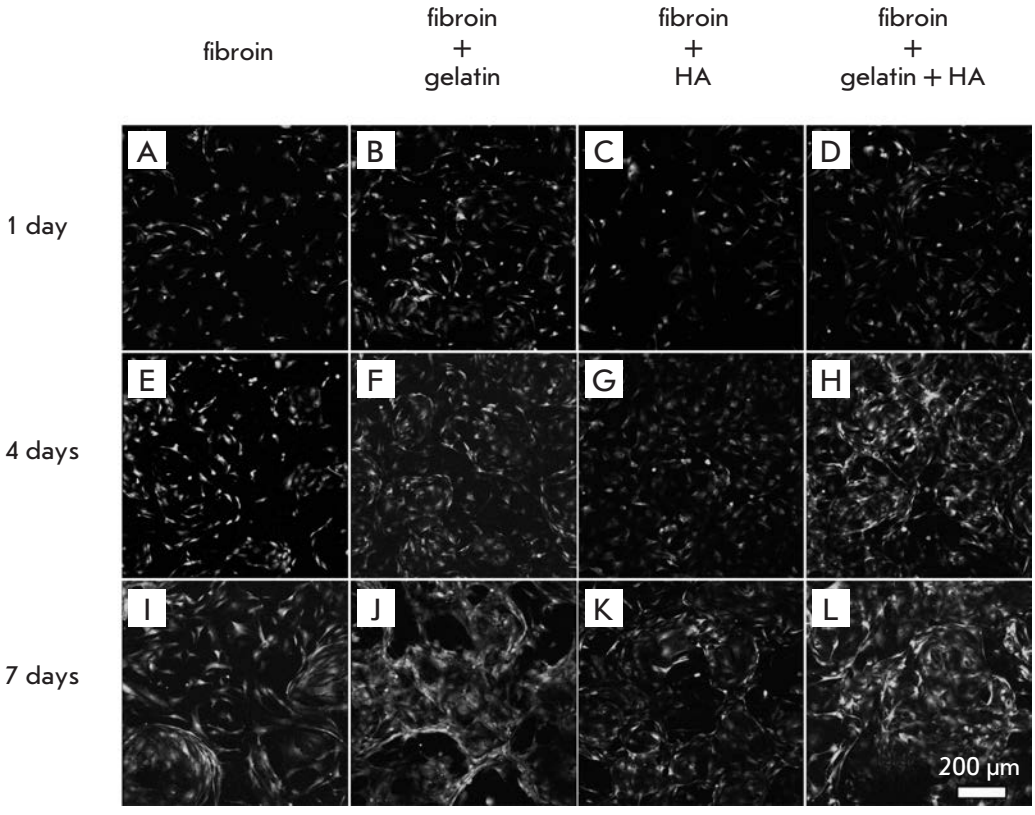


Fig. 4. GFP-expressing murine embryonic fibroblasts (MEF) on the silk fibroin scaffold (A, E, I), composite fibroin–gelatin scaffold (B, F, J), hydroxyapatite (C, G, K), gelatin and hydroxyapatite (D, H, L) after 1 (A–D), 4 (E–H), and 7 (I–L) days of cultivation. The images show surface projections of the optical sections

The examination of the sample structure showed that the amounts of gelatin and HA in a composite scaffold did not affect the conjunctivity of the pores, appearance of the articles, and their ink permeability. Three test samples had the same porosity and appearance due to the fact that substance porosity is governed by the parameters of the pore-forming agent (which forms pores 150–300 μm in diameter) and is independent of the amount of additives, gelatin, or HA.

The pore diameter dictates the mechanical properties of a structure and the rate of its biodegradation; it also affects the post-implantation tissue response and cell interaction with the scaffold surface. Larger pores facilitate a better and more rapid integration of the newly formed tissue, its vascularization, and a more effective bioresorption of a graft.

Three-dimensional cell culturing requires scaffolds with an unclosed structure. Pores connected with holes and channels form a complex, unclosed internal surface that facilitates cell migration to the internal layers of an artificial scaffold. Furthermore, an unclosed pore structure provides conditions for the medium exchange and removal of metabolites, thus facilitating the formation of a homogenous intra-scaffold medium [5, 7–9].

CLSM examination showed that a water medium affects the integrity and porosity of both the fibroin and all composite scaffolds neither immediately after immersion (1 h) nor a day later. This characteristic is very important, since disintegration or alteration of the basic structure and physical characteristics of a graft in a water medium prevents its use *in vivo*. Lack of considerable water-absorbing and water-retaining abilities allowed the articles to keep their preset parameters.

Adhesion of substrate-dependent cells on the scaffold surface is neccesary to maintain their viability in a 3D culture [10, 11]. A substrate affects the production of extracellular matrix components by the cells, its synthesis, and composition. The ability to maintain cellular adhesion and proliferation is considered to be an important *in vitro* biocompatibility parameter for a material used as a substrate [10–12]. Hence, a material with inhibiting properties will inhibit tissue regeneration *in vivo*.

Silk fibroin is a high-strength protein free of carcinogenic, toxicogenic, or allergenic properties. It preserves its functional characteristics for a given period, causes no local inflammatory response, does not trigger the spread of an infection, and is replaced with a patient's native tissue over time; therefore, it is a material suitable for bone tissue re-generation [5–7].

Fibroin is an amphiphilic protein with considerable prevalence of hydrophobic properties [13]; its isoelectric

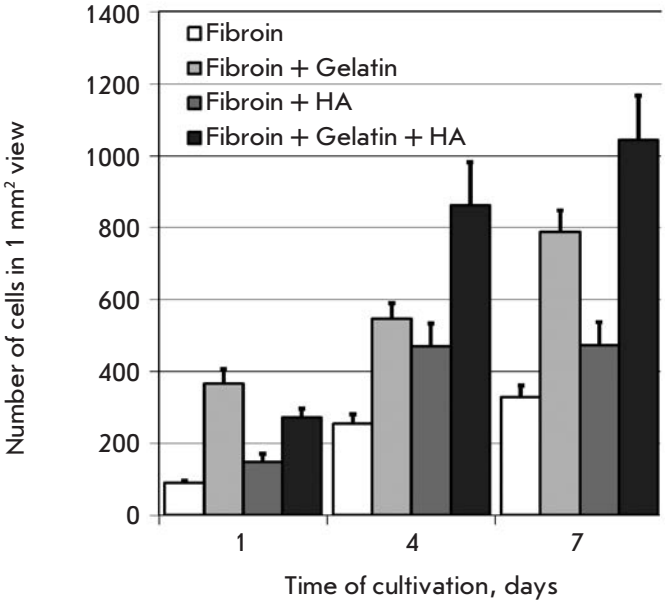


Fig. 5. Increasing count of murine embryonic fibroblasts (MEF) during cultivation on 3D porous silk fibroin and composite scaffolds

point p*I* is 4.2. Due to this parameter, it is soluble neither in water nor in the diluted solutions of some acids and bases [13], while it is negatively charged at physiological pH=7, in contrast to the positively charged spidroin [5], thus decreasing cell adhesion and increasing the cell proliferation rate [5].

A collagen derivative, gelatin, was used as an additive for composite materials. Collagen is the main fibrillar component of the extracellular matrix and connective tissue, with a molecular weight of 300 kDa. Collagen is found in almost all tissue types, ensuring their strength and structural stability. Thus, the protein comprises approximately 30% of the total protein mass in mammals. This material is not toxic and is a weak allergen; however, important shortcomings of collagen scaffolds include poor mechanical properties and short biodegradation time (it is regulated by cross-linking agents only partially, which limits the lifetime of collagen articles to one month). Gelatin is a product of collagen denaturation. It contains a large amount of glycine, proline, and 4-hydroxyproline, along with the three-amino-acid sequence (arginine, glycine, and aspartate – RGD), which bind to cell receptors (integrins), thus promoting cell adhesion and proliferation. Similar sequences are found in other proteins of the cell matrix; however, their use considerably increases the cost of these products.

We have examined the effects of scaffold additives on the adhesion and proliferation of primary MEF. Fibroblasts are a heterogeneous cell population capable of producing such extracellular matrix components as procollagen, fibronectin, proelastin, glucose aminoglycans, nidogen, laminin, tenastin, and chondroitin-2-sulfate. Fibroblasts take an active part in wound-healing and epithelization [14]. Moreover, they can secrete vascular epithelium growth factors (VEGF), thus stimulating angiogenesis and the formation of lymphatic vessels [15, 16]. We chose the primary culture of mouse embryonic fibroblasts, whose proliferative potential is higher than that in postnatal culture cells.

The images recorded by CLSM are a series of horizontal optical sections of a scaffold. Cells and scaffold structures up to 300 μm deep were available (*Fig. 4*). The images were used for cell counting. The changes in the number of cells cultivated on different scaffolds over time were compared. The gelatin and HA introduced into the scaffold structure enhanced cell adhesion and the proliferative rate (*Fig. 5*). Thus, within a day, the cellcount on a composite scaffold was 2.5-fold greater than that on a fibroin scaffold, while on days 4 and 7, it increased more than threefold.

## CONCLUSIONS

Silk fibroin scaffolds and composite scaffolds with gelatin and HA additives were produced in this study. These scaffolds have an unclosed structure, maintain their integrity, and are not mechanically disintegrated. Modification of fibroin scaffolds with gelatin and HA simultaneously alters the properties of their surface. These alterations enhance MEF adhesion and proliferation in a 3D culture, making the modified scaffolds a promising material for regenerative medicine, especially for bone tissue regeneration. ●

*The authors are grateful to G.N. Davidovich, Head of the Laboratory of Electron Microscopy, Lomonosov Moscow State University, for his assistance in recording the SEM images.*

*This study was performed on equipment purchased at the expense of the Program of Development of Moscow State University and equipment belonging to CUC MSU; with financial support from the Ministry of Education and Science of the Russian Federation.*

*This study is part of the Federal Target Program "Research and Development in the Priority Fields of the Science&Technology Complex of Russia for 2007–2013" (Government Contract № 14.512.11.0006, dated 07.03.2013), the Russian Foundation for Basic Research (grant № 14-04-01799), and Skolkovo Institute of Science and Technology (SkolTech) within the framework of MIT SkolTech Initiative.*

REFERENCES
1. Bonartsev A.P., Yakovlev S.G., Boskhomdzhiev A.P., Zharkova I.I., Bagrov D.V., Myshkina V.L., Mahina T.K., Charitonova E.P., Samsonova O.V., Zernov A.L., et al. // PLoS One. 2013. V. 8. № 2. P. e57200
2. Zhao Ya., Yan X., Ding F., Yang Yu., Gu X. // J. Biomed. Sci. Engineering. 2011. V. 4. P. 397–402.
3. Kundu B., Rajkhowa R., Kundu S.C., Wang X. // Adv. Drug Delivery Rev. 2013. V. 65. P. 457–470.
4. Kasoju N., Bora U. // Adv Healthc Mater. 2012. V. 1. № 4. P. 393–412.
5. Agapov I.I., Moisenovich M.M., Druzhinina T.V., Kamenchuk Y.A., Trofimov K.V., Vasilyeva T.V., Konkov A.S., Arhipova A.Yu., Sokolova O.S., Guzeev V.V. et al. // Dokl Biochem Biophys. 2011. V. 440. № 6. P. 830–833.
6. Moisenovich M.M., Pustovalova O., Shackelford J., Vasiljeva T.V., Druzhinina T.V., Kamenchuk Y.A., Guzeev V.V., Sokolova O.S., Bogush V.G., Debabov V.G., et al. // Biomaterials. 2012. V. 33. № 15. P. 3887–3898.
7. Moisenovich M.M., Pustovalova O.L., Arhipova A.Y., Vasiljeva T.V., Sokolova O.S., Bogush V.G., Debabov V.G., Sevastianov V.I., Kirpichnikov M.P., Agapov I.I., et al. // J. Biomed. Materials Res. 2011. V. 96. № 1. P. 125–131.
8. Agapov I.I., Pustovalova O.L., Moisenovich M.M., Bogush V.G., Sokolova O.S., Sevastyanov V.I., Debabov V.G., Kirpichnikov M.P. et al. // Dokl Biochem Biophys. 2009. V. 426. № 1. P. 127–130.
9. I.I.Agapov, M.M.Moisenovich, T.V.Vasilyeva, O.L.Pustovalova, A.S.Kon'kov, A.Yu Arkhipova, O.S.Sokolova, V.G.Bogush, V.I.Sevastianov, Corresponding Member of the RAS V.G. Debabov et al. // Dokl Biochem Biophys. 2010. V. 433. № 5. P. 699–702.
10. Bacakova L., Filova E., Rypacek F., Svorcik V., Stary V. // Physiol Res. 2004, V. 53 P. S35–S45.
11. Saltzman M.W. // Tissue Engineering: Engineering Principles for the Design of Replacement Organs and Tissues, Oxford: Oxford Academ. 2004. 538 p.
12. Edwards S.L., Mitchell W., Matthews J.B., Ingham E., Russell S.J. // AUTEX Res. J. 2004. V. 4. P. 86–94.
13. Wenk E., Merkle H.P., Meinel L. // J. Controlled Release. 2010. V. 150. P. 128–141.
14. Werner S., Krieg T., Smola H. // J. Invest. Dermatol. 2007. V. 127. № 5. P. 998–1008.
15. Trompezinski S., Berthier-Vergnes O., Denis A., Schmitt D., Viac J. // Exp. Dermatol. 2004. V. 13. № 2. P. 98–105.
16. Bauer S.M., Bauer R.J., Liu Z.J., Chen H., Goldstein L., Velazquez O.C. // J. Vasc. Surg. 2005. V. 41. № 4. P. 699–707.

# Impact of Surface Modification with Gold Nanoparticles on the Bioelectrocatalytic Parameters of Immobilized Bilirubin Oxidase

D. V. Pankratov[1,2], Y. S. Zeifman[2], A. V. Dudareva[3], G. K. Pankratova[1], M. E. Khlupova[1], Y. M. Parunova[2], D. N. Zajtsev[3], N. F. Bashirova[3], V. O. Popov[1,2], and S. V. Shleev[1,2,3*]

[1] A.N. Bach Institute of Biochemistry of Russian Academy of Sciences, Leninsky Ave. 33, building 2, 119071 Moscow, Russia

[2] National Research Center "Kurchatov Institute", Akademika Kurchatova Sq. 1, 123182 Moscow, Russia

[3] I.G. Petrovsky Bryansk State University, Bezhitskaya St. 14, 241036 Bryansk, Russia

*E-mail: shleev@inbi.ras.ru

Received 14.12.2013



**ABSTRACT** **We unveil experimental evidence that put into question the widely held notion concerning the impact of nanoparticles on the bioelectrocatalytic parameters of enzymatic electrodes. Comparative studies of the bioelectrocatalytic properties of fungal bilirubin oxidase from *Myrothecium verrucaria* adsorbed on gold electrodes, modified with gold nanoparticles of different diameters, clearly indicate that neither the direct electron transfer rate (standard heterogeneous electron transfer rate constants were calculated to be 31±9 $s^{-1}$) nor the biocatalytic activity of the adsorbed enzyme (bioelectrocatalytic constants were calculated to be 34±11 $s^{-1}$) depends on the size of the nanoparticles, which had diameters close to or larger than those of the enzyme molecules.**

**KEYWORDS** **gold nanoparticle; bilirubin oxidase; direct electron transfer; bioelectrocatalysis.**

**ABBREVIATIONS** **3D – three-dimensional; $A_{real}$ – real/electrochemical surface area; CV – cyclic voltammogram; ET – electron transfer; DET – direct electron transfer; $k_0$ – standard heterogeneous electron transfer rate constant; $k_{cat}^{app}$ – apparent bioelectrocatalytic constant; MCO – blue multicopper oxidase; *Mv*BOx – *Myrothecium verrucaria* bilirubin oxidase; $AuNP_n$ – gold nanoparticles with diameter of $n$ nm; $AuNP_n$/Au – gold electrode modified with $AuNP_n$ before and after cycling in sulfuric acid (m-AuNP/Au u-AuNP/Au, respectively); *Th*Lc – *Trametes hirsuta* laccase; PBS – phosphate buffered saline; NHE – normal hydrogen electrode; SEM – scanning electron microscopy; $A_{spr}$ – absorbance maximum; $A_{450}$ – absorbance at the wavelength of 450 nm; $\Gamma$ – enzyme surface concentration; $j_{max}$ – maximum current density.**

## INTRODUCTION

Numerous studies have reported on effective direct electron transfer (DET) of various enzymes (including blue multicopper oxidase – MCO) immobilized on the surface of nanostructured electrodes with metal and carbon nanoparticles, carbon nanotubes, graphene, etc. [1–3]. An increase in the bioelectrocatalytic current when using nanostructured surfaces was regarded as the defining evidence behind the acceleration of the DET reaction in these studies; however, neither a quantitative comparative analysis of DET based on a voltammograms analysis, nor a calculation of the standard constants of the heterogeneous electron transfer reaction ($k_0$) has been performed. Moreover, there are serious discrepancies in the data even for a single enzyme (in particular, laccase from the *Trametes hirsuta* (*Th*Lc) fungus immobilized on the gold surface). For instance, the use of AuNP and nanoporous gold helped to increase DET [4], whereas an extremely low bioelectrocatalytic activity of the enzyme was observed for DET [5] in nano/microstructured silicon chips modified with gold with the enzyme immobilized on their surface. Since the use of bioelectrodes without a nano-modified surface leads to a very low heterogeneous transfer rate and sometimes to a complete absence of DET, the routine explanation for enzyme "nanobinding" is the orientation of the enzyme on the nanostructured surface, which contributes to DET.

Despite the fact that a possible dependence of $k_0$ on the size of the metal or carbon nanoparticles has yet to be studied and that the two opposite dependences of the bioelectrocatalytic oxygen reduction current

on the diameter of AuNP on electrodes modified with MCO were recently demonstrated (*e.g.*, [6]), the belief remains that the size of AuNP used for electrode nanomodification is a very important factor that determines ET in the reactions between a redox enzyme and the electrode surface. This study offers experimental results that demonstrate the unlikeliness of this hypothesis.

## EXPERIMENTAL

### Materials and Methods

$Na_2HPO_4 \cdot 2H_2O$, $NaH_2PO_4 \cdot H_2O$, NaCl, $HAuCl_4 \cdot 3H_2O$, $H_2O_2$, $H_2SO_4$, $NaBH_4$, and sodium citrate were purchased from Sigma-Aldrich GmbH (Germany) and used without further purification. Oxygen was acquired from AGA Gas AB (Sweden). Buffers and other solutions were prepared using deionized water (18 MΩ·cm) produced using a PURELAB UHQ II system (ELGA Labwater, UK). All experiments were performed at room temperature in PBS (pH 7.4) consisting of a 50 mM $HPO_4^{2-}/H_2PO_4^-$ solution containing 150 mM NaCl.

*Mv*BOx was a gift from Amano Enzyme Inc. (Japan).

Electrochemical measurements were performed using a μAutolab Type III/FRA2 potentiostat/galvanostat (Metrohm Autolab BV, the Netherlands) using a three-electrode circuit with a saturated calomel reference electrode (242 mV *vs*. normal hydrogen electrode, NHE) and a platinum wire as an auxiliary electrode.

Sonication was performed using a Ultrasonic Cleaner XB2 bath (VWR International Ltd., UK). SEM was performed on a FEI Nova NanoLab 600 high-resolution scanning electron microscope (the Netherlands). Spectrophotometric studies were carried out using a PharmaSpec UV-1700 UV-visible spectrophotometer (China).

Nanoparticles with a diameter of 5 to 60 nm were synthesized to study the impact of the AuNP size on the biocatalytic properties of *Mv*BOx.

### Synthesis of gold nanoparticles with a preset particle size

AuNP with the expected diameter of 5 nm ($AuNP_5$, *Fig. 1A*) were synthesized as described in [7]. 50 ml of a 250 μM $HAuCl_4$ solution was stirred for 1 min at room temperature, then 1111 μl of a 38.8 mM sodium citrate solution was added to the initial solution, and the mixture was stirred for another 1 min. Next, 555 μl of a freshly prepared 0.075% (wt.) $NaBH_4$ solution in a 38.8 mM sodium citrate solution was poured into the reaction mixture and the solution was stirred for another 5 min.

AuNP with a diameter of 20–60 nm (*Fig. 1A*) were synthesized using sodium citrate as a reductant. 50 ml of a 250 μM $HAuCl_4$ solution was brought to boil under constant stirring; 750, 500, or 260 μl of a 1% (wt.) sodium citrate solution was subsequently added to obtain AuNP with diameters of 20, 40, and 60 nm ($AuNP_{20}$, $AuNP_{40}$ and $AuNP_{60}$), respectively. After adding sodium citrate, the mixture was incubated for 10 min under constant stirring without heating.

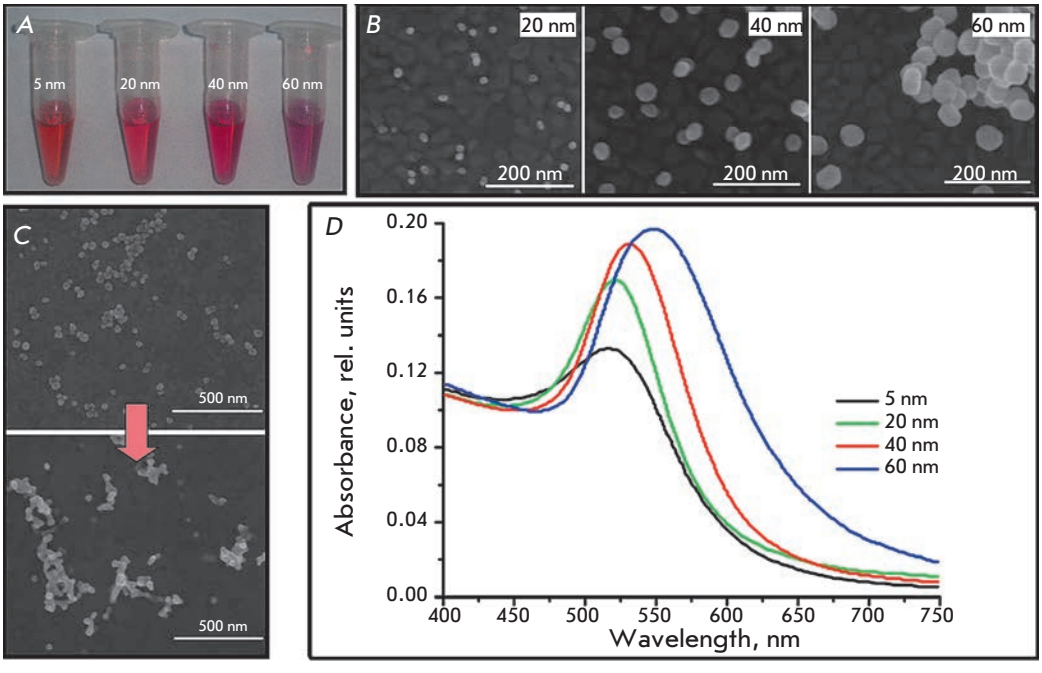


Fig. 1. A. Photos of the colloidal solutions of synthesized AuNPs; B. SEM images of AuNP/Au samples; C. SEM image of $AuNP_{40}$/Au before (top) and after (bottom) 2 cycles in $H_2SO_4$: D. Absorbance spectra of AuNP suspensions with different diameters

Table 1 | Comparative analysis of the diameters of synthesized AuNP as determined using different methods

| Diameter of AuNP, nm | | |
|---|---|---|
| Expected | Determined spectrophotometrically | Determined using the SEM data |
| 20 | 16 | 19±2 |
| 40 | 42-51 | 38±5 |
| 60 | 77 | 59±5 |

Table 2 | Real surface area vs. nanoparticles size

| AuNP diameter, nm | Real surface area, $cm^{-2}$ |
|---|---|
| 5 | 0.21±0.01 |
| 20 | 1.40±0.01 |
| 40 | 1.25±0.05 |
| 60 | 1.23±0.03 |

The diameter of the resulting nanoparticles was evaluated spectrophotometrically in accordance with the procedure described in [7] using the wavelength of maximum absorbance ($A_{spr}$, *Fig. 1D*). The diameter of a AuNP less than 35 nm in size was calculated using the $A_{spr}/A_{450}$ ratio.

Nanoparticles 20-60 nm in size were further identified using SEM. The samples for microscopy were prepared by applying a small amount of AuNP obtained from diluted colloidal solutions over the flat surface of gold electrodes (*Fig. 1B*). It should be emphasized that the surface structure of the electrodes used in further studies was fundamentally different from that shown in *Fig. 1* due to a significantly higher amount of applied AuNP and surface changes resulting from treatment with $H_2SO_4$ (see below); thus, it can only be used to evaluate the diameters of the synthesized AuNP.

The results of a size evaluation of the nanoparticles produced through independent methods are shown in Table 1.

The data shown in *Figs. 1B,D* allow one to conclude that a direct determination of the AuNP size using the SEM method provides the most accurate and consistent data suitable for a statistical evaluation of the particle size distribution. However, this method has sensitivity limitations; in particular, in this case it was impossible to estimate the size of nanoparticles smaller than 10 nm.

All the prepared AuNP solutions, except for AuNP with a diameter of 5 nm, were concentrated by centrifugation at 10,000 g for 30 min. 95% of the supernatant was removed, and the AuNP precipitate was re-suspended using sonication. Nanoparticles 5 nm in diameter could not be concentrated using the proposed method; thus, the diluted solution was used for further experiments.

## Purification of gold electrodes and their modification with AuNP

Polycrystalline gold disc electrodes (Bioanalytical Systems, USA) with a geometric surface area of 0.031 $cm^2$ were mechanically cleaned through polishing with Microcloth paper (Buehler, UK) in an aluminum oxide suspension with a particle size of 0.1 μm (Struers, Denmark) to obtain a mirror surface. The electrodes were further washed with deionized water and electrochemically purified through cycling in 0.5 M $H_2SO_4$ using a range of potentials from −0.1 to +1.9 V *vs*. NHE for 20 cycles at a scan rate of 0.1 $V \cdot s^{-1}$, then they were washed with water and dried in an air stream.

Following this, 5 μl of the solution (for concentrated suspensions) or 6 μl of the solution (for an AuNP suspension with a particle diameter of 5 nm ($AuNP_5$)) was applied to the cleaned gold electrode surface. The modified electrode was then dried at room temperature. The AuNP modification procedure was repeated twice for concentrated suspensions of nanoparticles and 5 times for $AuNP_5$. The obtained electrodes were cycled in 0.5 M $H_2SO_4$ with the potential ranging from 0.0 to +1.9 V *vs*. NHE. Two cycles were performed in order to avoid desorption and/or agglomeration of nanoparticles on the surface (*Fig. 1C*) at a scan rate of 0.1 $V \cdot s^{-1}$. The electrodes were then washed with water and dried. The electrochemically active (real) surface area of the electrodes ($A_{real}$) was calculated according to [8], assuming the level of the charge required for the reduction of gold oxide during electrochemical cycling under specified conditions to be equal to 390 ± 10 $\mu C \cdot cm^{-2}$ [9].

The results of the calculation of $A_{real}$ presented in Table 2 show no direct relationship between $A_{real}$ and the size of the AuNP used for surface modification. This fact indirectly confirms earlier results [10] on the formation of a disordered three-dimensional structure via repeated cycling of the AuNP/Au electrode in 0.5 M $H_2SO_4$. In connection to this, two types of AuNP/Au electrodes were used in further experiments: either treated with $H_2SO_4$ (m-AuNP/Au) or without cycling (u-AuNP/Au). $A_{real}$ for u-AuNP/Au electrodes was assumed to be equal to $A_{real}$ for m-AuNP/Au samples.

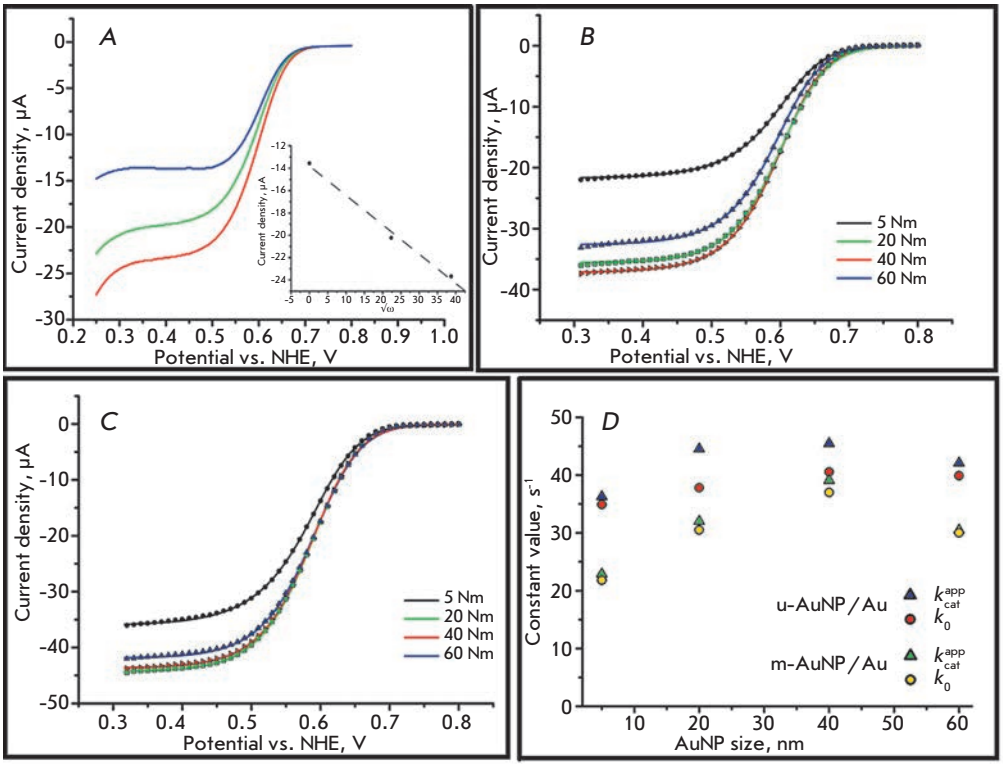


Fig. 2. A) Cyclic voltammograms (cathodic waves) of biomodified m-AuNP$_{20}$/Au electrodes recorded at different rotation rates, rpm: 0 (blue), 500 (green) and 1500 (red). Inset – current density at 0.35 V as a function of $\omega^{1/2}$; B), C). Cyclic voltammograms (cathodic waves) of *Mv*BOx modified m-AuNP/Au (B) and u-AuNP/Au (C) electrodes based on AuNPs of different diameters; D) Dependences of the calculated bioelectrocatalytic parameters on the size of AuNPs.
Conditions for all CVs: oxygen saturated PBS, scan rate – 20 mV s$^{-1}$, second cycle

Biomodification of the surface of AuNP/Au electrodes was carried out through direct adsorption of the enzyme for 20 min from a *Mv*BOx solution with a protein concentration of 0.25 mg·ml$^{-1}$. The surface concentration of the enzyme was assumed to be 3.0 pmol·cm$^{-2}$.

The $k_0$ and $k_{cat}^{app}$ values were calculated using the MathCAD 14 software package and the equation:

$$j = \frac{j_{max}}{1+\exp\left[\frac{F}{RT}\left(E-E_{T1}^{0'}\right)\right]+\frac{k_5}{k_0}\exp\left[\frac{\alpha F}{RT}\left(E-E_{T1}^{0'}\right)\right]},$$

$$k_5 = \frac{k_{cat}[O_2]}{K_M+[O_2]}.$$

The kinetic scheme of enzyme functioning used to establish the equation was presented in [11].

## RESULTS AND DISCUSSION

The bioelectrodes were placed in oxygenated PBS, followed by CV recording at an electrode rotation speed of 1,500 min$^{-1}$ to eliminate possible diffusion limitations (*Fig. 2A*). A pronounced bioelectrocatalytic response with an initial oxygen electrical reduction potential of about 0.75 V was registered for all the electrodes used. As illustrated in *Fig. 2B,C*, substantially similar $j_{max}$ values were obtained using the electrodes biomodified with m-AuNP/Au (31.4 ± 5.9 μA·cm$^{-2}$ ) and u-AuNP/Au (43.4 ± 5.6 μA·cm$^{-2}$) electrodes.

Taking these data into account, the $k_0$ (31 ± 9 s$^{-1}$) and $k_{cat}^{app}$ (34 ± 11 s$^{-1}$) values were calculated. The results are shown in *Fig. 2D*. The calculated $k_0$ and $k_{cat}^{app}$ values are similar regardless of the AuNP diameter and the electrode type used. The similarity of the constants for the electrodes based on m-AuNP/Au and u-AuNP/Au indicates that the assumption of identity of the $A_{real}$ (despite different structures) for both types of samples does not add a critical error to the calculations. The overestimated constants for u-AuNP/Au attest to the slightly higher surface area of those electrodes compared to m-AuNP/Au, owing to the absence of AuNP agglomerates (*Fig. 1C*), which also reduces the $A_{real}$. The pronounced bends of constant *vs.* AuNP size profiles observed when using m-AuNP/Au may be due to the surface modification because of the formation of different three-dimensional (3D) structures during the treatment of electrodes in $H_2SO_4$. The behavior of the enzyme on these heterogeneous surfaces cannot be fully described by the single theory used in this study to calculate biocatalytic parameters without introducing additional corrections. Moreover, the formation of 3D agglomerates yields errors when a single value of the surface concentration of the enzyme (3.0 pmol·cm$^{-2}$) is used for all the m-AuNP/

Au-based bioelectrodes. This fact can also explain the shape of the curves. However, based on the experimental data and simulation results, we can affirm that the bioelectrocatalytic properties of *Mv*BOx immobilized on the AuNP/Au surface show no dependence on the nanoparticle diameter. The increased electrocatalytic current of the bioelectrodes modified with nanoparticles of different sizes found in a number of previous studies is most likely associated with an increase in the geometrical surface area rather than the acceleration of the DET reactions or an increase in the bioelectrocatalytic constants of the immobilized enzymes.

## CONCLUSIONS

Our results have experimentally demonstrated no relationship between the bioelectrocatalytic parameters of *Mv*BOx immobilized on the AuNP/Au surface and the nanoparticle diameter. However, it should be noted that the results obtained in this study cannot be extrapolated to other nanobiomodified surfaces (*e.g.*, other nanoparticles and redox enzymes). In particular, it is of particular interest to study the impact of nanoparticles with a diameter lower than the size of the enzyme that can promote electron transfer between the enzyme and the electrode surface. Such experiments will provide a more complete picture of the impact of nanoparticles on the bioelectrocatalytic parameters of oxidoreductases. ●

*This study was supported by the Russian Foundation for Basic Research (grant № 12-04-33102-mol-a-ved).*

REFERENCES

1. Murata K., Kajiya K., Nakamura N., Ohno H. // Energy & Environmental Science. 2009. V. 2. № 12. P. 1280–1285.
2. Dagys M., Haberska K., Shleev S., Arnebrant T., Kulys J., Ruzgas T. // Electrochemistry Communications. 2010. V. 12. № 7. P. 933–935.
3. Pankratov D. V., Zeifman Y. S., Morozova O. V., Shumakovich G. P., Vasil'eva I. S., Shleev S., Popov V. O., Yaropolov A. I. // Electroanalysis. 2013. V. 25. № 5. P. 1143–1149.
4. Salaj-Kosla U, Poller S., Schuhmann W., Shleev S., Magner E. // Bioelectrochemistry. 2013. V. 91. P. 15–20.
5. Ressine A., Vaz-Dominguez C., Fernandez V. M., De Lacey A. L., Laurell T., Ruzgas, T., Shleev S. // Biosensors & Bioelectronics. 2010. V. 25. № 5. P. 1001–1007.
6. Gutierrez-Sanchez C., Pita M., Vaz-Dominguez C., Shleev S., De Lacey A. L. // Journal of the American Chemical Society. 2012. V. 134. № 41. P. 17212–17220.
7. Haiss W., Thanh N. T. K., Aveyard J., Fernig D. G. // Analytical Chemistry. 2007. V. 79. № 11. P. 4215–4221.
8. Murata K., Kajiya K., Nukaga M., Suga Y., Watanabe T., Nakamura N., Ohno H. // Electroanalysis. 2010. V. 22. № 2. P. 185–190.
9. Trasatti S., Petrii O. A. // Pure and Applied Chemistry. 1991. V. 63. № 5. P. 711–734.
10. Wang X., Falk M., Ortiz R., Matsumura H., Bobacka J., Ludwig R., Bergelin M., Gorton L., Shleev S. // Biosensors & Bioelectronics. 2012. V. 31. № 1. P. 219–225.
11. Climent V., Zhang J. D., Friis E. P., Østergaard L. H., Ulstrup, J. // The Journal of Physical Chemistry C. 2012. V. 116. № 1. P. 1232–1243.

## GENERAL RULES

*Acta Naturae* publishes experimental articles and reviews, as well as articles on topical issues, short reviews, and reports on the subjects of basic and applied life sciences and biotechnology.

The journal is published by the Park Media publishing house in both Russian and English.

The journal *Acta Naturae* is on the list of the leading periodicals of the Higher Attestation Commission of the Russian Ministry of Education and Science

The editors of *Acta Naturae* ask of the authors that they follow certain guidelines listed below. Articles which fail to conform to these guidelines will be rejected without review. The editors will not consider articles whose results have already been published or are being considered by other publications.

The maximum length of a review, together with tables and references, cannot exceed 60,000 symbols (approximately 40 pages, A4 format, 1.5 spacing, Times New Roman font, size 12) and cannot contain more than 16 figures.

Experimental articles should not exceed 30,000 symbols (20 pages in A4 format, including tables and references). They should contain no more than ten figures. Lengthier articles can only be accepted with the preliminary consent of the editors.

A short report must include the study's rationale, experimental material, and conclusions. A short report should not exceed 12,000 symbols (8 pages in A4 format including no more than 12 references). It should contain no more than four figures.

The manuscript should be sent to the editors in electronic form: the text should be in Windows Microsoft Word 2003 format, and the figures should be in TIFF format with each image in a separate file. In a separate file there should be a translation in English of: the article's title, the names and initials of the authors, the full name of the scientific organization and its departmental affiliation, the abstract, the references, and figure captions.

## MANUSCRIPT FORMATTING

The manuscript should be formatted in the following manner:

- Article title. Bold font. The title should not be too long or too short and must be informative. The title should not exceed 100 characters. It should reflect the major result, the essence, and uniqueness of the work, names and initials of the authors.
- The corresponding author, who will also be working with the proofs, should be marked with a footnote *.
- Full name of the scientific organization and its departmental affiliation. If there are two or more scientific organizations involved, they should be linked by digital superscripts with the authors' names. Abstract. The structure of the abstract should be very clear and must reflect the following: it should introduce the reader to the main issue and describe the experimental approach, the possibility of practical use, and the possibility of further research in the field. The average length of an abstract is 20 lines (1,500 characters).
- Keywords (3 – 6). These should include the field of research, methods, experimental subject, and the specifics of the work. List of abbreviations.
- INTRODUCTION
- EXPERIMENTAL PROCEDURES
- RESULTS AND DISCUSSION
- CONCLUSION

  The organizations that funded the work should be listed at the end of this section with grant numbers in parenthesis.
- REFERENCES

  The in-text references should be in brackets, such as [1].

## RECOMMENDATIONS ON THE TYPING AND FORMATTING OF THE TEXT

- We recommend the use of Microsoft Word 2003 for Windows text editing software.
- The Times New Roman font should be used. Standard font size is 12.
- The space between the lines is 1.5.
- Using more than one whole space between words is not recommended.
- We do not accept articles with automatic referencing; automatic word hyphenation; or automatic prohibition of hyphenation, listing, automatic indentation, etc.
- We recommend that tables be created using Word software options (Table → Insert Table) or MS Excel. Tables that were created manually (using lots of spaces without boxes) cannot be accepted.
- Initials and last names should always be separated by a whole space; for example, A. A. Ivanov.
- Throughout the text, all dates should appear in the "day.month.year" format, for example 02.05.1991, 26.12.1874, etc.
- There should be no periods after the title of the article, the authors' names, headings and subheadings, figure captions, units (s – second, g – gram, min – minute, h – hour, d – day, deg – degree).
- Periods should be used after footnotes (including those in tables), table comments, abstracts, and abbreviations (mon. – months, y. – years, m. temp. – melting temperature); however, they should not be used in subscripted indexes ($T_m$ – melting temperature; $T_{p.t}$ – temperature of phase transition). One exception is mln – million, which should be used without a period.
- Decimal numbers should always contain a period and not a comma (0.25 and not 0,25).
- The hyphen ("-") is surrounded by two whole spaces, while the "minus," "interval," or "chemical bond" symbols do not require a space.
- The only symbol used for multiplication is "×"; the "×" symbol can only be used if it has a number to its right. The "·" symbol is used for denoting complex compounds in chemical formulas and also noncovalent complexes (such as DNA·RNA, etc.).
- Formulas must use the letter of the Latin and Greek alphabets.

- Latin genera and species' names should be in italics, while the taxa of higher orders should be in regular font.
- Gene names (except for yeast genes) should be italicized, while names of proteins should be in regular font.
- Names of nucleotides (A, T, G, C, U), amino acids (Arg, Ile, Val, etc.), and phosphonucleotides (ATP, AMP, etc.) should be written with Latin letters in regular font.
- Numeration of bases in nucleic acids and amino acid residues should not be hyphenated (T34, Ala89).
- When choosing units of measurement, SI units are to be used.
- Molecular mass should be in Daltons (Da, KDa, MDa).
- The number of nucleotide pairs should be abbreviated (bp, kbp).
- The number of amino acids should be abbreviated to aa.
- Biochemical terms, such as the names of enzymes, should conform to IUPAC standards.
- The number of term and name abbreviations in the text should be kept to a minimum.
- Repeating the same data in the text, tables, and graphs is not allowed.

## GUIDENESS FOR ILLUSTRATIONS

- Figures should be supplied in separate files. Only TIFF is accepted.
- Figures should have a resolution of no less than 300 dpi for color and half-tone images and no less than 500 dpi.
- Files should not have any additional layers.

## REVIEW AND PREPARATION OF THE MANUSCRIPT FOR PRINT AND PUBLICATION

Articles are published on a first-come, first-served basis. The publication order is established by the date of acceptance of the article. The members of the editorial board have the right to recommend the expedited publishing of articles which are deemed to be a priority and have received good reviews.

Articles which have been received by the editorial board are assessed by the board members and then sent for external review, if needed. The choice of reviewers is up to the editorial board. The manuscript is sent on to reviewers who are experts in this field of research, and the editorial board makes its decisions based on the reviews of these experts. The article may be accepted as is, sent back for improvements, or rejected.

The editorial board can decide to reject an article if it does not conform to the guidelines set above.

A manuscript which has been sent back to the authors for improvements requested by the editors and/or reviewers is reviewed again, after which the editorial board makes another decision on whether the article can be accepted for publication. The published article has the submission and publication acceptance dates set at the beginning.

The return of an article to the authors for improvement does not mean that the article has been accepted for publication. After the revised text has been received, a decision is made by the editorial board. The author must return the improved text, together with the original text and responses to all comments. The date of acceptance is the day on which the final version of the article was received by the publisher.

A revised manuscript must be sent back to the publisher a week after the authors have received the comments; if not, the article is considered a resubmission.

E-mail is used at all the stages of communication between the author, editors, publishers, and reviewers, so it is of vital importance that the authors monitor the address that they list in the article and inform the publisher of any changes in due time.

After the layout for the relevant issue of the journal is ready, the publisher sends out PDF files to the authors for a final review.

Changes other than simple corrections in the text, figures, or tables are not allowed at the final review stage. If this is necessary, the issue is resolved by the editorial board.

## FORMAT OF REFERENCES

The journal uses a numeric reference system, which means that references are denoted as numbers in the text (in brackets) which refer to the number in the reference list.

*For books:* the last name and initials of the author, full title of the book, location of publisher, publisher, year in which the work was published, and the volume or issue and the number of pages in the book.

*For periodicals:* the last name and initials of the author, title of the journal, year in which the work was published, volume, issue, first and last page of the article. Must specify the name of the first 10 authors. Ross M.T., Grafham D.V., Coffey A.J., Scherer S., McLay K., Muzny D., Platzer M., Howell G.R., Burrows C., Bird C.P., et al. // Nature. 2005. V. 434. № 7031. P. 325–337.

References to books which have Russian translations should be accompanied with references to the original material listing the required data.

References to doctoral thesis abstracts must include the last name and initials of the author, the title of the thesis, the location in which the work was performed, and the year of completion.

References to patents must include the last names and initials of the authors, the type of the patent document (the author's rights or patent), the patent number, the name of the country that issued the document, the international invention classification index, and the year of patent issue.

The list of references should be on a separate page. The tables should be on a separate page, and figure captions should also be on a separate page.

**The following e-mail addresses can be used to contact the editorial staff: vera.knorre@gmail.com, actanaturae@gmail.com, tel.: (495) 727-38-60, (495) 930-87-07**